Measuring azimuthal asymmetries in semi-inclusive deep-inelastic scattering off transversely polarized protons

Heiner Wollny

Fakultät für Mathematik und Physik
Albert-Ludwigs-Universität Freiburg

Measuring azimuthal asymmetries in semi-inclusive deep-inelastic scattering off transversely polarized protons

Dissertation
zur
Erlangung des Doktorgrades
der
Fakultät für Mathematik und Physik
der
Albert-Ludwigs-Universität
Freiburg im Breisgau

vorgelegt von
Heiner Wollny
aus
Villingen im Schwarzwald

Freiburg, April 2010

Dekan:	Prof. Dr. Kay Königsmann
Leiter der Arbeit:	Prof. Dr. Horst Fischer
Referent:	Prof. Dr. Horst Fischer
Koreferent:	Prof. Dr. Karl Jakobs
Tag der Verkündigung des Prüfungsergebnisses:	08.06.2010

Contents

List of Figures

List of Tables

1. Introduction

The visible matter which surrounds us is built up of atoms, which themselves consist of electrons, protons and neutrons. Since the latter two form the atomic nucleus they are called nucleons. All three particles carry half-integer spin. Whereas the electron is point-like, measurements of the anomalous magnetic moment of the nucleon, as well as the large number of new particles observed in scattering experiments in the 1960's, suggested that the nucleon is not elementary, but has to be built up of constituents. In 1964 Gell-Mann and Zweig proposed that the nucleon is composed of three 'quarks', each of which carries spin $1/2\,\hbar$ and a fractional electric charge [1, 2].
In 1969 R. Feynman [3] formulated the so-called 'parton model' to explain the characteristics of the cross-section for high energetic lepton-nucleon scattering. He proposed that the scattering takes place at 'partons', free point-like spin $1/2\,\hbar$ particles inside the nucleon. In this formalism the 'partons' have each, compared to the nucleon, a negligible mass and the number of 'partons' is arbitrarily large, whereas the three 'quarks' in the 'quark model' carry each approximately one third of the nucleon mass.

This seeming difference between the two models and the fact that single 'quarks' or 'partons' could not be observed, was solved in 1973 by D. Gross and F. Wilczek [4] and D. Politzer [5]. They worked out a theoretical description of the 'quark' interactions. A field theory with 'gluons' as mediator particles, which couple to the color charge of the 'quarks' and to themselves. Six years later the 'gluons' could indeed be experimentally verified [6]. In the current understanding the nucleon is made up of three valence quarks surrounded by a cloud of gluons. The gluons can fluctuate for a short time into quark-antiquark pairs, the so-called sea-quarks.

Today it is well known, that half of the momentum of the nucleon is carried by the quarks and the remaining part by the gluons. However, to this day it is still a puzzle how the helicity of the nucleon is made up of its constituents. Former considerations, that it is dominantly carried by the three valence quarks have been ruled out in 1987 by the European Muon Collaboration [7]. Several other experiments confirmed this result and today it is established that only about 25 % of the nucleon spin is carried by the quarks. Consequently new models have been developed, taking also into account helicity contributions of the gluons and angular momenta of quarks and gluons. Due to the technical challenge to measure those quantities it is still not clear how the helicity of the nucleon is formed.

However, the number density and the helicity distribution of the constituents is not sufficient for the description of the nucleon. A third distribution function, called transversity is needed for a complete understanding at leading order. It was first introduced by Ralston and Soper [8] in 1979. As the name suggests this distribution function describes the spin structure of a transversely polarized nucleon. If the constituents of the nucleon would be non-relativistic objects the transversity distribution would coincide with the helicity distribution, because they could be transformed into each other by a simple rotation. Hence the difference between the two distribution functions is a direct indication of the relativistic nature of the constituents of the nucleon. Until today the transversity distribution function is poorly known, because of the fact that it is not accessible in deep-inelastic lepton-nucleon scattering (DIS), the standard tool for measuring the number density and the helicity distribution of the constituents of the nucleon.

In the 1990's the situation got even more complex. At that time theorists started to consider also intrinsic transverse momenta of the quarks inside the nucleon. So far those have been neglected by physicists, because the observable effects were expected to be small. However, large asymmetries observed in pion production in transversely polarized proton-proton scattering ($p^{\uparrow}\, p \rightarrow \pi\, X$) [9] changed this way of thinking. Taking into account intrinsic transverse momenta of the quarks inside the nucleon, in total eight distribution functions are needed to describe the nucleon at leading order. Among these eight the Sivers function, describing the correlation of transverse momentum of quarks with the spin of a transversely polarized nucleon, is of special interest, because it is linked to angular momentum of the quarks, which is one of the missing pieces in the nucleon spin puzzle. Like the transversity distribution the Sivers function is hardly known, as it cannot be accessed in DIS, too.

Several experiments, located in Europe, the United States and Japan, are presently collecting data to improve the knowledge about the spin structure of the nucleon. For a recent report on the progress in this field see [10].

The COMPASS experiment at the international research center CERN (European Organization for Nuclear Research) is dedicated to study the longitudinal and transverse spin structure of the nucleon. It is a fixed target experiment at the end of the M2 beam line of the SPS accelerator, which provides a high energy longitudinally polarized muon beam. In the years 2002, 2003, 2004 and 2006 COMPASS took data scattering off polarized deuterons and in the year 2007 scattering off polarized protons. The analysis of the data taken in 2007 with transversely polarized protons is the topic of this thesis.

The thesis is organized as follows. In Chapter 2 a theoretical introduction about transverse spin physics is given, with a main focus on the transversity distribution and the Sivers distribution, whose measurement in semi-inclusive deep-inelastic scattering off transversely polarized protons is the goal of this work. In Chapter 3 a brief overview of the COMPASS detector is given. Here the focus is on the description of the detector elements, which are relevant for the analysis of the data. The stability studies of the data taken in 2007 are discussed in Chapter 4. Here the developed algorithms to automatize the monitoring of instabilities during data taking are presented. The analysis of the single spin asymmetry in two hadron production, related to transversity is described in Chapter 5. Here the event selection, the fitting method to extract the single spin asymmetries, the studies to evaluate the systematical uncertainties and the obtained results are discussed in detail. In Chapter 6, the analysis of the single spin asymmetries in single hadron production, related to transversity and the Sivers distribution is described. Here, in particular, the systematical error of the results is discussed and the results are compared to measurements of the HERMES group and recent theoretical predictions. Finally the work of this thesis is summarized in Chapter 7.

2. Theory

In this chapter the theoretical background about transverse spin physics will be presented, following the review of [11] and [12], respectively. However, the main focus will be on the transversity and the Sivers distribution functions.

At the beginning inclusive deep-inelastic scattering (DIS) will be discussed to introduce the basic principles of the theoretical description and to demonstrate, that neither the transversity nor the Sivers distribution functions can be accessed in such a measurement. Next semi-inclusive deep-inelastic scattering (SIDIS) is discussed, which means that beside the scattered lepton parts of the hadronic final state are detected too. Here, both distribution functions contribute in leading order and can be measured via single spin asymmetries.

Several semi-inclusive channels have been proposed to measure transversity. In this thesis two of them are studied in detail, namely single hadron production, involving the Collins fragmentation function, and two hadron production, involving the dihadron interference fragmentation function. In Sec. 2.5, Drell-Yan and Λ-production, two further channels are mentioned very briefly.

2.1 Deep-Inelastic Scattering (DIS)

Deep-inelastic lepton-nucleon scattering is the common tool to investigate the structure of the nucleon. The process of a lepton l scattering off a nucleon P can be formulated as:

$$l + P \rightarrow l' + X, \tag{2.1}$$

in which l' is the outgoing scattered lepton and X denotes the undetected remainders, like for example the produced hadrons in the fragmentation of the struck quark. In Fig. 2.1 a schematic picture of the process for one photon exchange is shown. This approximation is well fulfilled for COMPASS, since the center of mass energy is about 18 GeV. The relevant variables to describe the reaction are listed in Tab. 2.1. In the following $\hbar = c = 1$ is used.

2.1.1 Inclusive Cross-Section and Structure Functions

The cross-section for polarized DIS lepton-nucleon scattering can be written as a contraction between a leptonic and a hadronic tensor [11]:

$$\frac{\mathrm{d}^3\sigma}{\mathrm{d}x\,\mathrm{d}y\,\mathrm{d}\phi} = \frac{\alpha^2 y}{2Q^4} L_{\mu\nu} W^{\mu\nu}, \tag{2.2}$$

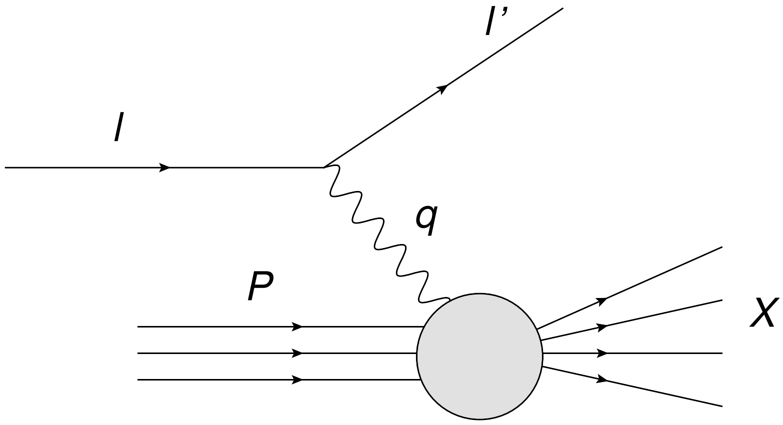

Figure 2.1: Schematic picture of deep-inelastic lepton-nucleon scattering for one photon exchange.

Table 2.1: Kinematic variables relevant for DIS and SIDIS.

Mass of target nucleon	M
Mass of incoming lepton	m
4-momentum of target nucleon	$P = (M, 0)$
4-momentum of incoming lepton	$l = (E, \boldsymbol{l})$
4-momentum of outgoing lepton	$l' = (E', \boldsymbol{l'})$
4-momentum of virtual photon	$q = l - l'$
Negative squared 4-momentum transfer	$Q^2 = -q^2$
Energy of the virtual photon	$\nu = \frac{P \cdot q}{M} \overset{\text{lab}}{=} E - E'$
Fractional energy of the virtual photon	$y = \frac{P \cdot q}{P \cdot l} \overset{\text{lab}}{=} \frac{\nu}{E}$
Bjorken scaling variable	$x = \frac{Q^2}{2P \cdot q} = \frac{Q^2}{2M\nu}$
Squared invariant center of mass energy	$s = (P + l)^2$
Squared invariant mass of the photon-nucleon system	$W^2 = (P + q)^2 = M^2 + 2M\nu - Q^2$
4-momentum of a hadron in the final state	$P_h = (E_h, \boldsymbol{P}_h)$
Fractional energy of the observed final state hadron	$z = \frac{P \cdot P_h}{P \cdot q} \overset{\text{lab}}{=} \frac{E_h}{\nu}$

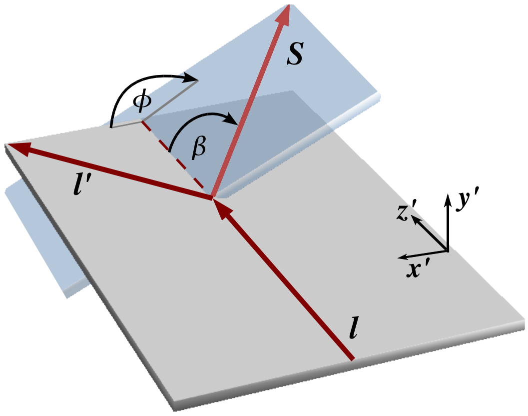

Figure 2.2: Definition of the azimuthal angle ϕ, measured around direction of incoming lepton $\boldsymbol{l}$ and definition of the angle β between $\boldsymbol{l}$ and $\boldsymbol{S}$.

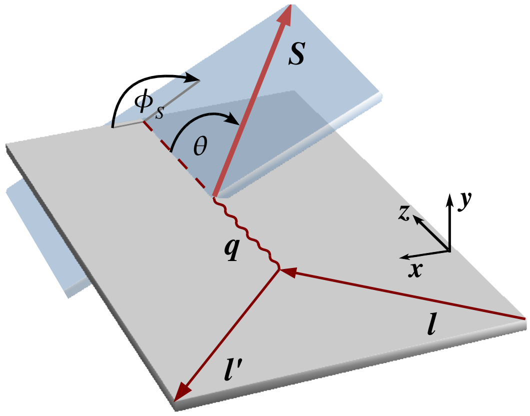

Figure 2.3: Definition of the azimuthal angle ϕ_S, measured around direction of virtual photon $\boldsymbol{q}$ and definition of the angle θ between $\boldsymbol{q}$ and $\boldsymbol{S}$.

where $\alpha = \frac{e^2}{4\pi}$ is the electromagnetic coupling constant and ϕ is the azimuthal angle measured around the direction of the incoming lepton between the scattering plane defined by incoming and outgoing lepton and the target nucleon spin $\boldsymbol{S}$, as shown in Fig. 2.2.

The leptonic tensor contains the information on the emission of the virtual photon by the incoming lepton, which can be computed in QED. It can be separated in a symmetric and an antisymmetric part:

$$L_{\mu\nu} = L_{\mu\nu}^{(S)}(l, l') + L_{\mu\nu}^{(A)}(l, s_l, l'). \tag{2.3}$$

Only the antisymmetric part $L_{\mu\nu}^{(A)}$ depends on the spin s_l of the incoming lepton. It is summed over the spin states of the outgoing lepton, since these are usually not measured.

The interaction between the virtual photon and the nucleon is described in the hadronic tensor. It contains the complex structure of the nucleon, which cannot be computed from QCD because of non-perturbative effects in the strong interactions. Symmetries and conservation laws of the strong interactions restrict the form of $W^{\mu\nu}$ and it can be parametrized by four structure functions, F_1, F_2, g_1 and g_2, which depend on x and Q^2 [13, 14]. The hadronic tensor can be divided into a symmetric and an antisymmetric part:

$$W^{\mu\nu} = W^{\mu\nu(S)}(P, q) + W^{\mu\nu(A)}(P, S, q). \tag{2.4}$$

Again only the antisymmetric part depends on the initial spin of the target nucleon. Therefore, since the contraction of a symmetric and an antisymmetric tensor cancels, the cross-section is separated in a part containing no spin and a part depending on the spin of the incoming lepton and the spin of the target:

$$\frac{\mathrm{d}^3\sigma}{\mathrm{d}x\,\mathrm{d}y\,\mathrm{d}\phi} = \frac{\alpha^2 y}{2Q^4}\left[L_{\mu\nu}^{(S)}(l, l')W^{\mu\nu(S)}(P, q) - L_{\mu\nu}^{(A)}(l, s_l, l')W^{\mu\nu(A)}(P, S, q)\right]. \tag{2.5}$$

This implies, in case of inclusive DIS, that one has to have a polarized beam as well as a polarized target to measure spin related properties of the nucleon. Decomposing the spin dependent part of the cross-section further into a part parallel $\mathrm{d}^3\sigma_\parallel$ and a part perpendicular $\mathrm{d}^3\sigma_\perp$ to the direction of the incoming lepton, one obtains:

$$\frac{\mathrm{d}^3\sigma}{\mathrm{d}x\,\mathrm{d}y\,\mathrm{d}\phi} = \frac{\mathrm{d}^3\bar{\sigma}}{\mathrm{d}x\,\mathrm{d}y\,\mathrm{d}\phi} - \lambda_l \cos\beta \frac{\mathrm{d}^3\sigma_\parallel}{\mathrm{d}x\,\mathrm{d}y\,\mathrm{d}\phi} - \lambda_l \sin\beta\cos\phi \frac{\mathrm{d}^3\sigma_\perp}{\mathrm{d}x\,\mathrm{d}y\,\mathrm{d}\phi}, \tag{2.6}$$

with $\lambda_l = \pm 1$ being the helicity of the incoming lepton $\boldsymbol{l}$ and β the angle between $\boldsymbol{l}$ and target spin $\boldsymbol{S}$ as shown in Fig. 2.2. Hence for a longitudinal polarized target $\sin\beta = 0$ and $\mathrm{d}^3\sigma_\perp$ vanishes and for a transversely polarized target $\mathrm{d}^3\sigma_\parallel$ vanishes, because of $\cos\beta = 0$.

The three parts of the cross-section can be parametrized as follows:

$$\frac{\mathrm{d}^3\bar{\sigma}}{\mathrm{d}x\mathrm{d}y\mathrm{d}\phi} = \frac{4\alpha^2}{Q^2}\left[\frac{y}{2}F_1(x,Q^2) + \frac{1}{2xy}\left(1 - y - \frac{y^2\gamma^2}{4}\right)F_2(x,Q^2)\right], \tag{2.7a}$$

$$\frac{\mathrm{d}^3\sigma_\parallel}{\mathrm{d}x\mathrm{d}y\mathrm{d}\phi} = \frac{4\alpha^2}{Q^2}\left[\left(1 - y - \frac{y^2\gamma^2}{4}\right)g_1(x,Q^2) - \frac{y}{2}\gamma^2 g_2(x,Q^2)\right], \tag{2.7b}$$

$$\frac{\mathrm{d}^3\sigma_\perp}{\mathrm{d}x\mathrm{d}y\mathrm{d}\phi} = \frac{4\alpha^2}{Q^2}\left[\gamma\sqrt{1 - y - \frac{y^2\gamma^2}{4}}\left(\frac{y}{2}g_1(x,Q^2) + g_2(x,Q^2)\right)\right], \tag{2.7c}$$

with $\gamma = \frac{2xM}{Q}$, which decreases to zero for $Q^2 \to \infty$. The structure functions F_1 and F_2, parameterizing the unpolarized part $\mathrm{d}^3\bar{\sigma}$ of the cross-section, have been measured in very high accuracy over a broad range in x and Q^2 for proton and deuteron targets [15]. In Fig. 2.4 a compilation of measurements of the proton structure function F_2^p as a function of Q^2 for different x is shown. It is experimentally verified that in the Bjorken limit ($\nu, Q^2 \to \infty$ and $x = \frac{Q^2}{2M\nu}$) $F_1(x,Q^2)$ and $F_2(x,Q^2)$ depend only on x and only weak on Q^2, as predicted by [16]. This is called Bjorken-scaling. In addition they fulfill the Callan-Gross relation [17]:

$$2xF_1(x) = F_2(x). \tag{2.8}$$

These results can be interpreted in the parton model, which will be introduced in Sec. 2.2. The scattering takes place at point-like particles, with spin $\frac{1}{2}$.

The two spin dependent parts of the cross-section $\mathrm{d}^3\sigma_\parallel$ and $\mathrm{d}^3\sigma_\perp$ are parametrized with the structure functions g_1 and g_2. For a longitudinal polarized target g_2 is strongly suppressed by γ^2, hence the cross-section is only sensitive to g_1. In the cross-section for a transversely polarized target both structure functions occur with the same strength, however the whole cross-section is suppressed by a factor γ with respect to the longitudinal one.

2.1.1.1 Orientation of Target Polarization

So far the direction of the incoming lepton was taken as reference for the orientation of the target polarization. This makes sense from experimental point of view, since this direction can be controlled. So the expressions ‘longitudinal’ or ‘transversely’ polarized target are always given in this frame. But from theoretical point of view the direction of the virtual photon is relevant. In Fig. 2.3 the definition of the angles ϕ_S and θ, with

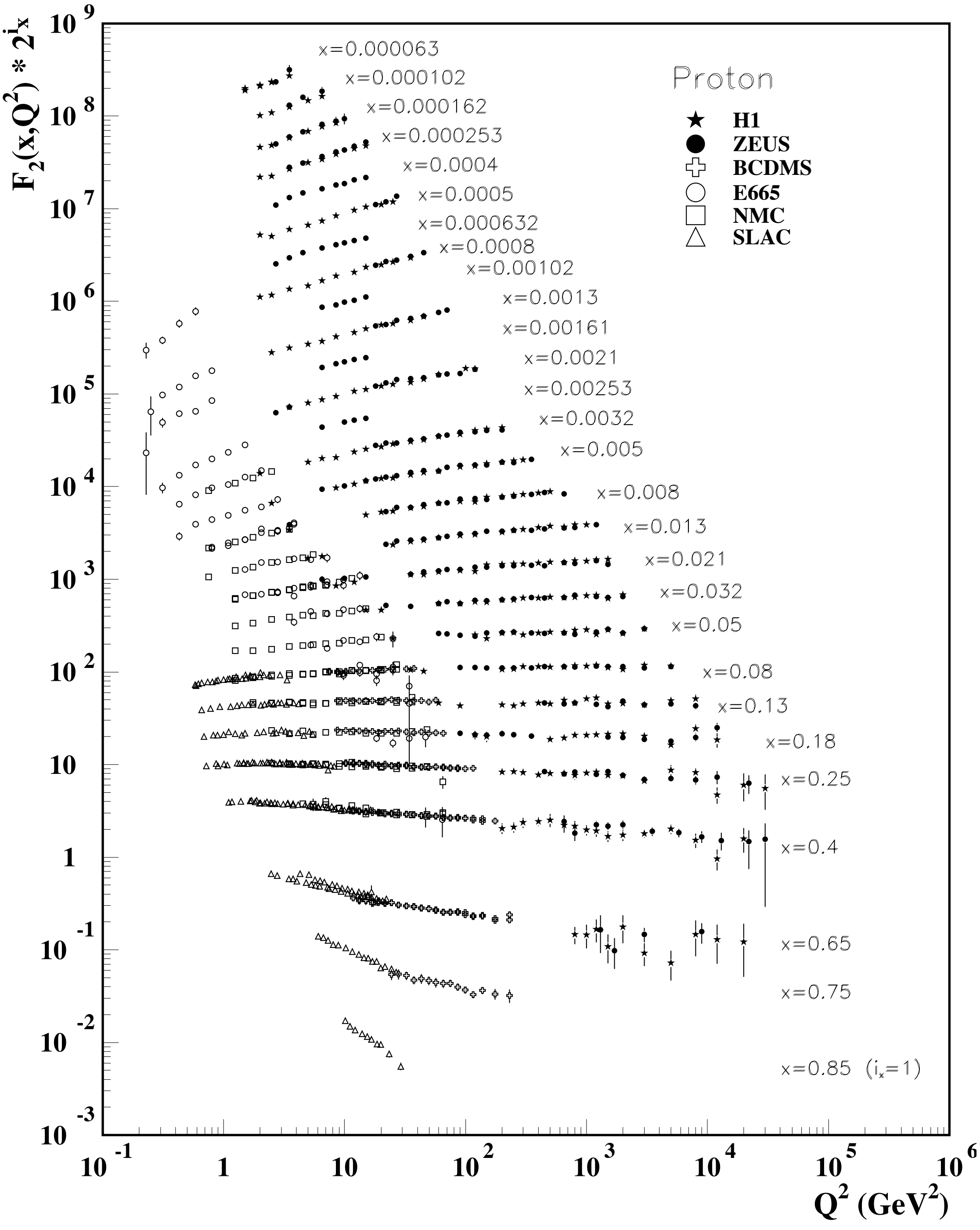

Figure 2.4: Compilation of measurements of the proton structure function F_2^p as a function of Q^2 for various values of x [15]. For the purpose of plotting, F_2^p has been multiplied by 2^{i_x}, where i_x is the number of the x bin, ranging from $i_x = 1$ ($x = 0.85$) to $i_x = 28$ ($x = 0.000063$).

respect to the virtual photon are given. Transformation from the reference system of the incoming lepton into the reference system of the virtual photon leads to the following relations for a longitudinal polarized target [11]:

$$\begin{aligned} \cos\theta &\approx 1 + \mathcal{O}(\gamma^2), \\ \sin\theta &\approx \gamma\sqrt{1-y} + \mathcal{O}(\gamma^2). \end{aligned} \tag{2.9}$$

For a transversely polarized target these relations are:

$$\begin{aligned} \cos\theta &\approx -\gamma\sqrt{1-y}\cos\phi + \mathcal{O}(\gamma^2), \\ \sin\theta &\approx 1 + \mathcal{O}(\gamma^2). \end{aligned} \tag{2.10}$$

Hence the target spin $\boldsymbol{S}$ has a small non-zero transverse and longitudinal component with respect to the virtual photon direction, respectively, which is however suppressed by a factor $\gamma \propto 1/Q$.

The azimuthal angle ϕ_S, as shown in Fig. 2.3, measured around the direction of the virtual photon, between the orientation of the target spin and the scattering plane is given by:

$$\phi_S = \frac{(\boldsymbol{q}\times\boldsymbol{l})\cdot\boldsymbol{S}}{|(\boldsymbol{q}\times\boldsymbol{l})\cdot\boldsymbol{S}|} \arccos\left(\frac{(\boldsymbol{q}\times\boldsymbol{l})\cdot(\boldsymbol{q}\times\boldsymbol{S})}{|\boldsymbol{q}\times\boldsymbol{l}||\boldsymbol{q}\times\boldsymbol{S}|}\right). \tag{2.11}$$

2.2 Parton Distribution Functions

2.2.1 Naive Parton Model

A simple physical picture interpreting the structure functions of deep-inelastic scattering is provided by the parton model. The target nucleon is considered to be made up of partons, point like spin $\frac{1}{2}$ particles. For large energy and momentum transfer to the nucleon the reaction can be described as incoherent scattering of the virtual photon off the partons. Considering the process in the infinite momentum frame, the target mass and transverse momenta of the partons can be neglected. In this frame the Bjorken variable x can be interpreted as the momentum fraction of the nucleon carried by the struck quark. A schematic picture of the process is given in Fig. 2.5. For unpolarized scattering the parton distribution function $q(x)$ is defined as the probability that the struck quark of flavor q carries the momentum fraction x of the parent nucleon. For DIS on a longitudinal polarized nucleon the distribution function $\Delta q(x) = q(x)^+ - q(x)^-$ is defined. This function gives the difference of the probabilities that the struck quark carries momentum fraction x and its spin is parallel $q(x)^+$ or anti-parallel $q(x)^-$ to the spin of the parent nucleon. In this context the unpolarized distribution function can be written as the sum of the two probabilities: $q(x) = q(x)^+ + q(x)^-$. These two parton distribution functions can be related to the structure functions F_1, F_2 and g_1 [18]:

$$F_1(x,Q^2) = \frac{1}{2}\sum_{q,\bar{q}} e_q^2 q(x), \tag{2.12a}$$

$$F_2(x,Q^2) = x\sum_{q,\bar{q}} e_q^2 q(x), \tag{2.12b}$$

$$g_1(x,Q^2) = \frac{1}{2}\sum_{q,\bar{q}} e_q^2 \Delta q(x), \tag{2.12c}$$

while the polarized structure function g_2 has no explanation in the parton model. The sums run over all quark and antiquark flavors and e_q^2 is the squared charge of the respective quark of flavor q.

Hence the structure functions can be written as squared charge weighted sums of the parton distribution functions. Since the parton distribution functions on the right hand side do not depend on Q^2, this simple model predicts Bjorken scaling [16], too.

2.2.2 Parton Model

So far the hadronic tensor was parametrized with structure functions, taking into account the deviation of the cross-section, which one expects for scattering off point like spin $\frac{1}{2}$ target nucleons. In order to take into account the knowledge of the parton model introduced in the previous section, it is useful to introduce the quark-quark correlation matrix Φ [11], which depends on the four-momentum k of the struck quark and on the four-momentum P and the spin S of the parent nucleon. It is a density matrix containing the information about the distribution of the quarks in the nucleon (and correspondingly the antiquark-antiquark correlation matrix $\overline{\Phi}$ [19], which will be omitted here for simplicity):

$$\Phi_{ji}(k,P,S) = \sum_X \int \frac{\mathrm{d}^3\boldsymbol{P}_X}{(2\pi)^3\,2E_X}\,(2\pi)^4\,\delta^{(4)}\Big(P-k-P_X\Big)\,\langle P,S|\,\bar{\psi}_j(0)\,|X\rangle\langle X|\,\psi_i(0)\,|P,S\rangle, \tag{2.13}$$

where the sum runs over all possible undetected hadronic final states X with four-momentum $P_X = (E_X, \boldsymbol{P}_X)$, $\psi_{i,j}$ is the quark field with spinor index i and j respectively, and the delta function accounts for momentum conservation. Using the completeness of the states $|X\rangle$ and translational invariance Φ can be written as a fourier transformation:

$$\Phi_{ji}(k,P,S) = \int \mathrm{d}^4\xi\;\mathrm{e}^{ik\cdot\xi}\,\langle P,S|\,\bar{\psi}_j(0)\psi_i(\xi)\,|P,S\rangle. \tag{2.14}$$

With this definition the hadronic tensor can be written as integral over traces of Φ, summed over the quark flavors q :

$$W^{\mu\nu} = \sum_q e_q^2 \int \frac{\mathrm{d}^4k}{(2\pi)^4}\,\delta\left(\left(k+q\right)^2\right)\,\mathrm{Tr}\left[\Phi(k,P,S)\gamma^\mu\left(\not{k}+\not{q}\right)\gamma^\nu\right]. \tag{2.15}$$

The correlation function Φ is constrained by hermiticity, parity and time reversal invariance [20]. Decomposing Φ in a basis of Dirac matrices $\Gamma = \{\mathbb{1}, \gamma^\mu, \gamma^\mu\gamma_5, i\gamma^5, i\sigma^{\mu\nu}\gamma_5\}$ and integrating over quark momenta k only the vector γ^μ, the axial vector $\gamma^\mu\gamma^5$ and the tensor term $i\sigma^{\mu\nu}\gamma^5$ survive in leading twist, which means that terms, which would appear in the cross-section with at least $\mathcal{O}(1/Q)$ are neglected (for a definition of twist see [13]):

$$\Phi(x) = \frac{1}{2}\left\{q(x)\not{P} + \lambda_N\Delta q(x)\gamma_5\not{P} + \Delta_T q(x)\not{S}_\perp\gamma_5\not{P}\right\}, \tag{2.16}$$

with λ_N being the helicity and $S \approx \lambda\frac{P}{M} + S_\perp$ the spin of the nucleon, x is the 'plus' component of the light-cone momentum fraction of the nucleon carried by the struck quark $x \equiv k^+/P^+$ (for the Sudakov decomposition of vectors into light-cone coordinates

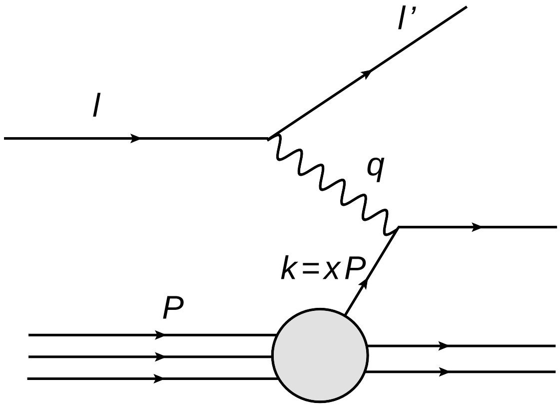

Figure 2.5: Schematic picture of deep-inelastic lepton-nucleon scattering in the quark parton model. The virtual photon scatters off a quark carrying momentum fraction x of the parent nucleon with momentum P.

and their relevance in DIS see [13]). In the Bjorken limit this is equal to the Bjorken scaling variable defined in Tab. 2.1. Due to hermiticity the three functions $q(x)$, $\Delta q(x)$ and $\Delta_T q(x)$ are real and have a probabilistic interpretation. The number density distribution $q(x)$ and the helicity distribution $\Delta q(x)$ are the ones already defined in Sec. 2.2. The third distribution $\Delta_T q(x)$ is called transversity distribution and is the number density of quarks with spin parallel to the parent nucleon minus the number density of quarks of flavor q with spin anti-parallel for a transversely polarized nucleon.

The following relations between quark and antiquark distributions apply, reflecting the properties under charge conjugation of vector, axial vector and tensor objects:

$$\bar{q}(x) = \; - q(-x), \tag{2.17a}$$
$$\Delta\bar{q}(x) = \; \Delta q(-x), \tag{2.17b}$$
$$\Delta_T\bar{q}(x) = -\Delta_T q(-x). \tag{2.17c}$$

As seen in Sec. 2.2 the first two parton distribution functions $q(x)$ and $\Delta q(x)$ can be related to the structure functions F_1, F_2 and g_1. The fact that $\Delta_T q(x)$ has no relation to a structure function in inclusive DIS is given because it is chiral-odd. Hence it includes a helicity flip of the struck quark, which is forbidden in leading twist DIS. This will be discussed in Sec. 2.2.5.

2.2.3 First Moments of Parton Distribution Functions

The integrated parton distribution functions are of interest, because these can be related to the fundamental vector-, axial- and tensor-charge, denoted with g_V, g_A and g_T, respectively :

$$\int_{-1}^{1} \mathrm{d}x\ q(x) = \int_{0}^{1} \mathrm{d}x\ \{q(x) - \bar{q}(x)\} = g_V, \tag{2.18a}$$

$$\int_{-1}^{1} \mathrm{d}x\ \Delta q(x) = \int_{0}^{1} \mathrm{d}x\ \{\Delta q(x) + \Delta\bar{q}(x)\} = g_A, \tag{2.18b}$$

$$\int_{-1}^{1} \mathrm{d}x\ \Delta_T q(x) = \int_{0}^{1} \mathrm{d}x\ \{\Delta_T q(x) - \Delta_T\bar{q}(x)\} = g_T, \tag{2.18c}$$

where the relations of Eq. (2.17a)-(2.17c) have been used. As can be seen in Eq. (2.18a) and Eq. (2.18c), because of the differences of quark and antiquark distributions the sea-quark contributions cancel and the vector-charge g_V can be identified with the valence number and the tensor-charge g_T with transversity for valence quarks only [21].

These first moments of the parton distribution functions are of particular importance since they can be calculated in lattice QCD. It will be interesting to compare the tensor-charge obtained from the measured transversity distribution with results from the lattice [22] and with results based on models [23, 24].

2.2.4 Quark Transverse Momenta

So far transverse momenta $\boldsymbol{k}_\perp$ of the quarks with respect to the virtual photon direction have been neglected, because they are small compared to the longitudinal component. Taking them into account eight distribution functions depending on x and $\boldsymbol{k}_\perp^2$ appear in the parametrization of the quark-quark correlation matrix $\Phi(x, \boldsymbol{k}_\perp)$ at leading twist [25, 26] (for clarity the index q of the quark flavor is omitted unless it contributes to the name of the distribution function):

$$\begin{aligned}\Phi(x,\boldsymbol{k}_\perp) = \frac{1}{2}\Bigg\{ &\left[q(x,\boldsymbol{k}_\perp^2) - \frac{\epsilon_\perp^{ij} k_{\perp i} S_{\perp j}}{M} f_{1T}^\perp(x,\boldsymbol{k}_\perp^2)\right] \not{P} \\ + &\left[\lambda_N \Delta q(x,\boldsymbol{k}_\perp^2) + \frac{\boldsymbol{k}_\perp\cdot\boldsymbol{S}_\perp}{M} g_{1T}(x,\boldsymbol{k}_\perp^2)\right]\gamma_5\not{P} + h_{1T}(x,\boldsymbol{k}_\perp^2)\not{S}_\perp\gamma_5\not{P} \\ + \frac{1}{M}&\left[\lambda_N h_{1L}^\perp(x,\boldsymbol{k}_\perp^2) + \frac{\boldsymbol{k}_\perp\cdot\boldsymbol{S}_\perp}{M} h_{1T}^\perp(x,\boldsymbol{k}_\perp^2) - \frac{\epsilon_\perp^{ij}k_{\perp j}}{M} h_1^\perp(x,\boldsymbol{k}_\perp^2)\right]\not{k}_\perp\gamma_5\not{P}\Bigg\},\end{aligned} \tag{2.19}$$

whereas the constraint of invariance under time reversal is dropped here, which permits the terms $f_{1T}^\perp$ and $h_1^\perp$. A priori this seems to be physically unjustified, since strong interaction processes have to be invariant. However, as will be discussed in Sec. 2.2.6, so-called initial or final state interactions may allow such terms.

A summary of the eight parton distribution functions ordered by their chirality and their properties under time reversal are given in Fig. 2.6. In addition illustrations of their probabilistic interpretations are given. The nucleon and the quark spins are represented

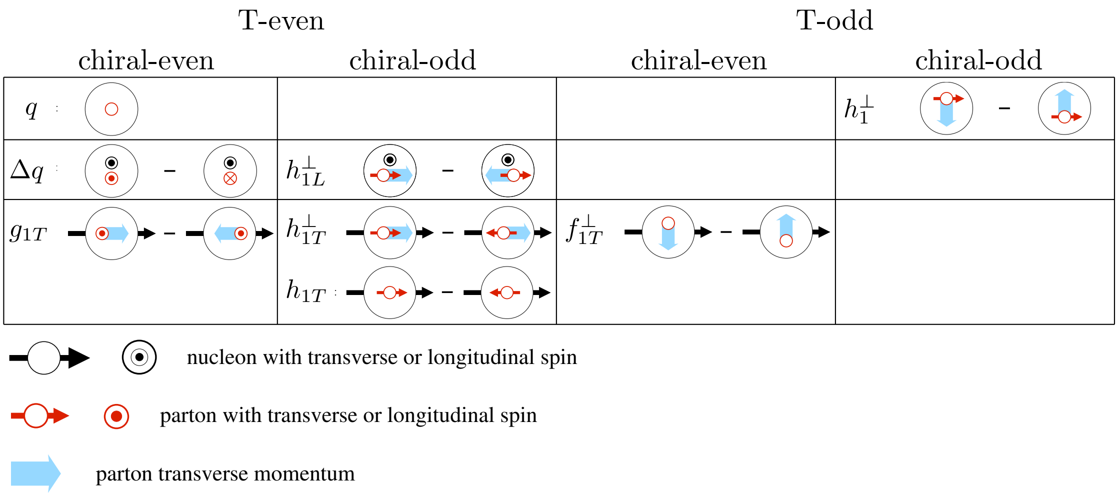

Figure 2.6: Probabilistic interpretations of leading twist transverse momentum dependent parton distribution functions [27]. The virtual photon direction points into the plane. All functions depend on x and $\boldsymbol{k}_\perp^2$.

by black and red arrows, respectively and the intrinsic quark momentum is indicated by light blue arrows. The incident virtual photon direction is always pointing into the plane.

When integrating over $\boldsymbol{k}_\perp$, what is done in an inclusive measurement, all distribution functions vanish except the three ones, which were already present in Eq. (2.16):

$$q(x) = \int \mathrm{d}\boldsymbol{k}_T \; q(x, \boldsymbol{k}_\perp^2), \tag{2.20a}$$

$$\Delta q(x) = \int \mathrm{d}\boldsymbol{k}_T \; \Delta q(x, \boldsymbol{k}_\perp^2), \tag{2.20b}$$

$$\Delta_T q(x) = \int \mathrm{d}\boldsymbol{k}_T \; \left\{ h_{1T}^q(x, \boldsymbol{k}_\perp^2) + \frac{\boldsymbol{k}_T^2}{2M} h_{1T}^{\perp q}(x, \boldsymbol{k}_\perp^2) \right\} \equiv \int \mathrm{d}\boldsymbol{k}_T \; \Delta_T q(x, \boldsymbol{k}_\perp^2). \tag{2.20c}$$

The goal of this thesis is to access the transversity distribution $\Delta_T q(x)$ and the so-called Sivers function $f_{1T}^{\perp}(x, \boldsymbol{k}_\perp^2)$ [28]. Therefore the next sections are in particular dedicated to the properties of these two functions. Both functions cannot be accessed in inclusive DIS. The transversity function because it is chiral-odd and the Sivers function because it is T-odd and depends on $\boldsymbol{k}_\perp$. But as will discussed in the next sections both can be accessed in semi-inclusive DIS.

2.2.5 Properties of the Transversity Distribution Function

The transversity distribution function is chiral-odd. This implies that the corresponding quark-nucleon scattering amplitude includes helicity flips of the quark and the nucleon. This gets comprehensible when considering the optical theorem.

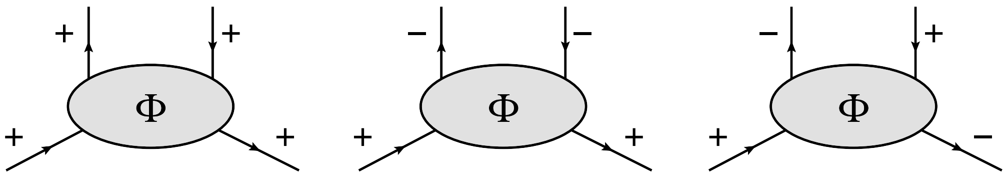

Figure 2.7: Diagrams, illustrating the three possible quark-nucleon helicity amplitudes. From left to right are shown: $\mathcal{A}_{++,++}$, $\mathcal{A}_{+-,+-}$ and $\mathcal{A}_{+-,-+}$.

2.2.5.1 Forward Virtual Compton Scattering (Optical Theorem)

The hadronic tensor can be related to the imaginary part of the forward virtual compton scattering amplitude $T_{\mu\nu}$:

$$W_{\mu\nu} = \frac{1}{2\pi}\mathrm{Im}T_{\mu\nu}. \tag{2.21}$$

The amplitudes in the helicity basis are denoted with $\mathcal{A}_{\Lambda\lambda,\Lambda'\lambda'}$, in which Λ, Λ' are the helicities of the incoming and outgoing nucleon, respectively and λ, λ' accordingly the helicities of the quark. The combinations of the helicities are constrained because of helicity and parity conservation. Hence only three independent amplitudes are left:

$$\mathcal{A}_{++,++}, \quad \mathcal{A}_{+-,+-}, \quad \mathcal{A}_{+-,-+}. \tag{2.22}$$

These can be visualized via the three diagrams in Fig. 2.7. Using the optical theorem, these three quark-nucleon amplitudes can be related to the three quark distribution functions $q(x)$, $\Delta q(x)$ and $\Delta_T q(x)$:

$$q(x) \propto \mathrm{Im}(\mathcal{A}_{++,++} + \mathcal{A}_{+-,+-}), \tag{2.23a}$$

$$\Delta q(x) \propto \mathrm{Im}(\mathcal{A}_{++,++} - \mathcal{A}_{+-,+-}), \tag{2.23b}$$

$$\Delta_T q(x) \propto \mathrm{Im}\mathcal{A}_{+-,-+}. \tag{2.23c}$$

Since in the helicity basis the amplitude $\mathcal{A}_{+-,-+}$ is off-diagonal, no probabilistic interpretation exists. However, transformation into a transversity basis $\{\uparrow, \downarrow\}$ leads to a difference of two diagonal amplitudes and hence to a probabilistic interpretation, analogue to $\Delta q(x)$:

$$\Delta_T q(x) \propto \mathrm{Im}(\mathcal{A}_{\uparrow\uparrow,\uparrow\uparrow} - \mathcal{A}_{\uparrow\downarrow,\uparrow\downarrow}). \tag{2.24}$$

The diagram on the right in Fig. 2.7 is related to transversity (represented in the helicity base). Inclusive DIS would be described with the handbag diagram shown in Fig. 2.8. As can be seen the helicity of the quark and the nucleon flips, which is due to the fact that transversity is a chiral-odd function. This is forbidden in inclusive DIS, where quark masses can be neglected in leading twist. However, as will be discussed in Sec. 2.3 and 2.4 transversity can be measured in semi-inclusive DIS, involving chiral-odd fragmentation functions. Another implication is that for gluons a transversity distribution $\Delta_T g(x)$ cannot exist, because gluons have helicity ± 1, thus leading to a total change of helicity of two units ± 2, which cannot be balanced by the nucleon. This has an impact on the Q^2 evolution of the transversity distribution function, which will be different to the one for the helicity distribution function, which contains contributions from gluons.

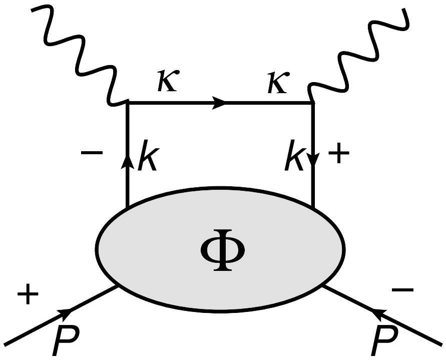

Figure 2.8: Handbag diagram for transversity in fully inclusive DIS. The process is forbidden, because of the helicity flip of the quark and the nucleon.

2.2.5.2 Bounds for the Transversity Distribution

Bounds for the transversity distribution function can be derived [29]. Because of $q(x) = q(x)^+ + q(x)^- = q(x)^\uparrow + q(x)^\downarrow$ the following two inequalities can be obtained:

$$|\Delta q(x)| \leq q(x), \tag{2.25a}$$
$$|\Delta_T q(x)| \leq q(x). \tag{2.25b}$$

A more complicated inequality, called Soffer bound [30], involves all three leading twist distribution functions simultaneously:

$$|\Delta_T q(x)| \leq \frac{1}{2}\left(q(x) + \Delta q(x)\right). \tag{2.26}$$

All three inequalities do not only hold at leading twist, but are also preserved by QCD evolution.

2.2.6 Properties of the Sivers Distribution Function

The Sivers distribution function $f_{1T}^{\perp}(x, \boldsymbol{k}_\perp^2)$ describes the correlation between the intrinsic transverse momentum of the quarks and the transverse polarization of the nucleon. It was first proposed by Sivers [28] to explain single-spin asymmetries observed in pion production in transversely polarized proton-proton scattering ($p^\uparrow\, p \to \pi\, X$) [9] and polarized antiproton-proton scattering ($\bar{p}^\uparrow\, p \to \pi\, X$) [31].

The Sivers function cannot be measured in inclusive DIS because it depends on the intrinsic transverse momentum k_T of the quarks and vanishes when integrating over k_T. This can be overcome in semi-inclusive DIS, which means that in addition to the scattered muon a final state hadron is detected, too (see Sec. 2.3). For some time it was argued, that the T-odd nature forbids the existence of the Sivers function in general [32]. However, it can be shown, that initial or final state interactions via gluon exchange between the incoming or outgoing quark and the target spectator system allow for the

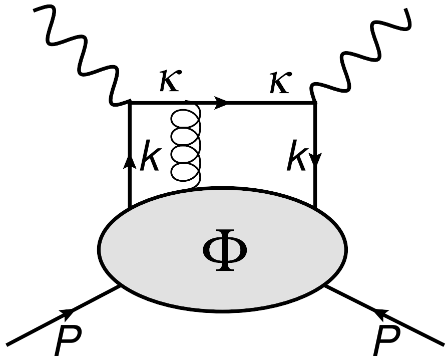

Figure 2.9: Handbag diagram for gluon exchange between quark and nucleon.

existence of T-odd parton distribution functions [33, 34, 35], which are called naïve T-odd. The reason for allowing those naïve T-odd parton distribution functions is a path dependent link operator $\mathcal{L}$, called Wilson line,

$$\mathcal{L}(0,\xi) = \mathcal{P}e^{-\mathrm{i}\int_0^\xi \mathrm{d}s_\mu A^\mu(s)}, \tag{2.27}$$

which connects the quark fields between 0 and ξ and has to be introduced in Eq. (2.14) to obtain a gauge invariant expression of the quark-quark correlator Φ. Here $\mathcal{P}$ denotes path ordering. So far this operator has been neglected, since in axial gauge $A^+ = 0$ one can choose a path that reduces $\mathcal{L}$ to unity [19]. When considering transverse quark momenta, gluon exchange for example between the nucleon and the quark, as shown in Fig. 2.9, has to be considered, which leads to non-trivial expressions of the Wilson line $\mathcal{L}$, which allow for naïve T-odd distribution functions [34].

This means that at least two hadrons are needed either in the final state (SIDIS) or in the initial state (Drell-Yan), which will be discussed in more detail in Sec. 2.3 and 2.5. Because of the different occurrence of the interactions in the final and in the initial state, respectively, the sign of the Sivers functions should be opposite for SIDIS and Drell-Yan [34].

An interesting aspect of the Sivers function is its connection to generalized parton distribution functions (GPD) [36, 37]. A non-zero Sivers function requires orbital angular momentum of the quarks, which is a missing part of the proton spin puzzle.

2.2.6.1 Bounds for the Sivers Distribution

An upper bound for the Sivers distribution function can be derived [29]:

$$\left|\frac{\boldsymbol{k}_\perp^2}{2M^2} f_{1T}^{\perp q}(x,\boldsymbol{k}_\perp^2)\right| \leq \frac{|\boldsymbol{k}_\perp|}{2M} q(x,\boldsymbol{k}_\perp^2). \tag{2.28}$$

With the definition $\Delta_0^T q(x,\boldsymbol{k}_\perp^2) = -2\frac{|\boldsymbol{k}_\perp|}{M} f_{1T}^{\perp q}(x,\boldsymbol{k}_\perp^2)$ this becomes:

$$|\Delta_0^T q(x,\boldsymbol{k}_\perp^2)| \leq 2q(x,\boldsymbol{k}_\perp^2). \tag{2.29}$$

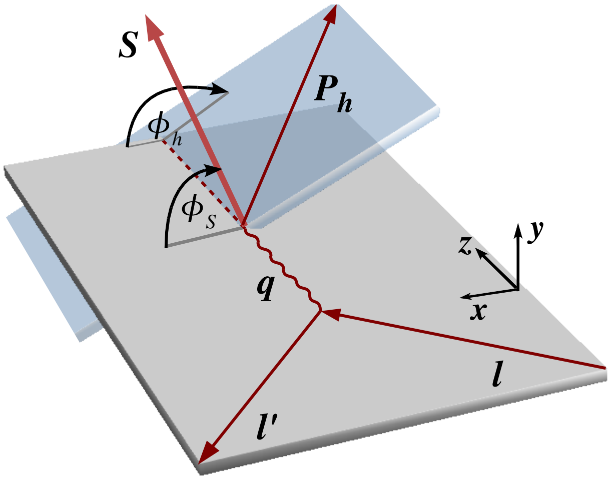

Figure 2.10: Definition of the azimuthal angles ϕ_h and ϕ_S, measured around the direction of the virtual photon $\boldsymbol{q}$.

2.3 Single Hadron Semi-Inclusive DIS

As explained before the transversity distribution and the Sivers function are not observable in inclusive DIS. However, as already pointed out both are allowed in semi-inclusive deep-inelastic scattering, where they both contribute in leading twist to the cross-section, as will be shown in the following.

The deep-inelastic scattering process is called semi-inclusive if in addition to the scattered lepton, at least one hadron h is detected in the final state, too.

$$l + P \rightarrow l' + h + X, \tag{2.30}$$

The cross-section for semi-inclusive DIS depends on x, y and ϕ_S, like the one for inclusive DIS and in addition on the momentum $\boldsymbol{P}_h$ of the detected hadron. With the energy fraction z, as defined in Tab. 2.1 and the assumption $|\boldsymbol{P}_{h\perp}| \ll E_h$, that the transverse momentum of the produced hadrons with respect to the virtual photon is much smaller than its energy, one can write:

$$\frac{\mathrm{d}^3\boldsymbol{P}_h}{E_h} = \frac{1}{z}\mathrm{d}z\; \mathrm{d}^2\boldsymbol{P}_{h\perp} = \frac{|\boldsymbol{P}_{h\perp}|}{z}\; \mathrm{d}z\; \mathrm{d}|\boldsymbol{P}_{h\perp}|\; \mathrm{d}\phi_h, \tag{2.31}$$

where ϕ_h is the azimuthal angle, measured around the virtual photon, of the hadron plane, defined by the virtual photon momentum $\boldsymbol{q}$ and the hadron momentum $\boldsymbol{P}_h$ with respect to the scattering plane.

$$\phi_h = \frac{(\boldsymbol{q} \times \boldsymbol{l}) \cdot \boldsymbol{P}_h}{|(\boldsymbol{q} \times \boldsymbol{l}) \cdot \boldsymbol{P}_h|} \arccos\left(\frac{(\boldsymbol{q} \times \boldsymbol{l}) \cdot (\boldsymbol{q} \times \boldsymbol{P}_h)}{|\boldsymbol{q} \times \boldsymbol{l}||\boldsymbol{q} \times \boldsymbol{P}_h|}\right). \tag{2.32}$$

A schematic picture of the definitions of the relevant angles and momenta is shown in Fig. 2.10. The azimuthal angle ϕ_S between the spin of the initial struck quark and the lepton scattering plane has already been defined in Eq. (2.11).

At lowest order the process can be described by the extended handbag diagram shown in Fig. 2.11. One sees that beside the quark-quark correlation matrix Φ, describing the structure of the nucleon, another correlation function Ξ is introduced to describe the fragmentation of the struck quark of flavor q, with four-momentum $\kappa = k + q$ into a hadron h with four-momentum P_h and spin S_h. With this additional correlation function the hadronic tensor reads [11]:

$$W^{\mu\nu} = \sum_q e_q^2 \int \frac{\mathrm{d}^4 k}{(2\pi)^4} \int \frac{\mathrm{d}^4 \kappa}{(2\pi)^4}\, \delta\left((k+q-\kappa)^2\right)\, \mathrm{Tr}\left[\Phi(k,P,S)\gamma^\mu \Xi(\kappa,P_h,S_h)\gamma^\nu\right], \tag{2.33}$$

whereas the fragmentation correlation function Ξ is defined as:

$$\Xi_{ij}(\kappa,P_h,S_h) = \sum_X \int \frac{\mathrm{d}^3 \boldsymbol{P}_X}{(2\pi)^3 2E_X} \int \mathrm{d}^4\, \xi \mathrm{e}^{i\kappa\cdot\xi} \langle 0|\, \psi_i(\xi)\, |P_h S_h, X\rangle \langle P_h S_h, X|\, \bar{\psi}_j(0)\, |0\rangle, \tag{2.34}$$

and the sum runs over all possible residual hadronic final states X.

The following results will be given in a frame where the target nucleon and the produced hadron are collinear and transverse components are defined with respect to this axis and will be indicated with subscript T. Whereas so far the results were given in a frame, where the virtual photon and the target nucleon were collinear and transverse components were indicated with $\perp$. It can be shown that, when neglecting corrections of the order $1/Q$, transverse vectors are approximately the same in both frames [11]. The relation between the transverse component of the virtual photon in the 'T' frame and of the outgoing hadron in the '$\perp$' frame is:

$$\boldsymbol{q}_T \approx -\frac{\boldsymbol{P}_{h\perp}}{z}. \tag{2.35}$$

In a similar way, as it was done for Φ in Sec. 2.2.2, the fragmentation correlator Ξ can be expanded on a basis of Dirac matrices . At leading twist, requiring hermiticity and parity invariance eight possible fragmentation functions are obtained [38]. After summation over the spin S_h of the produced hadron, only two of them remain, depending on the energy fraction $z = P_h^-/\kappa^-$, carried by the produced hadron and on $z^2\boldsymbol{\kappa}_T^2$ of the fragmenting quark:

$$\Xi(z, z^2\boldsymbol{\kappa}_T^2) = \frac{1}{2}\left\{D_1(z, z^2\boldsymbol{\kappa}_T^2) + \mathrm{i}H_1^\perp(z, z^2\boldsymbol{\kappa}_T^2)\right\}. \tag{2.36}$$

D_1 is the unpolarized fragmentation function, which describes the probability for an unpolarized quark with transverse momentum $\boldsymbol{\kappa}_T$ to fragment into an unpolarized hadron with energy fraction z. The Collins fragmentation function $H_1^\perp$ is the difference of the probabilities for an upward transversely polarized quark to fragment into an unpolarized hadron and a downward transversely polarized quark to fragment into an unpolarized hadron. The Collins fragmentation function is chiral-odd, just as the transversity distribution function and in addition T-odd.

The possibility of T-odd fragmentation functions is given due to final state interactions between the hadron and the nucleon remnants. Hence time reversal symmetry cannot be used to constraint the fragmentation functions [39].

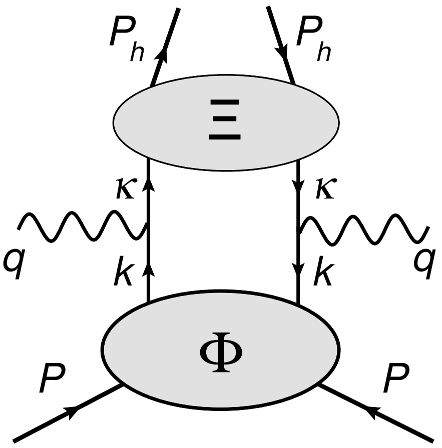

Figure 2.11: Diagram contributing to semi-inclusive deep-inelastic lepton-nucleon scattering at lowest order.

2.3.1 One Hadron Cross-Section

The complete cross-section for one photon exchange is for example given in [40]. For a transversely polarized target, in total eight different terms contribute. In this thesis the transversity distribution and the Sivers distribution are studied. Hence for better readability the result is restricted to terms, which either contain the momentum, the Sivers or the transversity distribution [19]:

$$\begin{aligned}\frac{\mathrm{d}^6\sigma}{\mathrm{d}x\,\mathrm{d}y\,\mathrm{d}\phi_S\,\mathrm{d}z\,\mathrm{d}^2\boldsymbol{P}_{h\perp}} &= \frac{2\alpha^2}{sxy^2}\sum_q e_q^2 A(y)\,\mathcal{I}\left[q(x,\boldsymbol{k}_T^2)\;D_1^q(z,z^2\boldsymbol{\kappa}_T^2)\right] \\ +\frac{2\alpha^2}{sxy^2}\sum_q e_q^2|\boldsymbol{S}_T| &\left\{B(y)\sin(\phi_h+\phi_S-\pi)\,\mathcal{I}\left[\frac{\boldsymbol{\kappa}_T\cdot\boldsymbol{P}_{h\perp}}{M_h|\boldsymbol{P}_{h\perp}|}\Delta_T q(x,\boldsymbol{k}_T^2)\;H_1^{\perp q}(z,z^2\boldsymbol{\kappa}_T^2)\right]\right. \\ &\left.+A(y)\sin(\phi_h-\phi_S)\,\mathcal{I}\left[\frac{\boldsymbol{k}_T\cdot\boldsymbol{P}_{h\perp}}{M|\boldsymbol{P}_{h\perp}|}f_{1T}^{\perp q}(x,\boldsymbol{k}_T^2)\;D_1^q(z,z^2\boldsymbol{\kappa}_T^2)\right]\right\}.\end{aligned} \tag{2.37}$$

The sum runs over all quark flavors q and $\mathcal{I}\,[..] = \int \mathrm{d}^2\boldsymbol{\kappa}_T \mathrm{d}^2\boldsymbol{k}_T \delta^{(2)}\left(\boldsymbol{k}_T + \boldsymbol{q}_T - \boldsymbol{\kappa}_T\right)[..]$ are convolution integrals, relating the transverse momentum dependence of the quarks in the nucleon with the one of the fragmenting quarks, hence the transverse momenta before and after the interaction with the virtual photon. The kinematical factors $A(y)$ and $B(y)$ are defined as:

$$\begin{aligned}A(y) &= 1 - y + \frac{y^2}{2}, \\ B(y) &= 1 - y.\end{aligned} \tag{2.38}$$

2.3.2 One Hadron Single Spin Asymmetries

The azimuthal modulations $\sin(\phi_h - \phi_S)$ and $\sin(\phi_h + \phi_S - \pi)$, in Eq. (2.37), related to the Sivers and the transversity distribution are orthogonal to each other (in fact all eight transverse target spin contributions lead to unique azimuthal modulations of the cross-section, which are orthogonal to each other [40]). Therefore they can be extracted independently from the same dataset (in general the situation is more complicated because of the imperfect acceptance of the detector. Therefore the acceptance is convoluted with the cross section leading to possible correlations between the different modulations. This will be discussed in Sec. 5.4). From the experimental point of view the most feasible way to measure such target spin dependent modulations of the cross-section is to built a so-called asymmetry where all spin independent contributions vanish:

$$\begin{aligned} A &= \frac{\mathrm{d}^6\sigma^{\uparrow} - \mathrm{d}^6\sigma^{\downarrow}}{\mathrm{d}^6\sigma^{\uparrow} + \mathrm{d}^6\sigma^{\downarrow}} \\ &= |\boldsymbol{S}_T| \cdot D_{nn}(y) \cdot A^{Collins} \cdot \sin(\phi_h + \phi_S - \pi) \; + \; |\boldsymbol{S}_T| \cdot A^{Sivers} \cdot \sin(\phi_h - \phi_S), \end{aligned} \tag{2.39}$$

with the following definitions and the approximation $\boldsymbol{P}_{h\perp}^2 \approx -z^2 \boldsymbol{\kappa}_T^2$, which is valid when ignoring intrinsic quark transverse motion:

$$D_{nn}(y) = \frac{B(y)}{A(y)} = \frac{1-y}{1-y+\frac{y^2}{2}}, \tag{2.40a}$$

$$A^{Collins} = \frac{\sum_q e_q^2 \cdot \mathcal{I}\left[\Delta_T q(x, \boldsymbol{k}_T^2)\; \Delta_T^0 D_q^h(z, \boldsymbol{P}_{h\perp}^2)\right]}{\sum_q e_q^2 \cdot \mathcal{I}\left[q(x, \boldsymbol{k}_T^2)\; D_q^h(z, \boldsymbol{P}_{h\perp}^2)\right]}, \tag{2.40b}$$

$$A^{Sivers} = \frac{\sum_q e_q^2 \cdot \mathcal{I}\left[\Delta_0^T q(x, \boldsymbol{k}_T^2)\; D_q^h(z, \boldsymbol{P}_{h\perp}^2)\right]}{\sum_q e_q^2 \cdot \mathcal{I}\left[q(x, \boldsymbol{k}_T^2)\; D_q^h(z, \boldsymbol{P}_{h\perp}^2)\right]}. \tag{2.40c}$$

New expressions for the Collins fragmentation function and for the Sivers distribution function have been introduced for convenience:

$$\Delta_T^0 D_q^h(z, \boldsymbol{P}_{h\perp}^2) = \tfrac{|\boldsymbol{P}_{h\perp}|}{z M_h} H_1^{\perp}(z, \boldsymbol{P}_{h\perp}^2), \tag{2.41}$$

$$\Delta_0^T q(x, \boldsymbol{k}_T^2) = -2 \tfrac{|\boldsymbol{k}_T|}{M} f_{1T}^{\perp q}(x, \boldsymbol{k}_T^2). \tag{2.42}$$

As seen in Eq. 2.40b and 2.40c the parton distribution functions appear convoluted in the transverse momenta with the particular fragmentation function. In order to extract the Sivers function or the transversity distribution, assumptions about the transverse momentum of the quarks in the nucleon and about the transverse momentum of the fragmenting quark have to be made. Therefore, transverse momentum weighted single spin asymmetries are preferred from the theoretical point of view [41]. However, from experimental point of view this weighting is complicated, because of a non complete acceptance in $|\boldsymbol{P}_{h\perp}|$. In this thesis the Collins and Sivers asymmetries will be extracted without any weighting.

The so-called Collins and Sivers asymmetry (the terms derive from the involved fragmentation function and the involved distribution function, respectively) are discussed in the next Sections 2.3.3 and 2.3.4.

2.3.3 The Collins Asymmetry

As can be seen in Eq. (2.40b), the single spin asymmetry amplitude $A^{Collins}$ depends on two distribution functions and on two fragmentation functions, whereas the number

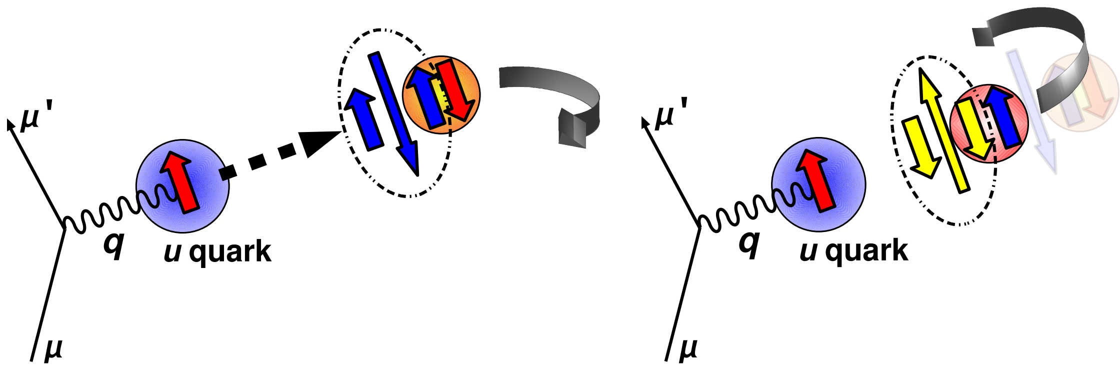

Figure 2.12: A simple interpretation of the Collins asymmetry, leading to a left right asymmetry of π^+-mesons (top) and π^--mesons (bottom). See text for details.

density distribution q and the unpolarized fragmentation function D_q^h are both well known. The Collins fragmentation function has recently been measured by the Belle collaboration in $e^+e^- \rightarrow q\bar{q}$ [42]. In fact in this process only the convolution of the quark and the antiquark Collins fragmentation function is measured $\Delta_T^0 D \otimes \overline{\Delta_T^0 D}$. With the assumption of a Gaussian dependence of the intrinsic quark transverse momentum this convolution can be factorized into a product, and hence the Collins fragmentation functions for quarks and for antiquarks can be assessed.

2.3.3.1 A Simple Picture of the Collins Asymmetry

A pictorial picture of the Collins effect is shown in Fig. 2.12. It is assumed that a virtual photon strikes a transversely up polarized u-quark, which flips its spin. On the left the favored fragmentation into a π^+-meson and on the right the followed up disfavored fragmentation into a π^--meson is shown. Where favored fragmentation means, that the produced hadron contains the struck quark (i.e. $u \rightarrow \pi^+(u\bar{d})$), in all other cases it is called disfavored fragmentation (i.e. $u \rightarrow \pi^-(\bar{u}d)$). In the favored fragmentation it is assumed, that in the current fragmentation a d$\bar{\text{d}}$-pair with vacuum quantum numbers, spin $S = 1$, angular momentum $L = 1$ and total angular momentum $J = 0$ is produced. Because the pion is a scalar meson with spin zero the angular momentum has to point downwards (as indicated by the long arrow) and hence the produced π^+ heads out of the page. In the disfavored fragmentation directly followed up the favored fragmentation it is assumed that a u$\bar{\text{u}}$-pair is produced. The same considerations as before leads to an angular momentum, now pointing upwards, as indicated with the long yellow arrow. Hence the produced π^- heads into the page. In summary, taking the plane defined by the virtual photon and the initial quark spin as reference, there will be an asymmetry in the number of produced charged pions. More positive pions will be detected on the right and more negative pions on the left.

Hence one can expect, that the favored fragmentation of transversely polarized quarks is of similar strength to their disfavored fragmentation, but of opposite sign:

$$\Delta_T^0 D_q^{favored} \simeq -\Delta_T^0 D_q^{disfavored}. \tag{2.43}$$

As discussed before, the Belle collaboration has measured the Collins fragmentation function in e^+e^- annihilation. However, the precision of the measurement does not allow to distinguish between the favored and the disfavored Collins fragmentation function [42]. But the measurement is compatible to the relation given in Eq. (2.43). As will be shown later in Sec. 6.6.1 the measured Collins asymmetries support this too, taking into account that for scattering off protons the process takes place dominantly on u-quarks.

2.3.4 The Sivers Asymmetry

Because of the correlation of orbital angular momentum of quarks with the transverse spin of the parent nucleon, the measurement of the Sivers asymmetry is of large interest. As seen in Eq. (2.39) the existence of the Sivers distribution leads to an azimuthal modulation of the cross-section in $\sin(\phi_h - \phi_S)$.

2.3.4.1 A Simple Picture of the Sivers Asymmetry

The effect of orbital angular momentum carried by u- and d-quarks inside a transversely polarized proton on their distribution functions is shown in Fig. 2.13. The distributions $u(x, \boldsymbol{b}_\perp)$ and $d(x, \boldsymbol{b}_\perp)$ show the probabilities of finding unpolarized u- and d-quarks inside an unpolarized proton, depending on the impact parameter b_x and b_y [43]. Those define the transverse distance of the center of momentum of the target proton. Both distributions are symmetric and centered at zero and they get sharper localized around zero for increasing values of x. This is of course expected due to the definition of b_x and b_y, since for $x \to 1$ the total momentum is carried by one single quark only, which therefore defines the center of momentum.

For a proton transversely polarized in direction of b_x, the distributions $u_X(x, \boldsymbol{b}_\perp)$ and $d_X(x, \boldsymbol{b}_\perp)$ represent the probabilities of finding unpolarized u- and d-quarks, respectively. It is assumed, that u-quarks and d-quarks have opposite angular momentum. Because of the angular momentum, the quarks which move towards the virtual photon direction have larger momenta than those which move away. Hence, in contrary to the unpolarized case for a certain momentum fraction x the distributions are now shifted in direction perpendicular to the orientation of the proton spin, whereas the shift for u- and d-quarks are opposite. Therefore, when probing the proton with a virtual photon in direction perpendicular to the $b_x b_y$-plane (perpendicular to the proton spin) it is more likely to strike a u-quark in the upper part and a d-quark on the lower part of the proton.

Due to the strong interactions between the struck quark and the target remnant, the fragmenting quark gets pulled towards the center of momentum when leaving the proton, as depicted in Fig. 2.14. Because of the nature of the strong force the more displaced the struck quark is inside the proton, the stronger it gets pulled towards the center of momentum. Because of its analogy in optics, when illuminating a convex lens with a laser beam displaced of its optical axis, this effect is called chromodynamic lensing [44]. Hence the non-symmetric quark densities lead to left right asymmetries of the produced hadrons.

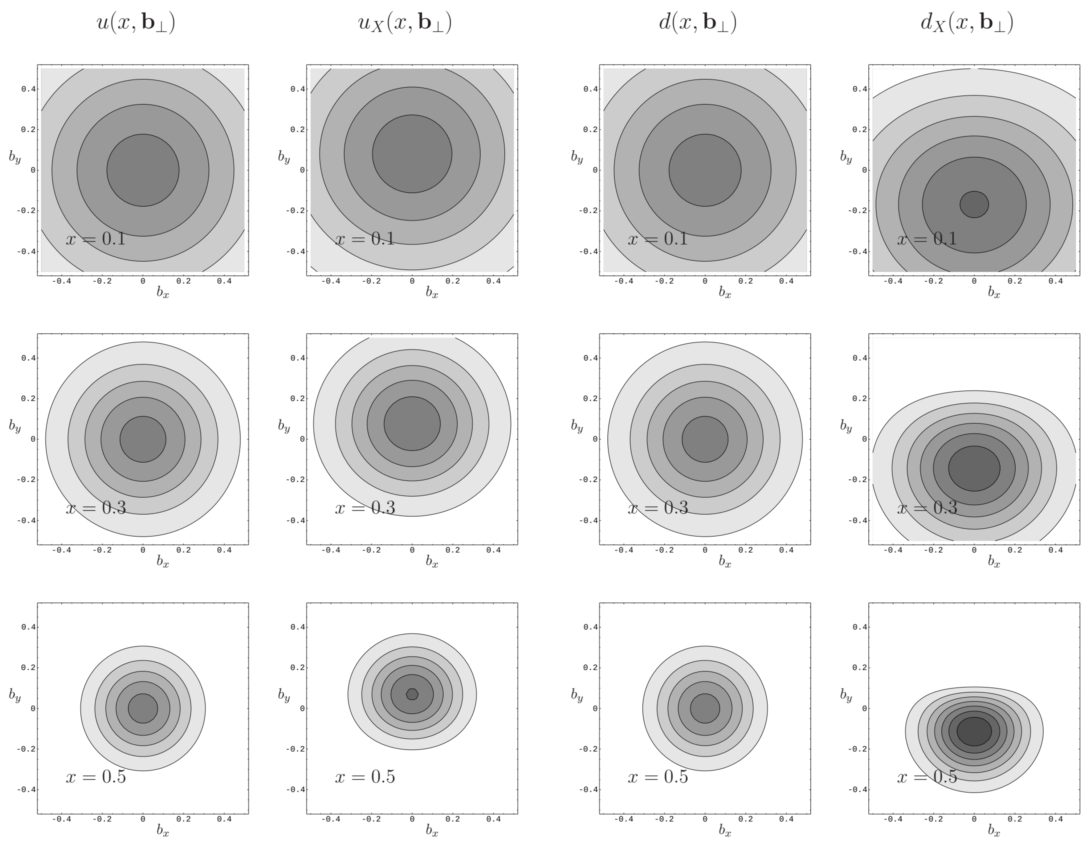

Figure 2.13: Probability distributions of finding unpolarized u-quarks (left) and d-quarks (right) in the transverse plane for three values of x. $u(x, \boldsymbol{b}_\perp)$ and $d(x, \boldsymbol{b}_\perp)$ inside an unpolarized proton and $u_X(x, \boldsymbol{b}_\perp)$ and $d_X(x, \boldsymbol{b}_\perp)$ for a transversely polarized proton in direction of b_x [43].

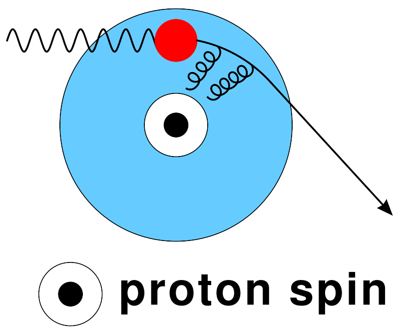

Figure 2.14: Chromodynamic lensing. Due to strong interactions the fragmenting quark gets pulled towards the center of momentum of the proton. In combination with a non-symmetric quark density this leads to a left right asymmetry of the produced hadrons.

2.4 Two Hadron Semi-Inclusive DIS

In the following the situation is considered, where the scattered lepton l' and two hadrons h_1 and h_2, produced in the current fragmentation region are detected in the final state:

$$l + P \rightarrow l' + h_1 + h_2 + X. \tag{2.44}$$

The fact that this process is sensitive to measure transversity was first pointed out in the early 1990s by [45, 46].

The two hadrons have four-momenta P_1 and P_2 and energies E_1 and E_2. The total four-momentum P_h and the relative momentum $\boldsymbol{R}$ of the two hadron system are defined as:

$$\begin{aligned} P_h &= P_1 + P_2, \\ \boldsymbol{R} &= \frac{1}{2}(\boldsymbol{P}_1 - \boldsymbol{P}_2). \end{aligned} \tag{2.45}$$

In this thesis oppositely charged hadron pairs are studied. With the choice that P_1 is the four-momentum of the positive hadron and P_2 respectively of the negative hadron, the sign of $\boldsymbol{R}$ is well defined. According to the single hadron case the energy fractions z_1 and z_2 carried by h_1 and h_2 are defined:

$$z_i = \frac{P \cdot P_i}{P \cdot q} \stackrel{\text{lab}}{=} \frac{E_i}{\nu}. \tag{2.46}$$

The energy fraction z carried by the two hadron system is the sum of z_1 and z_2:

$$z = z_1 + z_2 = \frac{P \cdot P_h}{P \cdot q}. \tag{2.47}$$

As will be shown later, the azimuthal angle ϕ_R between the two hadron plane and the scattering plane measured around the direction of the virtual photon is relevant for measuring transversity

$$\phi_R = \frac{(\boldsymbol{q} \times \boldsymbol{l}) \cdot \boldsymbol{R}_\perp}{|(\boldsymbol{q} \times \boldsymbol{l}) \cdot \boldsymbol{R}_\perp|} \arccos\left(\frac{(\boldsymbol{q} \times \boldsymbol{l}) \cdot (\boldsymbol{q} \times \boldsymbol{R}_\perp)}{|\boldsymbol{q} \times \boldsymbol{l}||\boldsymbol{q} \times \boldsymbol{R}_\perp|}\right), \tag{2.48}$$

where $\boldsymbol{R}_\perp$ is the transverse component of $\boldsymbol{R}$ with respect to the virtual photon direction. In Fig. 2.15 the above defined vectors and the azimuthal angle ϕ_R and ϕ_S are shown. In the following all calculations are carried out in a frame, where the nucleon and the two hadron system is collinear and transverse components, indicated with subscripts T, are measured with respect to $\boldsymbol{P}_h$. The difference of $\boldsymbol{R}_\perp$ and $\boldsymbol{R}_T$ is of the order $1/Q$. For the azimuthal angle ϕ_R defined in Eq. (2.48) the difference of using $\boldsymbol{R}_\perp$ or $\boldsymbol{R}_T$ is of the order $1/Q^2$ and can be neglected [47].

The process defined in Eq. (2.44) can be described for one photon exchange by the extended handbag diagram shown in Fig. 2.16. The fragmentation into two hadrons is described by the correlator $\Theta(\kappa, P_1, P_2)$, depending on the four-momenta κ, P_1 and P_2 of the struck quark and the two produced hadrons. As discussed before for the one hadron fragmentation correlator Ξ, the two hadron fragmentation correlator Θ can be expanded

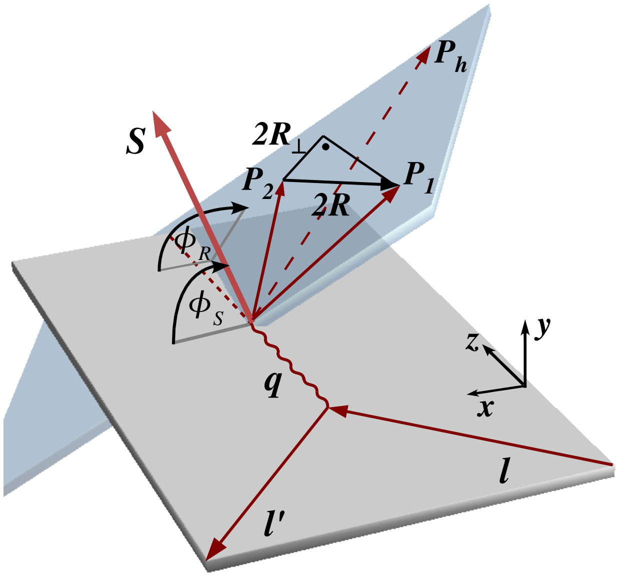

Figure 2.15: Definition of angles ϕ_R and ϕ_S and $\boldsymbol{R}_\perp$ in the cross-section of hadron-pair production.

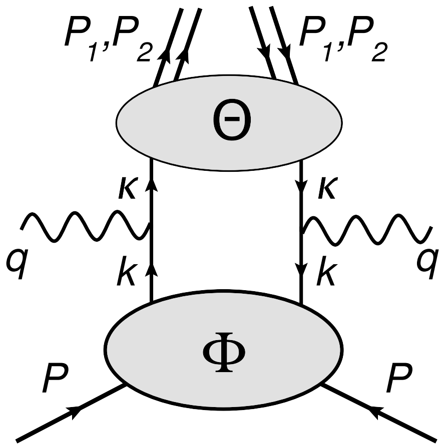

Figure 2.16: Diagram contributing to two hadron leptoproduction at lowest order.

on a basis of Dirac matrices and parametrized with fragmentation functions. Integrating over transverse momenta $\boldsymbol{P}_{h\perp}$ one obtains two fragmentation functions in leading-twist, which depend on the energy fraction z of the pair, on the way how the four-momentum of the pair is shared between the two hadrons $\zeta = 2R^-/P_h^-$ (where R^- and P_h^- are the 'minus' components of the light-cone representation of R and P_h) and on the invariant mass M_h of the pair [19]:

$$\mathcal{P}_-\Theta(z,\zeta,M_h^2)\gamma^- \;=\; \frac{1}{8\pi}\left\{D_1(z,\zeta,M_h^2) + iH_1^{\sphericalangle}(z,\zeta,M_h^2)\frac{\not{R}_T}{M_h}\right\}\mathcal{P}_-, \tag{2.49}$$

where $\mathcal{P}_- = 1/2\gamma^+\gamma^-$ is the projector on the 'minus' components of the light-cone representation. The function $D_1(z,\zeta,M_h^2)$ is a vector object and $H_1^{\sphericalangle}(z,\zeta,M_h^2)$ a tensor object. D_1 describes the fragmentation of unpolarized quarks into two unpolarized hadrons and $H_1^{\sphericalangle}$ describes the fragmentation of a transversely polarized quark into two unpolarized hadrons. Hence they have similar probabilistic interpretations as their analogues in the one hadron fragmentation discussed in Sec. 2.3. As the Collins fragmentation function, $H_1^{\sphericalangle}$ is chiral-odd and T-odd.

2.4.1 Two Hadron Cross-Section

With this two hadron fragmentation correlation matrix Θ the cross-section becomes:

$$\begin{aligned}\frac{\mathrm{d}^7\sigma}{\mathrm{d}\zeta\,\mathrm{d}M_h^2\,\mathrm{d}\phi_R\,\mathrm{d}z\,\mathrm{d}x\,\mathrm{d}y\,\mathrm{d}\phi_S} &= \frac{2\alpha^2}{4\pi s x y^2}\sum_q e_q^2\Bigg\{A(y)q(x)D_1^q(z,\zeta,M_h^2)\\ &+B(y)|\boldsymbol{S}_\perp|\frac{|\boldsymbol{R}_T|}{M_h}\sin(\phi_R+\phi_S-\pi)\Delta_T q(x)H_1^{\sphericalangle q}(z,\zeta,M_h^2)\Bigg\},\end{aligned} \tag{2.50}$$

whereas the term $\Delta q(x)D_1^q(z,\zeta,M_h^2)$ corresponding to longitudinally polarized target nucleons is left out. The definitions of the kinematical factors $A(y)$ and $B(y)$ are the same as given in Eq. (2.38).

The complete cross-section, taking also into account transverse momenta of quarks can be found in [48]. Here, according to the one hadron case several additional terms appear at leading twist, i.e. a term, which is connected to the Sivers function. The cross-section including also subleading twist effects was calculated in [47]. In this work only the part depending on transversity is studied.

2.4.2 Two Hadron Single Spin Asymmetry

As seen in Eq. 2.50 The term related to the transversity distribution has an azimuthal dependence in $\sin(\phi_R + \phi_S - \pi)$ and can therefore be accessed by building the following asymmetry:

$$A = \frac{\mathrm{d}^7\sigma^{\uparrow} - \mathrm{d}^7\sigma^{\downarrow}}{\mathrm{d}^7\sigma^{\uparrow} + \mathrm{d}^7\sigma^{\downarrow}} = |\boldsymbol{S}_T| D_{nn}(y) A^{RS}\sin(\phi_R+\phi_S-\pi), \tag{2.51}$$

with $D_{nn}(y) = B(y)/A(y)$ as defined in Eq. (2.40a) and the strength of the asymmetry A^{RS} is given by:

$$A^{RS} = \frac{\sum_q e_q^2 \frac{|\boldsymbol{R}_T|}{2M_h}\Delta_T q(x) H_1^{\sphericalangle q}(z,M_h^2)}{\sum_q e_q^2 q(x) D_1^q(z,M_h^2)}. \tag{2.52}$$

It is important to note, that because $H_1^{\sphericalangle q}(z, M_h^2)$ does not depend on transverse quark momenta, the transversity distribution and the two hadron fragmentation function appear factorized in the cross-section, whereas in the single hadron case they appear convoluted over intrinsic quark transverse momenta, making it more difficult to extract transversity. In addition the measurement of the interference fragmentation function in e^+e^- annihilation is easier to perform, since the product of $H_1^{\sphericalangle} \cdot \overline{H_1^{\sphericalangle}}$ is measured and not the convolution as it is the case for the Collins fragmentation function. And last, the evolution equations of $H_1^{\sphericalangle q}(z, M_h^2)$ are easier to perform [49].

2.4.3 Partial Wave Expansion

Intuitively the helicity flip of the quark is absorbed by angular momentum L of the produced hadron pair. This means in the handbag formalism that between the outgoing and the incoming hadron pairs the angular momentum has changed by one unit $\Delta L = \pm 1$. For example the outgoing hadron pair is in a relative s-wave state and the absorbed pair is in a relative p-wave state. Hence there is an interference between two production amplitudes with two different phases. Therefore the fragmentation function is called dihadron interference fragmentation function. For small invariant masses one can assume that only s- and p-wave states are dominant.

In order to separate the different possible contributions the fragmentation functions are expanded in partial waves [50]. Relevant for such an expansion is the angle θ between $\boldsymbol{P}_{1,cm}$ in the center of mass frame of the hadron pair and the boost axis $\boldsymbol{P}_h$ (see Fig. 2.17), because in the center of mass frame ζ depends linearly on $\cos\theta$:

$$\zeta = \frac{2R^-}{P_h^-} = \frac{1}{M_h}\left(\sqrt{M_1^2 + |\boldsymbol{R}|^2} - \sqrt{M_2^2 + |\boldsymbol{R}|^2} - 2|\boldsymbol{R}|\cos\theta\right), \tag{2.53}$$

with

$$|\boldsymbol{R}| = \frac{1}{2M_h}\sqrt{M_h^2 - 2\left(M_1^2 + M_2^2\right) + \left(M_1^2 - M_2^2\right)^2}. \tag{2.54}$$

Because of this $\cos\theta$ dependence the variable ζ and therefore the two hadron fragmentation correlator Θ can be expanded in the basis of Legendre polynomials in $\cos\theta$. The expansion of the two hadron fragmentation functions D_1 and $H_1^{\sphericalangle q}$ up to the p-wave level gives:

$$D_1^q(z, \zeta(\cos\theta), M_h^2) \approx D_{1,UU}^q(z, M_h^2) + D_{1,UL}^{q,sp}(z, M_h^2)\cos\theta + D_{1,LL}^{q,pp}(z, M_h^2)\frac{1}{4}(3\cos^2\theta - 1), \tag{2.55}$$

$$H_1^{\sphericalangle q}(z, \zeta(\cos\theta), M_h^2) \approx H_{1,UT}^{\sphericalangle q,sp}(z, M_h^2) + H_{1,LT}^{\sphericalangle q,pp}(z, M_h^2)\cos\theta. \tag{2.56}$$

Here the superscripts s and p denote the wave of outgoing and incoming hadron pair and the subscripts U, L and T denote the polarization state of the outgoing and incoming hadron pair: unpolarized, longitudinal polarized and transversely polarized, respectively.

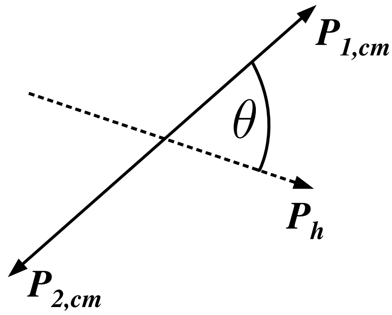

Figure 2.17: Definition of angle θ, which is in the center of mass frame of the hadron pair the angle between $\boldsymbol{P}_{1,cm}$ and the boost axis $\boldsymbol{P}_h$.

With $|\boldsymbol{R}_T| = |\boldsymbol{R}| \sin\theta$ and the expression of Eq. (2.56) for the fragmentation function $H_1^{\sphericalangle q}$ the cross-section for a transversely polarized target $\mathrm{d}\sigma(\boldsymbol{S}_\perp)$ measured with an unpolarized virtual photon, becomes:

$$\frac{\mathrm{d}^7\sigma(\boldsymbol{S}_\perp)}{\mathrm{d}\zeta\ \mathrm{d}M_h^2\ \mathrm{d}\phi_R\ \mathrm{d}z\,\mathrm{d}x\ \mathrm{d}y\ \mathrm{d}\phi_S} = \frac{2\alpha^2}{4\pi s x y^2}\sum_q e_q^2 \left\{ B(y)|\boldsymbol{S}_\perp|\frac{|\boldsymbol{R}|}{M_h} \right.$$
$$\left. \times \sin(\phi_R+\phi_S-\pi)\Delta_T q(x)\sin\theta \left[H_{1,UT}^{\sphericalangle q,sp}(z,M_h^2) + H_{1,LT}^{\sphericalangle q,pp}(z,M_h^2)\cos\theta\right] \right\}. \tag{2.57}$$

Hence transversity can be accessed via two different interference fragmentation functions $H_{1,UT}^{\sphericalangle q,sp}$ and $H_{1,LT}^{\sphericalangle q,pp}$. The former describes the interference of s- and p-waves and the latter describes the interference of two p-waves with longitudinal and transverse polarization.

However, due to the symmetry in the acceptance of the COMPASS detector in $\cos\theta$, as will be shown later in Sec. 5.3.6, the measurement is in first order only sensitive to $H_{1,UT}^{\sphericalangle q,sp}$ and the second term cancels.

2.4.4 Lorentz Invariant Definition of $\boldsymbol{R}_T$

The angle ϕ_R, defined in Eq. (2.48), based on the definition of $\boldsymbol{R}$ in Eq. (2.45) is not invariant against boosts in direction of the virtual photon, because P_1 and P_2 will be affected in a different way, leading to an azimuthal rotation of $\boldsymbol{R}$. With the definition [51]:

$$\boldsymbol{R} = \frac{z_2\boldsymbol{P}_1 - z_1\boldsymbol{P}_2}{z_1+z_2}, \tag{2.58}$$

the transverse component $\boldsymbol{R}_T$ is approximately invariant against boosts along the virtual photon direction and will be used in this thesis to compute the angle ϕ_R. The dependence of ϕ_R due to the two different definitions of $\boldsymbol{R}$ is studied in [52] and found to be small.

2.5 Other Possibilities to Measure Transversity and Sivers Distribution Functions

The Sivers distribution function can also be measured in single transversely polarized Drell-Yan dilepton production as performed at RHIC [53], $p\, p^{\uparrow} \rightarrow l\, \bar{l}\, X$, where the two leptons are produced via the annihilation of a $q\bar{q}$-pair.

The measurement of pion-induced Drell-Yan muon pair production, $\pi^{-}\, p^{\uparrow} \rightarrow \mu\, \bar{\mu}\, X$, is a future plan of the COMPASS-II experiment [54, 55]. Tests in the years 2007, 2008 and 2009 were performed to demonstrate the feasibility of such a measurement.

The PAX collaboration at GSI is planning to measure single transversely polarized proton antiproton Drell-Yan D-meson production [56], $p^{\uparrow}\, \bar{p} \rightarrow D\, X$ or $p\, \bar{p}^{\uparrow} \rightarrow D\, X$, because at the given energies the dominant process is $q\bar{q} \rightarrow c\bar{c}$, with the subsequent fragmentation into a charmed meson. Because of the annihilation process no transverse spin is transferred and the final c and $\bar{c}$ are unpolarized. Hence only the Sivers distribution can result in a single spin asymmetry without any contributions of the Collins effect.
As already discussed, it is expected that for these processes the sign of the measured Sivers distribution is opposite to the one measured in SIDIS.

The transversity distribution function can also be measured in double polarized Drell-Yan dilepton production at RHIC [53]:

$$p^{\uparrow}\, p^{\uparrow} \rightarrow l\, \bar{l}\, X. \tag{2.59}$$

In this process a double spin asymmetry, involving the product of two transversity functions, namely of quarks and antiquarks, can be measured. The advantage of this channel is that no fragmentation functions are involved.

However, in double polarized $p^{\uparrow}p^{\uparrow}$ collisions the asymmetry in the polarized cross-section will be small because of a presumably small transversity distribution for anti quarks. Therefore, double polarized proton antiproton $p^{\uparrow}\bar{p}^{\uparrow}$ scattering, as planned by the PAX collaboration are more promising [56].

Another channel to measure transversity is to study Λ and $\bar{\Lambda}$ production in SIDIS with a transversely polarized target. Here the polarization of the produced Λ-baryon can be used as a polarimeter of the initial transverse spin of the fragmenting quark. From theoretical point of view this is a very clean channel to access transversity, however from experimental side statistics are limited. These spin transfers were measured at COMPASS for deuteron and proton targets. For both targets the measured Λ and $\bar{\Lambda}$ polarizations were found to be small and within the statistical error compatible with zero [57, 58].

3. The COMPASS-Experiment

In the following a brief overview of the COMPASS-experiment is given, allowing to follow the discussions in Chapters 4, 5 and 6 dedicated to the data analysis. For a detailed description in particular for the large variety of tracking detectors used in COMPASS see [59].

In Fig. 3.1 an artistic view of the COMPASS detector used in 2007 is given. The 160 GeV/c muon beam, coming from bottom left, interacts in the polarized target, which can be optionally polarized longitudinally or transversely with respect to the beam direction. The scattered muon and the produced particles are detected in a 50 m long detector built downstream of the target. The characteristic feature of COMPASS are the two open field dipole-magnets, called SM1 and SM2. In the first stage, situated around SM1, particles with large polar angles and small momenta are detected. It is therefore called large angle spectrometer (LAS). In the second stage, the small angle spectrometer (SAS) which is built around SM2, particles with high momenta and small polar angles are detected. This setup provides an excellent polar angle acceptance of $0 \leq \theta_{lab} \leq 180$ mrad and enables a measurement in a broad kinematical range. Each stage is completed with an electromagnetic calorimeter, a hadronic calorimeter and a muon-filter for particle identification of electrons, hadrons and muons. In stage one a Ring Imaging Cerenkov detector allows to identify pions, kaons and protons and low energetic electrons. At the end of the detector, behind muon-filter 2, the main part of the trigger system is located, allowing to select events, with an interaction in the target.

Distributed over the whole spectrometer, a large variety of tracking detectors, depending on the requirements of the rate, spacial resolution or the covered solid angle, is used. Scintillating fibers and silicon detectors, standing out due to high rate capabilities and a good time resolution or spacial resolution respectively, are used for tracking of the beam particles. For the reconstruction of tracks with small scattering angles Micromegas- and GEM-detectors, with excellent spacial resolution, are used. And finally tracks with large angles, are detected with STRAW tube detectors, multiwire proportional chambers and drift chambers. They cover a large area and have a coarse granularity.

In the next sections details about the muon beam, the polarized target and the particle identification with calorimeters and muon-filters are given.

3.1 The Beam

The μ^+-beam is created using the proton beam of the Super-Proton-Synchrotron (SPS). With each cycle $1.2 \cdot 10^{13}$ protons are accelerated to 400 GeV/c and directed on a 500 mm

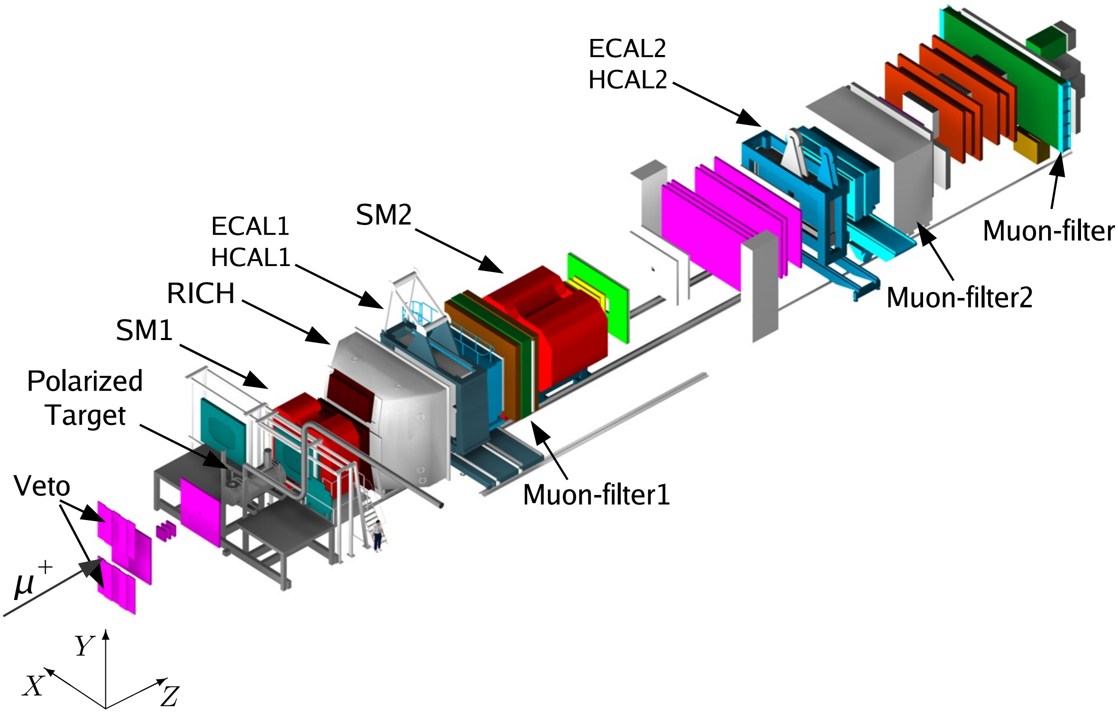

Figure 3.1: Artistic view of the 60 m long COMPASS detector [60].

thick target made of Beryllium. The complete cycle lasts 16.8 s, in which the extraction of the protons onto the production target takes 4.8 s. The latter time is called a spill. The produced positive particles are selected by their momentum and sent through a 600 m long tunnel, where the pions and kaons decay partially through weak decays in positive muons and muon neutrinos. The produced muons are focused and the remaining hadrons are filtered out with Beryllium absorbers. Finally muons with a momentum of 160 GeV/c are selected and transported via a 800 m long beam line to the COMPASS experiment. About $2 \cdot 10^8$ muons per spill cross the target whereas about $60 \cdot 10^3$ interactions per spill are recorded. A fact, which is however irrelevant for measuring the single spin asymmetries related to the transversity or the Sivers distribution, is that the muons are naturally longitudinally polarized ($\approx 80\,\%$) due to the parity violating weak decay: $\pi^+ \rightarrow \mu^+\nu_\mu$ or $K^+ \rightarrow \mu^+\nu_\mu$.

Since the muon beam is produced via particle decays and cannot be easily collimated like for example an electron beam, it is rather broad in its phase space and has a momentum spread of about 5 %. Therefore the momentum of each beam particle is measured individually with the so-called Beam Momentum Station (BMS), which is situated 100 m in front of the target. It consists of two scintillating fiber stations and four scintillating hodoscopes placed upstream and downstream of a bending magnet (B6) of the beam line. The reconstructed hits in front and behind the bending magnet can be bridged with the help of Monte Carlo simulations and the resulting bending radius provides finally the momentum of the particle [61].

3.2 The Polarized Target

A technical challenge is the construction of a polarized target for COMPASS. For precise measurements, large event yields on highly polarized nucleons are mandatory. Because of the low cross-section of the muon-nucleon interaction and the limitations in the intensity of the muon beam, a target with a high density of polarized nucleons is needed. This is achieved with a thick solid state Ammonium-target (NH_3). However, only the protons of the Hydrogen can be polarized, which results in a small dilution factor of about 15 %. The degree of polarization which can be reached for those protons is about 95 %. The inverse product of both quantities (≈ 7) scales directly the statistical error of the measurement of target spin dependent asymmetries.

A schematic view of the polarized target is shown in Fig. 3.2. On the left one can see the dilution refrigerator for cooling the target material to ≈ 60 mK. In red the three target cells are shown, surrounded by the cryostat, a superconducting solenoid and a dipole magnet. The angular acceptance is 180 mrad. The diameter of the target cells is 4 cm. The two outer cells are each 30 cm and the middle cell is 60 cm long. The direction of polarization of the two outer cells is the same and opposite to the one of the middle cell. This allows a simultaneous measurement of both spin states and is aimed to significantly reduce systematic effects.

The polarization of the target is performed in the 2.5 T longitudinal field of the solenoid and is achieved by dynamic nuclear polarization, transferring polarization from the electrons to the nucleons [62]. When the polarization is built up the spins are rotated adiabatically into transverse direction and are held by a 0.5 T dipole field.

The target polarization is destroyed every 4-5 days and the new polarization is built up reversely to reduce systematics (see Sec. 5.5.2). This is necessary because the dipole field has to be always kept in the same direction. Otherwise one would suffer from acceptance effects, because the dipole field deflects all charged particles. In particular one would need to change the beam line, because the beam has to enter the target with an angle, compensating the deflection received due to the dipole field, when crossing the target. And also the acceptance of the detector would be different for charged particles. In order to reach a polarization of about 90 % approximately 3 days are needed. The relaxation time of the polarization exceeds 3000 hours.

3.3 Particle Identification

3.3.1 Electromagnetic and Hadronic Calorimeters

At the end of both stages an electromagnetic and an hadronic calorimeter are situated. The aim of the electromagnetic calorimeters is to detect neutral particles, like the two photons coming from π^0 decay, or to identify electrons. The hadronic calorimeter measures the energies of the hadrons and can be used to identify muons, which deposit a characteristic small amount of energy. The calorimeters in the LAS (ECAL1 and HCAL1) and the hadronic calorimeter in the SAS (HCAL2) are included in the trigger, enabling to trigger on events with hadrons in the final state.

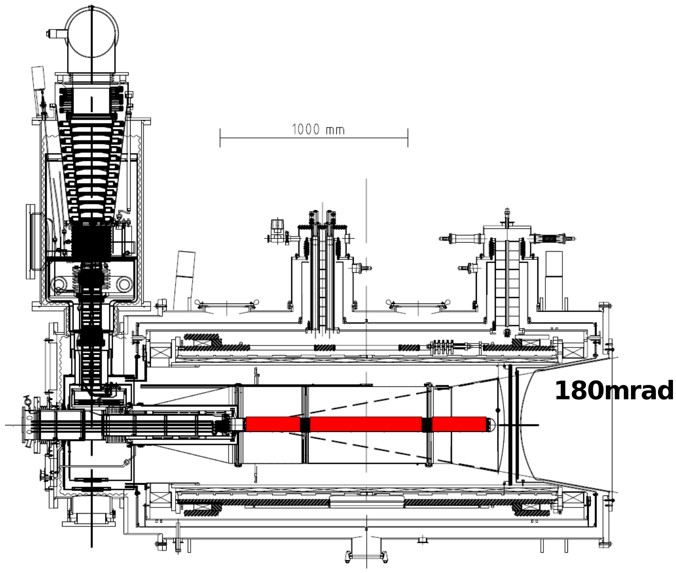

Figure 3.2: Technical drawing of the polarized target [63].

3.3.2 Muon Filters

At the very end of the LAS and of the SAS absorbers consisting of iron or concrete, are placed (Muon-filter 1 and 2). These absorbers filter out all non-muonic particles (for example high energetic pions which are not stopped in the hadronic calorimeter). The absorber at the end of the LAS has a hole near to the beam axis to enable particles, produced under small angles, to enter the SAS. Large area trackers are installed in front of and behind both absorbers, enabling a reliable identification of muons and in particular the identification of the scattered muon, which is important for the reconstruction of the DIS variables.

3.3.3 The RICH Detector

The Ring Imaging Cerenkov (RICH) detector in the LAS identifies particles in a broad momentum range. It makes use of the phenomenon that charged particles emit Cerenkov radiation if their velocity is larger than the speed of light in the medium in which they advance. The photons are emitted with a characteristic angle θ_{Ch} with respect to the direction of motion

$$\cos\theta_{Ch} = \frac{1}{n\beta} = \frac{1}{n}\frac{1}{\sqrt{1+m^2/p^2}}. \tag{3.1}$$

Hence, measuring θ_{Ch} and the momentum of the particle with the spectrometer, the mass and therefore the particle type can be determined. The minimum momentum p_{thr} for which Cerenkov photons get emitted follows from Eq. (3.1)

$$p_{thr} = \frac{m}{\sqrt{n^2-1}} \tag{3.2}$$

With the refractive index of about $n \approx 1.0015$ of the used radiator gas (C_4F_{10}) the momentum threshold is 2.5 GeV/c for pions, 9 GeV/c for kaons and 17 GeV/c for protons, respectively.

Looking again at Eq. (3.1) one sees, that for $\beta \rightarrow 1$ the angle θ_{Ch} reaches its maximum. Therefore, each particle type can be distinguished only up to a certain momentum from lighter particles. For example pions with momenta larger than 8 GeV/c cannot be distinguished from electrons anymore (which emit Cerenkov photons always with the maximum angle). Protons can be identified up to momenta of 60 GeV/c.

3.4 The Trigger System

The trigger system plays a central role in the experiment. Due to the high beam intensity but low interaction rates in the DIS regime it is important to discard all unphysical events already on hardware level, before reading out the detector channels [64].

Three different classes of triggers exists. The inclusive, called 'middle' and 'outer' trigger (incl. MT and OT), which solely requires the scattered muon. The semi-inclusive, called 'inner', 'middle' and 'ladder' trigger (IT, MT and LT), which requires the scattered muon and in addition a certain deposited amount of energy in at least one of the calorimeters ECAL1, HCAL1 or HCAL2. And finally an exclusive 'calorimeter' trigger (CT), which solely requires a certain deposited energy in one of the three calorimeters (ECAL1, HCAL1 and HCAL2). Here the required minimal deposited energy is higher with respect to the semi-inclusive case.

A schematic view of the arrangement of the essential trigger elements is shown in Fig. 3.3. The inclusive and the semi-inclusive triggers consist of pairs of scintillator hodoscopes, which are situated in front of and behind of a muon filter. By requiring timed and spacial correlations of the hits in pairs of hodoscopes one can trigger on muons, which have interacted in the target. In the direction perpendicular to the bending plane of SM1 and SM2 this is achieved by demanding, that the hit pattern in the hodoscopes corresponds to a track which points towards the target. In the bending plane one makes use of the fact that scattered muons have transferred some energy to the target nucleon and therefore get more deflected in the two magnets than muons, which have not interacted. The concept is schematically shown in Fig. 3.4. In 2007, for the data taking with transversely polarized protons, the 'inner' trigger was not in operation, since it collects quasi-real photo-production events with $Q^2 \ll 1\,(\mathrm{GeV}/c)^2$, which are not relevant for the analyses.

In 2007 a new trigger was set up called large Q^2 trigger [65]. It consists of a hodoscope in front of SM1 and is operated in coincidence with HCAL1 to trigger on scattered muons with such large scattering angles that they leave the detector without being detected by the yet existing trigger systems situated at the end of the detector.

3.4.1 The Veto Trigger System

The large amount of halo muons, which do not cross the target volume leads to a high rate of non physical events. In order to reduce this amount a veto trigger system is installed

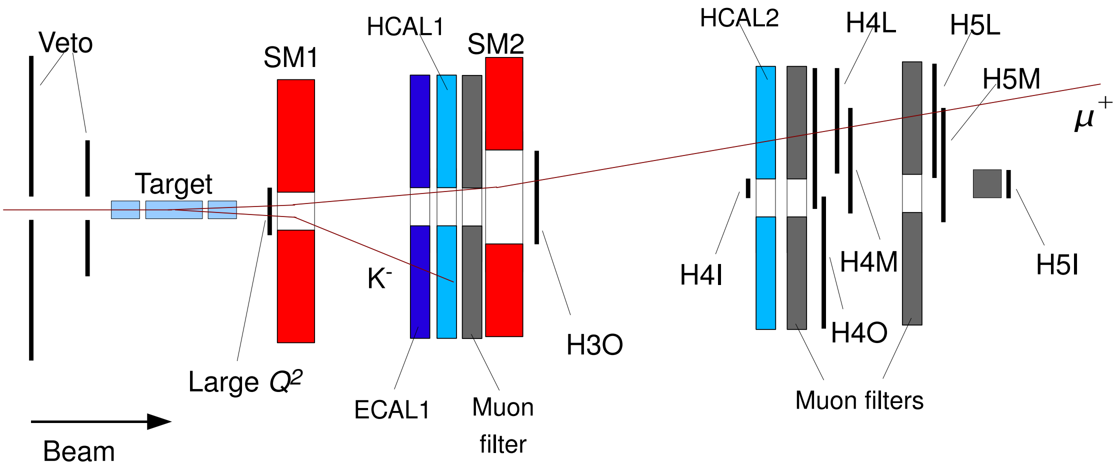

Figure 3.3: Schematic view of the arrangement of the essential trigger elements used in 2007. The muon triggers MT, OT and LT consist of pairs of hodoscopes (H4M,H5M), (H3O,H4O) and (H4L,H5L), respectively. The exclusive CT is built as logical OR of the three calorimeters ECAL1, HCAL1 and HCAL2. The large Q^2 trigger is operated in coincidence with HCAL1 to trigger on muons.

in front of the target. It consists of three planes of hodoscopes, leaving uncovered the central region around the beam. The geometrical arrangement of the two planes, which are closest to the target is shown in Fig. 3.5. They are placed such, that as much as possible divergent beam particles, with no interactions inside the target, are detected. With these two planes alone, whose relative distance is limited due to the experimental setup, it is however not possible to veto tracks which have polar angles smaller than 8 mrad. In order to effectively reject also halo muons with angles down to 4 mrad, which corresponds to the minimal angular acceptance of the 'middle' trigger, a third plane V_{bl} is placed 20 m upstream of the target (this rather huge distance is only caused by the fact, that no place was left to put it closer to the target). With these three planes two veto signals V' and V_{tot} are built, as quoted in the table in Fig. 3.5. The signal V_{tot} is used to veto the two inclusive triggers ('middle' and 'outer') and V' is used to veto the semi-inclusive 'ladder' trigger.

3.5 Data Acquisition and Reconstruction

The analog signals of the detectors in COMPASS are measured either with analog to digital converters (ADC), yielding the amplitude of the signal or they are discriminated and measured with time to digital converters (TDC), providing a time information of the hit. These informations combined with a unique channel number, to identify where in the experiment the signal was detected are read out with each trigger, written to disk and finally stored on CASTOR, which stands for CERN Advanced STORage manager. This so-called raw data contains all informations about the recorded events. Before it can be used for a physics analysis it has to be reconstructed to regain the essential informations

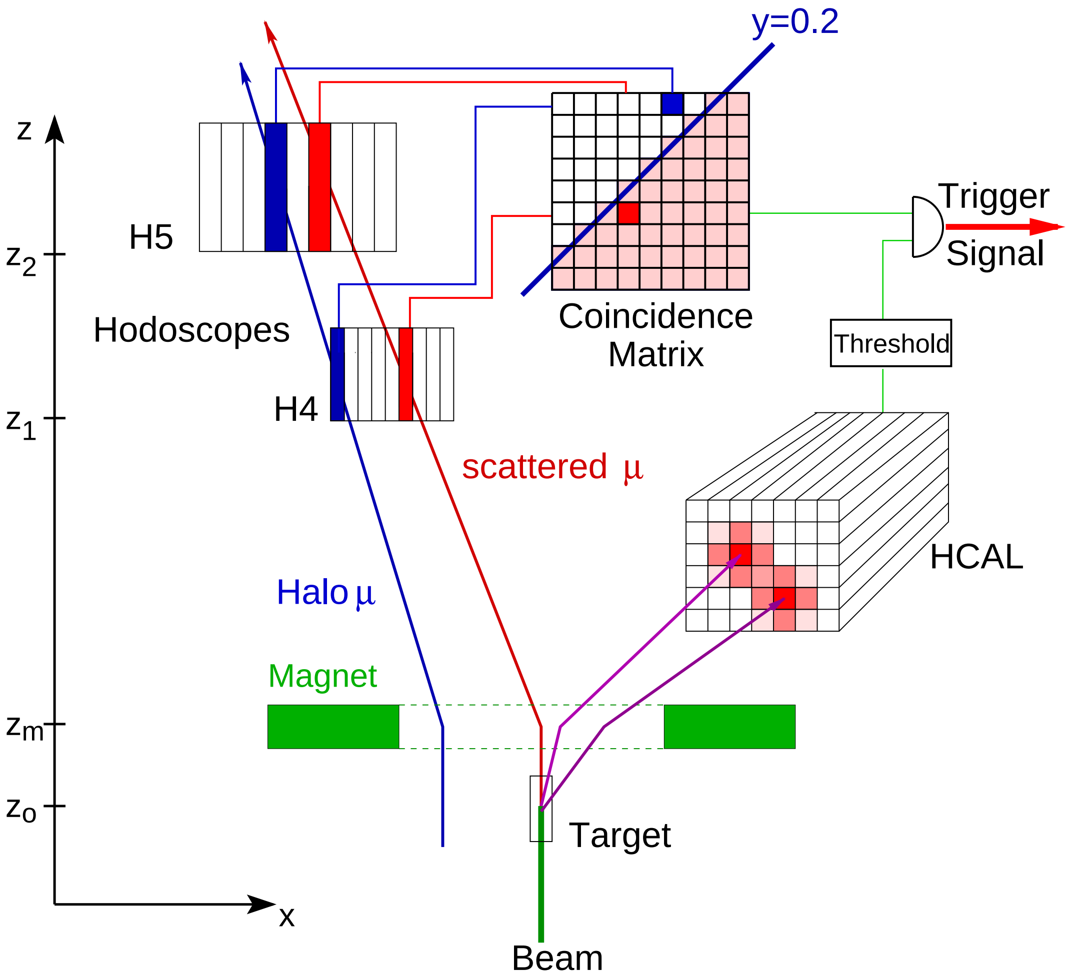

Figure 3.4: Concept of the trigger, which is based on the energy loss of the scattered muon. The scattered muon, leads to a coincidence in the activated (shaded) area of the coincidence matrix, while the halo muon fails. In addition, a minimum hadron energy can be required in the calorimeter [64].

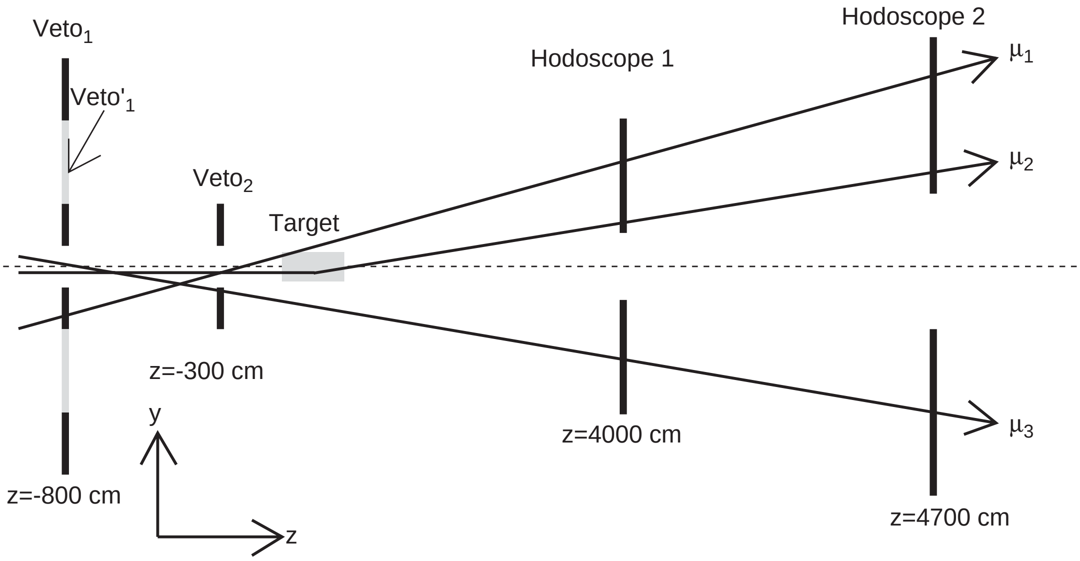

	Dimensions/ cm	z-pos./ cm	no. of elements	dead time/ %	Rate/ MHz
single Hodoscopes					
Veto_1	250×320, ∘ 4	-800	34	16	8.2
Veto'_1	250×120 ,□ 30×30	-800	24	1.7	4
Veto_2	30×30, ∘ 4	-300	4	5.9	9
V_{bl}	50×50, □ 10×10	-2000	4	1.9	4
combinations					
$\text{V'} = \text{Veto'}_1 + V_{\text{bl}}$				6	2.9
$\text{V}_{\text{tot}} = \text{Veto}_1 + \text{Veto}_2 + V_{\text{bl}}$				21	14.7

Figure 3.5: Schematic view of the arrangement of the veto trigger elements in front of the target. The tracks μ_1 and μ_3 are vetoed, whereas the track μ_2 fulfills the inclusive trigger condition. The table shows the dimensions of the various veto planes and the composition of the two veto signals V' and V_{tot} [64].

of the collected physical event. This means in practice reconstruction of tracks, vertices and clusters in the calorimeters and identification of particle types, using for example the RICH detector and the muon absorbers. This is done by using the software package CORAL, implemented in C++, which is the official COMPASS reconstruction program. The first step is the decoding, taking into account the position of the detector in the experiment and specific properties like timing or energy calibrations, which finally results in a list of hits. The second step is the clustering, which means that hits of neighboring channels are grouped into clusters. Based on this list of clusters tracks and vertices are reconstructed using a Kalman filter [66]. The output, like track parameters, interaction vertices, calorimeter clusters and RICH likelihoods, is written to so-called 'mDST' files (mini Data Summary Tape), which contain the informations in ROOT trees [67]. A schematic view of the reconstruction flow is shown in Fig. 3.6. It is worthwhile to mention, that the reconstruction algorithms for Monte Carlo data and real data are exactly the same.

The physics analyses are finally performed on these mDST files using the software package PHAST (Physics Analysis Software Tools), which provides a convenient interface for the user to access the features of the reconstructed events. In addition it provides a common set of algorithms to compute the relevant physical values of each event and an interface to store them in a user defined subsample tree, on which the final analysis, as in this thesis the extraction of asymmetries, is performed.

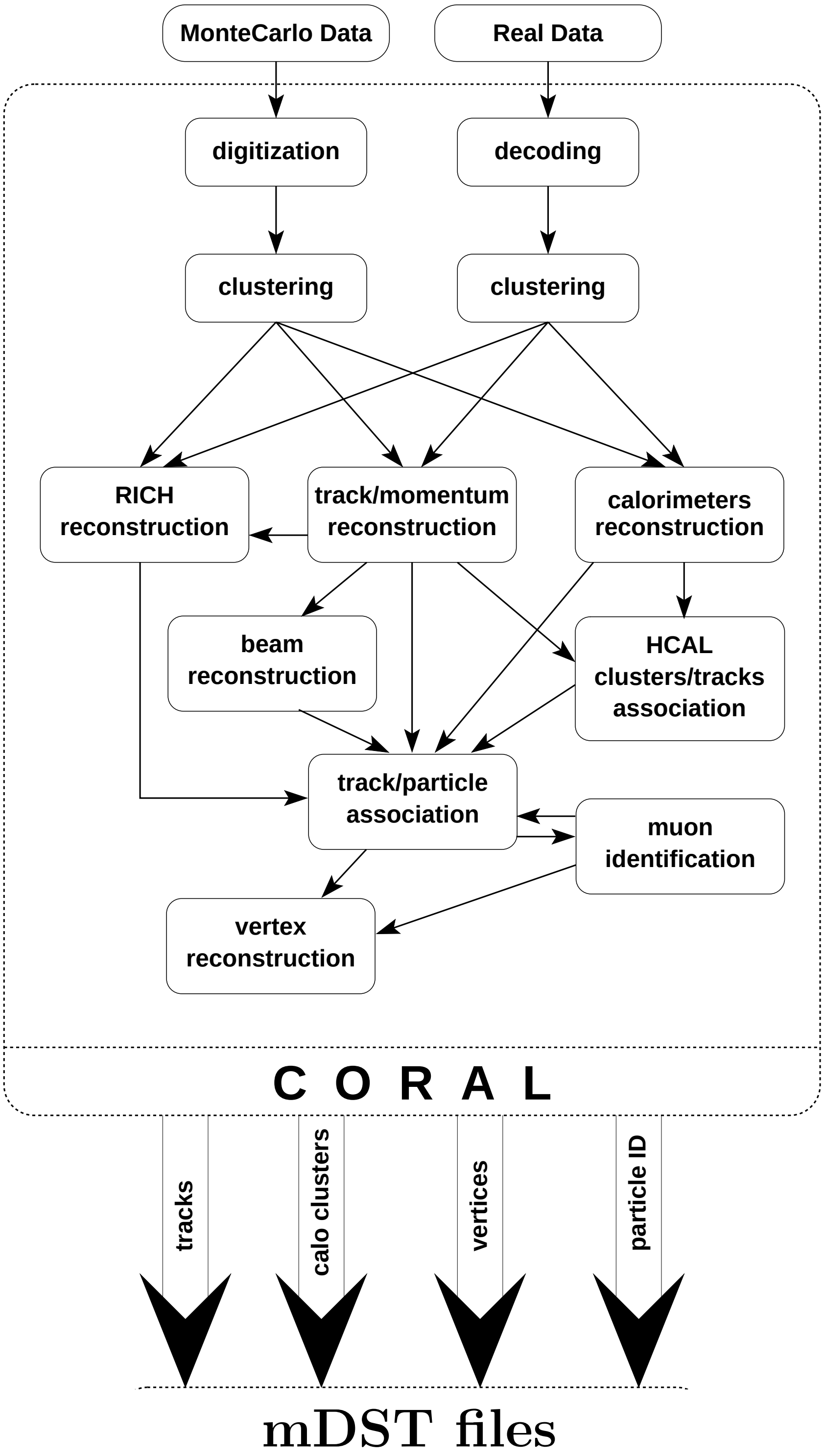

Figure 3.6: Schematic view of the COMPASS reconstruction software for Monte Carlo and for real data [59].

4. 2007 Transverse Proton Data

In 2007 COMPASS recorded 12 weeks of data taken with a transversely polarized NH_3 target. This corresponds to 440 TB of data written to tape. In between, six weeks with a longitudinally polarized target were taken. In the following 'first half' and 'second half' stand for the six weeks $25 - 31$ of data taking before and the six weeks $39 - 43$ of data taking after the longitudinal run, respectively.

The first production of the data was done with a quite preliminary alignment and especially for the first half of data taking with some missing detector calibrations. In addition CORAL was not able to correctly reconstruct events triggered by the large Q^2 trigger, which was active since week 26. This affected in particular also those events triggered simultaneously by CT and large Q^2 trigger, which as a result were partly lost during reconstruction [68]. This could not be fixed in CORAL. Therefore the large Q^2 trigger was later on completely switched off in reconstruction. The possible gain of the large Q^2 trigger has been studied in detail in [65], with the outcome that the kinematical region was already covered by the calorimeter trigger. In Tab. 4.1 the different CORAL versions are listed as they were used for the event reconstruction of the different weeks. In addition it is indicated if the large Q^2 trigger was switched on or off in the reconstruction. The horizontal lines indicate the groups of 'coupled weeks' with opposite target polarization, as they will be used in the data quality procedures described in Sec. 4.2. Because of the problems discussed above all data of all weeks were produced a second time. A discussion about the differences of the two productions can be found in [69, 70, 71, 72].

Due to the problems described in the previous paragraph, production 1 of week 25 till week 31 could not be used for the analysis. For those weeks production 2 is used. For week 39 till week 43 the situation is different. Here production 1 is used for these weeks.

4.1 Initial Data Sample

During the reconstruction process of the raw data with CORAL all events with at least one vertex are stored to the mDST file. Additional cuts are applied to reduce the amount of data for the analysis of SIDIS processes.

- Primary vertex with one uniquely reconstructed scattered muon
- Photon virtuallity $Q^2 > 1\,(\text{GeV}/c)^2$

The definition of 'primary vertex' will be given in Sec. 5.3.1. These cuts, as they will be anyhow applied in the physics analysis reduces the amount of data of about a factor of 15.

Table 4.1: CORAL versions used for the two productions, production slot and if large Q^2 trigger events have been reconstructed or not. The horizontal lines indicate the groups of 'coupled weeks' with opposite target polarization

	Production 1			Production 2		
Week	CORAL version	slot	large Q^2	CORAL version	slot	large Q^2
25	07-5-29-slc4	(0-7)	-	07-10-5-slc4-rev1	(1-7)	no
26	07-5-29-slc4	(0-7)	yes	07-10-5-slc4-rev1	(1-7)	no
27	07-7-31-slc4	(1-7)	yes	08-7-30-slc4	(3-7)	no
28	07-7-31-slc4	(1-7)	yes	08-7-30-slc4	(2-7)	no
30	07-7-31-slc4	(1-7)	yes	08-7-30-slc4	(2-7)	no
31	07-7-31-slc4	(1-7)	yes	08-7-30-slc4	(2-7)	no
39	07-10-5-slc4	(1-7)	yes	08-7-30-slc4	(3-7)	no
40	07-10-5-slc4	(1-7)	yes	08-7-30-slc4	(2-7)	no
41	07-10-5-slc4-rev1	(2-7)	no	08-7-30-slc4	(3-7)	no
42a	07-10-5-slc4-rev1	(2-7)	no	08-7-30-slc4	(4-7)	no
42b	07-10-5-slc4-rev1	(2-7)	no	08-7-30-slc4	(4-7)	no
43	07-10-5-slc4-rev1	(2-7)	no	08-7-30-slc4	(3-7)	no

4.2 Data Quality

In order to extract the transverse target spin dependent asymmetries two data samples with opposite target polarization will be combined. This will be discussed in detail in Sec. 5.2. Several checks have been developed to ensure that the measured asymmetries are not influenced by instabilities in the detector acceptance. The checks are performed on a spill by spill level and on a run by run level.

4.2.1 Spill by Spill Monitor of Pseudo Efficiencies

In order to monitor the reliability of the tracking detectors, their pseudo efficiencies are studied on a spill by spill level. In addition this is a good cross check whether the alignment of the various tracking planes of consecutive periods with opposite target polarization provides compatible results. The pseudo efficiencies are evaluated, using the number of detected hits and the expected number of hits in each tracking detector, which are provided by CORAL for each reconstructed track:

$$\epsilon_{pseudo} = \frac{N_{hits,detected}}{N_{hits,expected}}. \tag{4.1}$$

They are called pseudo efficiencies since all the detector planes contributed in the tracking procedure including the one which is being investigated. Hence those pseudo efficiencies will be systematically larger than the ‘real’ efficiencies. Tracking devices, which were unstable in time have been removed from the track reconstruction for the second production of the data [73].

4.2.2 Spill by Spill Stability Checks

The idea is to monitor variables which are strongly correlated to the stability of the detector and which play important roles in the analysis. For example the number of charged and neutral clusters in the hadronic calorimeters, since one use them to reject muons.

Assuming the detector was stable during the whole period of data taking, the chosen distributions should be constant in time. As time unit a spill is chosen. The idea for detecting deviations in time and mark them as bad was adopted along the line of [74]. The algorithm was adapted and improved for the needs of the measurement with a transversely polarized target and the number of monitored distributions has been increased. This will be described in the next paragraph.

Six classes of distributions are chosen, where ‘#’ is used as abbreviation for ‘number of’:

- Macro variables class:
  - #beam particles per vertex
  - #tracks per primary vertex
  - #primary vertices per event
- Inclusive Trigger class:

  - #inclusive trigger per #beam particles (MT, LT, OT, CT, incl. MT)
- Exclusive Trigger class:
  - #exclusive trigger per #beam particles (MT, LT, OT, CT, incl. MT)
- RICH class:
  - mean likelihoods (background, μ, π, K, P, e)
  - angle which maximizes the likelihood
  - ring angle
  - #Cerenkov photons per spill
- Electromagnetic calorimeter class:
  - #charged cluster per event (ECAL1)
  - #neutral cluster per event (ECAL1)
  - charged cluster energy per event (ECAL1)
  - neutral cluster energy per event (ECAL1)
- Hadronic calorimeters class:
  - #charged cluster per event (HCAL1, HCAL2)
  - charged cluster energy per event (HCAL1, HCAL2)

In order to classify a spill as good or bad, it is for all variables of a class, compared to its neighboring spills. Where the interval is restricted to 600 spills to the left and 600 to the right. If a spill has to the left (or to the right) not so many neighbors the interval to the right (or to the left) is enlarged accordingly to ensure, that each spill is compared with 1200 spills in total. For each spill the so-called 'number of good neighbors' is determined, by counting the number of spills whose variables are within certain boundaries around the values of the regarded spill. The optimal size of these limits is found, if the 'number of good neighbors' distribution shows two separated peaks, one close to zero and one close to 1200. Figure 4.1 shows the distributions exemplarily for four different sizes of the limit for the macro variables class. A cut on #neighbors $>$ 300 for the 5 sigma limit provides a good separation. In which sigma is indeed the RMS of the distribution, however determined in a restricted region where the distributions have no steps and show no large fluctuations, which would spoil up the RMS value. The result after applying the cut on the number of neighbors is shown in Fig. 4.2, where bad spills are marked in red. As one can see all short time fluctuations are correctly classified as bad.

The final list of which spills have to be rejected in the analysis is built as an logical 'OR' of the classification of the six classes. Which means if in at least one class a spill is classified as bad it is excluded from the analysis.

Finally the cleaned distributions for two coupled weeks are checked. In particular the trigger and the calorimeter sub-trigger rates are checked carefully for long term stability. Due to changed thresholds, steps in the ECAL1 sub-trigger rate for week 27/28, 39/40 and 41/42a are present and consequently the CT trigger events, purely fired by ECAL1, are rejected for these periods. The calorimeter sub-trigger rates for week 41/42a for events exclusively triggered by the CT are exemplarily shown in Fig. 4.3.

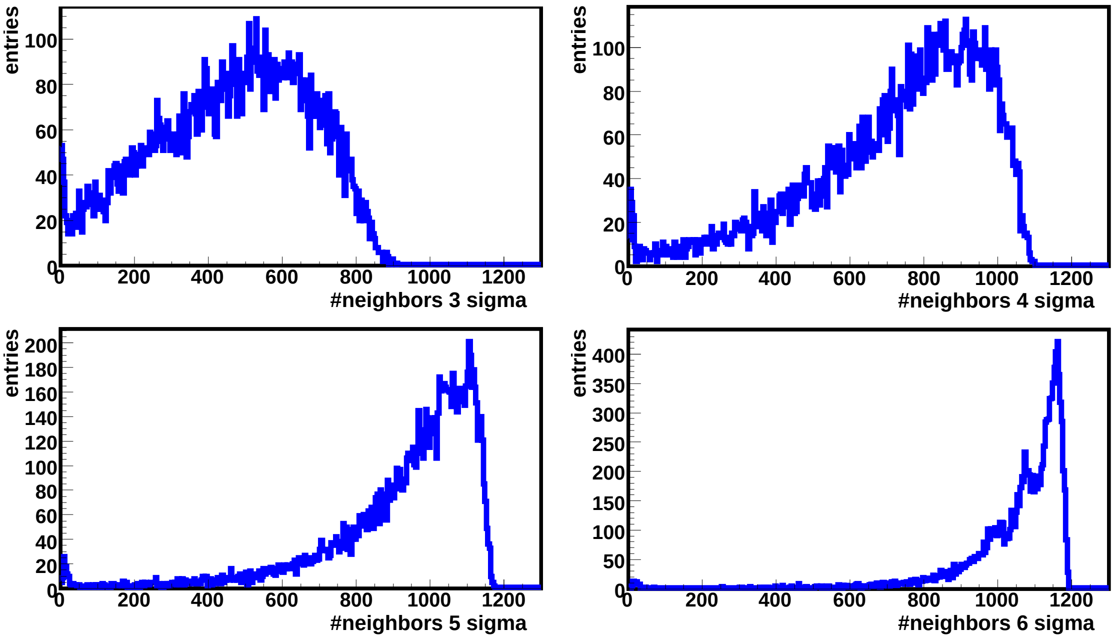

Figure 4.1: Example of 'number of good neighbors' distribution for four different values of the limits.

4.2.3 Run by Run Stability Checks on Observables

After cleaning the sample on a spill by spill level, as described in Sec. 4.2.2 the compatibility of several kinematical distributions is checked on a run by run level. This is done after applying the cuts for the single hadron analysis as described in Sec. 6.2.

The following 15 variables are taken into account:

- Z_{prim}, Z-position of the primary vertex
- $E_{\mu'}$, energy of scattered muon
- $\Theta_{\mu'}$, polar angle of scattered muon in laboratory system
- $\phi_{\mu'}$, azimuthal angle of scattered muon in laboratory system
- x_{bj}, longitudinal momentum fraction of struck quark
- Q^2, photon virtuallity
- y, energy fraction of virtual photon
- W, invariant mass of final hadronic state
- E_{had}, energy of hadron
- Θ_{had}, polar angle of hadron in laboratory system
- Φ_{had}, azimuthal angle of hadron in laboratory system

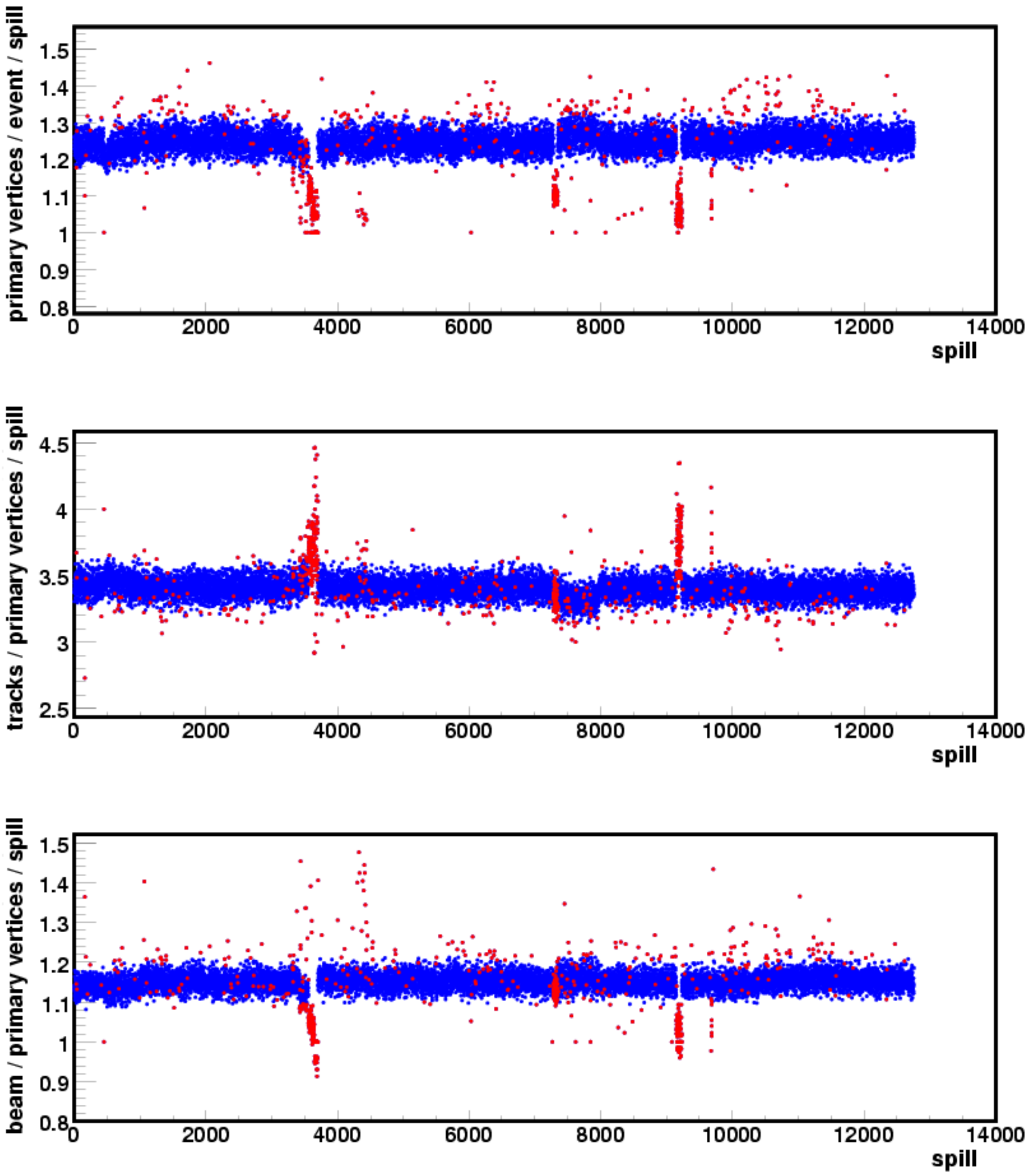

Figure 4.2: Example of applying cut on 'number of good neighbors' distribution. Bad spills are marked in red. Shown are the three distributions of the 'macro variables' class.

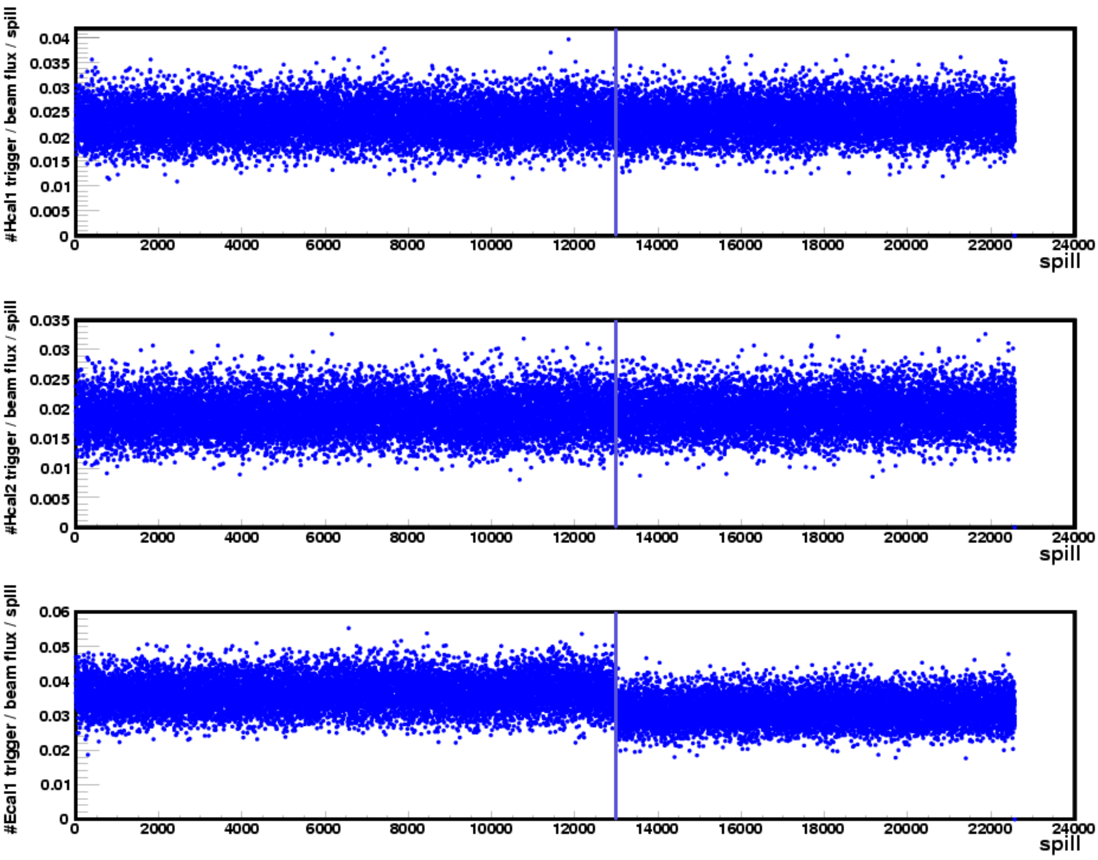

Figure 4.3: HCAL1, HCAL2 and ECAL1 sub-trigger rates versus spill number for week 41/42a (for the condition that CT exclusively triggered the event).

- p_T, transverse momentum of hadron
- z, energy fraction of hadron
- ϕ_h, azimuthal angle of the hadron plane in gamma-nucleon system (GNS)
- ϕ_S, azimuthal angle of target spin in GNS

Since the acceptance for the three target cells is not similar the distributions are binned in the three target cells. The ϕ_h and ϕ_S distributions are binned furthermore for positive and negative hadrons. The binning in the kinematical distributions have to be carefully chosen, to avoid empty bins. At the borders where the distributions quickly fall off a coarse binning is used.

If data taking was stable all these distributions should be statistically compatible for all runs. The idea is to compare the distributions of each run for a coupled week with all other runs of the coupled weeks.

4.2.3.1 The Algorithm

For all runs in a coupled double period the distributions are drawn and normalized with their integral. For each combination of pairs of runs the normalized distributions are subtracted from each other and via a χ^2-test it is tested whether the resulting distribution is compatible with zero. For each distribution and each run the resulting reduced χ^2_{red} is extracted and filled into a histogram. In the end one gets for each run and each distribution a histogram with $N-1$ entries (in which N is the number of runs of the coupled double period). In total $N \cdot (N+1)/2$ χ^2_{red} values per variable have to be determined, but because of the symmetry of the differences only $N \cdot (N+1)/4$ combinations have to be computed. A good run should have a χ^2_{red} distribution with a mean compatible with one and a RMS, which depends on the number of degrees of freedom. Fig. 4.4 shows exemplarily a result for a bad and a good run, respectively. Due to the comparison of each run with all the $(N-1)$ other runs in the two coupled weeks of data taking the signature of a bad run is quite evident.

In order to tag bad-runs the mean values of the χ^2_{red}-distributions of each run i $\langle\chi^2_{red,i}\rangle$ are filled in a histogram, resulting in a Gaussian distribution with a certain mean x_0 and a certain σ. Runs for which in at least one kinematical distribution $|\langle\chi^2_{red,i}\rangle - x_0| > 3.5\,\sigma$ applies are classified as bad and are rejected for the analysis.

4.2.4 Run by Run K^0 Stability Checks

For each run the number of reconstructed K^0-mesons per primary vertex is determined. The K^0-mesons are identified by their decay into $\pi^+\pi^-$-pairs, originating from vertices, which lie downstream of the target and have no incoming particles. By a fit to the invariant mass distribution of those reconstructed pairs the number of K^0-mesons is obtained. For each period these numbers are filled into histograms and the resulting distributions are fitted with Gaussian distributions. Runs for which the number of K^0-mesons deviates more than three σ are classified as bad and are excluded from the analysis [75, 76].

Table 4.2: Rejection rates of data quality checks.

Week	rejected trigger	event rejection rate [%]
25	-	36.6
26		21.7
27	pure ECAL1	55.0
28		53.2
30	-	19.2
31		24.7
39	pure ECAL1	35.4
40		22.8
41	pure ECAL1	25.4
42a		44.6
42b	-	15.6
43		33.0

In Fig. 4.5 the difference of the measured invariant mass of the $\pi^+\pi^-$-pair and the PDG value for the K^0-mass is plotted against the run number. The vertical red lines indicate the weeks of data taking, as written in the plots. For the first four weeks of data taking the shift in the K^0-mass is $0.5\,\mathrm{MeV}/c^2$. For week 30 and 31 it is about $1.5\,\mathrm{MeV}/c^2$. For week 39, 40 and 41 it is $-1\,\mathrm{MeV}/c^2$ and for week 42a, 42b and 43 it is about $0.5\,\mathrm{MeV}/c^2$. Problematic might be the different shift in the mass for week 41 and 42a, since those weeks are coupled to compute the asymmetries. In Fig. 4.6 the same is shown but now with production 2 for the second half of data taking. Now the shift is the same for all six weeks and about $1\,\mathrm{MeV}/c^2$. This indicates the improvement of the alignment provided for the second production.

4.3 Clean Data Sample

The rejection rates obtained for the twelve weeks of data taking are summarized in Tab. 4.2. In total 34 % of the data is rejected. The rejection rates for the single weeks are quite different and the total rate seem to be large with respect to the rejection rates for the deuteron data, taken in the years 2002, 2003 and 2004. However, it has to be mentioned, that for the production of the 2007 data all runs with more than 10 spills have been produced, independently of their rating in the electronic logbook, since this strongly depends on the people on shift. In addition less strict data quality checks were performed for the deuteron data. For week 27 the first half of the data had to be rejected because the detector setup was changed after a few days of data taking. In the beginning of week 28 problems with the ‘outer’-trigger occurred [77].

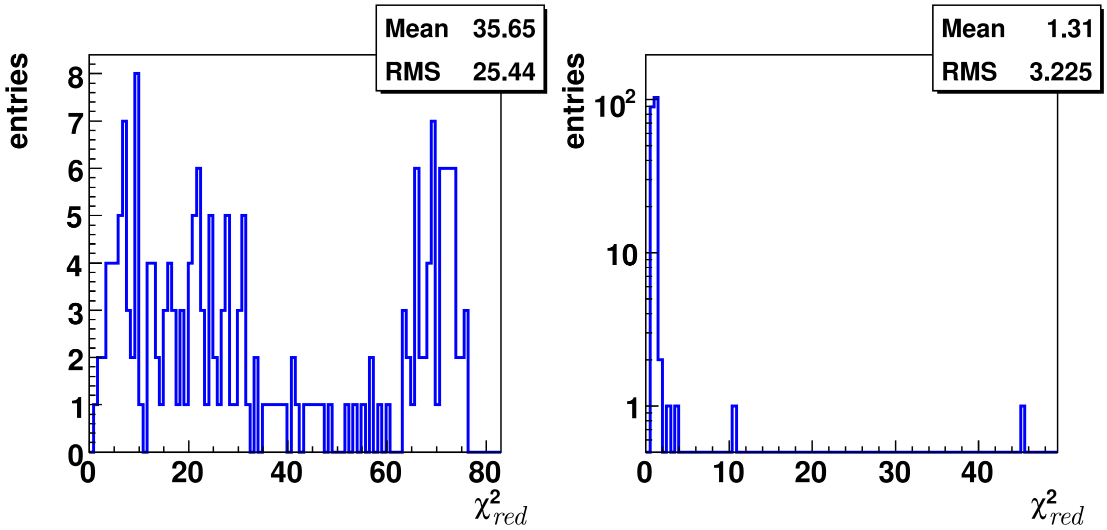

Figure 4.4: Example of a χ^2_{red} distribution for a bad (left) and a good (right) run. On the right the y-scale is drawn logarithmic.

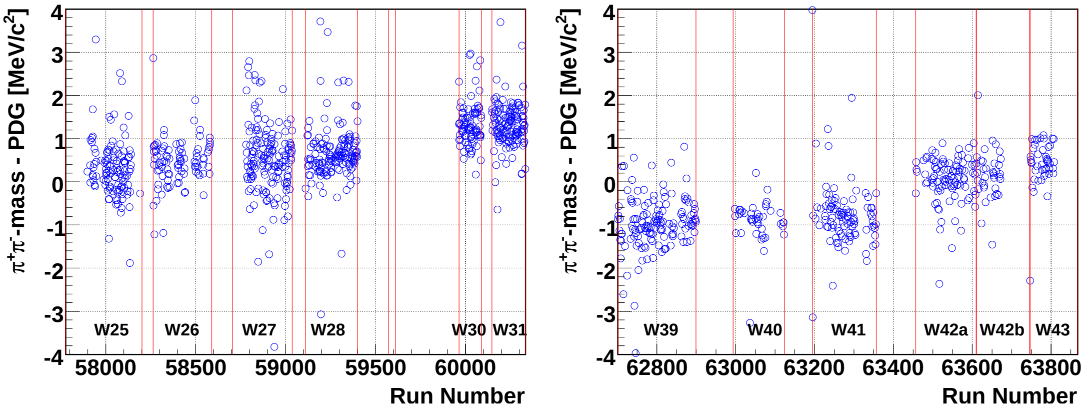

Figure 4.5: Difference of measured invariant mass of $\pi^+\pi^-$-pair and PDG value for K^0-mass plotted against run number. On the left for first half (production 2) and on the right for second half of data taking (production 1).

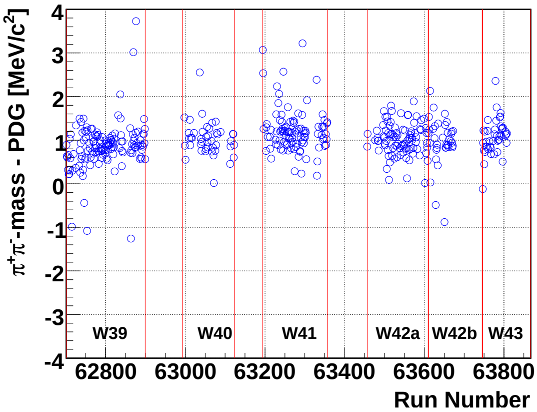

Figure 4.6: Difference of measured invariant mass of $\pi^+\pi^-$-pair and PDG value for K^0-mass plotted against run number, shown for second half of data taking (production 2).

5. Hadron Pair Asymmetries

5.1 General Framework

As discussed in Sec. 2.4.2 the chiral-odd transversity distribution $\Delta_T q(x)$ can be measured in combination with the chiral-odd polarized dihadron interference fragmentation function (DiFF) $H_1^{\sphericalangle}(z, M^2_{h^+h^-})$ in SIDIS. The fragmentation of a transversely polarized quark into two unpolarized hadrons leads to an azimuthal modulation in $\Phi_{RS} = \phi_R + \phi_S - \pi$ in the SIDIS cross section. The number of produced oppositely charged hadron pairs $N_{h^+h^-}$ can be written as:

$$N_{h^+h^-} \;\propto\; 1 \pm f \cdot P_T \cdot D_{nn} \cdot A^{RS} \cdot \sin\Phi_{RS} \cdot \sin\theta, \tag{5.1}$$

where θ is the angle between the momentum vector of h^+ in the center of mass frame of the h^+h^--pair and the momentum vector of the dihadron system in the laboratory frame (see Fig. 2.17) and $D_{nn} = (1-y)/(1-y+y^2/2)$ is the transverse spin transfer coefficient from target quark to struck quark, which depends on the energy fraction y of the virtual photon. The factors f and P_T account for the fact that only a fraction f of the target material are polarizable protons and that their degree of polarization P_T is less then 100 %. In the fit to extract the asymmetries the factor $f \cdot P_T \cdot D_{nn}$ will be omitted and the so called extracted 'raw' asymmetry will be corrected afterwards by multiplication with the mean value $1/\langle f \cdot P_T \cdot D_{nn}\rangle$. The $\sin\theta$ distribution was measured and is, as illustrated in Fig. 5.1, strongly peaked at one. Therefore the dependence is neglected in this analysis.

The measured amplitude A^{RS} is proportional to the product of the transversity distribution and the polarized DiFF

$$A^{RS} \propto \frac{\sum_q e_q^2 \cdot \Delta_T q(x) \cdot H_1^{\sphericalangle}(z, M^2_{h^+h^-})}{\sum_q e_q^2 \cdot q(x) \cdot D_1(z, M^2_{h^+h^-})}. \tag{5.2}$$

The sums run over the quark flavors q, e_q is the charge of the quark and $D_1(z, M^2_{h^+h^-})$ is the unpolarized DiFF. The polarized DiFF can be expanded in the relative partial waves of the hadron pair system, which up to the p-wave level gives:

$$H_1^{\sphericalangle} = H_{1,UT}^{\sphericalangle,sp} + \cos\theta H_{1,LT}^{\sphericalangle,pp}, \tag{5.3}$$

where $H_{1,UT}^{\sphericalangle,sp}$ is given by the interference of s- and p- waves, whereas the function $H_{1,LT}^{\sphericalangle,pp}$ originates from the interference of two p-waves with different polarization. The measured $\cos\theta$ distribution is shown in Fig. 5.2. Due to the acceptance of the COMPASS

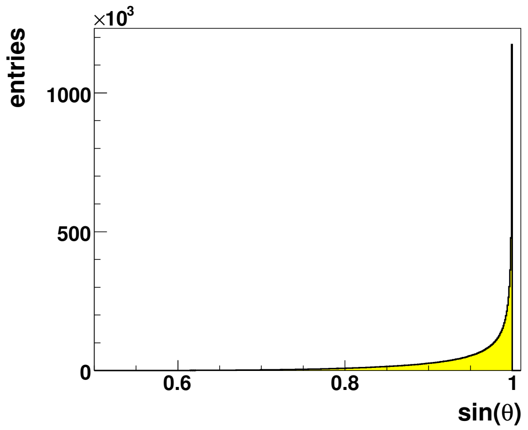

Figure 5.1: $\sin\theta$ distribution of final h^+h^--pair sample, with $\langle \sin\theta \rangle = 0.94$.

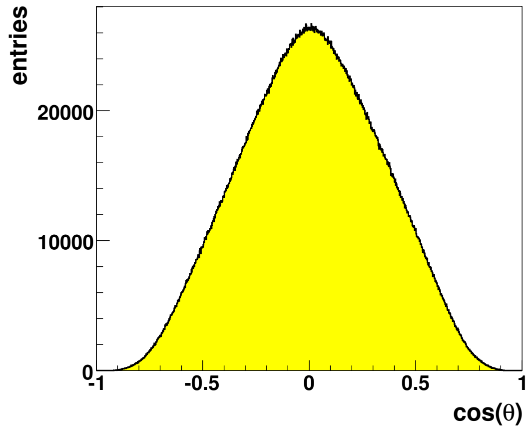

Figure 5.2: $\cos\theta$ distribution of final h^+h^--pair sample.

experiment it is symmetric around zero. Hence, the second term in Eq. (5.3) vanishes and the measurement is only sensitive to $H_{1,UT}^{\sphericalangle,sp}$.

Since the transversity distribution depends on x and the polarized DiFF on the energy fraction z and on the invariant mass M_{inv} of the hadron pair, the asymmetries will be extracted in bins of x, z and M_{inv}. Due to the limited statistics it is not possible to do a multidimensional binning in those three variables, but one has to integrate over the other two variables respectively. In the following analysis nine bins in x, eight bins in z and ten bins in M_{inv} are used. The chosen binning is listed in App. B.1.

5.2 How to Build Asymmetries

The standard way of building asymmetries is to combine two consecutive weeks of data taking with opposite target polarization. If the detector was stable all unpolarized effects cancel leaving only the spin dependent parts behind. Hence, for this kind of measurement the stability of the detector is important. In fact, as will be discussed in Sec. 5.5 and 6.4, tests with Monte Carlo data show that changes in the acceptance of the detector, which do not depend on the Z-position of the primary vertices, i.e. affects the whole target equally, have only a small impact on the extracted asymmetries.

In order to profit in the best way of the three cell target the data from the middle cell is split into two samples. The resulting 4 data samples are numbered consecutively from 1 to 4, as shown in Fig. 5.3.

Two data sets are used to extract the asymmetries. One with target polarization $+--+$ and one with $-++-$. In which $+$ stands for transverse spin up and $-$ for transverse spin down. In the following N_i denotes the number of events in target cell i, for the data set where the target was polarized $+--+$ and N_i' stands for the measured number of events in target cell i in the data set with $-++-$. Several combinations of N_i and N_i' can be build to study real or false asymmetries, as will be described in Sec. 5.7.

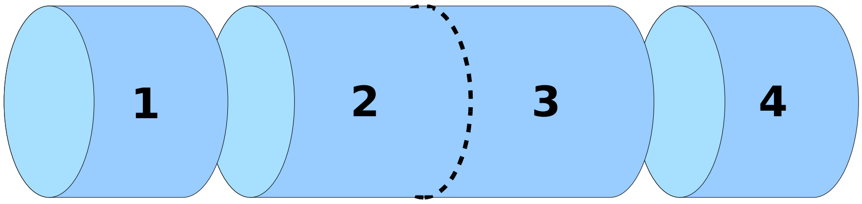

Figure 5.3: Definition of target cells used in analysis.

For extracting the physics asymmetries all 8 data samples are used in building the following ratio:

$$\mathrm{c20} = \frac{N_1 \cdot N_2' \cdot N_3' \cdot N_4}{N_1' \cdot N_2 \cdot N_3 \cdot N_4'}. \tag{5.4}$$

Several methods for the extraction of the asymmetries have been implemented. They will be discussed in Sec. 5.4. For the binned methods the number of events N_i are either binned in Φ_{RS} or binned in (ϕ_R,ϕ_S), depending on the fit method one uses. The event numbers N_i can be written as:

$$N_i(\Phi_{RS}) = c_i(1 + a_i \sin\Phi_{RS})(1 \pm \epsilon \sin\Phi_{RS}). \tag{5.5}$$

The constant c_i accounts for the unpolarized cross-section and muon flux. The last part describes the physical spin dependent modulation with strength ϵ, whereas the sign depends on the target spin orientation. The term in the middle describes the acceptance. Here only the part containing the same modulation as the physics asymmetry is considered, assuming that most likely only a change of acceptance in this angle could possibly bias the result. Inserting Eq. (5.5) in Eq. (5.4) and keeping only linear terms in $\sin\Phi_{RS}$ leads to:

$$\mathrm{c20} \approx C\frac{1 + (a_1 + a_2' + a_3' + a_4 + 4\epsilon)\sin\Phi_{RS}}{1 + (a_1' + a_2 + a_3 + a_4' - 4\epsilon)\sin\Phi_{RS}}, \tag{5.6}$$

with $C = \frac{c_1 c_2' c_3' c_4}{c_1' c_2 c_3 c_4'} \approx 1$, because of the crossed ratios and the requirement that the beam particle would have crossed all three target cells (see Sec. 5.3.1).

Performing a Taylor expansion in $\sin\Phi_{RS}$ with $\mathcal{O}(\sin^2\Phi_{RS})$ and defining $e_i = a_i - a_i'$ leads finally to:

$$\mathrm{c20} \approx C(1 + (e_1 - e_2 - e_3 + e_4 + 8\epsilon)\sin\Phi_{RS}). \tag{5.7}$$

With a fit $f(\Phi_{RS}) = c \cdot (1 + 8A^{c20}_{meas}\sin\Phi_{RS})$ for the measured asymmetry applies

$$A^{c20}_{meas} = \epsilon + (e_1 - e_2 - e_3 + e_4)/8. \tag{5.8}$$

The real asymmetry ϵ cannot be disentangled from the change of acceptances e_i. Assuming that for each target cell the change of acceptance is equal $e_1 \approx e_2 \approx e_3 \approx e_4$, implies that the measured asymmetry is unbiased. If this assumption is ‘slightly’ broken, the bias is still small, because of the factor of 8.

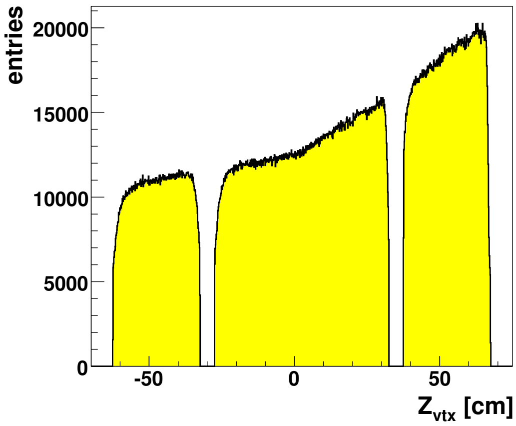

Figure 5.4: Distribution of the Z coordinate of the primary vertex of final h^+h^--pair sample.

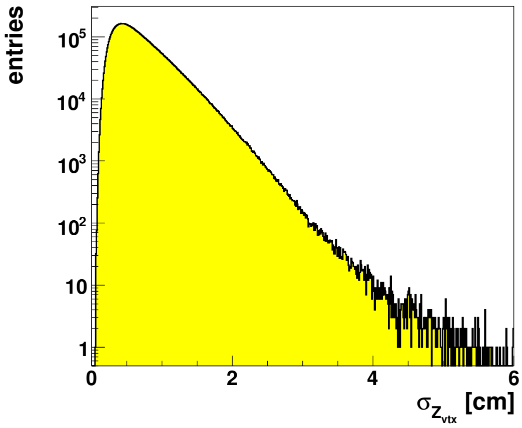

Figure 5.5: Distribution of the error of the Z coordinate of the primary vertex of final h^+h^--pair sample.

The standard method so far is to combine the data sets of two consecutive weeks of data taking. The final asymmetry is built as weighted mean of the single double periods. In this thesis for computing the final asymmetries the 'total' data set is used, meaning that all data sets of weeks with polarization $+--+$ and all data sets of weeks with $-++-$ are in each case combined. Hence, finally one has only one $+--+$ and only one $-++-$ data set, from which the asymmetries are extracted. For the binned extraction methods, in this approach the problems which arise due to low statistics is overcome. In App. B.2 the comparison between the two approaches will be discussed.

5.3 Data Selection

5.3.1 Primary Vertex

The interaction point of the beam muon with the target nucleon is called primary vertex. In approximately 13.5 % of the cases more than one primary vertex is reconstructed. In those cases the one with the maximum number of outgoing tracks is taken. If this is still inconclusive the vertex with the smallest χ^2_{red} of the fit is taken.

The vertex has to be within the limits of one of the three target cells. The position of the three target cells was determined in [78]. Identical beam intensities over the whole range of the target is achieved by requiring that the beam muon would cross all three target cells. The resulting distribution of the Z coordinate of the primary vertex for the final h^+h^--pair sample is shown in Fig. 5.4. In Fig. 5.5 the distribution of the error on the Z-position of the primary vertex is shown in logarithmic scale. Since the distance between the target cells is 5 cm, it is ensured that the target polarization is correctly assigned to the reaction.

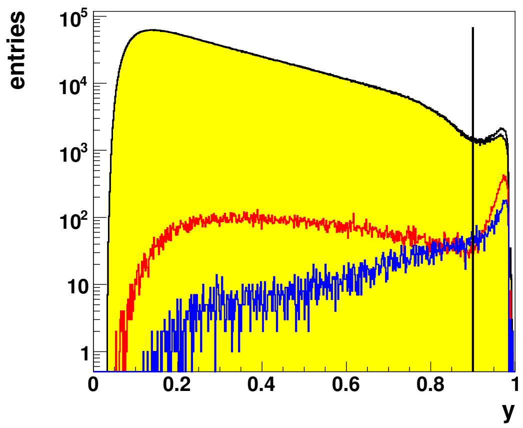

Figure 5.6: y distribution, without cut on W. Red: events to be rejected due to extrapolation test. Blue: events to be rejected due to muon recovery procedure.

5.3.2 Beam Muon

The beam muon associated with the best primary vertex is taken as the beam particle. A cut on a maximum momentum of $p_{beam} < 200\,\mathrm{GeV}/c$ is applied. In addition the fit of the reconstructed track must have $\chi^2_{red} < 10$.

5.3.3 Scattered Muon

The muon tagged by the reconstruction software CORAL as scattered muon is taken [79]. Additionally one looks for positively charged tracks with hits before and behind muon-filter 1. If the number of hits before the filter is larger 4 and behind larger 6 the track is considered as scattered muon candidate. In both cases it is additionally required that the χ^2_{red} of the track fit has to be better than 10 and the track must have passed more than 30 radiation length nXX_0. The event is rejected if in the end no or more than one scattered muon candidate exists.

Additionally all outgoing positively charged tracks with momentum larger $5\,\mathrm{GeV}/c$, except the scattered muon, are tested not to be a misidentified scattered muon, which has passed through the hole of the detector and therefore has only passed a small amount of radiation length. In order to overcome this the tracks are extrapolated to the entrance of muon-filter 2 and checked if they pass through the hole. If this is the case the event is rejected except when the track goes through the active area of the inner trigger hodoscope but without leaving a signal. This means it is a hadron which was stopped in the iron absorber placed in front of the hodoscope.

In Fig. 5.6 the effect of the muon recovery and the extrapolation test is shown. The red distribution shows the contribution of the extrapolation test. One sees, that over the whole y range misidentified muon candidates exists and that it is enhanced especially for $y \approx 1$. The blue distribution shows the contribution of the muon recovery. Events are gained in the large y region, but especially for $y \to 1$ it seems that most of them are misidentified muons. Both types of events are rejected. But as indicated by the yellow

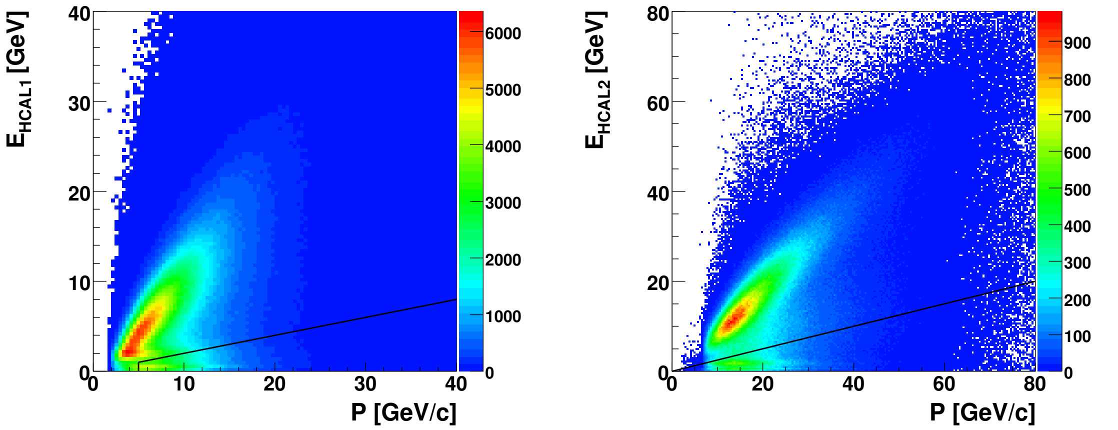

Figure 5.7: Left: Cluster energy deposited in HCAL1 vs momentum of track for hadrons. Right: Cluster energy deposited in HCAL2 vs momentum. The black lines indicates the cuts.

filled distribution there are still some events with misidentified muons left. However, these are finally cut away anyhow in requiring $y < 0.9$, as indicated by the vertical line, to avoid radiative corrections which in this region become sizable.

5.3.4 DIS Cuts

With the identified beam muon and the scattered muon the kinematical variables of the event are determined and deep inelastic scattering events are selected by applying a cut on the photon virtuallity $Q^2 > 1\,\mathrm{GeV}^2/c^2$ and a cut on the invariant mass of the final hadronic state to avoid the region of nucleon resonances $W > 5\,\mathrm{GeV}/c^2$ (Fig. 5.17). Furthermore a cut on the relative energy in the muon scattering process is done $0.1 < y < 0.9$ (Fig. 5.18). The lower cut rejects elastic scattering events and the higher cut discards events where radiative corrections become important.

5.3.5 Hadron Selection

The tracks have to be associated to the primary vertex and must have $\chi^2_{red} < 10$ and a penetration length of $nXX_0 < 10$ to be considered as hadron candidates. A well defined momentum is ensured in requiring, that the first measured point of the track Z_{first} is before and the last measured point Z_{last} is behind SM1. Which means $Z_{first} < 350\,\mathrm{cm}$ and $Z_{last} > 350\,\mathrm{cm}$. The following cuts are performed to remove muons from the sample:

- The last measured point must be in front of muon filter 2:
  $Z_{last} < 3300\,\mathrm{cm}$.
- Tracks which have associated clusters in the calorimeters of both stages are discarded.
- Tracks with an associated cluster in HCAL1 are discarded if:
  $P_{had} > 5\,\mathrm{GeV}/c \ \wedge \ E_{HCAL1} < P_{had} \cdot 0.2$ (see Fig. 5.7 left)
- Tracks with an associated cluster in HCAL2 are discarded if:
  $E_{HCAL2} < P_{had} \cdot 0.25$ (see Fig. 5.7 right)

In addition tracks which have more than one cluster in one calorimeter are discarded. For the energy fraction of the hadron it is required $z_i > 0.1$ and in addition $x_{F,i} > 0.1$ to remove hadrons originating from the target fragmentation. Where in the center of mass frame $x_{F,i}$ is defined as the longitudinal momentum $P_{z,i}$ of the hadron (with respect to the virtual photon) divided by the total available energy $\sqrt{s}$ ($x_{F,i} \approx P_{z,i}/\sqrt{s}$). The correlation between z_i and $x_{F,i}$ is shown in Fig. 5.8.

5.3.6 Hadron Pairs Selection

After the selection of the hadrons all possible combinations of oppositely charged hadron pairs in the event are built. For a good definition of the plane defined by the two hadrons (see Fig. 2.15) a cut on $R_T > 0.07\,\mathrm{GeV}/c$ is applied. This cut was tuned with Monte Carlo data. The correlation between reconstructed and generated R_T is shown in Fig. 5.9. One sees in the right plot, that for R_T below $0.07\,\mathrm{GeV}/c$ in a large number of cases the value is wrongly reconstructed. The dependence between R_T and invariant mass M_{inv} is shown in Fig. 5.10. For $R_T < 0.07\,\mathrm{GeV}/c$ the linear dependence between R_T and M_{inv} breaks down. The influence of the R_T cut on the invariant mass is shown in Fig. 5.12. In the mass spectrum one clearly sees the peaks of the K^0- and the ρ^0-meson at around $0.5\,\mathrm{GeV}/c^2$ and $0.77\,\mathrm{GeV}/c^2$, respectively.

Exclusively produced hadron pairs are removed by a cut on missing energy $E_{miss} > 3\,\mathrm{GeV}/c^2$. The E_{miss} distribution in the relevant region is shown in Fig. 5.11 and the impact on the energy fraction distribution z of the hadron pair is shown in Fig. 5.13. One clearly sees, that the cut on missing energy more smoothly removes the exclusive events than a cut on $z < 0.9$ do as it was done in the deuteron analysis. Moreover one sees that down to $z \approx 0.8$ a sizable amount of hadron pairs is rejected. The correlation of the energy fraction z_2 of the negative hadrons and of the energy fraction z_1 of the positive hadrons is shown in Fig. 5.14.

The $\sin\theta$ and $\cos\theta$ distributions of the h^+h^--pairs are shown in Fig. 5.1 and Fig. 5.2. As already discussed in Sec. 5.1 the cross-section and therefore the asymmetry depends on these two quantities. However, these dependencies can be safely neglected for this analysis, because the $\sin\theta$ distribution is strongly peaked at one and the $\cos\theta$ distribution is symmetric around zero.

5.3.7 Final DIS Distributions

The Figures 5.15 - 5.18 show the Q^2, x, W^2 and y distribution for the final oppositely charged hadron pair sample. Which means for each hadron pair the respective variable is filled in the histogram. In Fig. 5.19 the distribution of the transverse spin transfer parameter $D_{nn} = (1-y)/(1-y+y^2/2)$ is shown, which is relevant for the correction of the RS asymmetries (see Eq. (5.1)).

In Fig. 5.20 the correlation between W and y is shown (where the cuts on $W > 5\,\mathrm{GeV}/c^2$ and $0.1 < y < 0.9$ are released). The two variables are strongly correlated and furthermore one sees, that a cut on $y > 0.1$ already effectively cuts away almost all events with $W < 5\,\mathrm{GeV}/c^2$. In Fig. 5.21 the correlation for Q^2 and x is shown. Fig. 5.22 shows the same but without cut on W and y. Compared to Fig. 5.21, one sees the influence of the cut, namely diminishing the distribution in x. The Figures 5.23 and 5.24 show the correlation of Q^2 versus y and of Q^2 versus W, respectively.

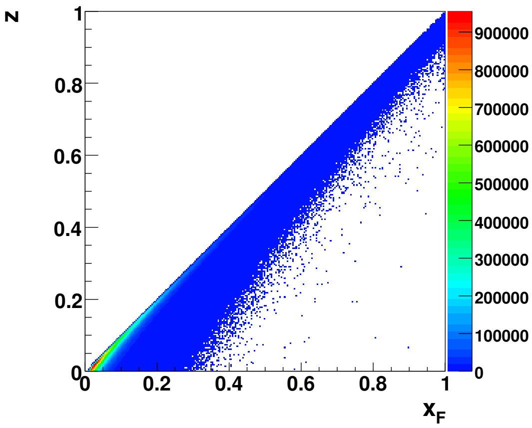

Figure 5.8: Correlation between energy fraction z and x_F for hadrons of h^+h^--pair sample.

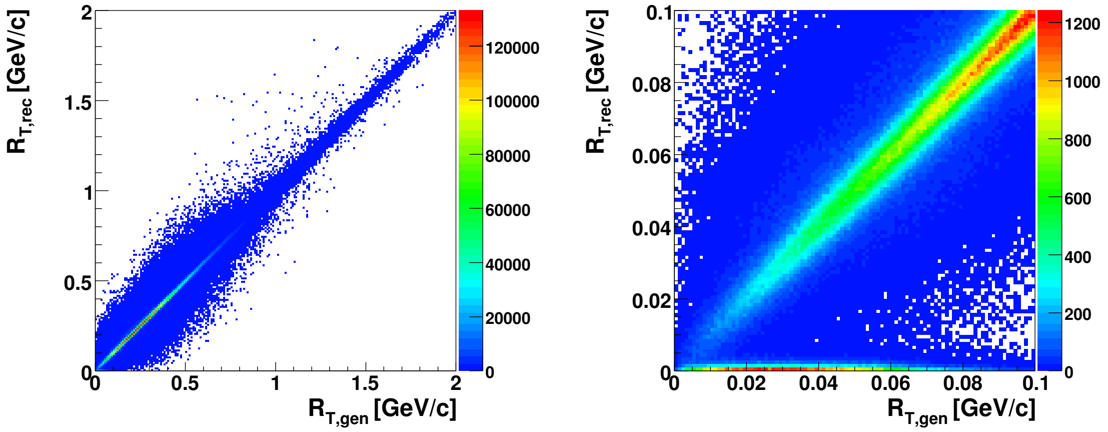

Figure 5.9: Reconstructed vs generated R_T (Monte Carlo data). On the left the whole region is shown and on the right a zoom with a finer binning of the lower region.

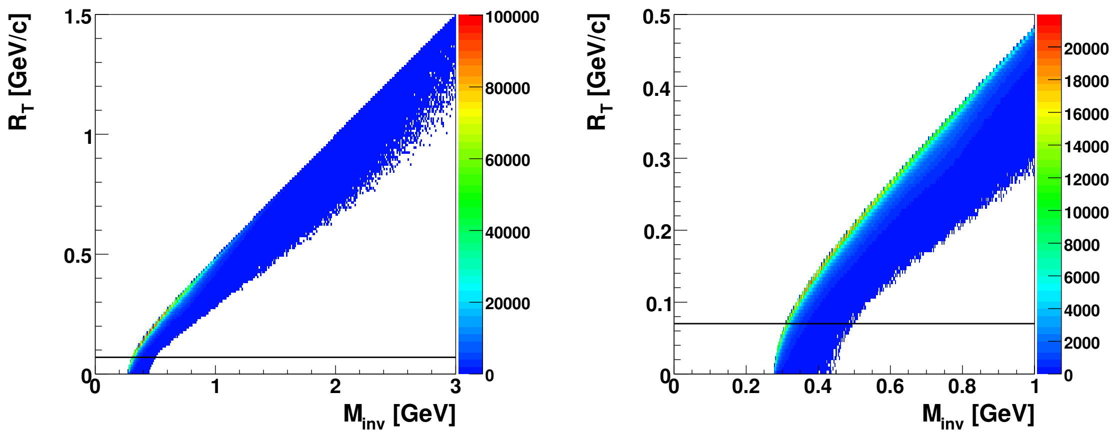

Figure 5.10: R_T versus invariant mass M_{inv} of h^+h^--pair sample. On the left the whole region is shown and on the right a zoom of the lower region. The horizontal line indicates the cut $R_T > 0.07\,\mathrm{GeV}/c$.

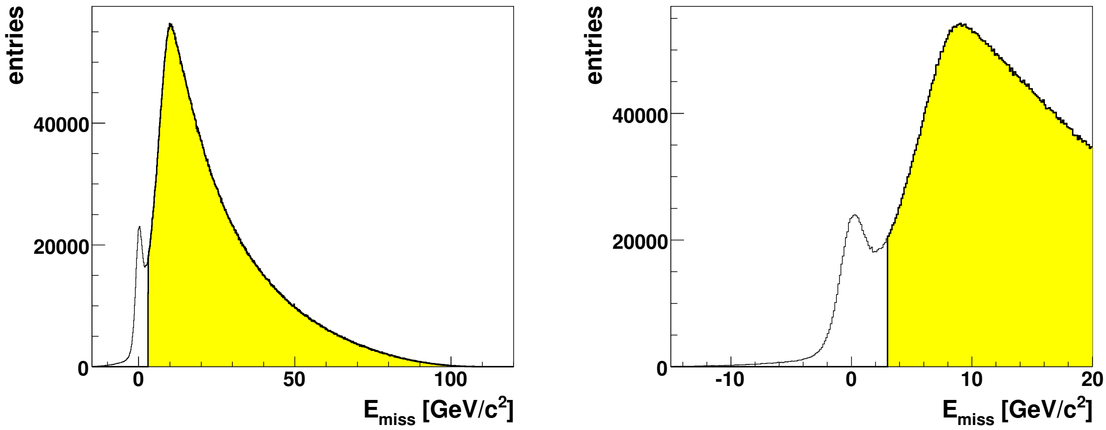

Figure 5.11: E_{miss} distribution of h^+h^--pair sample. On the right the relevant region is zoomed out.

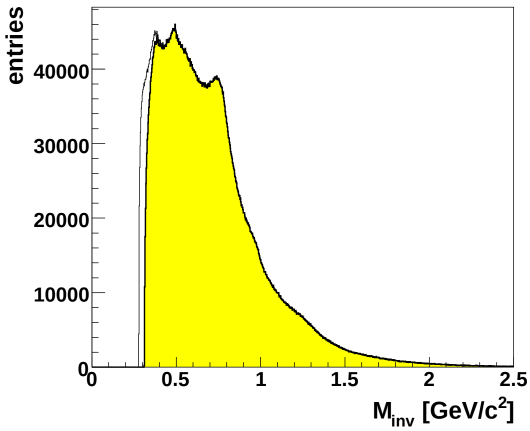

Figure 5.12: M_{inv} distribution of h^+h^--pair sample with and without cut on $R_T > 0.07\,\mathrm{GeV}/c$.

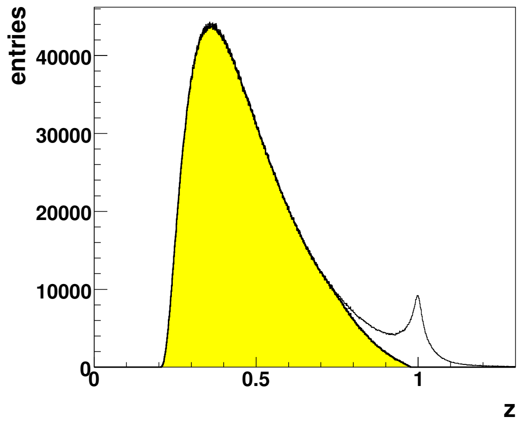

Figure 5.13: z distribution of h^+h^--pair sample with and without cut on $E_{miss} > 3\,\mathrm{GeV}/c^2$.

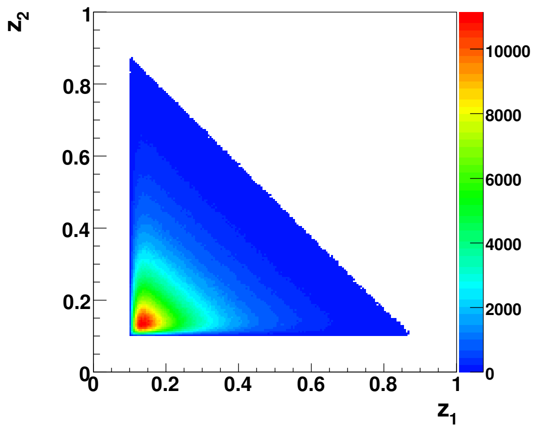

Figure 5.14: z_2 vs z_1 distribution of final h^+h^--pair sample.

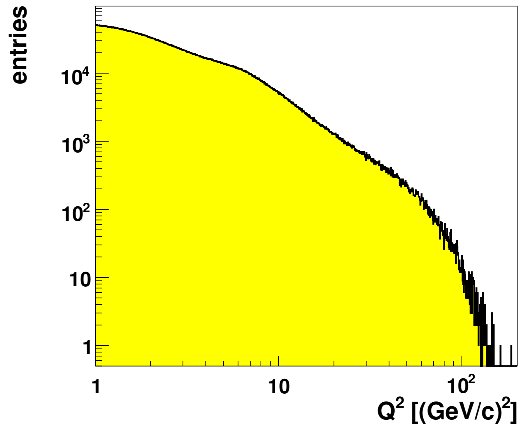

Figure 5.15: Q^2 distribution of final h^+h^--pair sample.

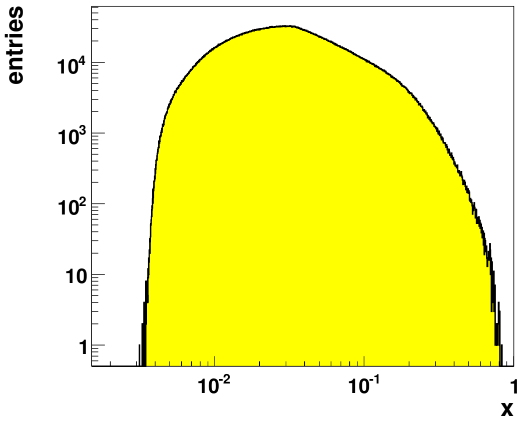

Figure 5.16: x_{bj} distribution of final h^+h^--pair sample.

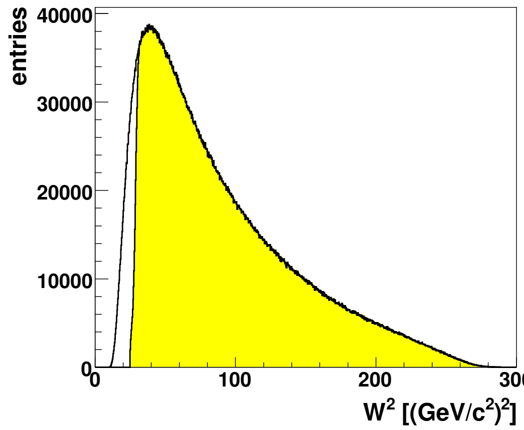

Figure 5.17: W^2 distribution of final h^+h^--pair sample (yellow). For the white histogram the cut on W and y is released.

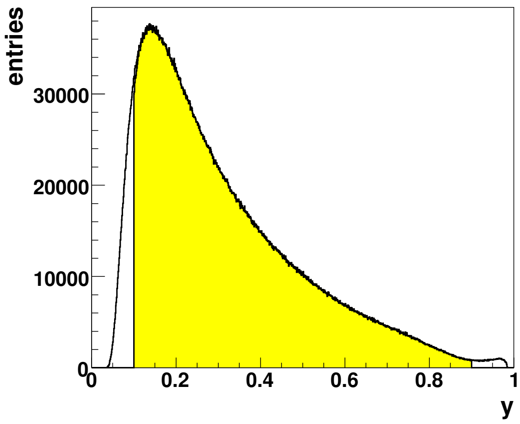

Figure 5.18: y distribution of final h^+h^--pair sample (yellow). For the white histogram the cut on W and y is released.

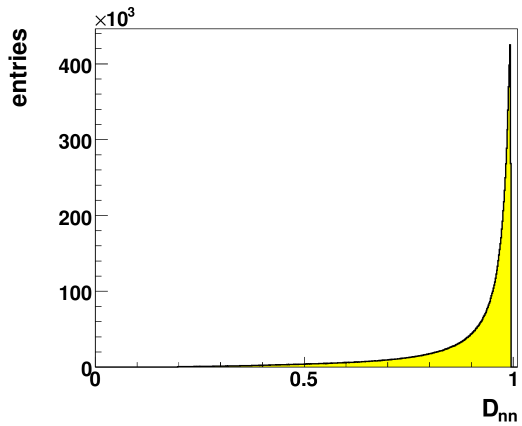

Figure 5.19: D_{nn} distribution of final h^+h^--pair sample, relevant for the correction of the RS asymmetry.

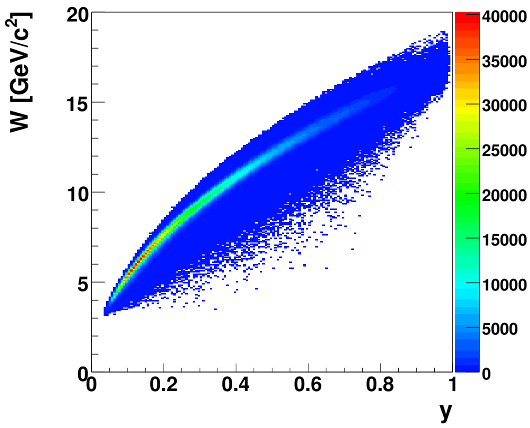

Figure 5.20: W vs y distribution of h^+h^--pair sample, with released cut on y and W.

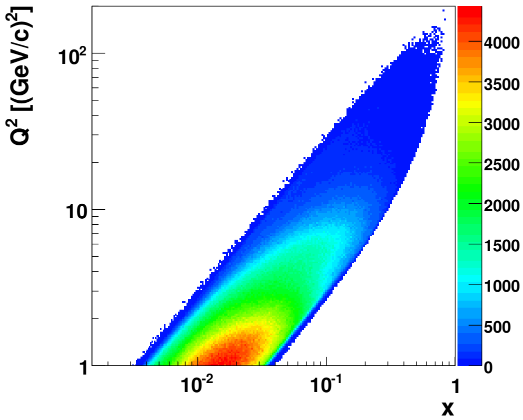

Figure 5.21: Q^2 vs x_{bj} distribution of final h^+h^--pair sample.

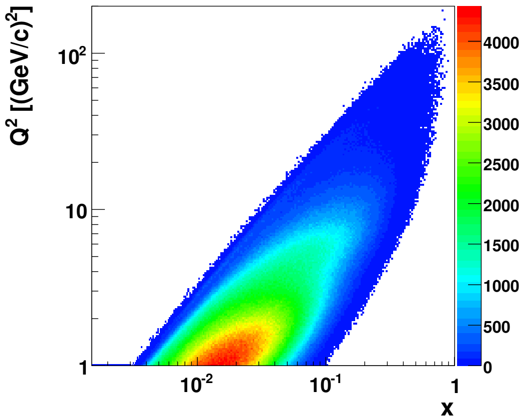

Figure 5.22: Q^2 vs x_{bj} distribution of h^+h^--pair sample, with released cut on y and W.

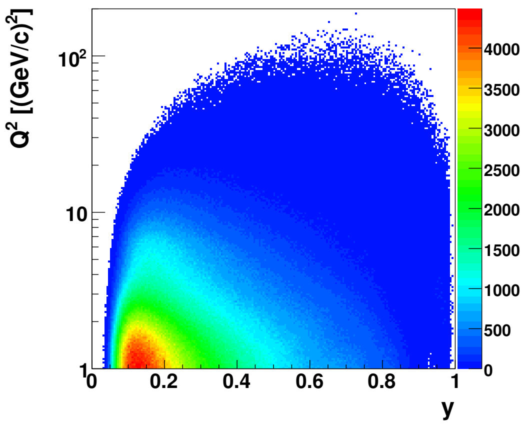

Figure 5.23: Q^2 vs y distribution of h^+h^--pair sample, with released cut on y and W.

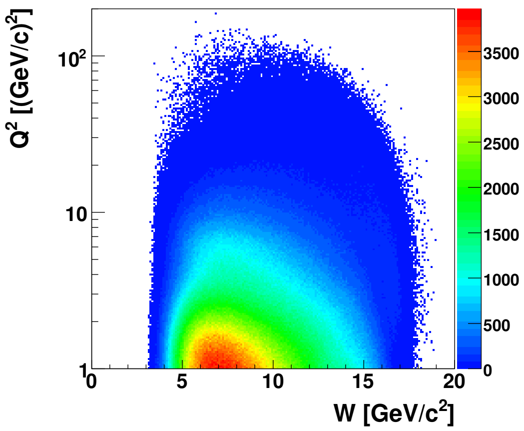

Figure 5.24: Q^2 vs W distribution of h^+h^--pair sample, with released cut on y and W.

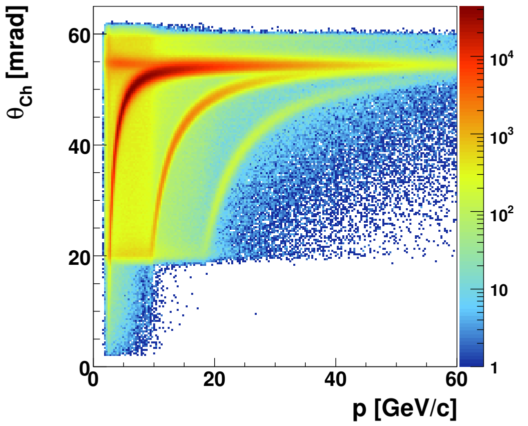

Figure 5.25: Cerenkov-angle θ_{Ch} versus particle momentum p of final h^+h^--pair sample. The color scale is logarithmic.

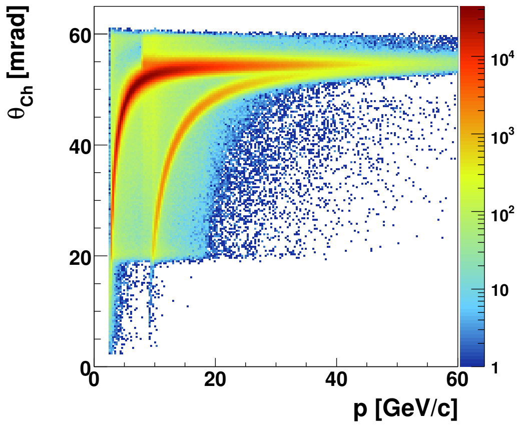

Figure 5.26: Cerenkov-angle θ_{Ch} versus particle momentum p for identified pions and kaons only. The color scale is logarithmic.

5.3.8 Identified $\pi^+\pi^-$- and K^+K^--Pairs

The particles produced in COMPASS are mostly pions. But due to analyzing all oppositely charged pair combinations the contribution of pairs contaminated with kaons, protons and electrons gets sizable (i.e.: always three particles per event: π^+, π^- and $X^\pm$, where $X^\pm$ denotes any charged particle except pions. Hence 66 % of all particles are pions, however, the number of pure $\pi^+\pi^-$-pairs is only 50 % and the remaining 50 % are pairs contaminated with $X^\pm$). In order to study the effects on the asymmetries, pions and kaons are identified using the RICH detector. As already seen in Sec. 3.3.3 only pions with momenta $p > 2.5\,\text{GeV}/c$ and only kaons with $p > 9\,\text{GeV}/c$ can be identified by this device. The Cerenkov angle θ_{Ch} plotted against the momentum p for each charged particle is shown in Fig. 5.25. One can clearly see the three bands starting at $2.5\,\text{GeV}/c$, $9\,\text{GeV}/c$ and $17\,\text{GeV}/c$ corresponding to pions, kaons and protons, respectively. Moreover one sees in the top left corner the horizontal band originating from electrons. Above $8\,\text{GeV}/c$ electrons and pions cannot be distinguished anymore. In Fig. 5.26 the Cerenkov angle against the momentum of the particle is shown for identified pions and kaons only. For the identification the likelihoods provided by the RICHONE class are used. Likelihoods for five mass hypothesis are computed, corresponding to electron, pion, kaon, proton and background. For the identification the largest likelihood $\mathcal{L}$ and the second largest $\mathcal{L}_{2nd}$ are considered [80]. For pions the following cuts are applied:

- $p_\pi > p_{\pi,thr}$ and $\frac{\mathcal{L}_\pi}{\mathcal{L}_{2nd}} > 1.02$.

For kaons the following cuts are applied:

- $p_K > p_{K,thr}$ and $\frac{\mathcal{L}_K}{\mathcal{L}_{2nd}} > 1.06$.

in which p_{thr} is the momentum threshold defined in Eq. (3.2), which is computed on a run by run basis, using the refractive indices which are determined for each run individually.

Table 5.1: Number of h^+h^--pairs, identified $\pi^+\pi^-$-pairs and identified K^+K^--pairs for the 12 weeks. In the last column the configuration of the target polarization is specified.

Week	DIS events	h^+h^--pairs	$\pi^+\pi^-$-pairs	K^+K^--pairs	target config.
25	649841	846367	530089	16868	$-++-$
26	718153	934928	585881	17924	$+--+$
27	489099	640708	384440	11395	$-++-$
28	861684	1127407	679723	19646	$+--+$
30	892013	1168310	704026	19475	$+--+$
31	1238737	1623416	978752	27071	$-++-$
39	918541	1188416	716335	21220	$+--+$
40	625763	809745	487347	14313	$-++-$
41	849258	1102117	667961	19993	$-++-$
42a	615337	799048	486615	14143	$+--+$
42b	358776	465584	282494	8142	$+--+$
43	389522	504975	307760	8785	$-++-$
Sum	8606724	11211021	6811423	198975	

The obtained efficiencies for pion and kaon identification are approximately 94 % and 99 %, respectively [80].

The invariant mass distribution for $\pi^+\pi^-$-pairs is shown in Fig. 5.27. Compared to the mass distribution of unidentified h^+h^--pairs (Fig. 5.12) the peak corresponding to ρ^0-mesons is much more dominant. For K^+K^--pairs the invariant mass spectrum is shown in Fig. 5.28. The dominant peak at around $1.02\,\mathrm{GeV}/c^2$ corresponds to the ϕ-meson.

The $\sin\theta$ and $\cos\theta$ distributions for identified $\pi^+\pi^-$- and K^+K^--pairs are shown in Fig. 5.29-5.32. As for the unidentified pairs the $\sin\theta$ distributions are strongly peaked at one, meaning that the dependence on $\sin\theta$ can be neglected as well. The $\cos\theta$ distributions are both symmetric around zero leading to the conclusion that this dependence can be neglected too, as in case of the unidentified pairs. The mixed π^+K^-- and $K^+\pi^-$-pairs have not been looked at because the corresponding $\cos\theta$ distributions are asymmetric. This is because of the different momentum cuts for pion and kaon identification with the RICH. Therefore the assumption that the second term in the polarized DiFF $H_1^{\sphericalangle}$ can be neglected is no longer valid (see Sec. 5.1).

5.3.9 Final Statistics

In Tab. 5.1 the number of DIS events and the number of oppositely charged hadron pairs are shown for the 12 weeks of data taking. The horizontal lines indicate, which pairs of weeks are coupled to compute the asymmetries used for the evaluation of the systematical error (see Sec. 5.7). In total $11.2 \cdot 10^6$ h^+h^--pairs contribute to the analysis. On average 1.3 h^+h^--pairs per event could be reconstructed. In addition the number of $\pi^+\pi^-$- and K^+K^--pairs are given. On average the unidentified h^+h^--sample is composed to 60 % of identified $\pi^+\pi^-$- and to 1.8 % of identified K^+K^--pairs. In the last column of the table the configuration of the target polarization is specified.

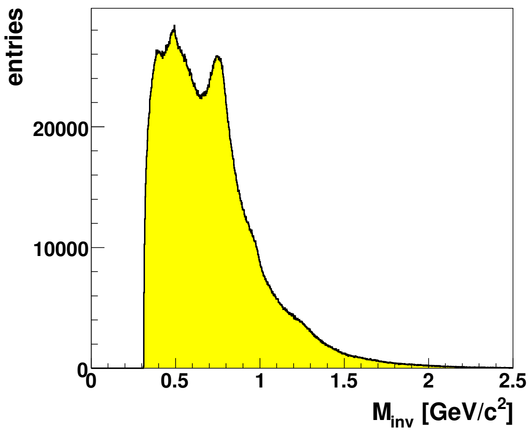

Figure 5.27: Invariant mass distribution of final $\pi^+\pi^-$-pairs.

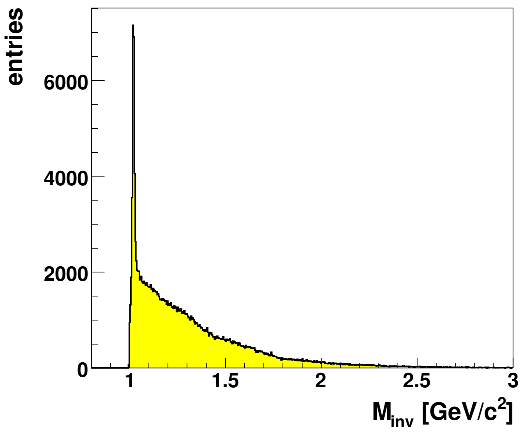

Figure 5.28: Invariant mass distribution of final K^+K^--pairs.

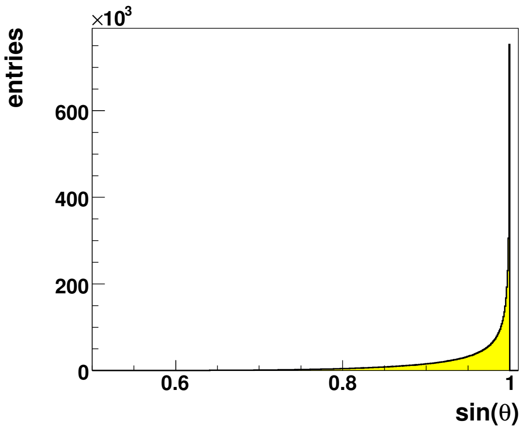

Figure 5.29: $\sin\theta$ distribution of final $\pi^+\pi^-$-pairs, with $\langle\sin\theta\rangle = 0.95$.

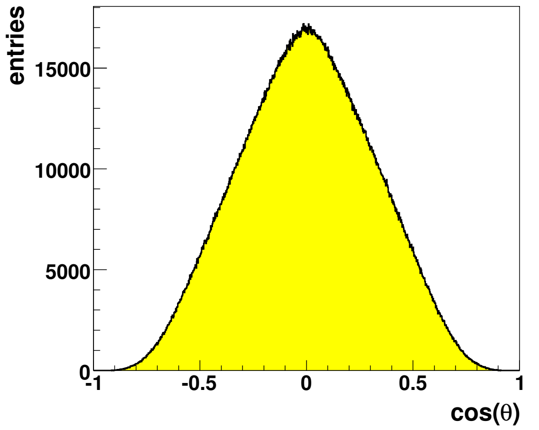

Figure 5.30: $\cos\theta$ distribution of final $\pi^+\pi^-$-pairs.

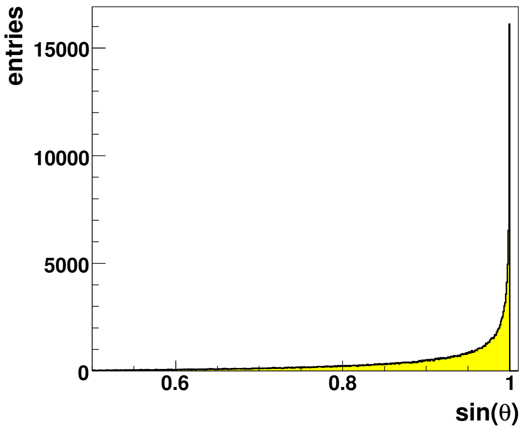

Figure 5.31: $\sin\theta$ distribution of final K^+K^--pairs, with $\langle\sin\theta\rangle = 0.90$.

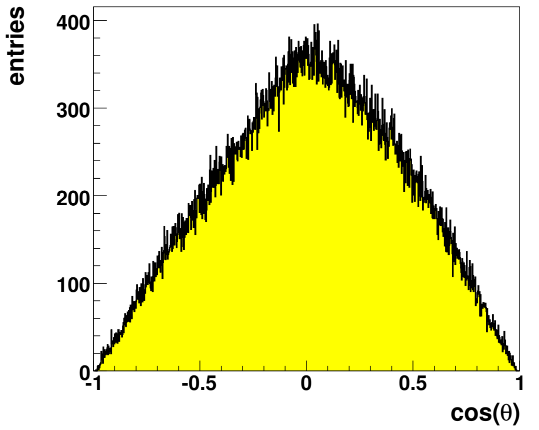

Figure 5.32: $\cos\theta$ distribution of final K^+K^--pairs.

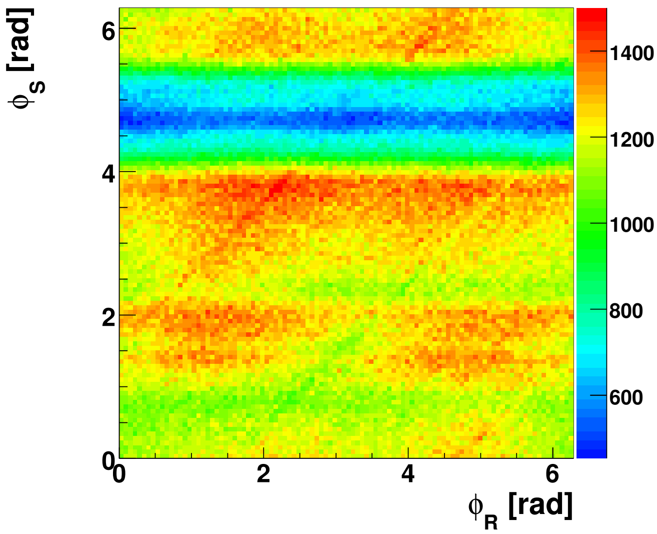

Figure 5.33: Correlation between azimuthal spin angle ϕ_S and azimuthal angle ϕ_R of the two hadron plain of the final h^+h^--pair sample.

5.4 Single Spin Asymmetry Extraction

In Fig. 5.33 the azimuthal spin angle ϕ_S is plotted against the azimuthal angle ϕ_R of the two hadron plain, as defined in Fig. 2.15. The size of the 'raw' asymmetry in $\sin(\phi_R + \phi_S - \pi)$ is due to the scaling factor of $1/\langle f \cdot P_T \cdot D_{nn}\rangle \approx 10$ in the order of few per mille. Hence it is much smaller in size than the variations shown in Fig. 5.33, which gives reason for sophisticated methods to extract the asymmetry in $\sin(\phi_R + \phi_S - \pi)$. The visible variations in ϕ_S and ϕ_R are dominantly caused by the complex acceptance of the COMPASS detector. In particular the large changes in ϕ_S are given due to the positioning of the trigger hodoscopes. For technical reasons it is not possible to trigger on scattered muons in the complete region.

Several methods have been implemented to extract the asymmetries. The method which has been used to analyse the deuteron data [81, 82, 83], is called one dimensional double ratio method. The two dimensional double ratio, avoids possible biases of the extracted asymmetries due to the detector acceptance [84]. Both methods have been studied very carefully in the past and will therefore only be mentioned very briefly.

New methods like the binned maximum likelihood and the extended unbinned maximum likelihood fit have been developed, to overcome problems, which possibly arise using the double ratio methods, as will be discussed in Sec. 5.4.1. These methods were for the first time studied in [85] with Monte Carlo data. In the course of this thesis they have been implemented independently and further developed to successfully apply them on real data. For the final results the unbinned maximum likelihood is used.

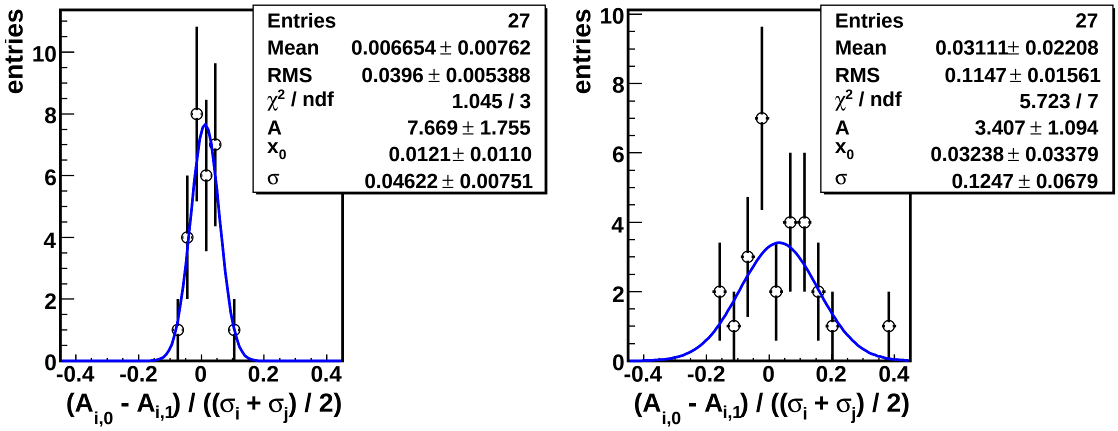

Figure 5.34: Pulls between A^{RS} results obtained fitting standard ratio and fitting inverse ratio. On the left for the one dimensional ratio method and on the right for the two dimensional ratio method.

5.4.1 Ratio Methods

The ratio methods directly fit the ratio of number of events as for example Eq. (5.4) with:

$$f(\Phi_{RS}) = c \cdot (1 + 8 \cdot A \sin \Phi_{RS}). \tag{5.9}$$

This can be done in one dimension, binning the number of events in Φ_{RS} or in two dimensions, using bins in ϕ_R and ϕ_S. An advantage of the ratio methods is their simple implementation.

In the one dimensional approach, due to the projection of ϕ_R and ϕ_S on Φ_{RS} the acceptance is convoluted with the physical modulations, which in the presence of large asymmetries leads to biased results [84]. This problem is overcome in the two dimensional approach. However, low statistics is here an issue due to the larger number of bins. Fitting the ratio is only justified as long as the statistics in each bin is large enough, that the Gaussian error propagation for the error of the ratio is valid. Therefore, the number of events per bin should be at least 10. If this is not the case in at least one sample, the ratio for that bin has to be ignored in the fit, leading to a loss of information.

A drawback of both methods is, that the result changes when the inverse ratio is fitted. Pulls between the results of A^{RS} obtained for the 27 kinematical bins in x, z and M_{inv}, fitting the standard ratio and fitting the inverse ratio are shown in Fig. 5.34. On the left for the one dimensional and on the right for the two dimensional ratio method. For the two methods deviations up to $0.1\,\sigma$ and $0.4\,\sigma$, respectively are present.

Since the deuteron data has been analysed with these two methods they have been implemented also for this analysis to compare the results with the newly developed methods, namely the binned and the unbinned maximum likelihood methods, which will be described in Sec. 5.4.2 and Sec. 5.4.4, respectively. In the following for the one dimensional ratio method the abbreviation '1D DR' and for the two dimensional '2D DR' is used.

5.4.2 Binned Maximum Likelihood

A different approach of extracting the asymmetries is to fit directly the number of counts in each target cell in bins of ϕ_R and ϕ_S [86]. In contrast to the ratio methods one can introduce Poisson statistics and can consider all non empty bins in the fit.

Using an m by m binning in ϕ_R and ϕ_S, the bin number in each data sample $cell = \{1, 2, 3, 4\}$ with target spin configuration $\{+, -\}$ is in the range $j = \{1, 2, ..m^2\}$ and the number of counts in a given bin j can be described by

$$N^{\pm}_{j,cell} = a^{\pm}_{j,cell} g^{\pm}_j(\vec{A}). \tag{5.10}$$

Here $a^{\pm}_{j,cell}$ describes the detector acceptance. It has to be understood as a normalized acceptance, including the unpolarized cross-section, the muon flux and the number of target nucleons. $g^{\pm}_j$ contains the transverse spin dependent modulations, in which $\vec{A}$ is the vector of asymmetry amplitudes and can be parametrized as:

$$g^{\pm}_j = 1 \pm\ A^{RS} \sin(\Phi_{RS}). \tag{5.11}$$

The sign of the amplitude A^{RS} depends on the polarization in the corresponding target cell and period (cf. Tab. 5.1). The dependence on target dilution f, target polarization P_{Target} and transverse spin transfer coefficient D_{nn} is omitted in the fit and is applied afterwards, by multiplying A^{RS} with the mean value $1/\langle f P_{Target} D_{nn}\rangle$. It has to be noted, that one can add any further orthogonal functions of ϕ_R and ϕ_S to $g^{\pm}_j$, like for example the seven modulations describing the single hadron cross-section. This is discussed in Sec. 5.4.5.

In order to disentangle the acceptance from the physics asymmetry one uses the reasonable assumption: The change of acceptance in each bin and each target cell can be described by a single constant C:

$$C = \frac{a^{+}_{j,1} a^{+}_{j,2} a^{+}_{j,3} a^{+}_{j,4}}{a^{-}_{j,1} a^{-}_{j,2} a^{-}_{j,3} a^{-}_{j,4}}. \tag{5.12}$$

When using the data samples of all four target cells one ends up with a system of $8m^2$ non-linear equations with $7m^2+1+n_A$ free parameters (Due to the reasonable assumption defined in Eq. (5.12), in total $7m^2 + 1$ acceptance parameters are needed and n_A is the number of fitted physics modulations). These $8m^2$ equations can be written as follows:

$$\begin{aligned} N^{+}_{j,1} &= C \frac{a^{-}_{j,1} a^{-}_{j,2} a^{-}_{j,3} a^{-}_{j,4}}{a^{+}_{j,2} a^{+}_{j,3} a^{+}_{j,4}} g^{+}_j(\vec{A}), \\ N^{-}_{j,1} &= a^{-}_{j,1} g^{-}_j(\vec{A}), \\ N^{\pm}_{j,cell} &= a^{\pm}_{j,cell} g^{\pm}_j(\vec{A}), \quad cell = \{2, 3, 4\}. \end{aligned} \tag{5.13}$$

It has to be noted, that this method works also when using only part of the target, for example only the data samples of one or two target cells.

Eq. (5.13) is a nonlinear system of equations. A maximum likelihood fit with Poisson statistics is used to solve it. Therefore, each equation is transformed into a probability $P^{\pm}_{j,cell}(\vec{a})$. In which $\vec{a}$ denotes the $7m^2 + 1 + n_A$ free parameters. For convenience in the following the $8m^2$ equations are numbered consecutively with $k = \{1, ..., 8m^2\}$:

$$P_k(\vec{a}) = \frac{e^{-f_k(\vec{a})} f_k(\vec{a})^{N_k}}{N_k!}, \tag{5.14}$$

where N_k is the measured number of counts (in bin j of data sample $cell = \{1, 2, 3, 4\}$ with configuration $\{+, -\}$) and $f_k(\vec{a})$ is the expected number of events, as defined in Eq. (5.13).

Maximizing the product $\mathcal{L}$ of the probabilities defined in Eq. (5.14) corresponds to solve the non-linear system of equations (Eq. (5.13)):

$$\max_{\vec{a}}(\mathcal{L}) = \max_{\vec{a}} \left(\prod_k P_k(\vec{a}) \right). \tag{5.15}$$

For technical reasons one minimizes the negative logarithm:

$$\min_{\vec{a}}(-\ln(\mathcal{L}) = \min_{\vec{a}} \left(-\sum_k \ln(P_k(\vec{a})) \right). \tag{5.16}$$

Constant terms do not contribute in the minimization and Eq. (5.16) can be transformed into:

$$\min_{\vec{a}} \left(-2 \sum_k (f_k(\vec{a}) - N_k) + N_k \ln(N_k / f_k(\vec{a})) \right), \tag{5.17}$$

whereas the factor of two has to be added for a correct estimation of the statistical error in the sense of a least square fit. This minimization problem can be solved using the Levenberg-Marquardt (LM) algorithm [87, 88] implemented in the GNU Scientific Library (GSL) [89]. The LM-algorithm solves the problem of minimizing $\|\vec{F}(\vec{a})\|^2$, with respect to the vector of parameters $\vec{a}$ of the target function $\vec{F}(\vec{a})$. It combines the advantages of the Gauss-Newton and the gradient descent method.

Defining the target functions

$$F_k(\vec{a}) = \sqrt{2}\sqrt{(f_k(\vec{a}) - N_k) + N_k \ln\left(N_k / f_k(\vec{a})\right)}, \tag{5.18}$$

solves finally Eq. (5.13), when minimizing $\|\vec{F}(\vec{a})\|^2$. In the following the abbreviation MF RA is used for the binned maximum likelihood method

5.4.3 Accounting for Finite Bin Size

When using bins in ϕ_R and ϕ_S (or in Φ_{RS}) one has to account for effects due to the finite bin size [90]. This is because the fit is performed at the center of the bin or at the center of gravity and the integral over the bin is not considered. Instead of taking this into account in the fit routines, the difference can be analytically calculated in comparing

$$\mathrm{f}(\Phi_i + \Delta\Phi/2) \leftrightarrow 1/\Delta\Phi \int_{\Phi_i}^{\Phi_i+\Delta\Phi} \mathrm{d}\Phi\ \mathrm{f}(\Phi), \tag{5.19}$$

and the result can be corrected for this afterwards.

In the one dimensional case for the general fit function

$$\mathrm{f}(\Phi) = a_{k,fit}\sin(k\Phi) + b_{k,fit}\cos(k\Phi), \qquad k \in \{1, 2, 3, ..\}, \tag{5.20}$$

the correction factors for n bins with bin width $\Delta\Phi = 2\pi/n$ are:

$$\frac{a_{k,fit}}{a_k} = \frac{b_{k,fit}}{b_k} = \frac{2}{k\Delta\Phi}\sin\left(\frac{k\Delta\Phi}{2}\right), \tag{5.21}$$

where a_k and b_k are the 'true' amplitudes. For $n = 16$ bins in $\Phi = \Phi_{RS}$ and $k = 1$ the factor is 0.9936. Hence the effect due to finite bin size is very small.

In the two dimensional case for the general fit function

$$\mathrm{f}(\phi_R, \phi_S) = a_{k,fit}\sin(k\phi_R \pm \phi_S) + b_{k,fit}\cos(k\phi_R \pm \phi_S), \qquad k \in \{1, 2, 3, ..\}, \tag{5.22}$$

the correction factors for $n\,\mathrm{x}\,m$ bins with bin widths $\Delta\phi_R = 2\pi/n$ and $\Delta\phi_S = 2\pi/m$ are:

$$\frac{a_{k,fit}}{a_k} = \frac{b_{k,fit}}{b_k} = \frac{4}{k\Delta\phi_R\Delta\phi_S}\sin\frac{k\Delta\phi_R}{2}\sin\frac{\Delta\phi_S}{2}. \tag{5.23}$$

For $n = m = 8$ the factor for $\sin(\phi_R + \phi_S - \pi)$ is 0.9496.

5.4.4 Unbinned Maximum Likelihood

A further approach of extracting the asymmetries is to perform an unbinned maximum likelihood fit in ϕ_R and ϕ_S. For each measured event with (ϕ_R, ϕ_S) the probability is described by a probability density function $P(\phi_R, \phi_S)$, which is parametrized as product of an acceptance function $a^{\pm}_{cell}$ and a physics modulation function $g^{\pm}$:

$$\mathrm{P}^{\pm}_{cell}(\phi_R, \phi_S) = a^{\pm}_{cell}(\phi_R, \phi_S) \cdot g^{\pm}(\vec{A}, \phi_R, \phi_S), \tag{5.24}$$

where $g^{\pm}$ is parametrized as shown in Eq. (5.11). For each target cell and both polarization states $^{\pm}$ the acceptance functions $a^{\pm}_{cell}$ are different. The separation between $a^{\pm}_{cell}$ and $g^{\pm}$ is achieved by assuming, that the change of acceptance for each target cell i can be described by one single constant each:

$$C_i = \frac{a_i^{+}(\phi_R, \phi_S)}{a_i^{-}(\phi_R, \phi_S)}, \qquad i = \{1, 2, 3, 4\}. \tag{5.25}$$

This seems less constraining than the assumption in Eq. (5.12) used for the binned methods. However, tests showed, that the result for both assumptions is the same, but the minimization process using Eq. (5.12) converges less stable. Therefore Eq. (5.25) is used.

An extended maximum likelihood fit is performed. In such a fit the probability density function is not normalized to one, but to the theoretically expected number of events μ.

$$\int_0^{2\pi}\int_0^{2\pi} \mathrm{d}\phi_R \mathrm{d}\phi_S P^{\pm}_{cell}(\phi_R, \phi_S) = \mu^{\pm}_{cell}. \tag{5.26}$$

The likelihood function $\mathcal{L}(\vec{a})$ to be maximized with respect to the vector of parameters $\vec{a}$ is:

$$\begin{aligned}\mathcal{L}(\vec{a}) = \prod_{i=1}^{4} \Bigg[& \left(e^{\mu_i^+} \prod_{m=1}^{N_i^+} a_i^+(\phi_{R_m}, \phi_{S_m}) g^+(\vec{A}, \phi_{R_m}, \phi_{S_m}) \right) \\ & \cdot \left(e^{\mu_i^-} \prod_{n=1}^{N_i^-} C_i a_i^+(\phi_{R_n}, \phi_{S_n}) g^-(\vec{A}, \phi_{R_n}, \phi_{S_n}) \right) \Bigg]. \end{aligned} \tag{5.27}$$

It has to be noted, that the outer product over the data samples of the different target cells can be chosen depending on the problem/quantity one wants to extract, for example using only the data samples of two target cells, as it is done in Sec. 5.7.5 to compute false asymmetries.

Extensive checks on Monte Carlo data showed, that the functional form in ϕ_R and ϕ_S of the acceptance has only a negligible effect on the extracted asymmetries. Therefore constant values a_i^+ are used, which account for the different flux in the two periods. With this simplification the expected number of events in the data sample of target cell i is $\mu_i^{\pm} = 4\pi^2 a_i^{\pm}$ and the vector of parameters is $\vec{a} = \{a_1^+, .., a_4^+, C_1, .., C_4, \vec{A}\}$.

The events need to be weighted with power of $\bar{N}/N_i^{\pm}$, where $\bar{N} = \frac{1}{8}\sum_{i=1}^{4}\{N_i^+ + N_i^-\}$ is the average number of events. Otherwise the results are biased in case of unbalanced statistics between the data samples N_i^+ and N_i^- [91]. Therefore the final likelihood function is:

$$\mathcal{L}(\vec{a}) = \prod_{i=1}^{4} \left[\left(e^{\mu_i^+} \prod_{m=1}^{N_i^+} a_i^+ g^+(\vec{A}, \phi_{R_m}, \phi_{S_m}) \right)^{\frac{\bar{N}}{N_i^+}} \left(e^{\mu_i^-} \prod_{n=1}^{N_i^-} C_i a_i^+ g^-(\vec{A}, \phi_{R_n}, \phi_{S_n}) \right)^{\frac{\bar{N}}{N_i^-}} \right]. \tag{5.28}$$

Taking the negative logarithm and neglecting constant terms, because they do not contribute in the minimization, the following expression has to be minimized:

$$\begin{aligned} -\ln(\mathcal{L}(\vec{a})) = -\sum_{i=1}^{4} \Bigg[& \frac{\bar{N}}{N_i^+} \left(\mu_i^+ + N_i^+ \ln(a_i^+) + \sum_{m=1}^{N_i^+} \ln(g^+(\vec{A}, \phi_{R_m}, \phi_{S_m})) \right) \\ & - \frac{\bar{N}}{N_i^-} \left(\mu_i^- + N_i^- \ln(C_i a_i^+) + \sum_{n=1}^{N_i^-} \ln(g^-(\vec{A}, \phi_{R_n}, \phi_{S_n})) \right) \Bigg]. \end{aligned} \tag{5.29}$$

The minimization of this function is done with the Broyden-Fletcher-Goldfarb-Shanno (BFGS) algorithm (version 2), implemented in the GNU Scientific Library [89]. It is a quasi-Newton method, which builds up an approximation to the second derivatives of the likelihood function using the difference between successive gradient vectors. By combining the first and the second derivatives the algorithm is able to take Newton-type steps towards the minimum, assuming quadratic behavior in that region.

A binned maximum likelihood fit, with the same acceptance description as used for the unbinned maximum likelihood, is performed to obtain adequate good start values. It was checked, that the result does not depend on the choice of the starting values.

In the following the abbreviation UB SA is used for the unbinned maximum likelihood method.

A summary of the abbreviations used for the four fitting methods is given in Tab. 5.2.

Table 5.2: Abbreviations used for the four fitting methods.

1D DR	One dimensional ratio method
2D DR	Two dimensional ratio method
MF RA	Binned maximum likelihood fit
UB SA	Extended unbinned maximum likelihood fit

5.4.5 Dependence of Results on Number of Fitted Modulations

As already mentioned in Sec. 5.4.2 one can add to the fit function of the binned and unbinned maximum likelihood methods (also to the two dimensional ratio method) not only the physical modulation in $A^{RS}\sin(\phi_R + \phi_S - \pi)$, but any further orthogonal modulations of ϕ_R and ϕ_S. From the theoretical point of view the results must be the same. However, due to the rather complex acceptance of the COMPASS detector it might be possible that there are correlations leading to a change of the results. Therefore the fits have been performed twice, once only fitting $\sin(\phi_R + \phi_S - \pi)$ and once fitting all eight spin dependent modulations known from the single hadron cross-section and for the unbinned method additionally $\cos\phi_R$ and $\cos 2\phi_R$ related to the Cahn and the Boer-Mulders effect.

In Fig. 5.35 the pulls between both extractions for the 27 kinematical bins in x, z and M_{inv} for the binned (left) and the unbinned (right) maximum likelihood fit are shown. One can see, that the results are statistically scattering around zero with a sigma of 8.5 %. Therefore no systematics are obtained, which means the fitting methods are stable. The final results have been obtained by fitting only the $\sin(\phi_R + \phi_S - \pi)$ modulation.

5.5 Tests on Monte Carlo Data

Monte Carlo data with the 2007 COMPASS setup is generated to verify the correctness of the extraction methods described in Sec. 5.4 and to study effects related to changes in acceptance.

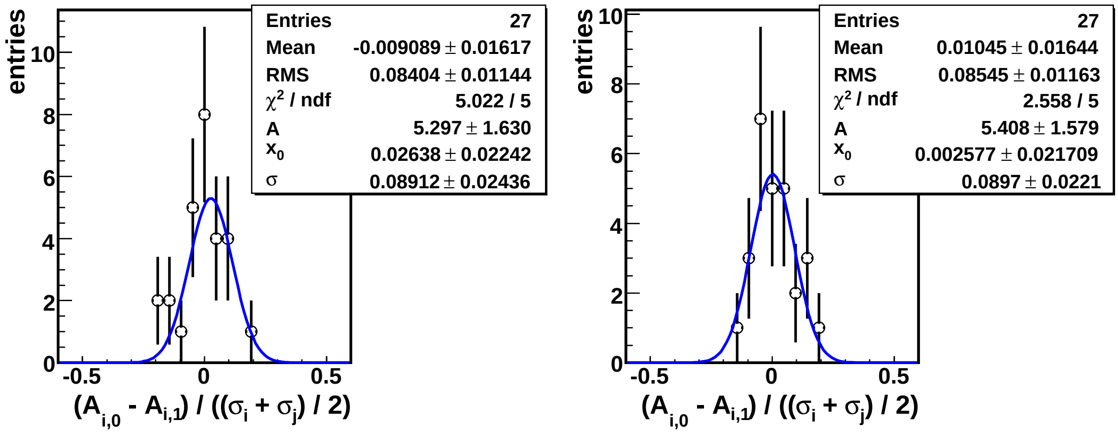

Figure 5.35: Pulls between results obtained fitting only $\sin(\phi_R+\phi_S)$ and results obtained fitting all further modulations known from the single hadron cross-section. Left: binned maximum likelihood. Right: unbinned maximum likelihood.

Pythia [92] as event generator is used with MRST 2004 [93] as parton distribution functions (LHAPDF Version 5.7.0). The detector simulation is done with COMGEANT version 7.3. using the 2007 setup for transversely polarized target. For the event reconstruction the CORAL version 08-7-30-slc4 is used. Since this version was used for the majority of the data of the second production (see Tab. 4.1).

In total 8000 'runs' with 10000 events each were generated. A cut $y > 0.08$ and $Q^2 > 1.0\,\mathrm{GeV}/c^2$ has been applied on generator level, before propagating the tracks through the detector. The final Monte Carlo sample contains about $9.7 \cdot 10^6$ SIDIS events with $12.1 \cdot 10^6$ oppositely charged hadron pairs. Hence the statistics is compatible to the one of the 2007 run.

The distributions of important kinematical variables like M_{inv}, z, Q^2, x, W^2 and y and for the h^+h^--pair sample for Monte Carlo data are shown in the Figures 5.36 - 5.41. The correlation between Q^2 and x is shown in Fig. 5.42. The agreement with the corresponding distributions for real data, shown in Figures 5.12 - 5.13, Figures 5.15 - 5.18 and Fig. 5.21 is fairly good. In Fig. 5.43 the distribution of the Z coordinate of the primary vertex is shown. It shows, as the distribution for real data in Fig. 5.4, a similar increase of the number of reactions with Z. In Fig. 5.44 the comparison of real data (week 30) and Monte Carlo data for the azimuthal angle of scattered muon $\phi_{\mu',lab}$ and for charged hadrons $\phi_{h,lab}$ is illustrated. The agreement is within $\pm 10\,\%$. Hence the sample is appropriate for acceptance related studies, like for tests of the extraction methods and investigations about changes of the detector acceptance between $+--+$ and $-++-$ data sets.

The generated sample contains no asymmetries on generator level. These are generated afterwards by rejecting a fraction of h^+h^--pairs with certain ϕ_R and ϕ_S angles. The benefit of this approach is that the very time consuming detector simulation and event reconstruction is performed only once and hence many different asymmetries can be generated and tested in a short time.

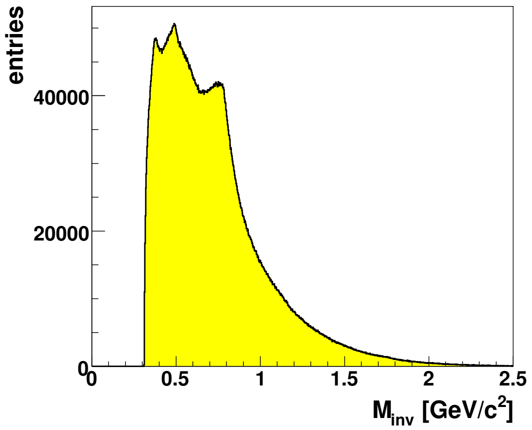

Figure 5.36: M_{inv} distribution of h^+h^--pair sample for Monte Carlo data.

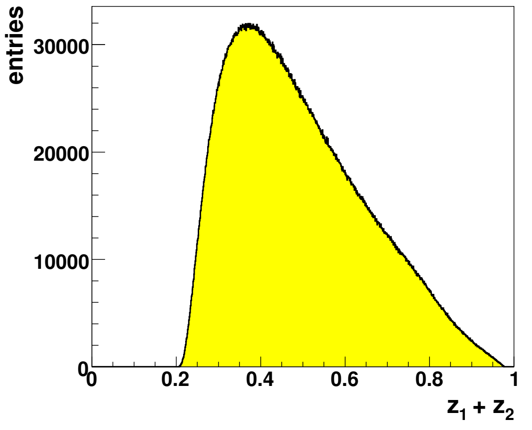

Figure 5.39: z distribution of h^+h^--pair sample for Monte Carlo data.

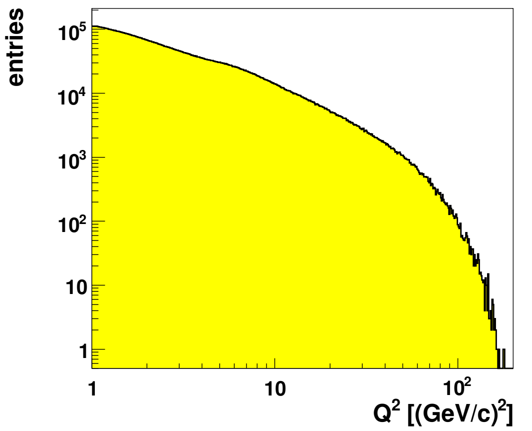

Figure 5.37: Q^2 distribution of h^+h^--pair sample for Monte Carlo data.

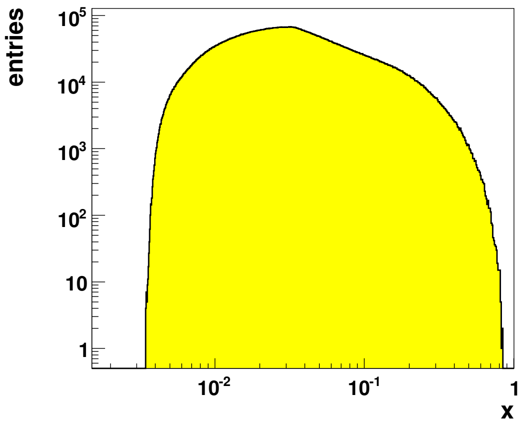

Figure 5.40: x_{bj} distribution of h^+h^--pair sample for Monte Carlo data.

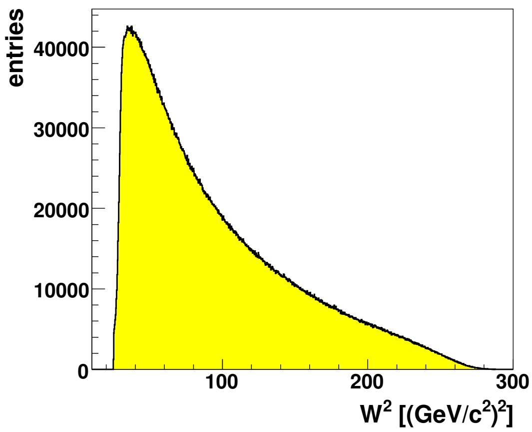

Figure 5.38: W^2 distribution of h^+h^--pair sample for Monte Carlo data.

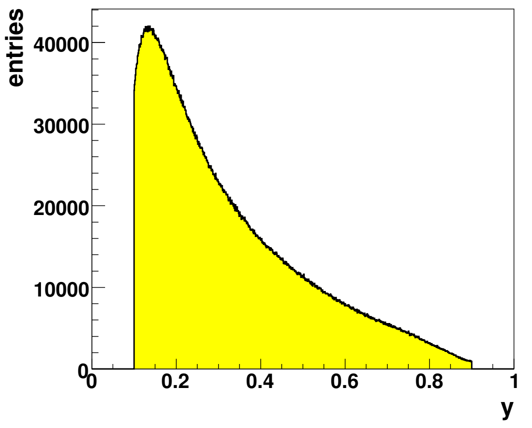

Figure 5.41: y distribution of h^+h^--pair sample for Monte Carlo data.

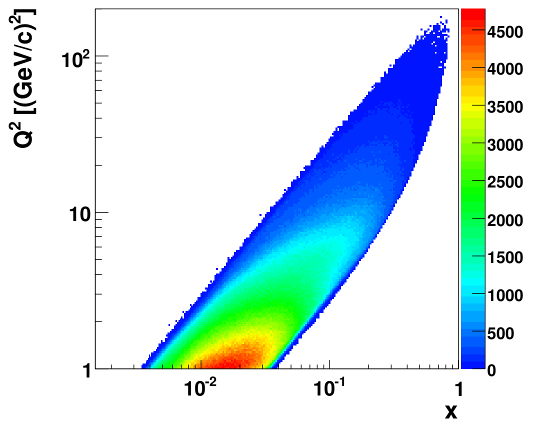

Figure 5.42: Q^2 vs x_{bj} distribution of h^+h^--pair sample for Monte Carlo data.

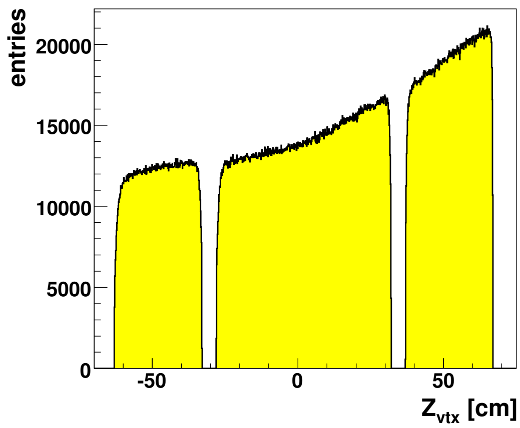

Figure 5.43: Distribution of the Z coordinate of the primary vertex of h^+h^--pair sample for Monte Carlo data.

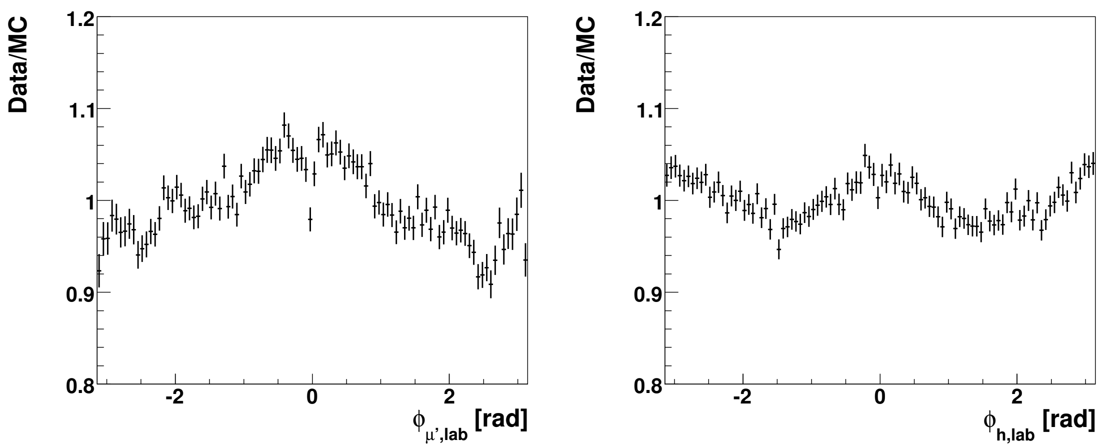

Figure 5.44: Ratio of real data (week 30) and Monte Carlo data of h^+h^--pairs. Left: azimuthal angle of scattered muon. Right: azimuthal angle of hadrons.

For the following tests the sample is divided into two parts, whereas the target polarization $+ - -+$ is assigned to the first data set and $- + +-$ to the second data set. A modulation in $\sin \Phi_{RS}$ with an amplitude of $A_{MC}^{RS} = -0.004$ is generated. In addition an asymmetry in $\sin(\phi_R - \phi_S)$ ('Sivers-like') with strength $A_{MC}^{Sivers} = 0.006$ is generated too, to study if this has an effect on the asymmetry extraction in $\sin \Phi_{RS}$. The asymmetries are simulated as 'raw' asymmetries. Thus after correcting for target dilution, target polarization and depolarization factor they become about 10 times larger. Both asymmetries are generated without any x, z and M_{inv} dependence.

5.5.1 Tests of Estimators

First of all the original sample (without generated asymmetries) is used and it is checked, if the extracted asymmetries are compatible with zero. The results for the four extraction methods are shown in Fig. 5.45 as a function of x, z and M_{inv}. All four results are compatible with zero, as the mean values, $\bar{\mathrm{A}}$, indicate. The fluctuations are, as the probabilities, p, of the χ^2 tests indicate within the statistical expectations. Fig. 5.46 shows the pulls of the binned methods with respect to the unbinned method and in addition the pulls between the 2D ratio method and the binned likelihood method. As one can see, all four methods are strongly correlated. However, comparing the sigma of the pull distribution between 1D ratio method (1D DR) and unbinned likelihood (UB SA) with the sigma of the pull between 2D ratio method (2D DR) and binned likelihood (MF RA) it is noticeable that they are in the same order, whereas the sigmas of the pulls between the two 2D binned methods (2D DR and MF RA) and the unbinned likelihood are about a factor of three larger. In addition the mean of these pulls seems to be systematically shifted.

The second test is performed on the sample with the generated asymmetries of $A_{MC}^{RS} = -0.004$ and $A_{MC}^{Sivers} = 0.006$. The results are shown in Fig. 5.47. Within statistical precision all four estimators give the correct result of $A_{MC}^{RS} = -0.004$. Looking at the pull distributions in Fig. 5.48, one sees that the correlation between the 1D ratio method and the unbinned method is worse compared to the one obtained for zero asymmetries (Fig. 5.46), whereas the pulls between the other methods stay the same. This clearly demonstrates the limited capability of the 1D ratio method to extract the asymmetries in the case when more then one 'strong' modulation is present.

The previous two tests show, that the two dimensional ratio method, the binned likelihood and the unbinned method are suitable to extract the asymmetries in COMPASS. The results of the 1D ratio method has to be taken with care as seen in the previous paragraph. In the following the unbinned maximum likelihood method is used to extract the asymmetries. For the evaluation of the systematical error in Sec. 5.7, the sample with generated asymmetries is used for comparison of the obtained results.

5.5.2 Extraction of Asymmetries Within One Week of Data Taking

The target used in 2007 consists of three target cells, whereas the two outer cells are polarized in the same direction and the middle cell is polarized oppositely (Sec. 3.2). Since the target volume of the two outer cells is identical to the volume of the middle cell, the number of interactions in the two outer cells is quite similar to the one in the

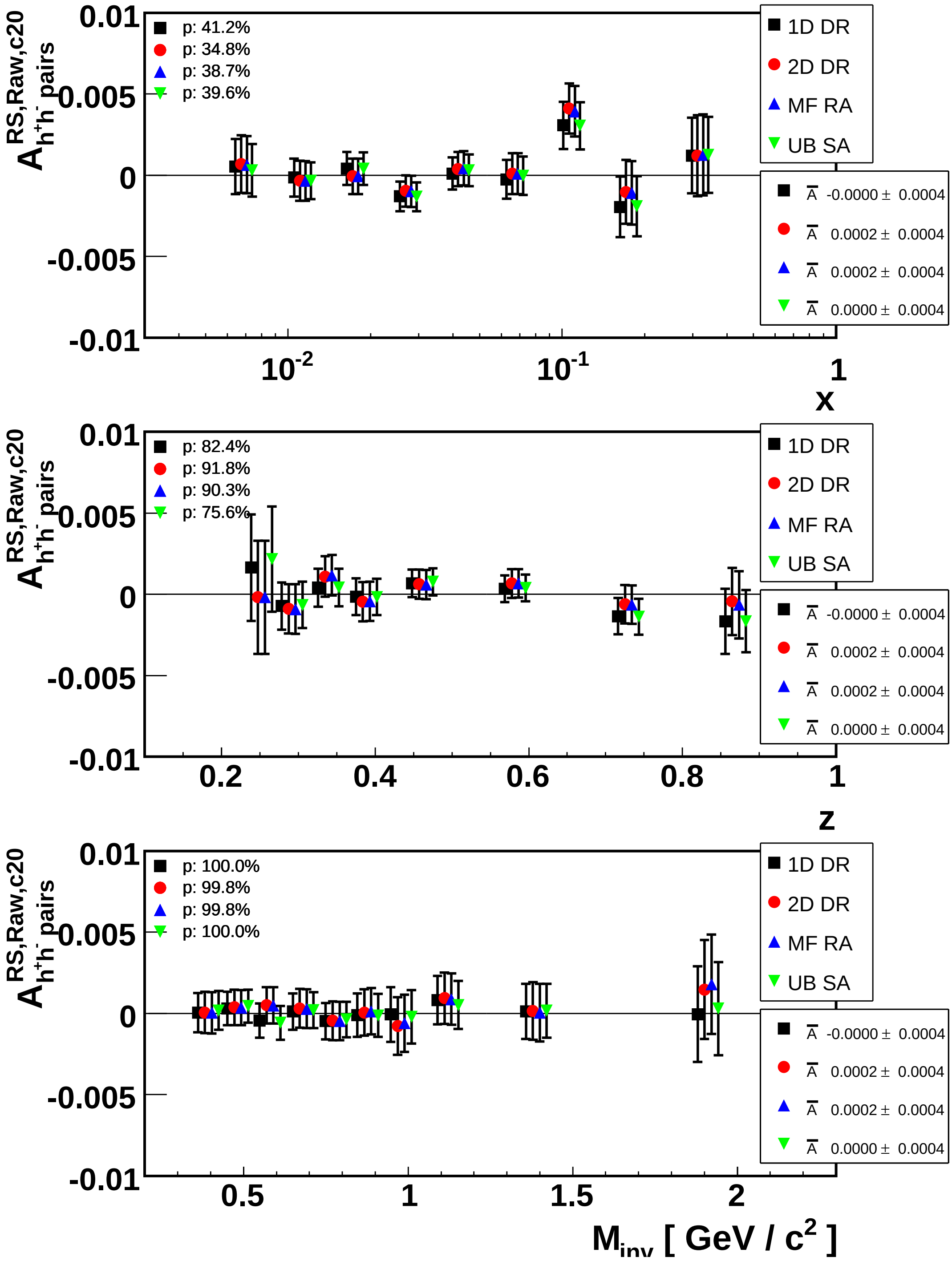

Figure 5.45: Raw RS asymmetries of the four different estimators for Monte Carlo data as a function of x, z and M_{inv}. The asymmetries are not multiplied with $1/\langle D_{nn} f P_T \rangle$. Mean asymmetries, Ā, and probabilities, p, of χ^2 test with respect to $A^{RS}_{MC} = 0$ are given.

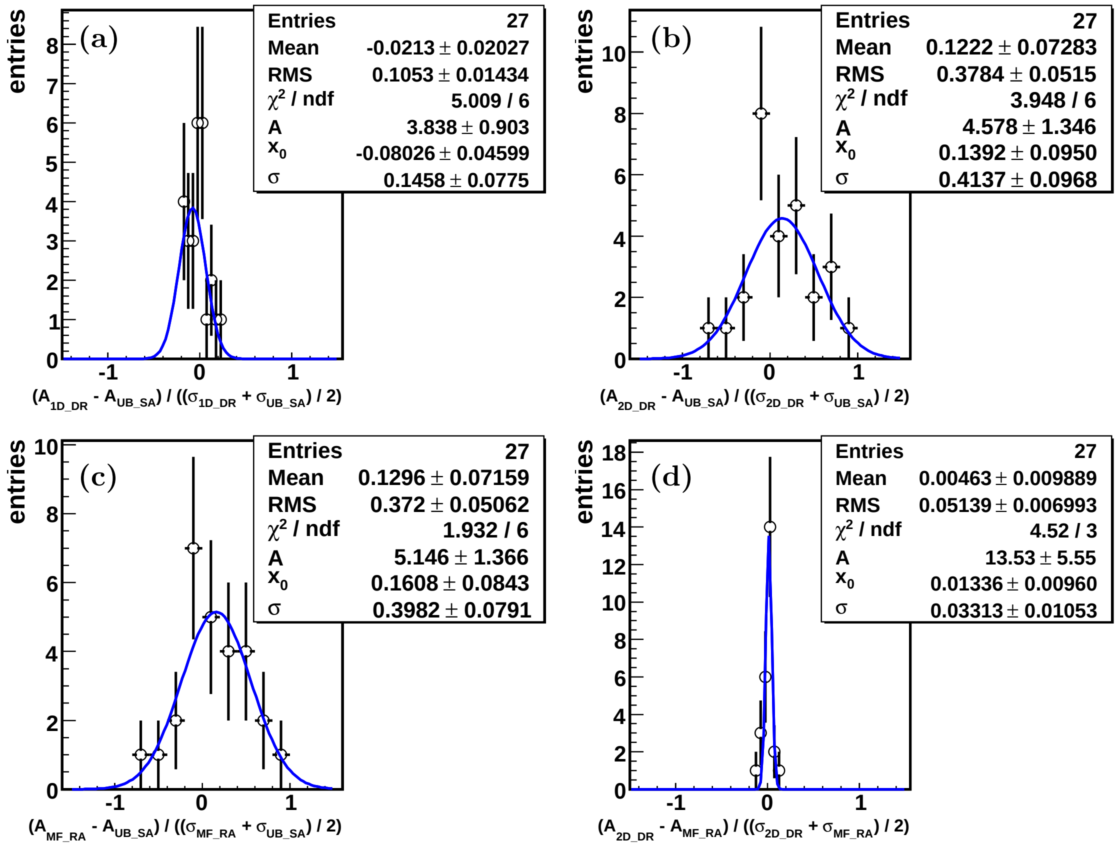

Figure 5.46: Pulls of (a) 1D ratio method, (b) 2D ratio method and (c) binned maximum likelihood with respect to the unbinned likelihood, for Monte Carlo Data without generated asymmetries. Bottom right (d) shows the pull between 2D ratio method and binned likelihood.

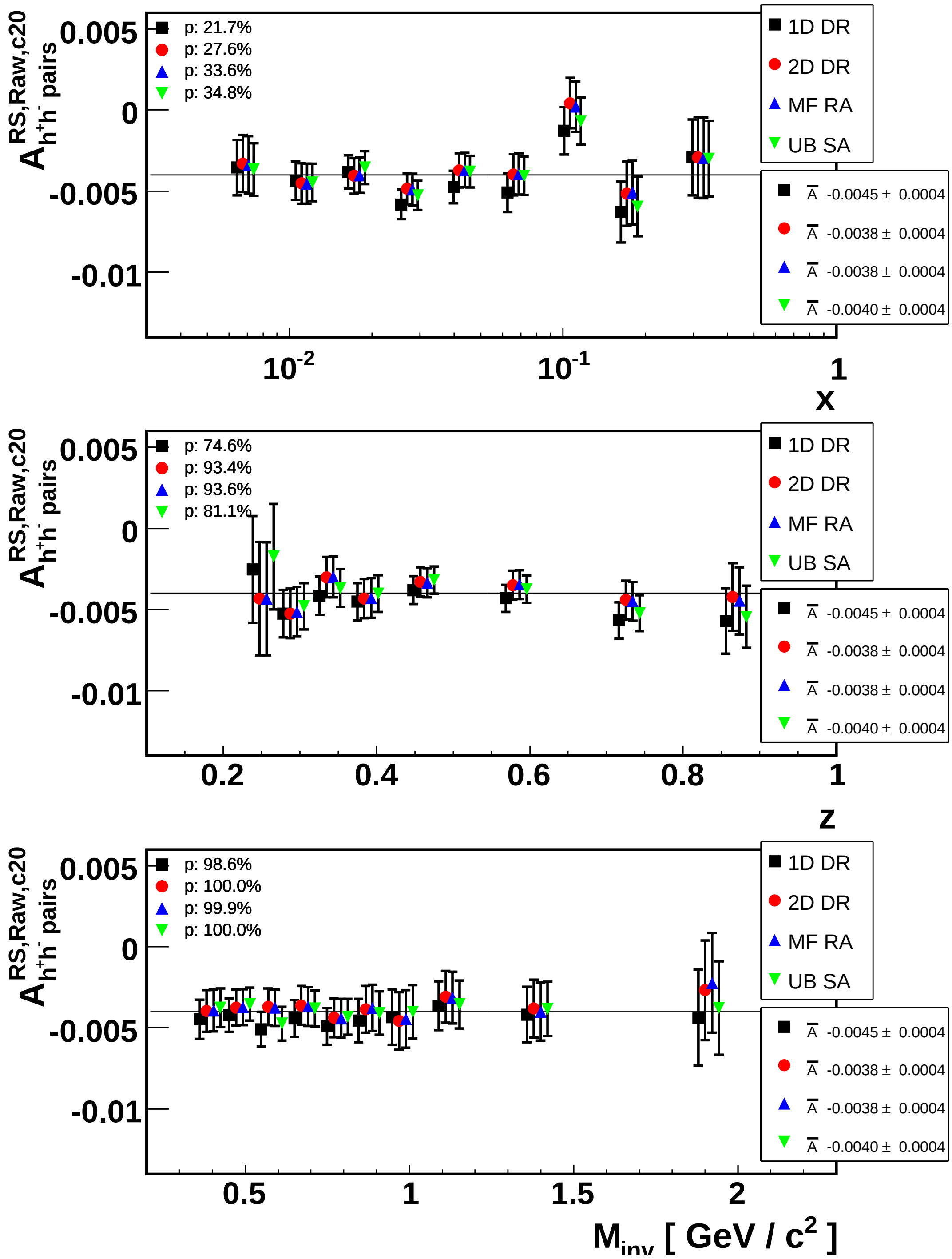

Figure 5.47: Raw RS asymmetries of the four different estimators for Monte Carlo data with generated asymmetries as a function of x, z and M_{inv}. The asymmetries are not multiplied with $1/\langle D_{nn} f P_T \rangle$. Mean asymmetries, $\bar{\mathrm{A}}$, and probabilities, p, of χ^2 test with respect to $A^{RS}_{MC} = -0.004$ (horizontal lines) are given.

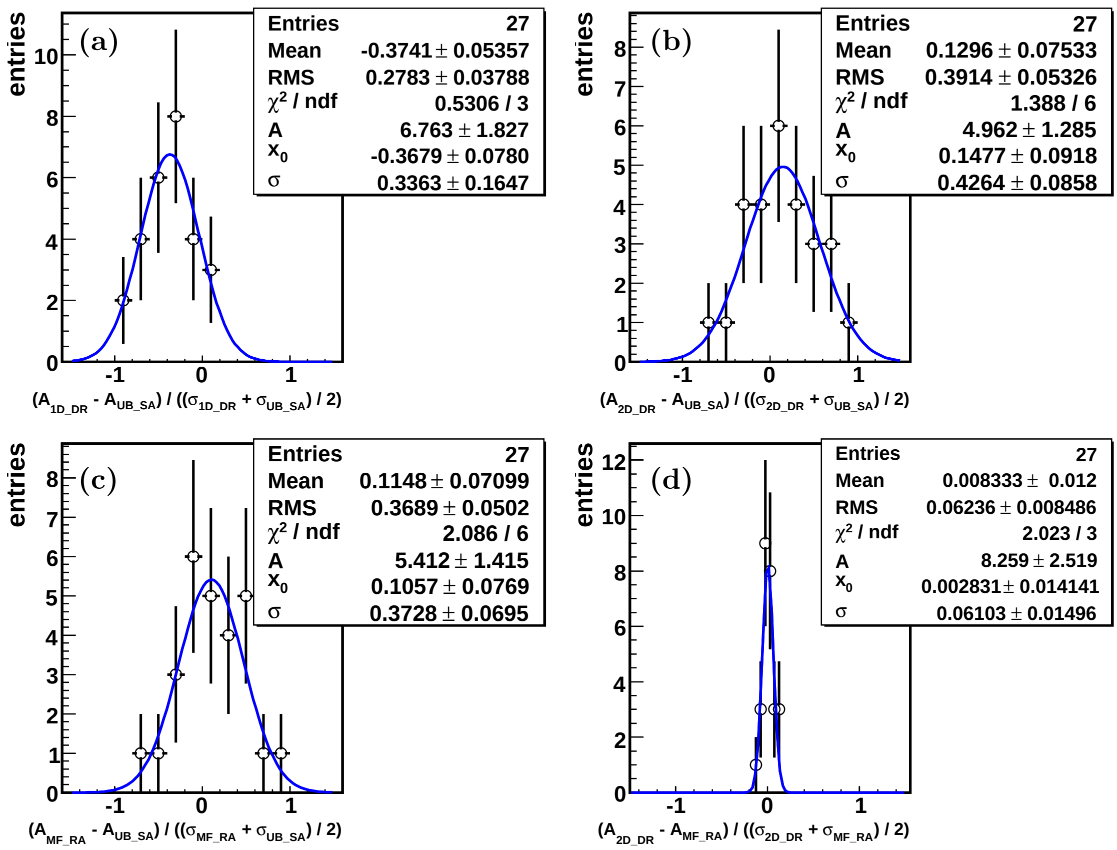

Figure 5.48: Pulls of (a) 1D ratio method, (b) 2D ratio method and (c) binned maximum likelihood with respect to the unbinned likelihood. Bottom right (d) shows the pull between 2D ratio method and binned likelihood.

middle cell. So the question is obvious if asymmetries can be extracted within one single week. The benefit of this would be that the overall stability of the detector is much more guaranteed, because efficiency fluctuations should affect both polarization states equally. The following configurations are built:

$$\mathrm{c7} = \frac{N_1 N_4}{N_2 N_3}, \tag{5.30}$$

$$\mathrm{c8} = \frac{N_2' N_3'}{N_1' N_4'}. \tag{5.31}$$

Which means A^{c7} is the asymmetry extracted with the $+--+$ sample only and A^{c8} is extracted with the $-++-$ sample only. The result for the unbinned likelihood as a function of x is shown in Fig. 5.49. One clearly sees that both results are systematically biased with respect to the generated asymmetry of $A^{RS}_{MC} = -0.004$. Whereas taking the mean of both values one obtains the correct asymmetry. It is therefore not possible to use only one week of data taking to extract the asymmetries. A second measurement with oppositely polarized target is needed to fulfill the assumption made about the change of acceptance in each target cell. The complete results, also as a function of z and M_{inv}, are shown in Fig. A.1. Even more striking is the effect for the 'Sivers-like' modulation, shown exemplarily as a function of x in Fig. 5.50. The reason for this is the '-' sign in $\sin(\phi_R - \phi_S)$. Hence the modulation is strongly correlated to the azimuthal angle of the scattered muon. Again, taking the mean of both measurements, the acceptance effects cancel and the extracted result gets compatible to the generated asymmetry of $A^{Sivers}_{MC} = 0.006$. The complete results, also as a function of z and M_{inv}, are shown in Fig. A.2. The huge discrepancy between A^{c7} and A^{c8} appears only in x.

5.5.3 Simulation of Changes in Detector Acceptance

In Sec. 4.2 several tests have been described to select data sets for which the COMPASS detector was stable. In this section instabilities in the scattered muon acceptance and in the hadron acceptance are generated and their potential impact on the extracted asymmetries is evaluated.

In order to simulate the inefficiencies cuts on the XY-distribution of hadron tracks and muon tracks extrapolated to $Z = 600\,\mathrm{cm}$, which corresponds to the entrance of the RICH detector, are performed. The definition of the coordinate system is given in Fig. 3.1. In Fig. A.3 the XY-distributions for scattered muons (left) and for hadrons (right) are shown, indicating that most of the tracks are close to zero. In Fig. A.4 the ratios for the XY-distribution of the data sets with $+--+$ and $-++-$ target polarization are illustrated. The ratios are constant over the whole plane. These plots serve in the following as a references, when performing cuts on the muon and on the hadron acceptance.

Changes in Muon Acceptance

The following scenarios are studied:

- Scenario 1: 30 % inefficiency in period $+--+$ for μ'-tracks with: $-100\,\mathrm{cm} < X < -5\,\mathrm{cm}$ and $10\,\mathrm{cm} < Y < 20\,\mathrm{cm}$.

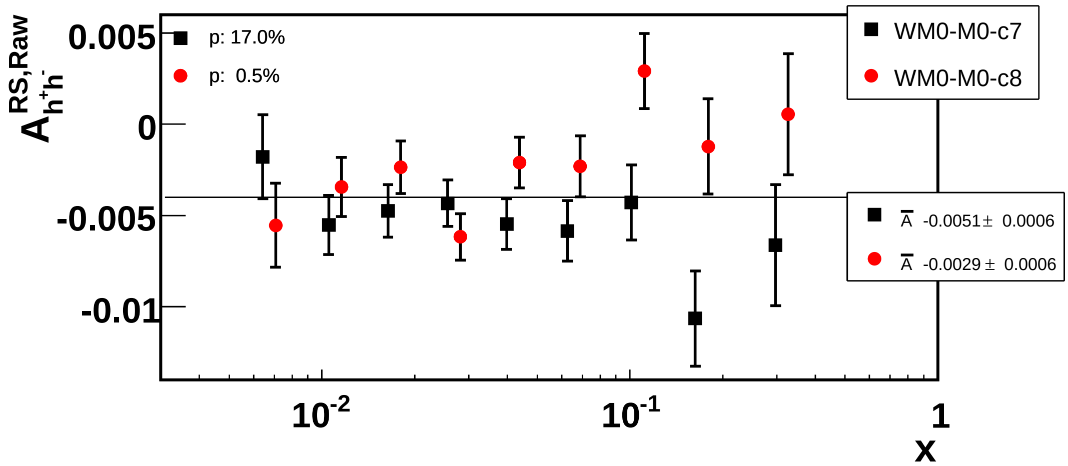

Figure 5.49: Raw RS asymmetries for +−+ (A^{c7}) and -++- (A^{c8}) sample extracted with UB SA as a function of x. Mean asymmetries, Ā, and probabilities, p, of χ^2 test with respect to $A_{MC}^{RS} = -0.004$ (horizontal line) are given.

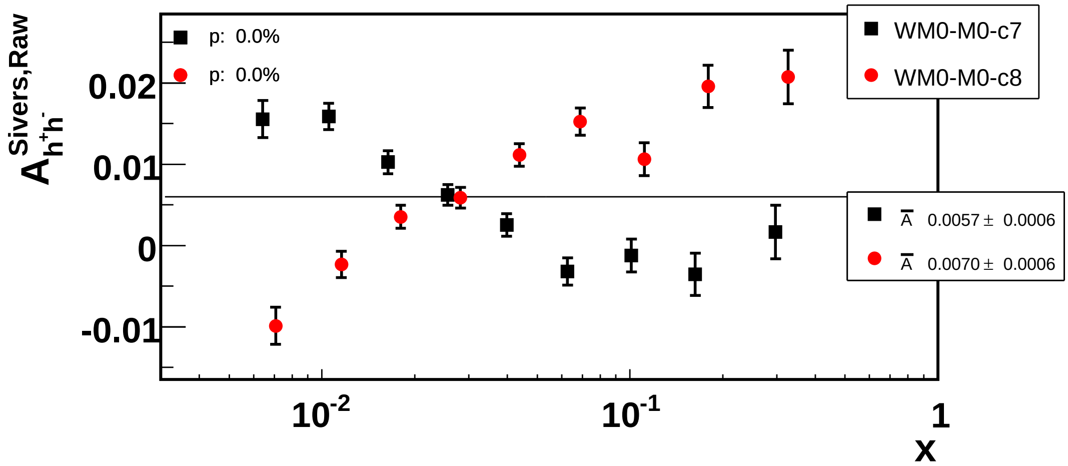

Figure 5.50: Raw 'Sivers-like' Asymmetries for +−+ (A^{c7}) and -++- (A^{c8}) sample extracted with UB SA as a function of x. Mean asymmetries, Ā, and probabilities, p, of χ^2 test with respect to $A_{MC}^{Sivers} = 0.006$ (horizontal line) are given.

- Scenario 2: 80 % inefficiency of Outer Trigger in period $+--+$.

The impact on the ratios of the XY-distribution of scattered muon and hadron tracks for scenario 1 is illustrated in Fig A.5 and for scenario 2 in Fig A.6. In both cases one sees clearly the inefficient region in the μ'-distribution. The second scenario has also a clear impact for hadron tracks in the outer region, visualizing the correlation between the scattered muon and the produced hadrons.

The extracted asymmetries as a function of x, z and M_{inv} for scenario 1 are shown in Fig. 5.51 and for scenario 2 in Fig. 5.52. For both scenarios the asymmetries are correctly extracted. This is, in particular, for scenario 2 with its strong impact on the hadron acceptance, a big surprise. In conclusion, a change in the μ' acceptance has no systematic effects on the measurement of the asymmetries.

Changes in Hadron Acceptance

The following two scenarios are investigated to simulate inefficiencies of the large area trackers, namely the STRAWs:

- Scenario 3: 50 % inefficiency in period $+--+$ for hadron tracks with: $-260\,\text{cm} < X < -80\,\text{cm}$ and -240 cm$< Y < 240\,\text{cm}$.

- Scenario 4: 50 % inefficiency in period $+--+$ for hadron tracks with: $-260\,\text{cm} < X < 260\,\text{cm}$ and $70\,\text{cm} < Y < 240\,\text{cm}$.

The impact on the ratio of the XY-distributions of hadron tracks is illustrated in Fig. A.7 on the left for scenario 3 and on the right for scenario 4. The results for scenario 3 as a function of x, z and M_{inv} are shown in Fig. 5.53 and for scenario 4 in Fig. 5.54. Compared to the reference asymmetries (Fig. 5.47) the mean value of the asymmetry for scenario 3 is slightly shifted by half a sigma, but it is still well compatible with the generated value of $A^{RS}_{MC} = -0.004$. The result for scenario 4 stays the same.

The following scenario simulates inefficiencies of the small area trackers like GEMs:

- Scenario 5: 20 % inefficiency in period $+--+$ for hadron tracks with: $-20\,\text{cm} < X < 20\,\text{cm}$ and -20 cm$< Y < 20\,\text{cm}$.

The impact on the ratio of the XY-distributions of hadron tracks is illustrated in Fig. A.8. The results as a function of x, z and M_{inv}, are shown in Fig. 5.55. As in the previous scenarios the extracted asymmetries are not affected by the change of acceptance.

Changes in Muon and Hadron Acceptance

The following scenario is simulated:

- Scenario 6: 10 % inefficiency in period $+--+$ for scattered muon and hadron tracks with: $-260\,\text{cm} < X < -20\,\text{cm}$ and -240 cm$< Y < 240\,\text{cm}$.

The ratios of the XY-distribution for scattered muon and hadron tracks are shown in Fig. A.9 and the results as a function of x, z and M_{inv} in Fig. 5.56. Again, despite of the large change in acceptance, the asymmetries are extracted without bias.

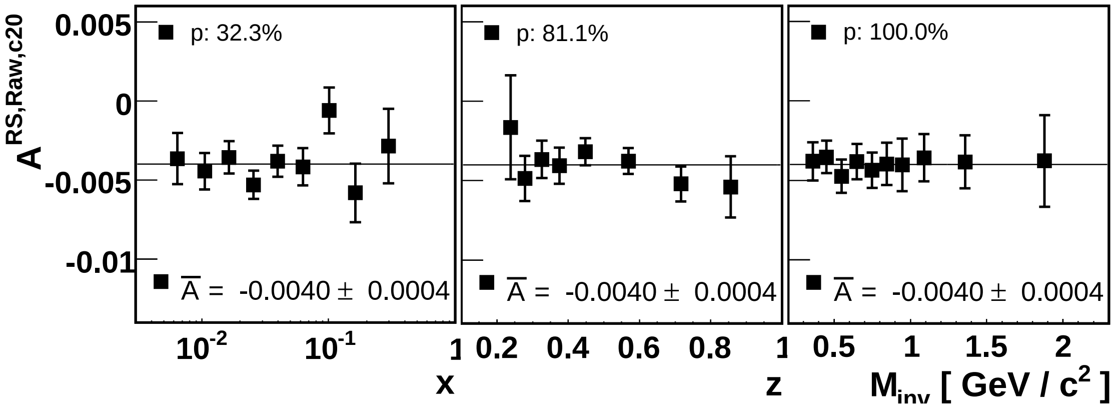

Figure 5.51: Raw RS asymmetries for scenario 1 extracted with UB SA as a function of x, z and M_{inv}. Mean asymmetries, Ā, and probabilities, p, of χ^2 test with respect to $A_{MC}^{RS} = -0.004$ (horizontal line) are given.

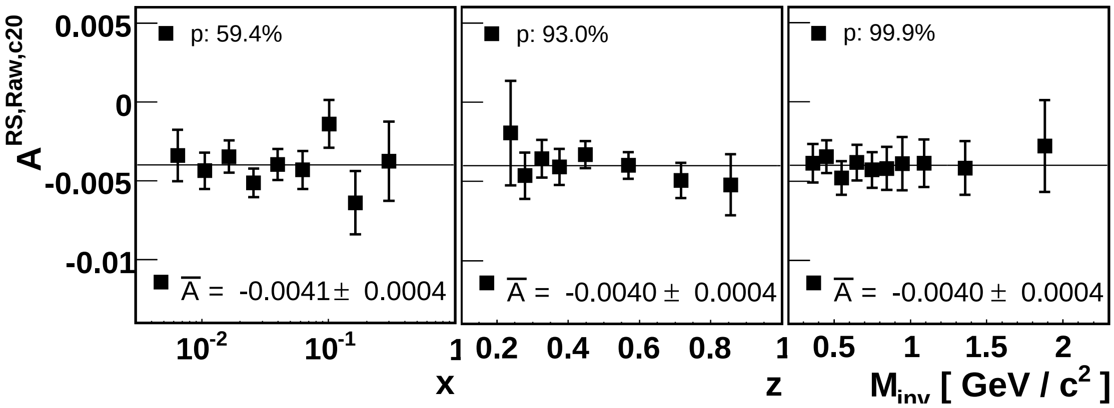

Figure 5.52: Raw RS asymmetries for scenario 2 extracted with UB SA as a function of x, z and M_{inv}. Mean asymmetries, Ā, and probabilities, p, of χ^2 test with respect to $A_{MC}^{RS} = -0.004$ (horizontal line) are given.

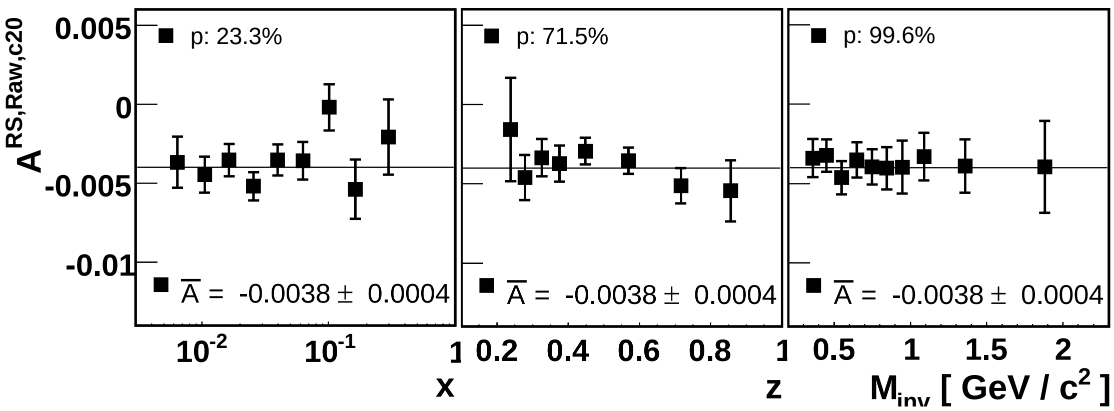

Figure 5.53: Raw RS asymmetries for scenario 3 extracted with UB SA as a function of x, z and M_{inv}. Mean asymmetries, Ā, and probabilities, p, of χ^2 test with respect to $A_{MC}^{RS} = -0.004$ (horizontal line) are given.

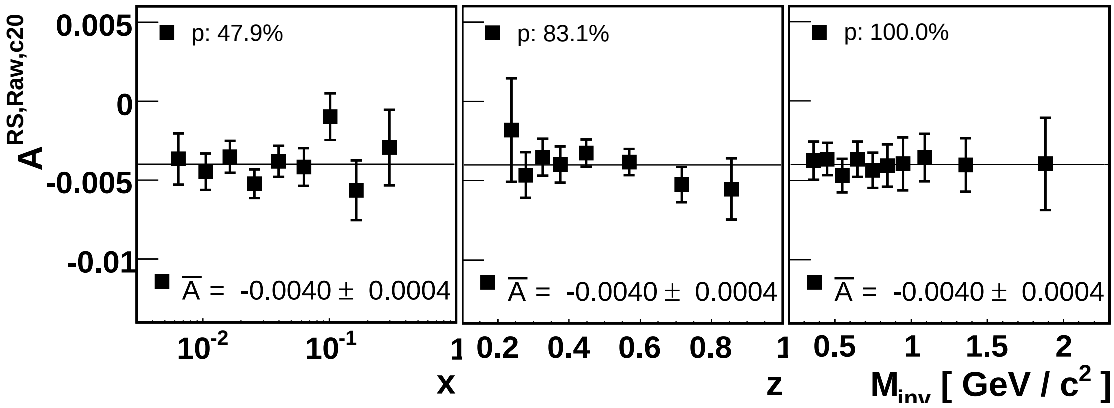

Figure 5.54: Raw RS asymmetries for scenario 4 extracted with UB SA as a function of x, z and M_{inv}. Mean asymmetries, Ā, and probabilities, p, of χ^2 test with respect to $A^{RS}_{MC} = -0.004$ (horizontal line) are given.

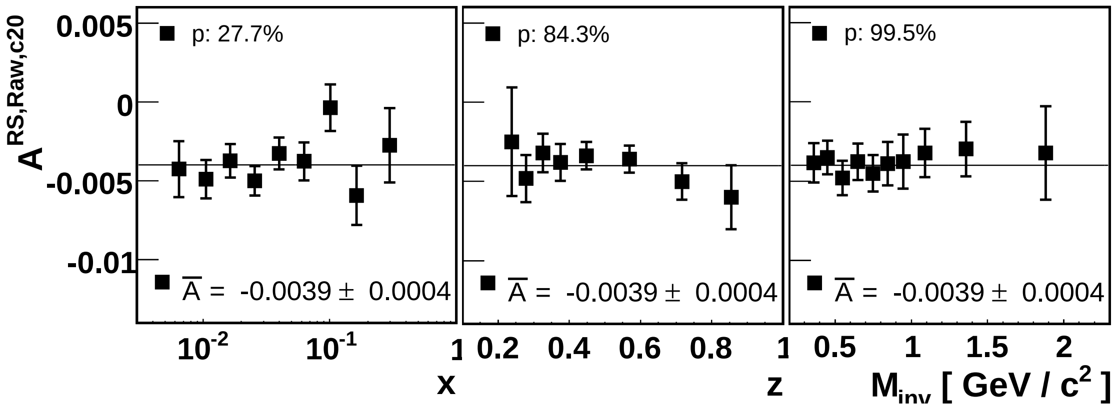

Figure 5.55: Raw RS asymmetries for scenario 5 extracted with UB SA as a function of x, z and M_{inv}. Mean asymmetries, Ā, and probabilities, p, of χ^2 test with respect to $A^{RS}_{MC} = -0.004$ (horizontal line) are given.

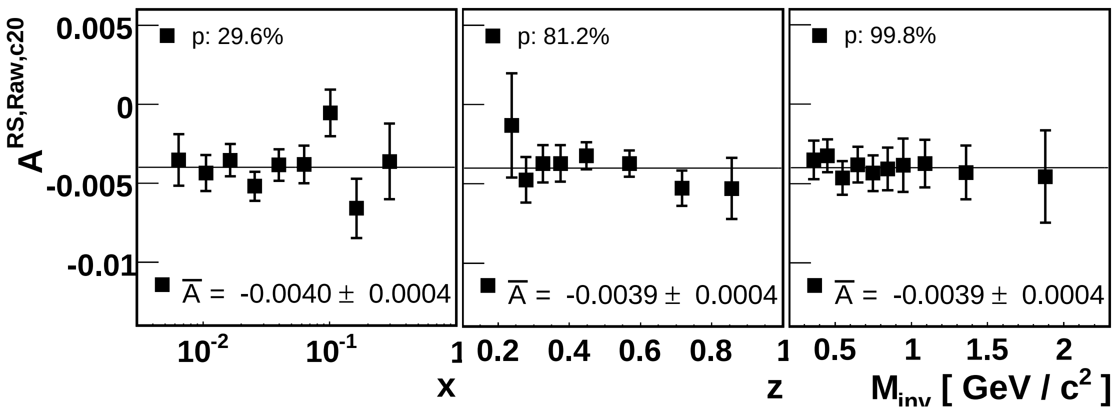

Figure 5.56: Raw RS asymmetries for scenario 6 extracted with UB SA as a function of x, z and M_{inv}. Mean asymmetries, Ā, and probabilities, p, of χ^2 test with respect to $A^{RS}_{MC} = -0.004$ (horizontal line) are given.

In summary all simulated changes in the μ' and/or hadron acceptance had no impact on the extracted asymmetry in $\sin\Phi_{RS}$, leading to the conclusion that the results are quite robust under changes of the detector acceptance. In addition the presence of a large 'Sivers'-like asymmetry in $\sin(\phi_R - \phi_S)$ showed no sizable impact on the extraction of the RS asymmetry, except for the one dimensional ratio method.

5.6 Asymmetries

The final results for the transverse 2007 proton data, obtained with the unbinned maximum likelihood method, are shown as a function of x, z and M_{inv} for h^+h^--pairs in Fig. 5.57. A strong asymmetry is observed in the valence x-region, which implies a non-zero transversity distribution and a non-zero polarized dihadron interference FF. In the invariant mass one observes a strong signal around the ρ^0-mass at around $0.77\,\mathrm{GeV}/c^2$ and the asymmetry is negative over the whole mass range. The results will be discussed in more details in Sec. 5.8.1.

The asymmetries for identified $\pi^+\pi^-$-pairs are shown in Fig. 5.58. The trend is the same as for the unidentified h^+h^--pairs but the size of the asymmetry is slightly smaller. The result for the K^+K^--pairs is shown in Fig. 5.59. The asymmetries are small and compatible with zero.

The error bars shown so far include only the statistical error. In the next sections the systematical error of the result for unidentified h^+h^--pairs are investigated in detail. The systematics for the identified pairs will not be investigated in this thesis, since the cuts for the particle identification are preliminary anyhow.

5.7 Systematic Studies

For the evaluation of the systematical error several checks are used. They will be performed on the six data sets of pairs of consecutive weeks with opposite target polarization as well as on the 'total' data set. In the latter case all data sets of weeks with polarization $+--+$ and all data sets of weeks with $-++-$ are in each case combined, resulting in only one $+--+$ and only one $-++-$ data set. The results worked out for real data will be checked against the results obtained for Monte Carlo data with generated asymmetries of $A_{MC}^{RS} = -0.004$ and $A_{MC}^{Sivers} = 0.006$, as discussed in Sec. 5.5.

5.7.1 Compatibility of the Estimators

All four estimators are used to extract the asymmetries. The results of the final asymmetries are shown in Fig. 5.60. The mean values of all four methods are within the statistical errors well compatible with each other. The pull distributions of the binned methods with respect to the unbinned method and the pull distribution between two dimensional ratio method and binned likelihood method are shown in Fig 5.61. The sigma values of the four distributions are similar to the one obtained for Monte Carlo data (Fig. 5.46) and the mean values of the pulls are even better compatible with zero. Since from Monte Carlo data one cannot judge, which method gives the less biased results, the half of the shifted mean between binned maximum likelihood and unbinned maximum likelihood fit is taken into account as a systematical uncertainty. This amounts to $0.04\,\sigma^{stat}$.

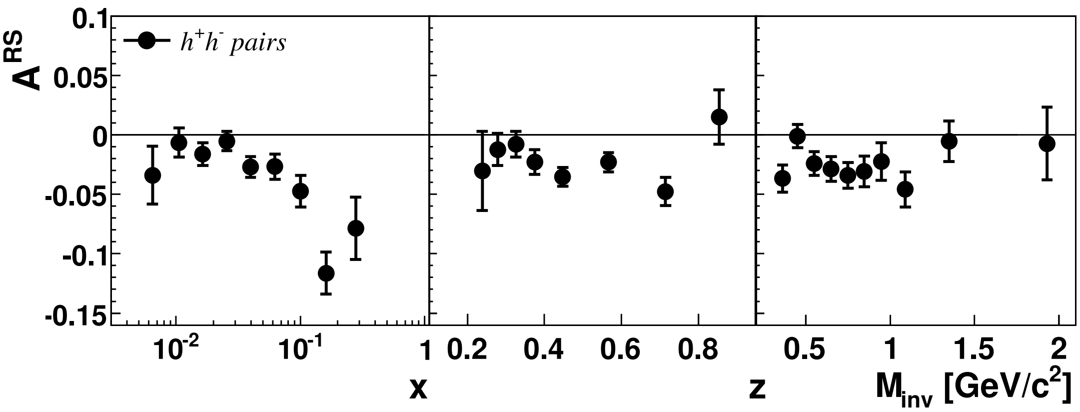

Figure 5.57: Final RS asymmetries for h^+h^--pairs as a function of x, z and M_{inv}. Only statistical errors are shown. The mean asymmetry is: $A^{RS} = 0.025 \pm 0.004$.

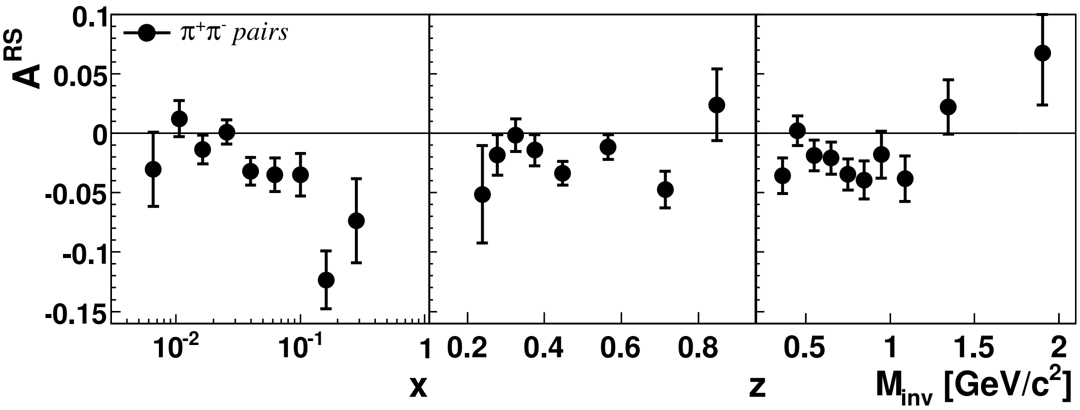

Figure 5.58: Final RS asymmetries for $\pi^+\pi^-$-pairs as a function of x, z and M_{inv}. Only statistical errors are shown. The mean asymmetry is: $A^{RS} = 0.020 \pm 0.005$.

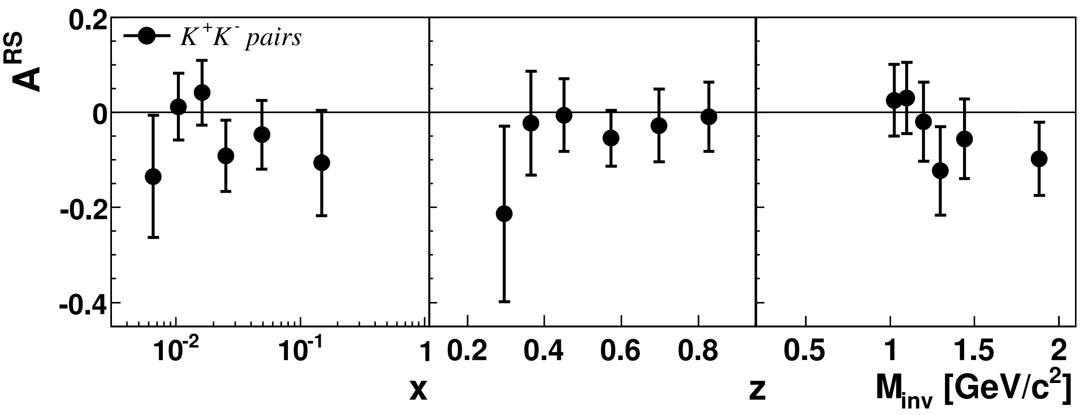

Figure 5.59: Final RS asymmetries for K^+K^--pairs as a function of x, z and M_{inv}. Only statistical errors are shown. The mean asymmetry is: $A^{RS} = 0.03 \pm 0.03$.

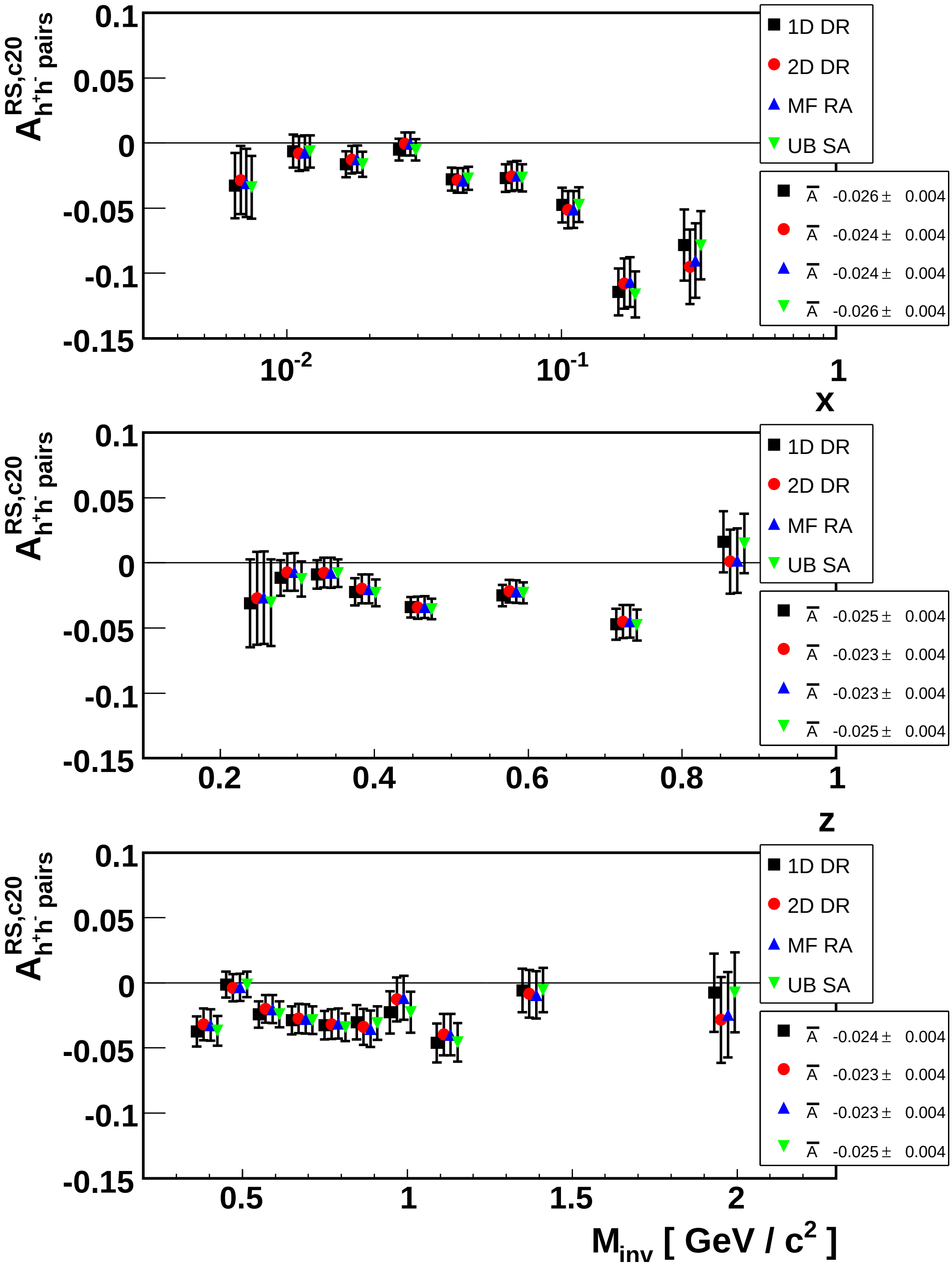

Figure 5.60: Comparison of the RS asymmetries extracted with the four different methods, as a function of x, z and M_{inv}. Mean asymmetries, $\bar{A}$, are given.

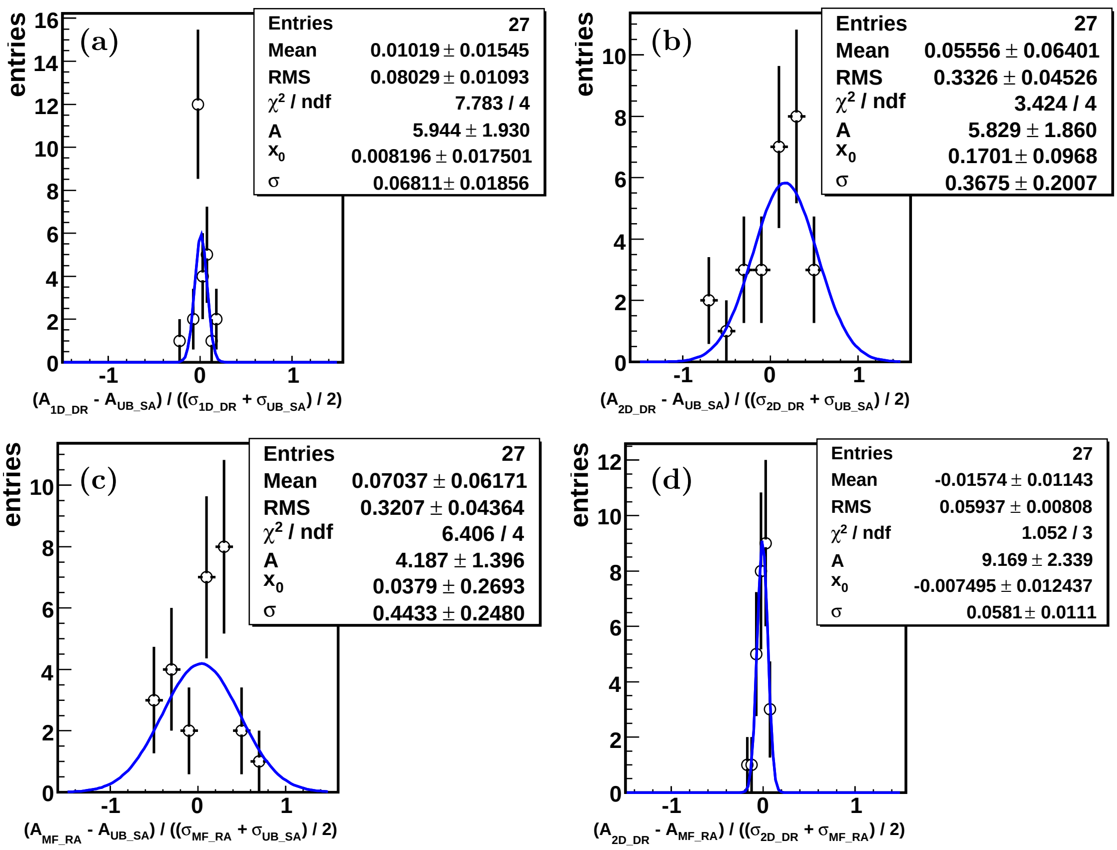

Figure 5.61: Pulls of (a) 1D ratio method, (b) 2D ratio method and (c) binned maximum likelihood with respect to the unbinned likelihood. Bottom right (d) shows the pull between 2D ratio method and binned likelihood.

5.7.2 Period Compatibility

Due to the twelve weeks of data taking with change of target polarization between two consecutive weeks each, six independent asymmetry values can be extracted. The results of the six measurements are shown in Fig. 5.62

In order to check if the six measurements in the 27 kinematical bins in x, z and M_{inv} are statistically compatible one can build the pull defined as:

$$\frac{A_{i,j} - \langle A_i \rangle}{\sqrt{\sigma^2_{A_{i,j}} - \sigma^2_{\langle A_i \rangle}}}. \tag{5.32}$$

In which index i denotes the kinematical bin and j stands for the j-th measurement. If the 6 measurements (in the 27 kinematical bins) are within statistical fluctuations compatible with each other the resulting distribution is a Gaussian with mean $x_0 = 0$ and $\sigma = 1$.

The pull distribution is shown in Fig. 5.63. The mean is compatible with zero and the σ is compatible with one. However, the χ^2 of the fit is quite bad. Therefore, the RMS of the distribution is considered for an estimate of the systematical error

$$\sigma^{sys} \leq \sqrt{\mathrm{RMS}^2 - 1} \cdot \sigma^{stat}.$$

This results in $\sigma^{sys} = 0.37 \cdot \sigma^{stat}$.

5.7.3 Dtest

A check for the stability of the acceptance is the so-called Dtest. Here the events from the four target cells are binned in a two dimensional grid in ϕ_R and ϕ_S and normalized to its total integral. The four normalized distributions are summed up for both periods separately and finally subtracted from each other.

$$D(\phi_R, \phi_S) = \sum_{i=1}^{4} \tilde{N}_i(\phi_R, \phi_S) - \sum_{i=1}^{4} \tilde{N}'_i(\phi_R, \phi_S), \tag{5.33}$$

in which $\tilde{N}_i(\phi_R, \phi_S) = N_i(\phi_R, \phi_S) / \int\int d\phi_R d\phi_S N_i(\phi_R, \phi_S)$.

If the detector was stable the two dimensional distribution $D(\phi_R, \phi_S)$ should be compatible with zero. The resulting χ^2-distributions for the six double periods are shown in Fig. 5.64. For the chosen 8x8 binning in ϕ_R and ϕ_S the distributions should have a mean of 63. In most of the cases the mean values are slightly increased. But the distributions are pretty narrow and no drastic outliers are present. It has to be mentioned, that a bad Dtest does not necessarily result in a bias of the measured asymmetry. But it is a useful global check, that the acceptance in ϕ_R and ϕ_S of the two coupled samples is compatible and no severe difference between the samples is present. For example in Fig. A.10 the Dtest results of scenario 3 and 5 for Monte Carlo data (see Sec. 5.5.3), are shown. Both distributions show large deviations from the expected behavior. The asymmetries however, have been extracted correctly without any significant bias.

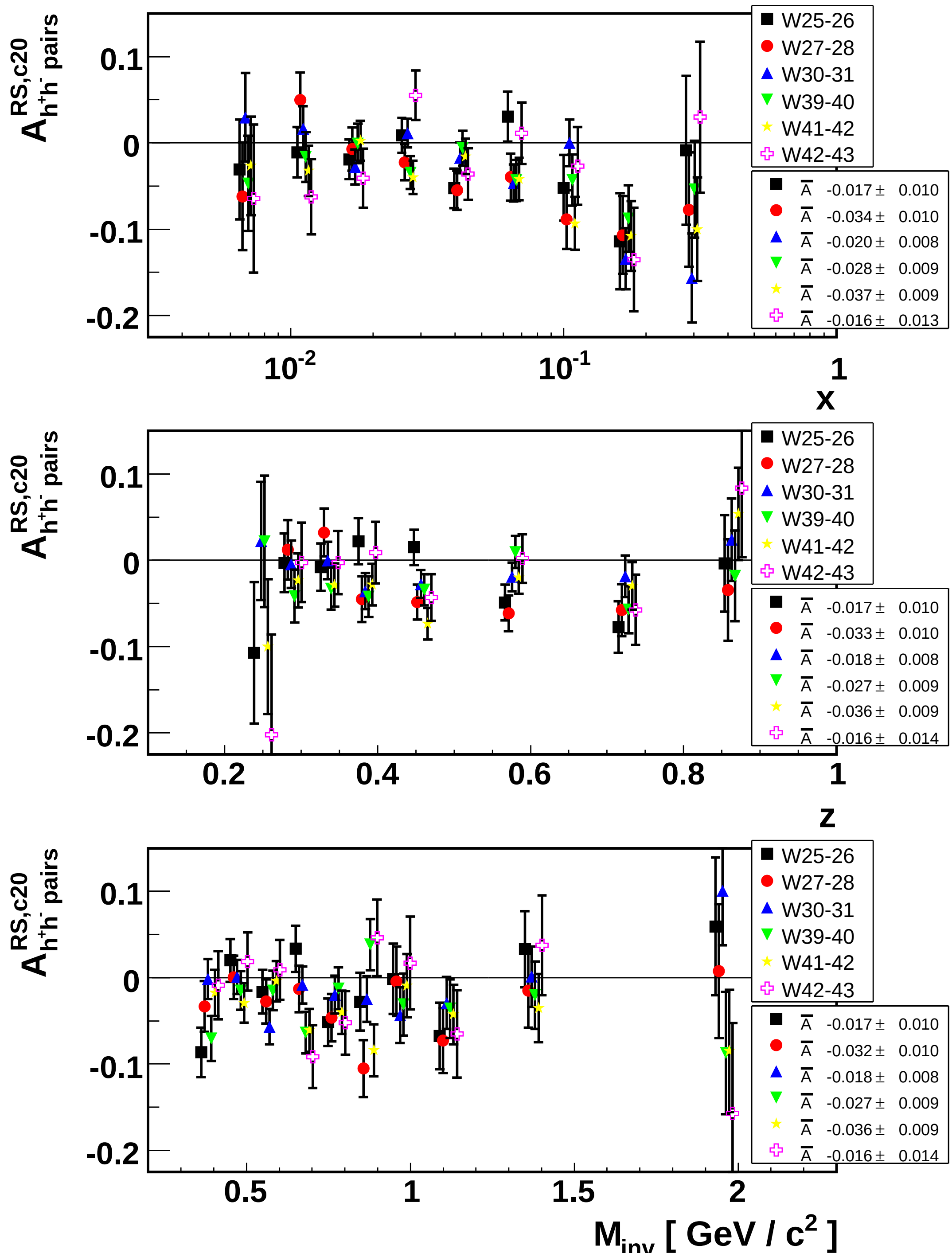

Figure 5.62: RS asymmetries of the six independent measurements as a function of x, z and M_{inv}. Mean asymmetries, $\bar{\mathrm{A}}$, are given.

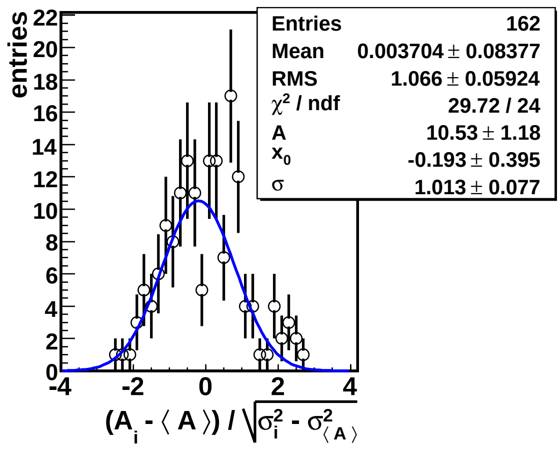

Figure 5.63: Compatibility pull distribution of the six independent measurements in the 27 kinematical bins for the RS asymmetry.

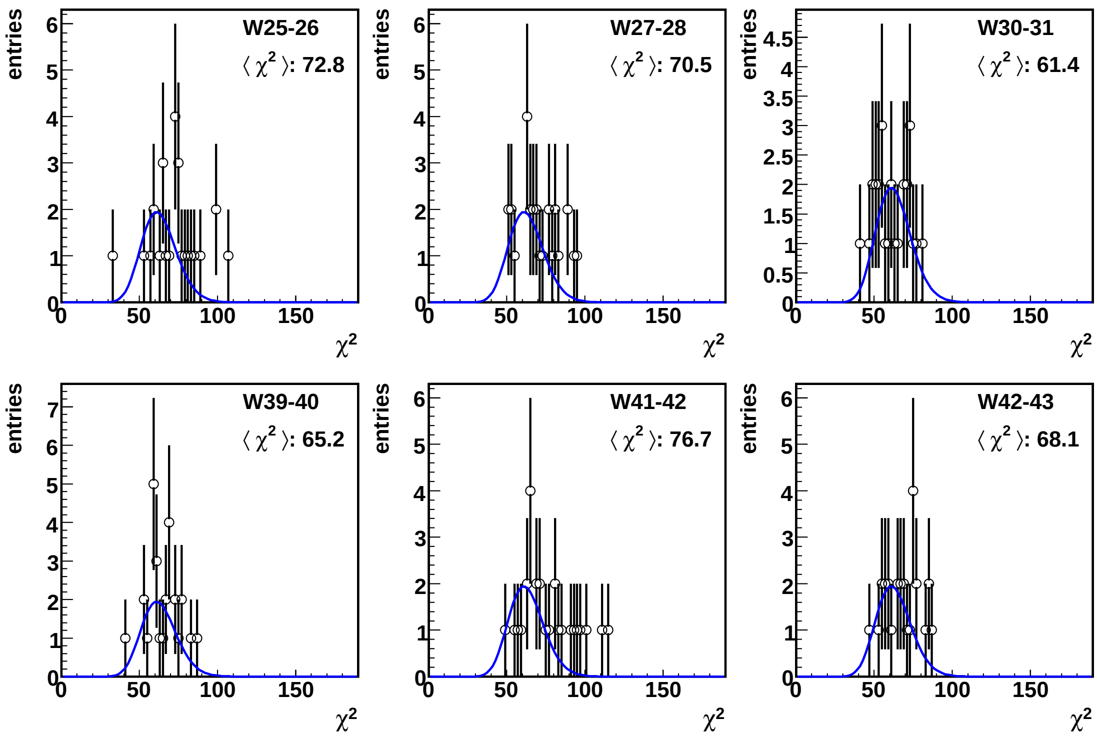

Figure 5.64: χ^2-distribution of Dtest for the six double periods. The blue lines indicate the expected distributions with mean value 63.

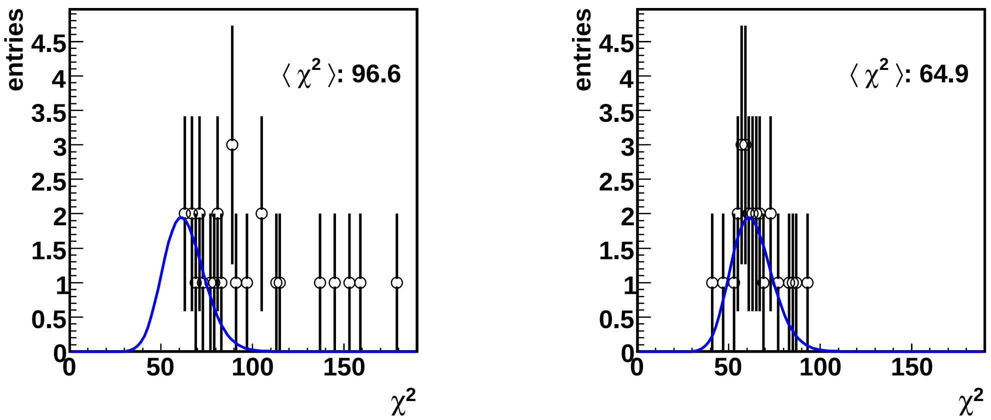

Figure 5.65: χ^2-distribution of Dtest. On the left for the 'total' data set and on the right for the Monte Carlo sample with generated asymmetries. The blue lines indicate the expected distributions with mean value 63.

On the left in Fig. 5.65 the Dtest of the 'total' data set is shown. The mean of the distribution is shifted and five bins show a rather large χ^2. An explanation for the shifted mean, which is not seen for the six double periods, is the smaller statistical error of the 'total' data set and therefore the increased sensitivity for systematics. On the right in Fig. 5.65 the Dtest result for the Monte Carlo data is plotted, reproducing the expected distribution. Comparing the results for real data and Monte Carlo it seems that the acceptance in the real data for the two data samples has changed. Further tests are performed to quantify if those acceptance changes affects the extraction of the asymmetry in $\sin \Phi_{RS}$.

5.7.4 Ttest

In order to check whether the acceptance in the angle Φ_{RS} has changed between the two samples, one can study the following ratio.

$$T(\Phi_{RS}) = \frac{\prod_{i=1}^{4} N_i(\Phi_{RS})}{\prod_{i=1}^{4} N_i'(\Phi_{RS})}, \tag{5.34}$$

in which N_i, as described in Sec. 5.2, can be written as:

$$N_i(\Phi_{RS}) = c_i(1 + a_i \sin \Phi_{RS})(1 \pm \epsilon \sin \Phi_{RS}). \tag{5.35}$$

The second term containing the physics asymmetry cancels in Eq. (5.34) and only the first part, describing the acceptance survives. Performing a Taylor expansion in $\sin \Phi_{RS}$ and neglecting quadratic terms in $\sin \Phi_{RS}$ one gets

$$T(\Phi_{RS}) \approx c \cdot (1 + (e_1 + e_2 + e_3 + e_4) \sin \Phi_{RS}), \tag{5.36}$$

in which $e_i = a_i - a_i'$ is the change of acceptance of cell i. The quantity T is therefore an indicator if the acceptance of the detector in $\sin \Phi_{RS}$ has changed. Fitting the ratio T with the function

$$f(\Phi_{RS}) = c \cdot (1 + 4A^{RS,Ttest} \sin \Phi_{RS}), \tag{5.37}$$

the resulting amplitude $A^{RS,Ttest}$ can be interpreted as the mean acceptance change of the four cells.

As seen in Eq. (5.8) the measured physics asymmetry A^{c20}_{meas} is biased by

$$A^{c20}_{meas} = \epsilon + (e_1 - e_2 - e_3 + e_4)/8.$$

Therefore, even if $A^{RS,Ttest}$ is large the measured asymmetry is not necessarily biased. In particular, if $e_1 = e_2 = e_3 = e_4$ the amplitude $A^{RS,Ttest}$ can be arbitrarily large, without affecting the physical asymmetry.

Assuming that all e_i have the same sign, one can conclude, that if $A^{RS,Ttest}$ is small the possible bias of the real asymmetry should also be small. The result of the Ttest as a function of x is shown in Fig. 5.66. For all six double periods the distributions are compatible with zero, as can be seen by the probabilities of the χ^2-test and the mean values which are given on the top left and on the bottom right respectively.

The same test is done for the 'total' data set. The result as a function of x, z and M_{inv} is shown in Fig. 5.67. The mean value is compatible with zero. This already qualify the detected change of acceptance by the Dtest found for the 'total' data set (see Fig. 5.65). It seems that the change contains no parts in $\sin\Phi_{RS}$.

As a function of x and M_{inv} the χ^2-test with respect to zero show probabilities below 6 %. The Ttest result for Monte Carlo data is shown in Fig. 5.68. As a function of x the probability of the χ^2-test is rather small too. In addition, by consulting the corresponding real asymmetries in Fig. 5.48, one sees that they are not affected, although the Ttest shows in some bins large deviations from zero.

5.7.5 False Asymmetries

Another check is to build false asymmetries in combining data samples with common target polarization, namely the data of the two outer cells (c2) or the data of the two inner cells (c3). If the acceptance between the cells has changed a false asymmetry should be present. The asymmetries of these two configurations can be written as:

$$\mathrm{c2} = \frac{N_1 \cdot N_4'}{N_1' \cdot N_4}, \tag{5.38}$$

$$\mathrm{c3} = \frac{N_2 \cdot N_3'}{N_2' \cdot N_3}. \tag{5.39}$$

With Eq. (5.5) and assigning N_3 and N_4 the opposite target polarization (and correspondingly N_3' and N_4'), the physics asymmetry does not cancel. Performing a Taylor expansion analogue to the one for the double ratio, leads to:

$$\mathrm{c2} \approx c \cdot (1 + (4\epsilon + (e_1 - e_4))\sin\Phi_{RS}), \tag{5.40}$$

$$\mathrm{c3} \approx c \cdot (1 + (4\epsilon + (e_2 - e_3))\sin\Phi_{RS}). \tag{5.41}$$

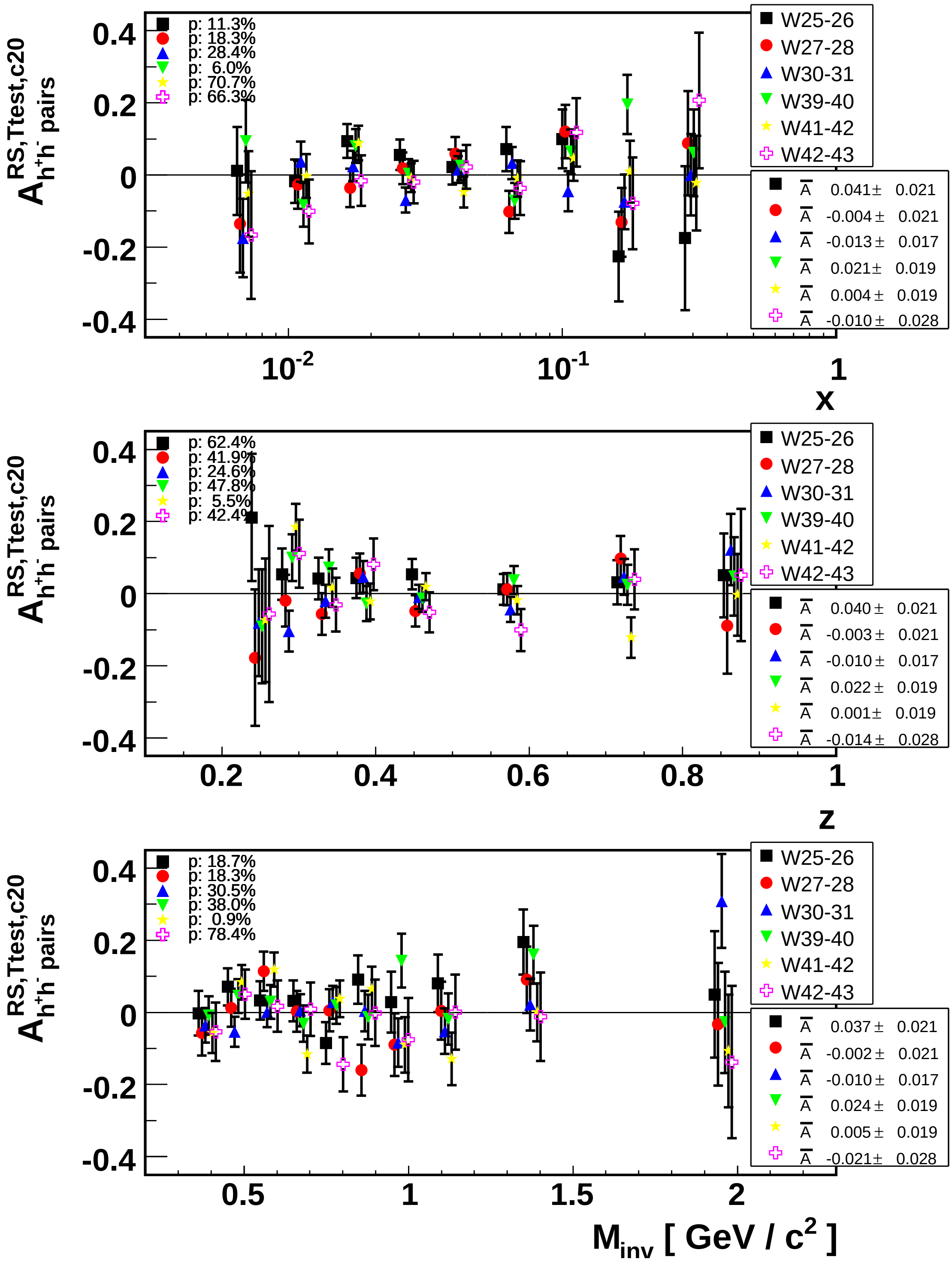

Figure 5.66: Result of Ttest for the six double periods. Mean Ttest values, Ā, and probabilities, p, of χ^2 test with respect to $A^{RS,Ttest} = 0$ are given.

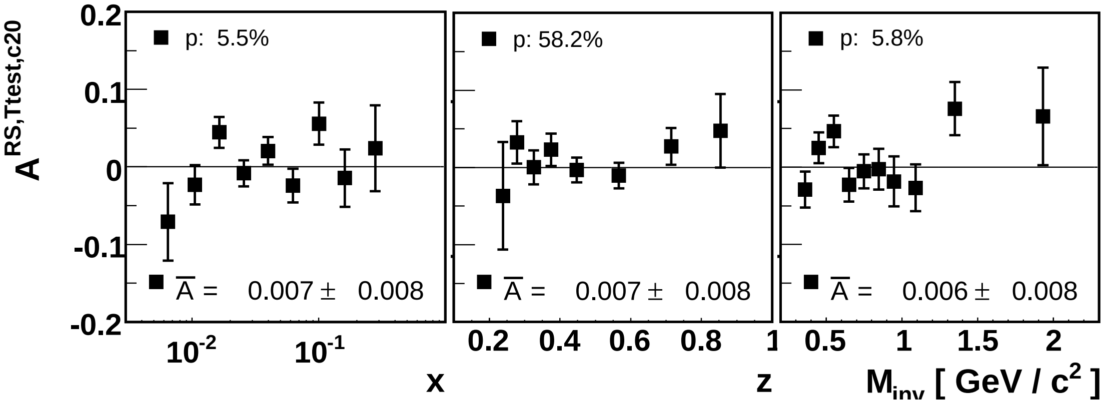

Figure 5.67: Result of Ttest for the 'total' data set as function of x, z and M_{inv}. Mean Ttest values, Ā, and probabilities, p, of χ^2 test with respect to $A^{RS,Ttest} = 0$ are given.

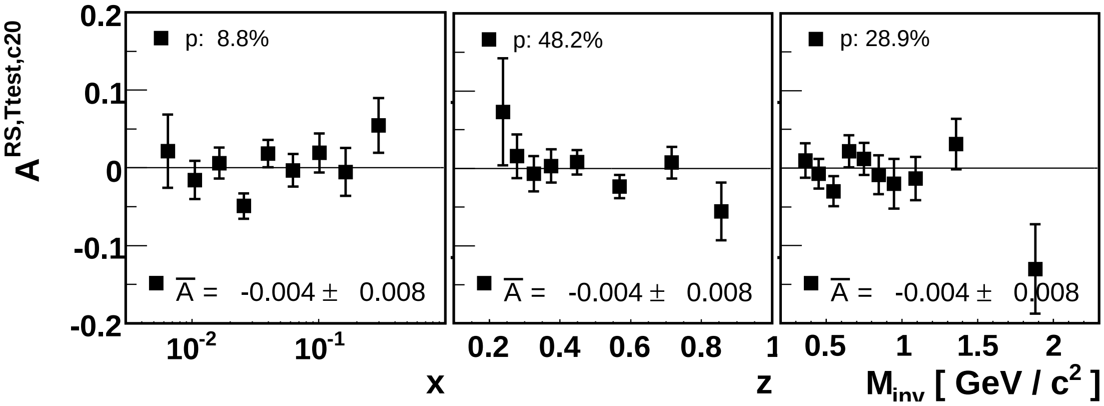

Figure 5.68: Result of Ttest for Monte Carlo data with generated asymmetries as function of x, z and M_{inv}. Mean Ttest values, Ā, and probabilities, p, of χ^2 test with respect to $A^{RS,Ttest} = 0$ are given.

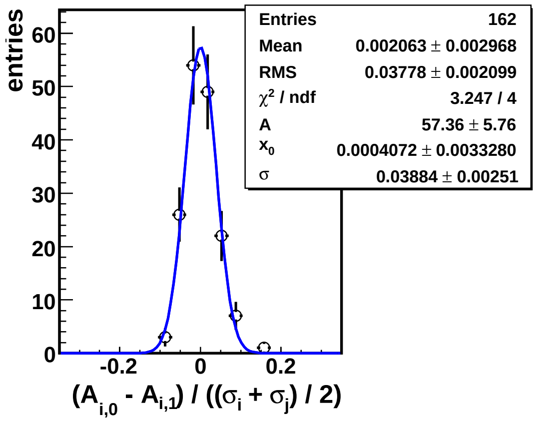

Figure 5.69: Pull distribution between $A^{RS,(c2-c3)/2}$ and $A^{RS,(c0-c1)/2}$.

Assuming that all e_i have the same sign, half the difference (c2-c3)/2 gives an estimate of the bias of the real asymmetry ϵ:

$$A^{RS,(\mathrm{c2\ \text{-}c3})/2} \approx \frac{1}{8}(e_1 - e_2 + e_3 - e_4). \tag{5.42}$$

The factor of $\frac{1}{8}$ accounts for the fact, that the amplitudes in Eq. (5.40) and (5.41) are divided by a factor 4 for the fit, as it is also done for the real asymmetries.
This quantity is equal to the difference (c0-c1)/2, which is half the difference of the real asymmetries measured with the two upstream cells (N_1 and N_2) and the two downstream cells (N_3 and N_4). Fig. 5.69 shows the pulls between $A^{RS,(c2-c3)/2}$ and $A^{RS,(c0-c1)/2}$. The distribution is centered around zero with a small sigma of 0.04.

In Fig. 5.70 the false asymmetries $A^{RS,(c2-c3)/2}$ for the six double periods are shown as a function of x, z and M_{inv}. For all weeks the measured false asymmetries are compatible with zero. Only week W25/W26 shows a three σ deviation. However, the fluctuations of some weeks are, as indicated by the low probabilities of the χ^2 test with respect to zero, larger than statistically expected. Fig. 5.71 shows the same quantity but for the 'total' data set. The measured false asymmetry is well compatible with zero. Especially in the region $x > 0.03$, where the strong signal is measured, the false asymmetries are very small. For $x < 0.03$ the false asymmetries are at the edge of one sigma. As a function of the invariant mass M_{inv}, at the ρ^0 mass ($0.7\,\mathrm{GeV}/c^2$) a deviation of two sigma is present. However, compared to the results obtained for Monte Carlo data shown in Fig. 5.72 one sees also, especially in the invariant mass, fluctuations up to three sigma, which however do not affect the real asymmetries as one can see in Fig. 5.47.

In order to quantify the deviations the weighted mean deviation $\Delta_{|c2-c3|}$ of the 27 bins in terms of the statistical error is built:

$$\frac{\Delta_{|c2-c3|}}{\sigma^{stat}} = \frac{\sum_{i=1}^{27} \frac{|A_i^{RS,(c2-c3)/2}|}{\sigma_i} \frac{1}{\sigma_i^2}}{\sum_{i=1}^{27} \frac{1}{\sigma_i^2}}, \tag{5.43}$$

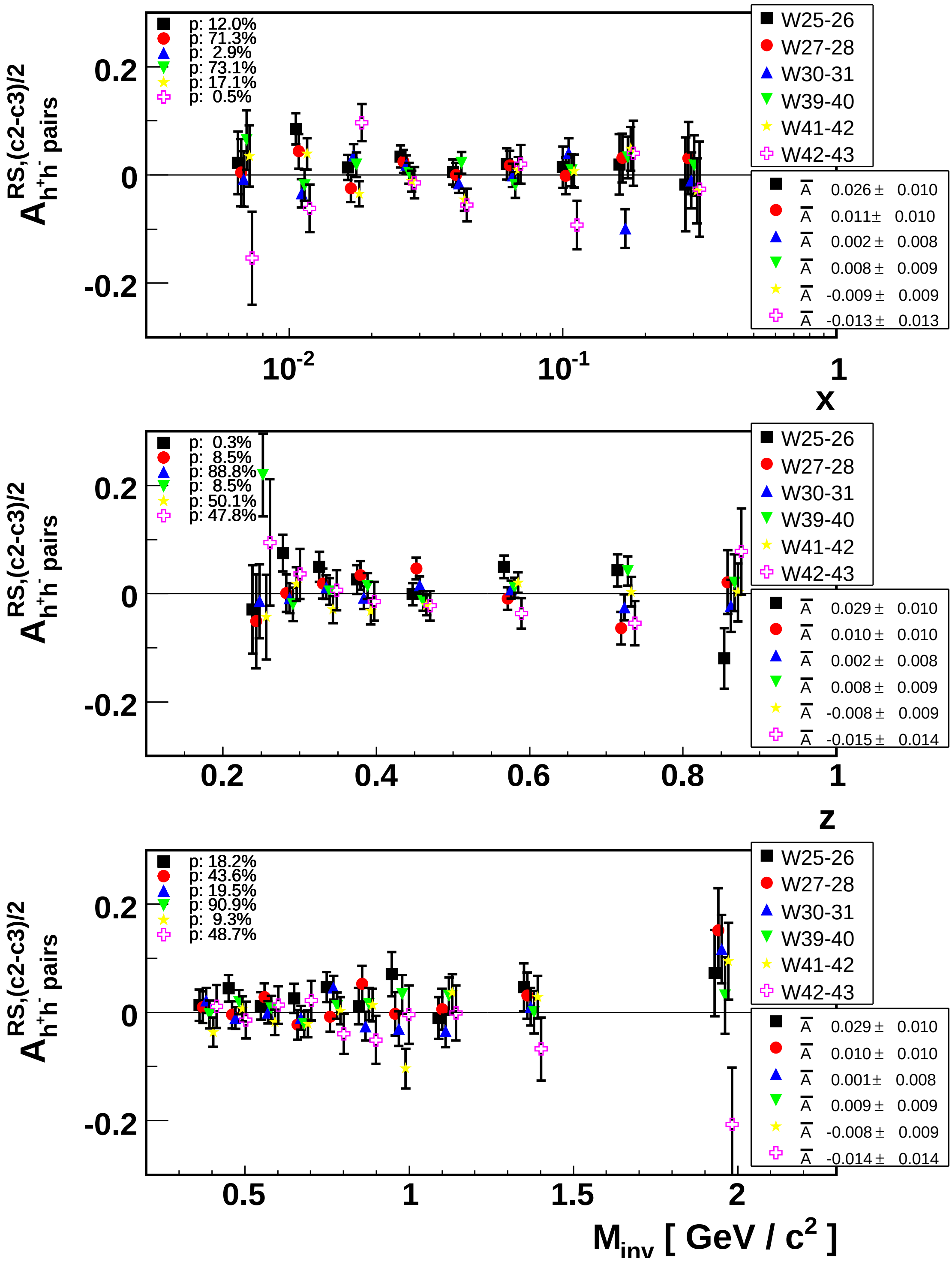

Figure 5.70: Results of $A^{RS,(c2-c3)/2}$ for the six double periods as a function of x, z and M_{inv}. Mean values, $\bar{\text{A}}$, and probabilities, p, of χ^2 test with respect to $A^{RS,(c2-c3)/2} = 0$ are given.

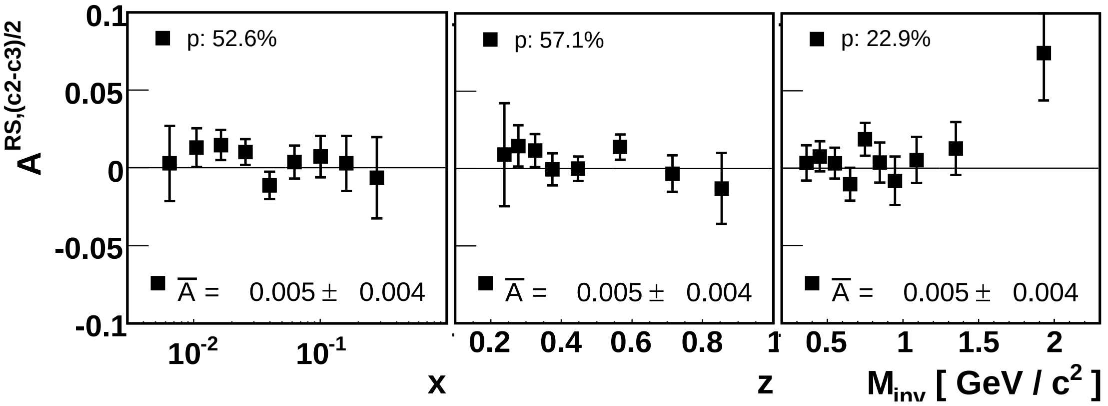

Figure 5.71: Results of $A^{RS,(c2-c3)/2}$ for the 'total' data set as a function of x, z and M_{inv}. Mean values, Ā, and probabilities, p, of χ^2 test with respect to $A^{RS,(c2-c3)/2} = 0$ are given.

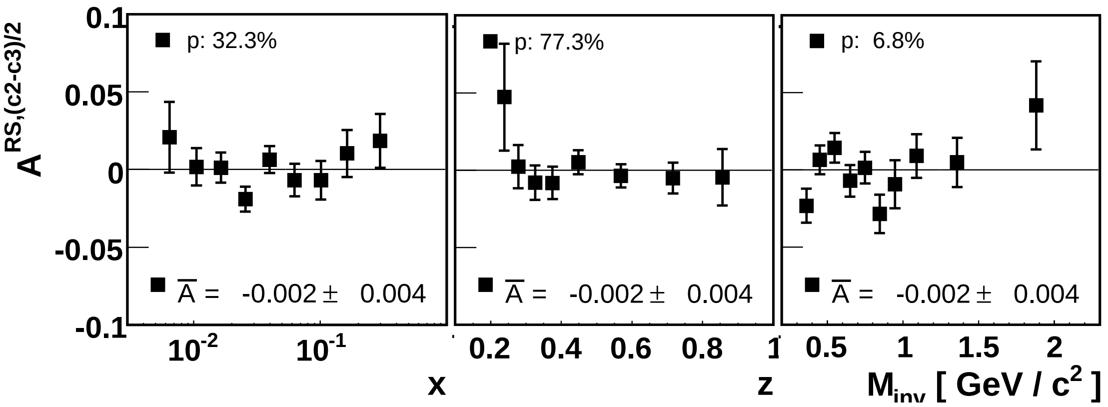

Figure 5.72: Results of $A^{RS,(c2-c3)/2}$ for Monte Carlo data with generated asymmetries as a function of x, z and M_{inv}. Mean values, Ā, and probabilities, p, of χ^2 test with respect to $A^{RS,(c2-c3)/2} = 0$ are given.

in which $|A_i^{RS,(c2-c3)/2}|$ is the absolute value of the amplitude in bin i and σ_i the corresponding error. For the 'total' data set one obtains: $\Delta_{|c2-c3|} = 0.81 \cdot \sigma^{stat}$. The same quantity is computed for the Monte Carlo sample. Here $\Delta_{|c2-c3|,MC} = 0.84 \cdot \sigma^{stat,MC}$ is obtained, indicating that such kind of deviation is statistically expected. Therefore this will not be considered in the evaluation of the systematical error.

Summation of Eq. (5.40) and (5.41) and division by two, leads to:

$$A^{RS,(\mathrm{c2\,+\,c3})/2} \approx \epsilon + \frac{1}{8}(e_1 + e_2 - e_3 - e_4). \tag{5.44}$$

The real asymmetry ϵ should be zero, since samples with the same target polarization are used. Hence only the term containing the change of acceptance is left. The interpretation of this quantity is not so clear in terms of bias to the real asymmetries. But if the extracted amplitudes $A^{RS,(\mathrm{c2\,+\,c3})/2}$ are small, the bias of the real asymmetries should be small too. The results for the six double periods are shown in Fig. 5.73. All mean values are within the statistical error compatible with zero. Only W27/W28 shows a three σ deviation. The false asymmetries $A^{RS,(\mathrm{c2\,+\,c3})/2}$ of the 'total' data set are shown in Fig. 5.74. The mean is within one σ compatible with zero. However, the probability of the χ^2-test for the amplitudes as a function of invariant mass is only 2.9 %. The result for Monte Carlo data is shown in Fig. 5.75. In some bins the values deviate several sigmas. However, compared to the real asymmetries shown in Fig. 5.47, those fluctuations have no impact on them.

Analogue to Eq. (5.43) the weighted mean deviation $\Delta_{|c2+c3|}$ in terms of the statistical error is built. For the 'total' data set it is $\Delta_{|c2+c3|} = 0.88 \cdot \sigma^{stat}$. For Monte Carlo data it is 0.76 of the statistical error. The square root of the squared difference of the two results will be taken into account in the systematical error:

$$\sigma^{sys} = \sqrt{0.88^2 - 0.76^2} \cdot \sigma^{stat} = 0.44 \cdot \sigma^{stat}. \tag{5.45}$$

5.7.6 Compatibility of Results of Single Cells

For the 'total' data set the asymmetries are also evaluated for all four cells individually:

$$\mathrm{c14} \;= \tfrac{N_1}{N_1'} \;\longrightarrow\; A^{c14} = \epsilon + \tfrac{e_1}{2}, \tag{5.46}$$
$$\mathrm{c15} \;= \tfrac{N_2}{N_2'} \;\longrightarrow\; A^{c15} = \epsilon - \tfrac{e_2}{2}, \tag{5.47}$$
$$\mathrm{c16} \;= \tfrac{N_3}{N_3'} \;\longrightarrow\; A^{c16} = \epsilon - \tfrac{e_3}{2}, \tag{5.48}$$
$$\mathrm{c17} \;= \tfrac{N_4}{N_4'} \;\longrightarrow\; A^{c17} = \epsilon + \tfrac{e_4}{2}. \tag{5.49}$$

The results of these four asymmetries as a function of x, z and M_{inv} are shown in Fig. 5.76. The mean value of A^{c14} deviates up to $2\,\sigma$ from the other three values. The pulls, evaluated analogue to Eq. (5.32) are shown on the left in Fig. 5.78. The sigma of the pull is not compatible with one. The same test is performed on Monte Carlo data. The results are shown in Fig. 5.77. As for real data the result obtained with the first cell deviates from the other three values. The corresponding compatibility pulls are shown on the right in Fig. 5.78. The distribution looks similar to the one for real data, shown on the left. Which means that it is not possible to extract the asymmetries with one cell only. One needs to combine the results of all four cells to obtain an unbiased result.

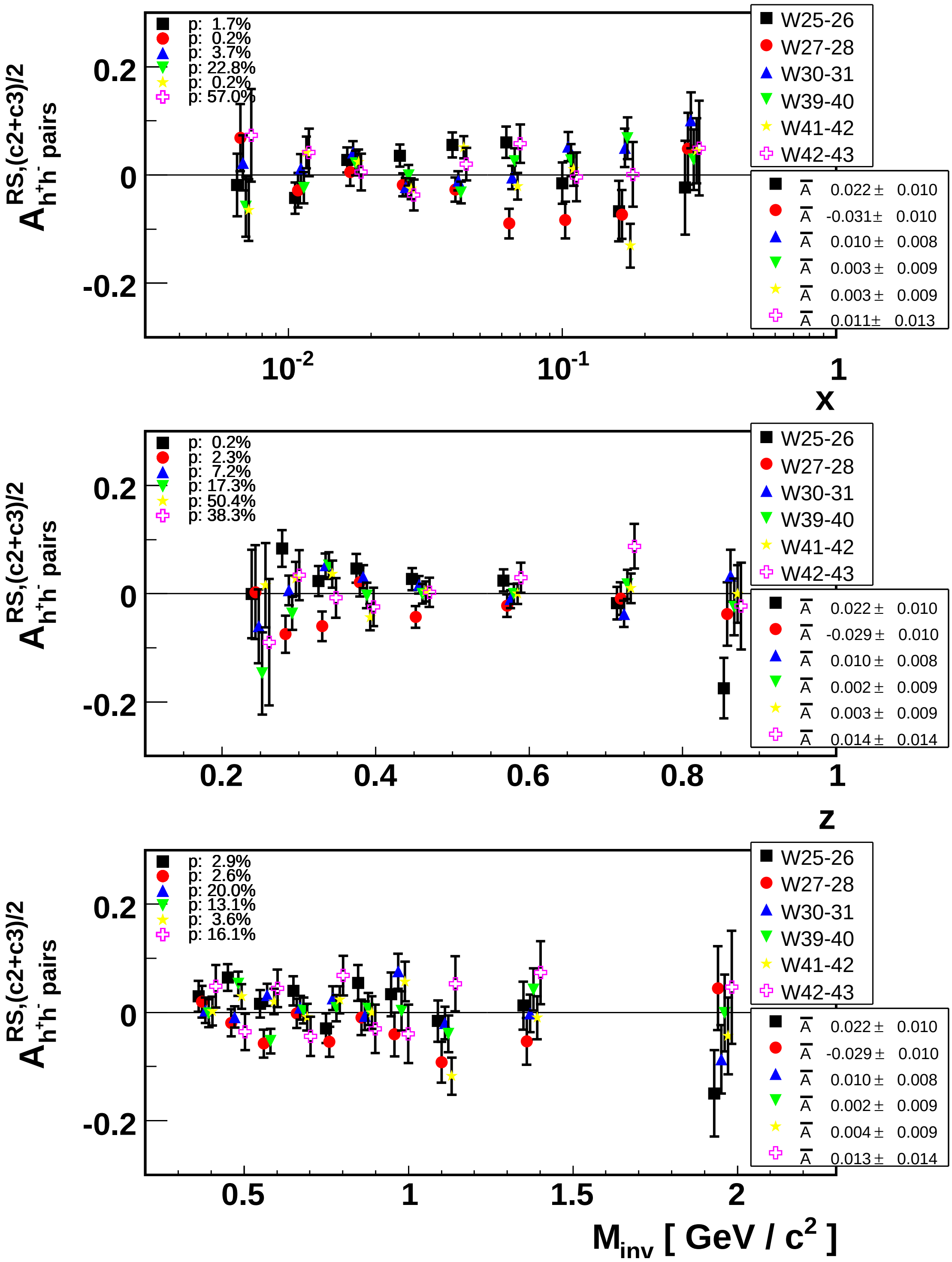

Figure 5.73: Results of $A^{RS,(c2+c3)/2}$ for the six double periods as a function of x, z and M_{inv}. Mean values, $\bar{\mathrm{A}}$, and probabilities, p, of χ^2 test with respect to $A^{RS,(c2+c3)/2} = 0$ are given.

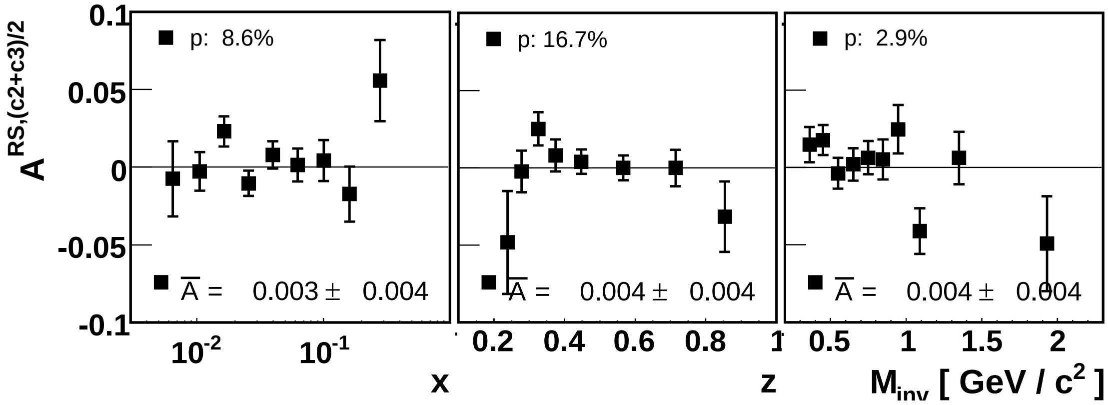

Figure 5.74: Results of $A^{RS,(c2+c3)/2}$ for the 'total' data set as a function of x, z and M_{inv}. Mean values, Ā, and probabilities, p, of χ^2 test with respect to $A^{RS,(c2+c3)/2} = 0$ are given.

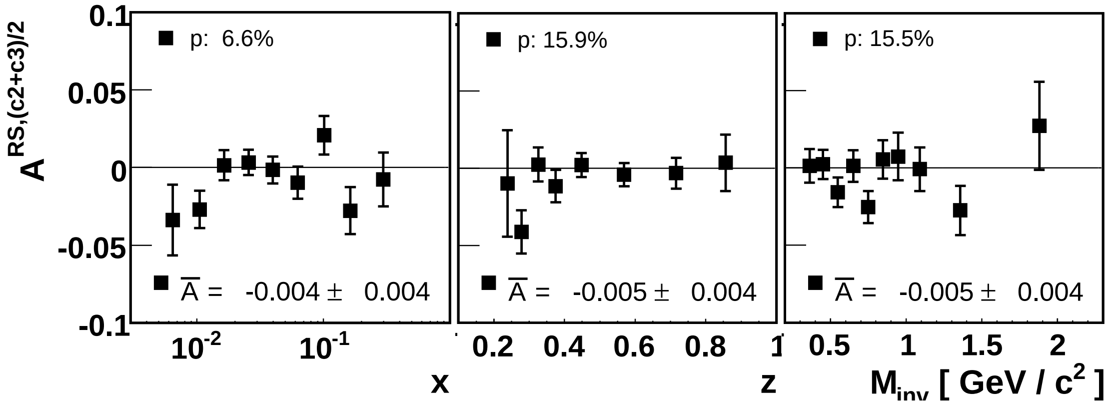

Figure 5.75: Results of $A^{RS,(c2+c3)/2}$ for Monte Carlo data with generated asymmetries as a function of x, z and M_{inv}. Mean values, Ā, and probabilities, p, of χ^2 test with respect to $A^{RS,(c2+c3)/2} = 0$ are given.

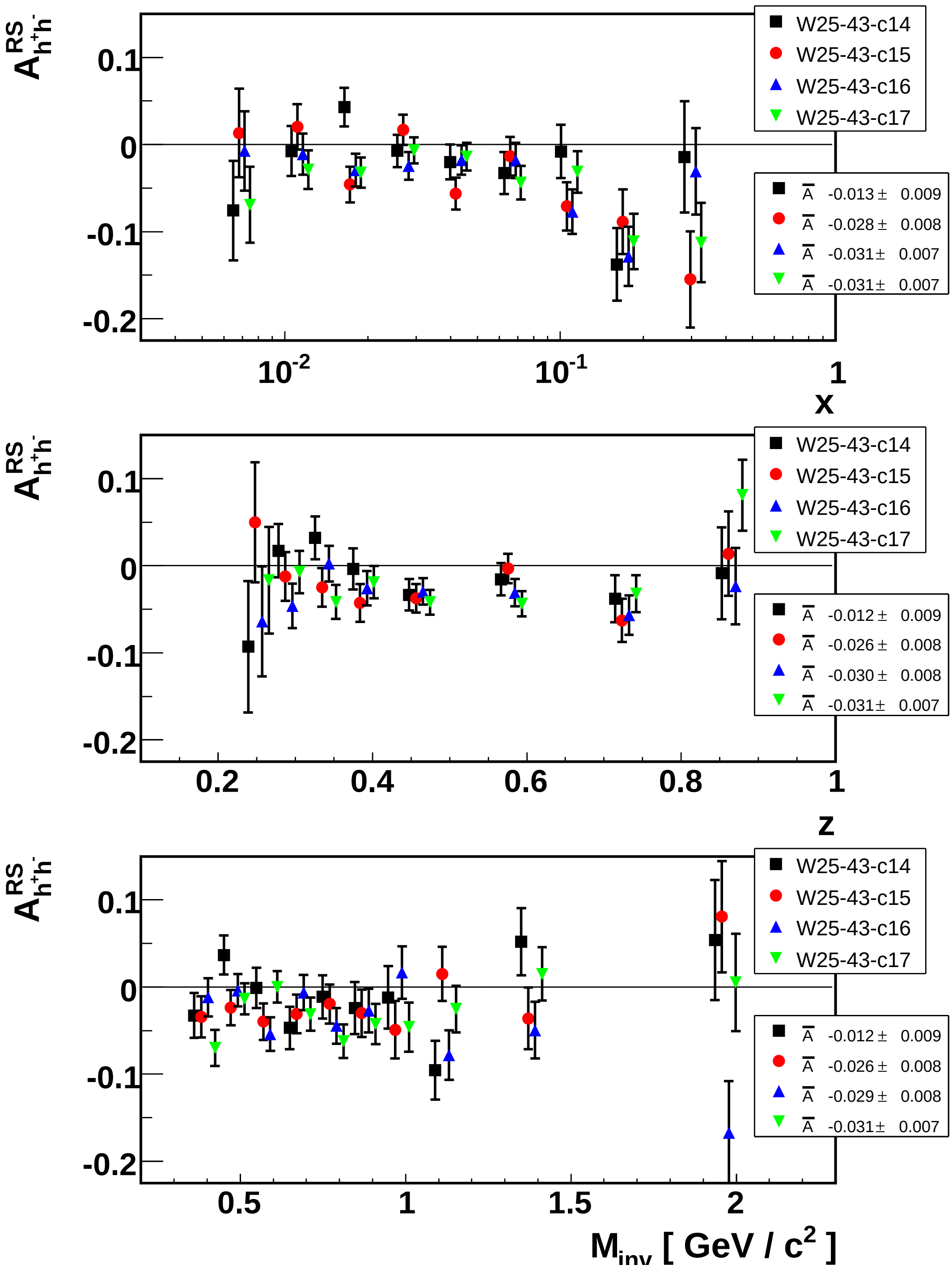

Figure 5.76: RS asymmetries extracted with the four target cells individually as a function of x, z and M_{inv}. A^{c14}, A^{c15}, A^{c16} and A^{c17} correspond to asymmetries evaluated with cell 1, 2, 3 and 4, respectively. Mean values, $\bar{\mathrm{A}}$, are given.

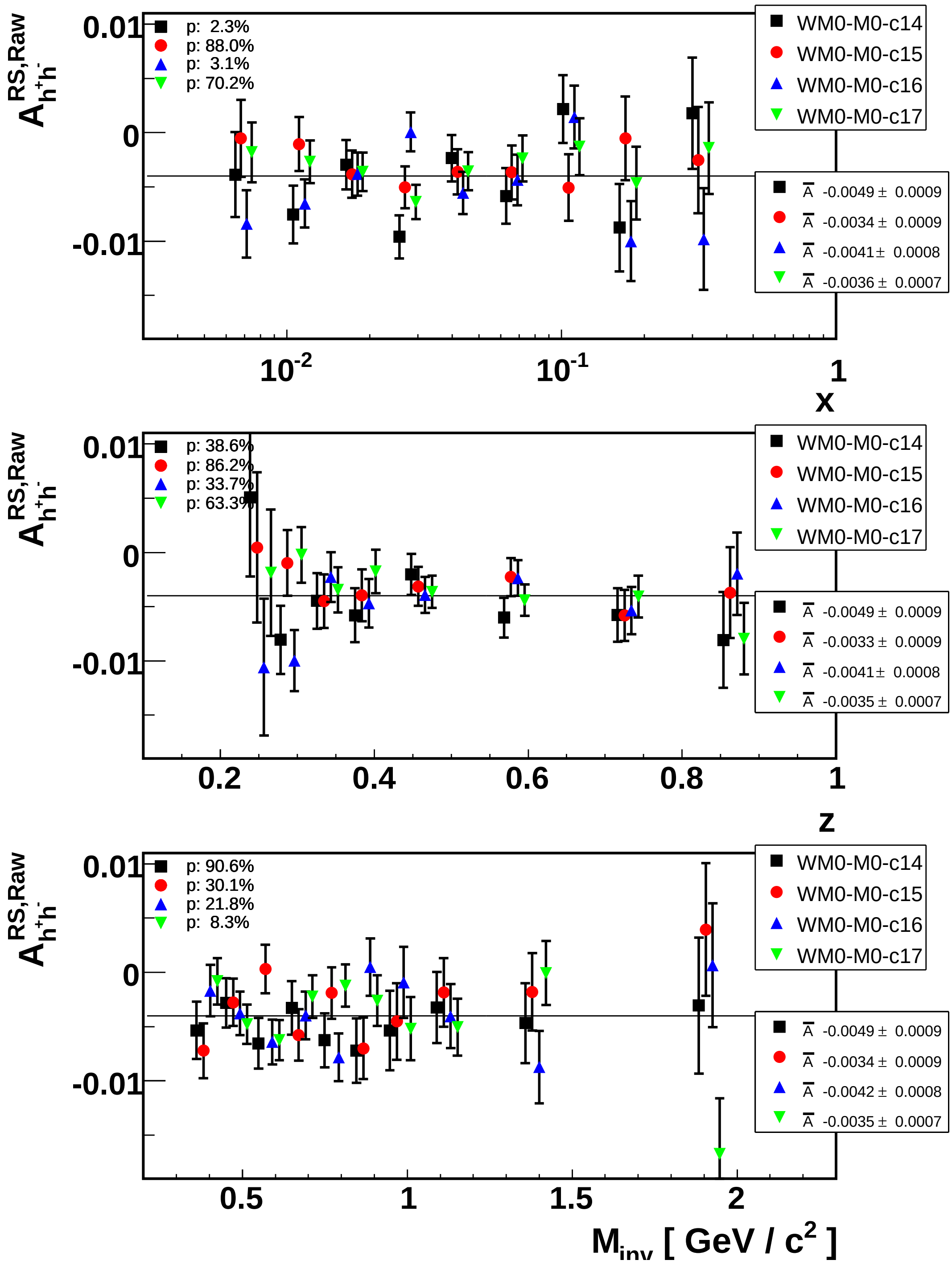

Figure 5.77: Raw RS asymmetries extracted with the four target cells individually for Monte Carlo data with generated asymmetries as a function of x, z and M_{inv}. A^{c14}, A^{c15}, A^{c16} and A^{c17} correspond to asymmetries evaluated with cell 1, 2, 3 and 4, respectively. Mean values, $\bar{A}$, and probabilities, p, of χ^2 test with respect to $A^{RS}_{MC} = -0.004$ (horizontal lines) are given.

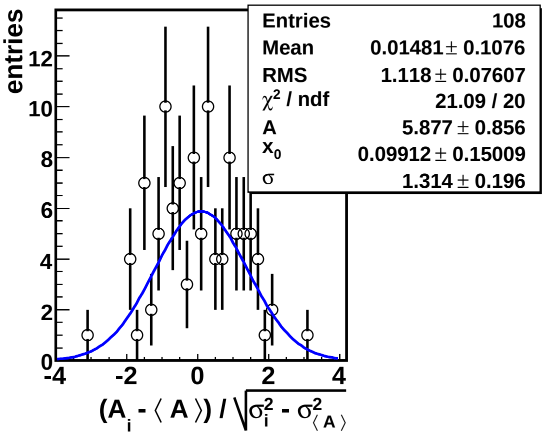

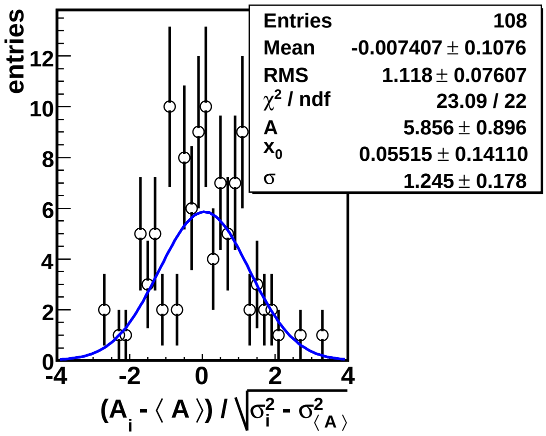

Figure 5.78: Compatibility pulls for the RS asymmetry evaluated with the four cells individually. Left: Real data. Right: Monte Carlo data with generated asymmetries.

5.7.7 Left/Right and Top/Bottom Dependence

The results are checked for a dependence on $\phi_{\mu'}$, the azimuthal angle of the scattered muon in the laboratory frame. Therefore the spectrometer is divided into left and right and into top and bottom. The four parts are defined as follows:

- Left (c20s1): $0 \leq \phi_{\mu'} < \pi/2$ and $3/2\pi \leq \phi_{\mu'} < 2\pi$
- Right (c20s2): $\pi/2 \leq \phi_{\mu'} < 3/2\pi$
- Top (c20s3): $0 \leq \phi_{\mu'} < \pi$
- Bottom (c20s4): $\pi \leq \phi_{\mu'} < 2\pi$

Fig. 5.79 shows the striking impact on the (ϕ_S,ϕ_R)-distribution, when segmenting the detector into left/right and top/bottom parts. The results for the four samples are shown in Fig. 5.80. The mean values of the asymmetries for which the scattered muon is detected in top (c20s3) and bottom (c20s4) part are compatible with each other. However, for left (c20s1) and right (c20s2) the difference is one sigma. Figure 5.82 shows on the left the corresponding pulls between the results of left/right and on the right for top/bottom. In both cases the sigma of the distributions is compatible with one. But as already seen before for left/right the mean value is shifted. For top/bottom it is compatible with zero.

In order to judge if this has to be taken into account in the systematical error, the same test is performed on the Monte Carlo sample. The results are shown in Fig. 5.81. Even larger deviations between the measurements of left/right and top/bottom are observed, which are also clearly visible in the corresponding pull distributions in Fig 5.83. However, the RMS values of the distributions are more narrow than obtained for real data. The largest RMS value of 1.086 will be taken into account in the systematical error:

$$\sigma^{sys} = \sqrt{\mathrm{RMS}^2 - 1} \cdot \sigma^{stat} = 0.42 \cdot \sigma^{stat}.$$

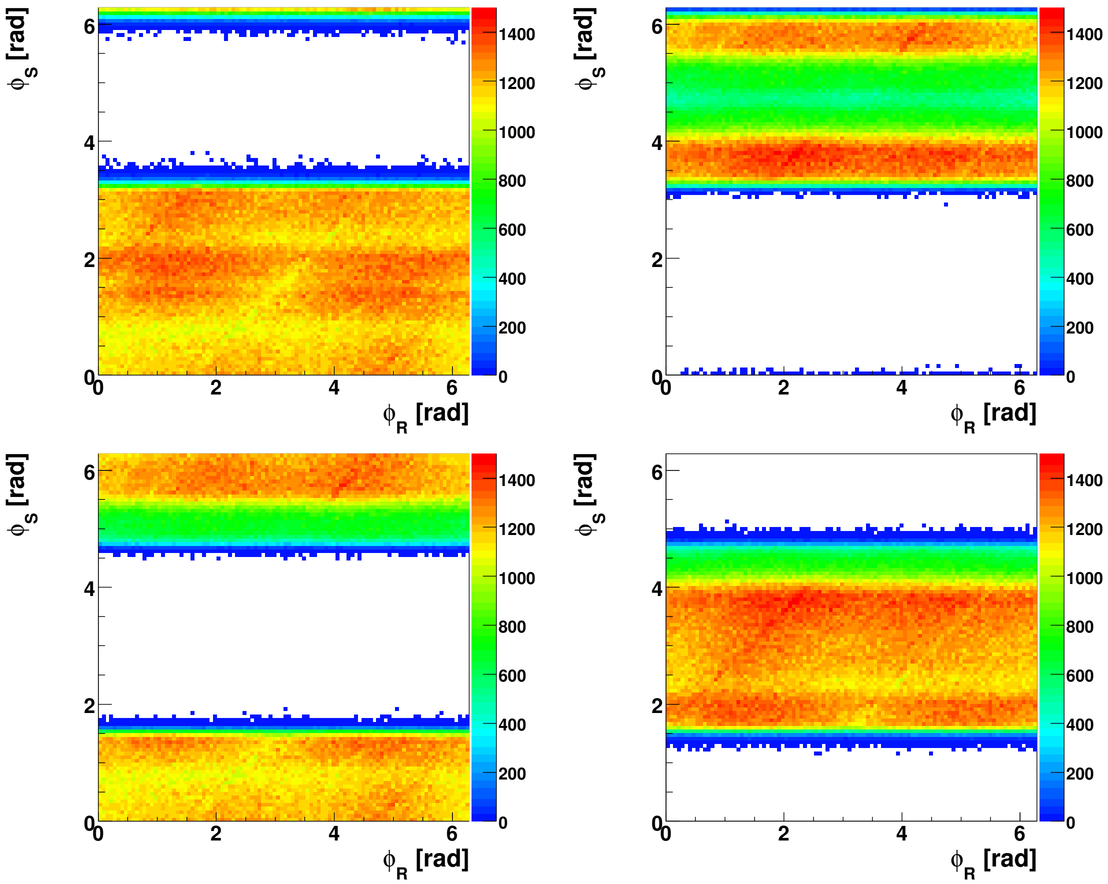

Figure 5.79: ϕ_S versus ϕ_R for various cuts on $\phi_{\mu'}$ in the laboratory frame. Top panel: μ' detected in the left and in the right part, respectively. Bottom panel: μ' detected in the top and in the bottom part, respectively.

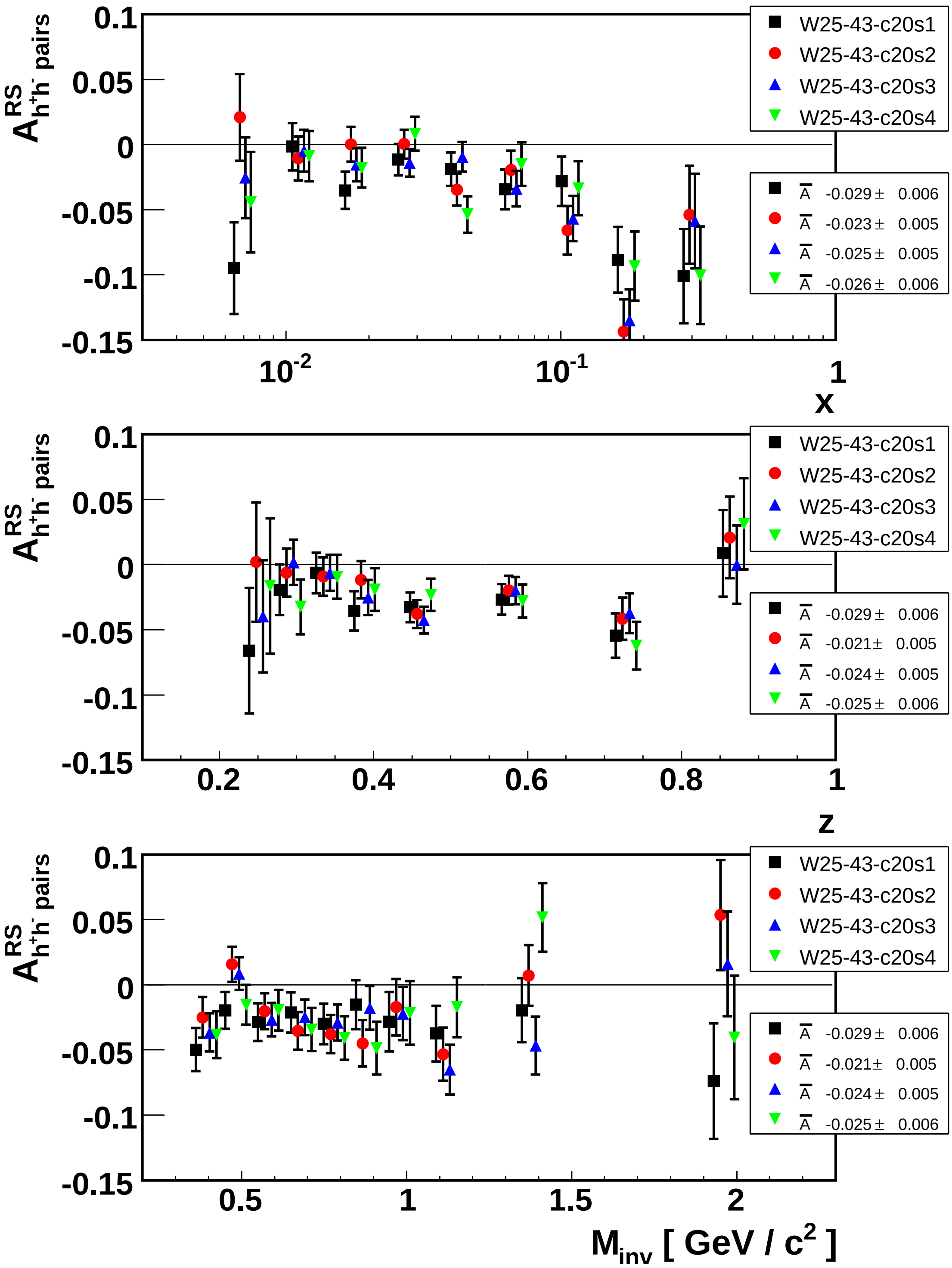

Figure 5.80: RS asymmetries for segmenting the detector in left (c20s1), right (c20s2), top (c20s3) and bottom (c20s4). Mean values, Ā, are given.

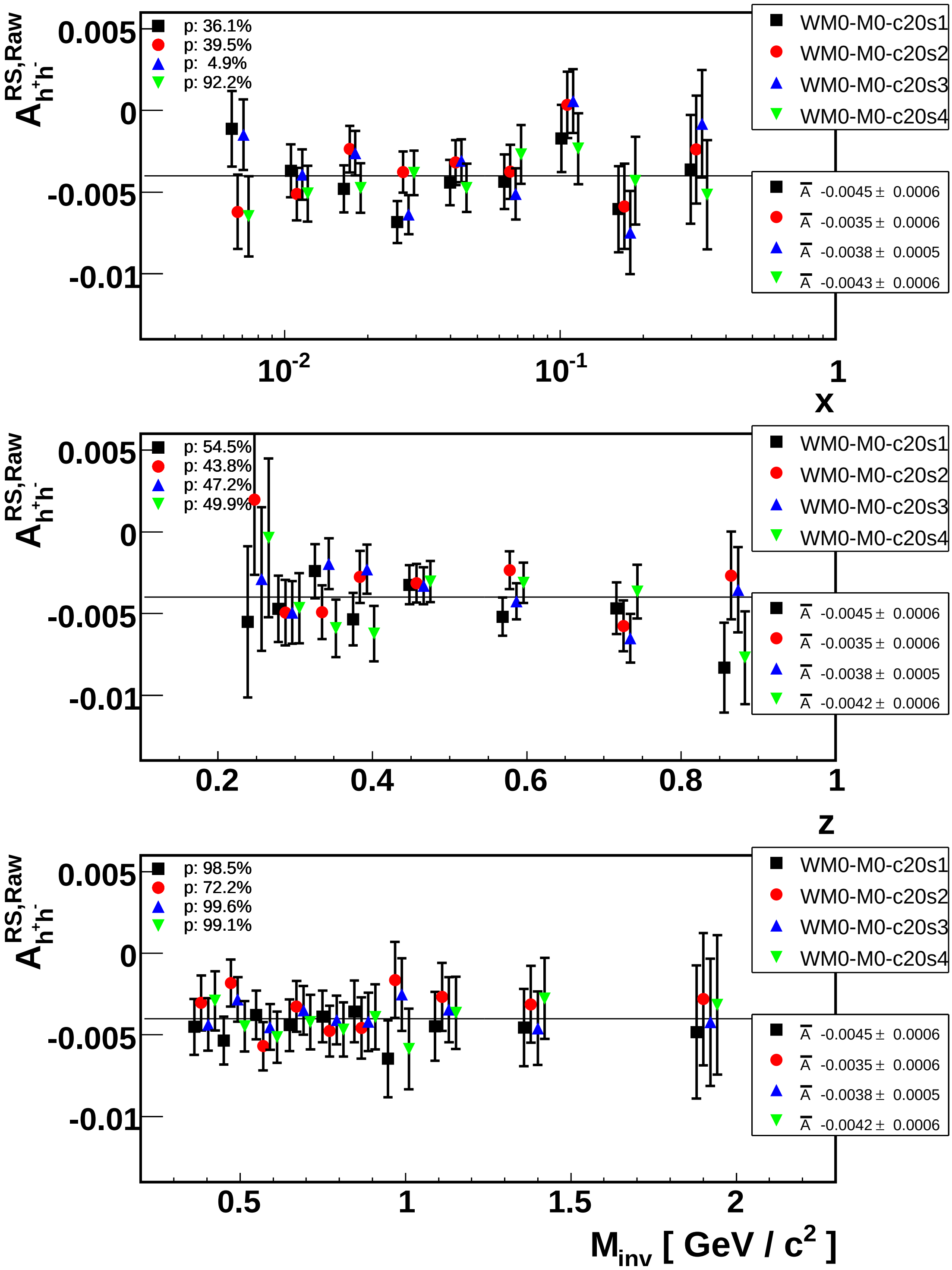

Figure 5.81: Raw RS asymmetries for segmenting the detector in left (c20s1), right (c20s2), top (c20s3) and bottom (c20s4) for Monte Carlo data with generated asymmetries. Mean values, Ā, and probabilities, p, of χ^2 test with respect to $A^{RS}_{MC} = -0.004$ (horizontal lines) are given.

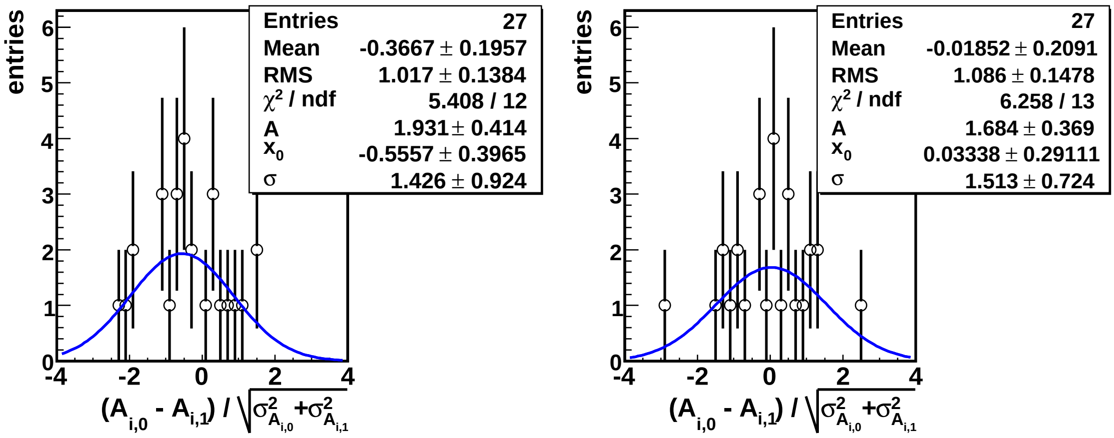

Figure 5.82: Real data. Left: Pulls between μ' detected in left and right half, respectively. Right: Pulls between μ' detected in top and bottom half, respectively.

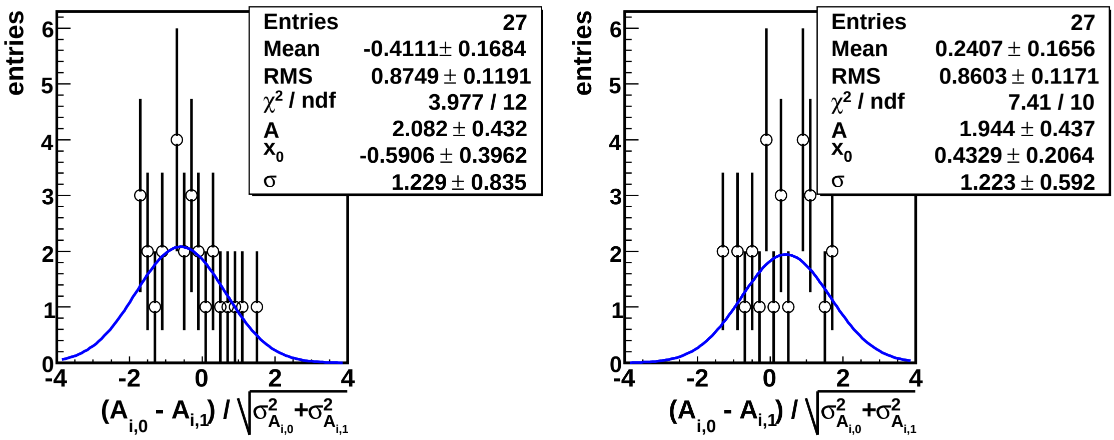

Figure 5.83: Monte Carlo data with generated asymmetries. Left: Pulls between μ' detected in left and right half, respectively. Right: Pulls between μ' detected in top and bottom half, respectively.

Table 5.3: Summary of systematical error of RS asymmetries. The total error is obtained as square root of the quadratic sum.

Type	$\sigma^{sys}/\sigma^{stat}$
estimators	0.04
period compatibility	0.37
False asymmetries	0.44
Single cells	0
Detector segments	0.42
Total	0.71

5.7.8 Summary of Systematical Error

For the evaluation of the systematical error the results as summarized in Tab. 5.3 are taken into account. The final systematical error of 71 % of the statistical error is obtained by assuming uncorrelated errors. Therefore the square root of the quadratic sum is taken. For the value of target polarization an error of 2 % and for the target dilution an error of 1 % is assigned. The square root of the quadratic sum of these two values evaluates to an error of 3 %, which acts as a scale error. Hence the systematical error of the asymmetry A_i in bin i is given by:

$$\sigma_i^{sys} = \sqrt{(0.71 \cdot \sigma_i^{stat})^2 + (0.03 \cdot |A_i|)^2}. \tag{5.50}$$

5.8 Final Results

The final results as a function of x, z and M_{inv}, including the systematical error are shown in Fig. 5.84. The corresponding numerical results as a function of x, z and M_{inv} are listed in Tab. B.1, B.2 and B.3, respectively. The numerical values for the integrated asymmetry, obtained without any binning is shown in Tab. B.4. The mean asymmetry is:

$$A^{RS} = -0.025 \pm 0.004_{stat} \pm 0.003_{sys}.$$

In order to enhance the signal binned in z and M_{inv} a cut on $x > 0.032$ is applied. The results are shown in Fig. 5.85. With respect to Fig. 5.84 the number of bins in z and M_{inv} is reduced to take care of the lower statistics. The distribution in z becomes rather constant, maybe slightly falling. For M_{inv} the amplitude is enhanced in the region of the ρ^0-mass and it is negative over the whole mass range. This rules out the prediction made in [94], where a sign change of the asymmetry around the ρ^0-mass is proposed.

5.8.1 Comparison With Other Experiments and Predictions

The HERMES collaboration measured the RS asymmetry for oppositely charged pion pairs [95]. In Fig. 5.86 the comparison of this measurement with the results of this thesis

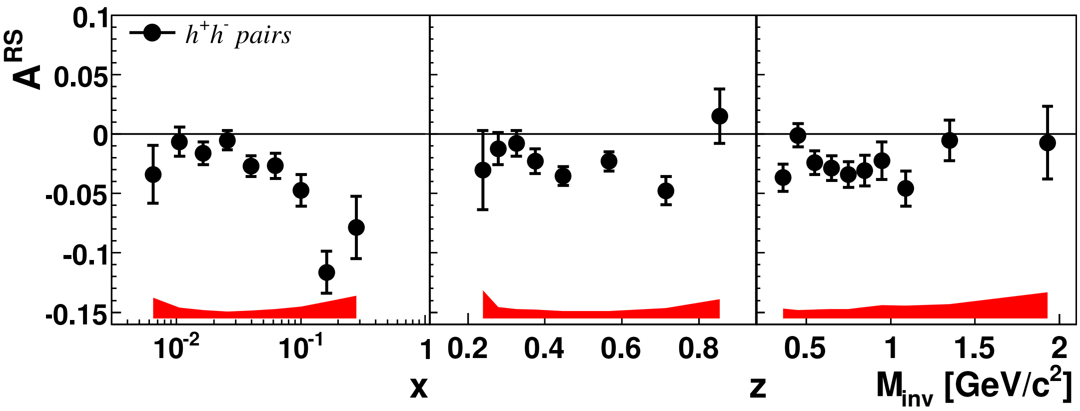

Figure 5.84: Final RS asymmetries as a function of x, z and M_{inv}. The red band indicates the systematical uncertainty.

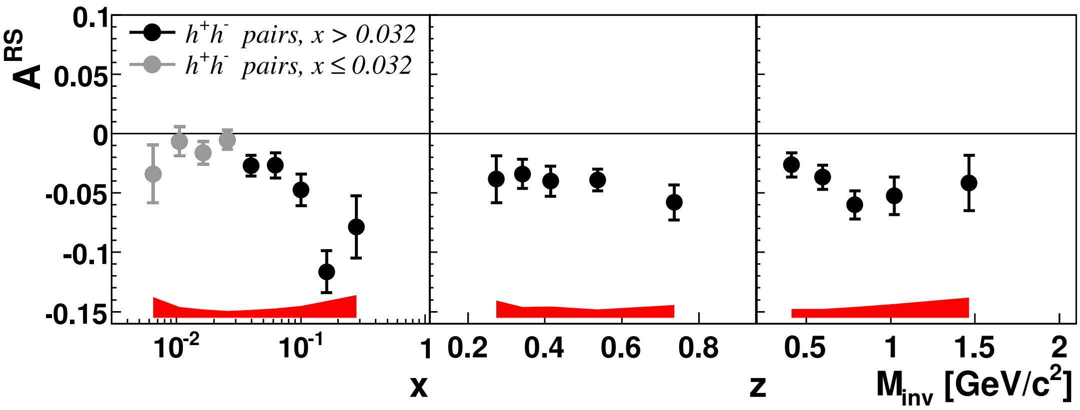

Figure 5.85: Final RS asymmetries for $x > 0.032$ as a function of x, z and M_{inv}. The red band indicates the systematical uncertainty.

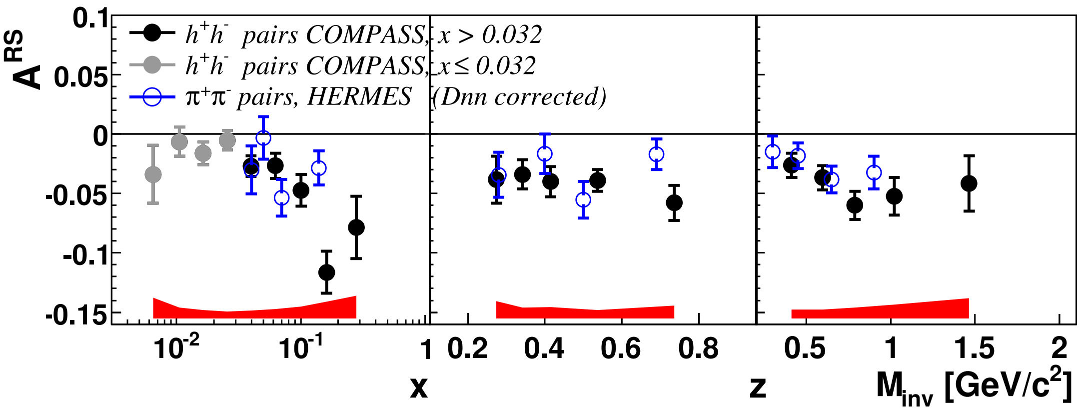

Figure 5.86: Final RS asymmetries as a function of x, z and M_{inv} together with HERMES results [95], which are scaled with $-1/D_{nn}$, as described in the text.

is shown. In order to compare the results, the HERMES values are scaled with $-1/D_{nn}$. The minus sign accounts for the different definition of Φ_{RS} and the transverse spin transfer coefficient D_{nn} accounts for the different y-kinematics of the two experiments. The D_{nn} values for each bin are approximated by using the corresponding mean values of y taken from [96]. Quite striking is the difference in the covered x-range between the two measurements. COMPASS reaches lower as well as larger x-values. Comparing the results binned in x one obtains a quite good agreement in the overlap region. For the comparison as a function of z and M_{inv} a cut of $x > 0.032$ is applied. Again the results of both measurements are quite compatible. Noticeable is the fact that, due to the larger beam momentum, COMPASS reaches higher invariant masses than HERMES (160 GeV/c compared to 27.5 GeV/c).

Predictions have been made for COMPASS by Bacchetta et al. [97], both for the whole and the $x > 0.032$ restricted x-range. These are based on the transversity distribution from Anselmino et al. [98] and on the fit to the HERMES data [99]. The comparison is shown in Fig. 5.87 and Fig. 5.88 respectively. The data overshoots the predictions by about a factor of three. This is interesting since the model for the polarized DiFF has been scaled by a factor of three to describe the HERMES data. In addition the prediction as a function of the invariant mass M_{inv}, does not fit the shape of the data for masses greater than 1 GeV/c^2, because those contributions are not yet considered in the model of the DiFF. This is at best seen in Fig. 5.88, where the measured asymmetries stay at the same level, but the size of the prediction decreases to zero.

In Fig. 5.89 the results are shown with predictions made by Ma et al. [100]. The two curves correspond to two different models for the transversity distribution function, which however, in the x-range covered by the data, results in almost the same effect. The model for the polarized DiFF is the one of Bacchetta and Radici [101] but without any scaling. As a function of x the agreement is rather good. But as discussed before, as a function of M_{inv} the description of the polarized DiFF does not fit the data.

Both predictions are based on models of the polarized DiFF, since no experimental data was available at that time. Very recently the Belle collaboration has presented first results of their measurement of the polarized DiFF [102]. They report on large asymmetries, which rise with z. Furthermore they report, that the measured dependence of M_{inv} does not match the model predictions. The asymmetries rise towards the mass of the ρ^0 and stay large with increasing mass. This qualitatively coincides with the measured asymmetry A^{RS} of this thesis, shown in Fig. 5.88, which shows the same behavior.

In the years 2002, 2003 and 2004 COMPASS took data scattering off transversely polarized deuterons. From this data the RS asymmetries for unidentified h^+h^--pairs and identified $\pi^+\pi^-$, K^+K^-, π^+K^- and $K^+\pi^-$-pairs have been extracted [103, 104, 105]. In addition also different charge combinations have been analysed, considering the two most energetic hadrons in each event. All asymmetries found to be small and compatible with zero within the statistical errors. Hence for deuteron the transversity distribution must be small or even vanishing due to isospin symmetry, because the proton results and the recent Belle results, confirmed the existence of a non-zero polarized interference fragmentation function.

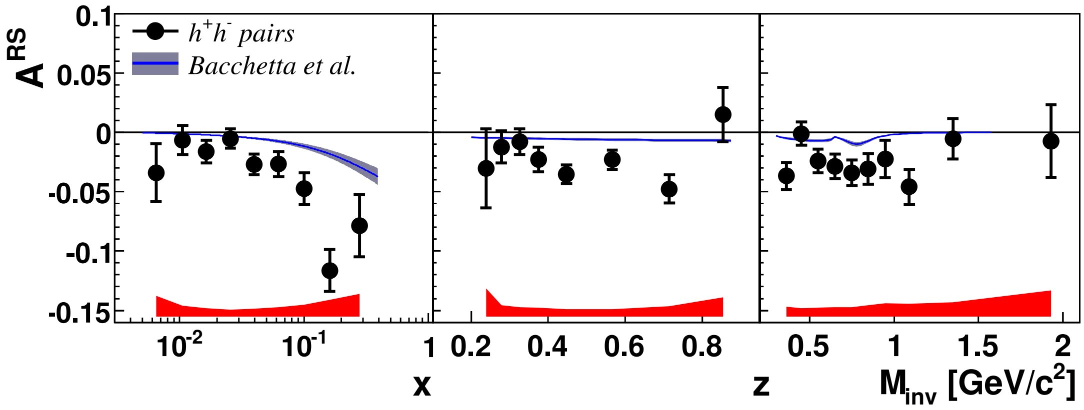

Figure 5.87: Final RS asymmetries as a function of x, z and M_{inv} together with a prediction from Bacchetta et al. [97].

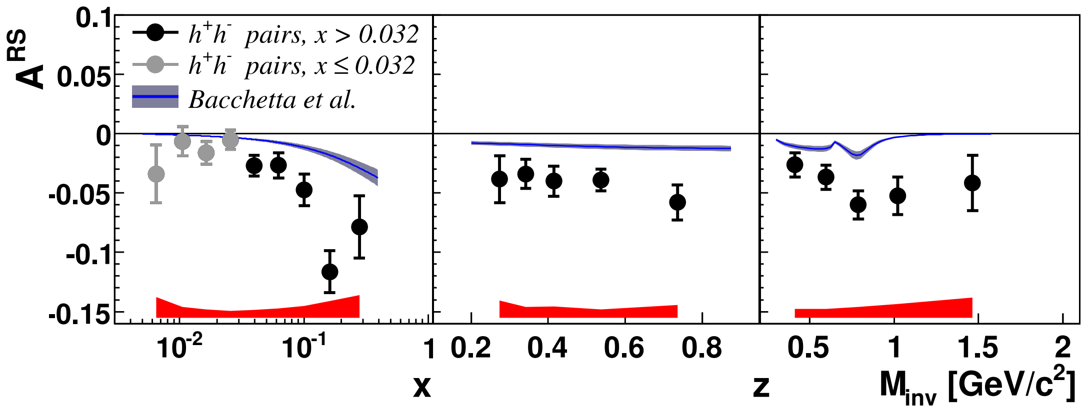

Figure 5.88: Final RS asymmetries for $x > 0.032$ as a function of x, z and M_{inv} together with a prediction from Bacchetta et al. [97].

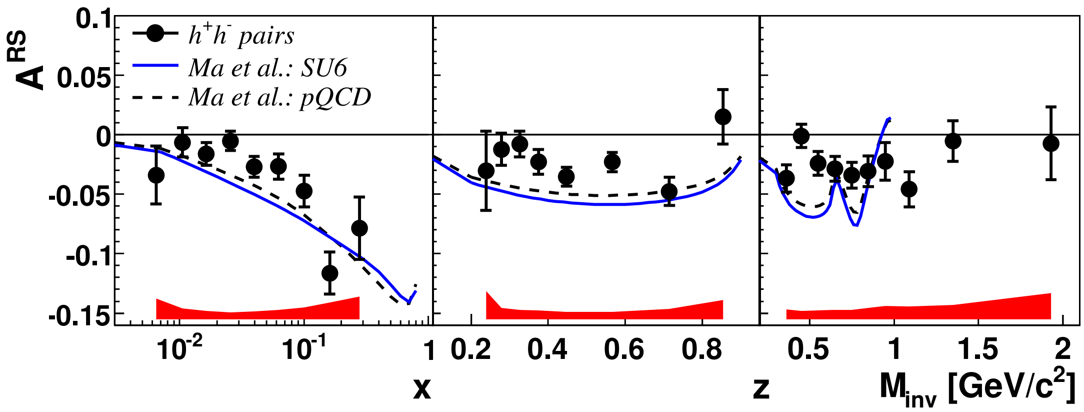

Figure 5.89: Final RS asymmetries as a function of x, z and M_{inv} together with a prediction from Ma et al. [100].

Now, with the measurement of the polarized DiFF at Belle and the measurement of the RS asymmetries at COMPASS and HERMES all informations are finally available for the extraction of transversity, which would be an ultimate cross-check of the determination via single hadrons, as will be discussed in Sec. 6.6.1. A very interesting aspect is the comparison of the results with the results of the Collins asymmetry, which will be analysed in Chapter 6. The final Collins asymmetries are shown in Fig. 6.51. The trend in x is the same as for the hadron pairs. However, the mean Collins asymmetries are approximately only half the size of the RS asymmetries, indicating the larger analyzing power of the polarized dihadron interference fragmentation function with respect to the Collins fragmentation function.

6. Single Hadron Asymmetries

6.1 General Framework

As mentioned in Sec. 2.3, in leading twist eight transverse spin dependent asymmetries are possible in the SIDIS cross-section. Two of them, the Collins and the Sivers asymmetry will be studied in this thesis. Those have been discussed in Sec. 2.3.3 and 2.3.4, respectively.

The Collins asymmetry gives access to the measurement of the transversity distribution. According to Collins the fragmentation of a transversely polarized quark into an unpolarized hadron results in a sine modulation in $\Phi_{Collins} = \phi_h + \phi_S - \pi$ and the number of produced hadrons N can be written as:

$$N(\Phi_{Collins}) \propto \left(1 + f \cdot P_T \cdot D_{nn} \cdot A^{Collins} \cdot \sin \Phi_{Collins}\right). \tag{6.1}$$

As for the two hadron pairs the factor $f \cdot P_T \cdot D_{nn}$ is omitted in the fit and the result is afterwards corrected with the mean value $1/\langle f \cdot P_T \cdot D_{nn}\rangle$. The measured asymmetry is proportional to the convolution of the transversity distribution and the Collins FF

$$A^{Collins} = \frac{\sum_q e_q^2 \cdot \mathcal{I}\left[\Delta_T q(x, \boldsymbol{k}_T^2) \Delta_T^0 D_q^h(z, \boldsymbol{P}_{h\perp}^2)\right]}{\sum_q e_q^2 \cdot \mathcal{I}\left[q(x, \boldsymbol{k}_T^2) D_q^h(z, \boldsymbol{P}_{h\perp}^2)\right]}. \tag{6.2}$$

The Sivers asymmetry results in a sine modulation in $\Phi_{Sivers} = \phi_h - \phi_S$ and the number of produced hadrons is:

$$N(\Phi_{Sivers}) \propto \left(1 + f \cdot P_T \cdot A^{Sivers} \cdot \sin \Phi_{Sivers}\right). \tag{6.3}$$

Again $f \cdot P_T$ is not included in the fit but the extracted 'raw' asymmetry is corrected with the mean value $1/\langle f \cdot P_T\rangle$. The asymmetry is proportional to the convolution of the Sivers function and the unpolarized fragmentation function

$$A^{Sivers} = \frac{\sum_q e_q^2 \cdot \mathcal{I}\left[\Delta_0^T q(x, \boldsymbol{k}_T^2) D_q^h(z, \boldsymbol{P}_{h\perp}^2)\right]}{\sum_q e_q^2 \cdot \mathcal{I}\left[(x, \boldsymbol{k}_T^2) D_q^h(z, \boldsymbol{P}_{h\perp}^2)\right]}. \tag{6.4}$$

Since the Collins and the Sivers asymmetry are orthogonal to each other in ϕ_h and ϕ_S, both can be determined independently from the same dataset. As both asymmetries depend on two azimuthal angles, like the asymmetry for the two hadron pairs, exactly the same concepts, as described in Sec. 5.2 and Sec. 5.4 can be used to extract the asymmetries.

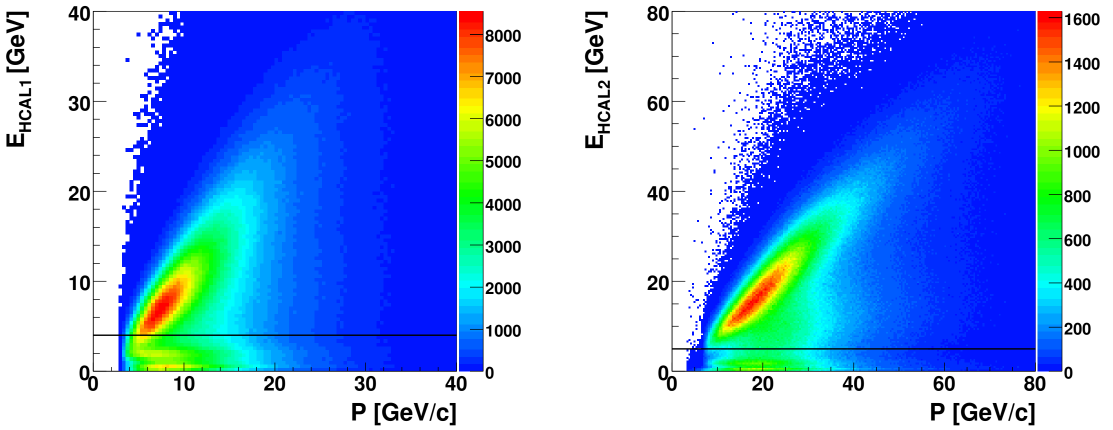

Figure 6.1: Cluster energy versus momentum for HCAL1 (left) and HCAL2 (right) for the single hadron sample. The black lines indicates the cuts on the deposited energies.

Since the transversity distribution and the Sivers function depend on x and the Collins and the unpolarized FF depend on z and p_T the asymmetries will be evaluated in bins of those variables. As for the hadron pairs a multidimensional binning in all three variables is not possible due to limited statistics. In the following analysis nine bins in x and p_T and eight bins in z are used. The chosen binning is quoted in App. C.1.

6.2 Data Selection

For the selection of beam muon, scattered muon, primary vertex and DIS events the same cuts are applied as for the hadron pairs (see Sec. 5.3.1 - 5.3.4). The hadron selection is the same as described in Sec. 5.3.5, except for the cut on x_F, z and the energy cuts for associated clusters in HCAL1 and HCAL2. For the single hadrons no cut on x_F is performed and for the energy fraction it is required that $z > 0.2$ to avoid hadrons from the target fragmentation region. Due to this higher cut the energy versus momentum distributions in HCAL1 and HCAL2 change and cutting particles with $E_{HCAL1} < 4\,\text{GeV}$ and $E_{HCAL2} < 5\,\text{GeV}$ is appropriate to remove muons, as can be seen in Fig. 6.1. In order to have a well defined hadron plane spanned by the virtual photon and the hadron and thus a good definition of the relevant azimuthal angle ϕ_h, the transverse momentum p_T with respect to the virtual photon has to be larger than $0.1\,\text{GeV}/c$. This cut removes also a significant amount of electrons from the sample.

6.2.1 Final Statistics

The final number of DIS events and the number of charged hadrons for the 12 weeks of data taking are listed in Tab. 6.1. In total $23 \cdot 10^6$ DIS events were selected. This corresponds to $15 \cdot 10^6$ positive hadrons and $12 \cdot 10^6$ negative hadrons contributing to the analysis, which means on average about 1.18 charged hadrons could be reconstructed per event. In addition the number of identified charged pions and kaons are given. For the identification the same cuts as described in Sec. 5.3.8 are applied. On average about 70 % of the hadrons could be identified as pions and about 11 % as kaons.

Table 6.1: Number of charged hadrons, identified charged pions and kaons for the 12 weeks of data taking.

Week	DIS events	h^+	h^-	π^+	π^-	K^+	K^-
25	1773995	1155164	929213	785264	689398	151074	95555
26	1962323	1279770	1026048	869214	761884	166635	104557
27	1297646	857331	676858	564012	488597	109077	67929
28	2284820	1502879	1197192	997408	873108	184702	114977
30	2344325	1541184	1222422	1027079	893658	186824	115890
31	3261030	2146183	1698773	1430158	1241241	260739	161319
39	2505027	1643663	1293087	1082822	939699	204659	126385
40	1699194	1119816	872793	738051	634066	139274	84815
41	2284931	1501745	1183241	992452	863006	191835	117600
42a	1662611	1088920	865659	726218	636030	134995	83499
42b	962823	630406	500693	420607	368161	77432	47621
43	1050034	689236	543618	459843	399763	85427	52075
Sum	23088759	15156297	12009597	10093128	8788611	1892673	1172222

6.3 Asymmetries

The final results for the Collins asymmetry of charged hadrons are shown in Fig. 6.2. For positive hadrons the asymmetry is negative and for negative hadrons it is positive. For both charges the size of the asymmetry increases with x and is compatible in their strengths. These results confirm nicely the expectations of a simple interpretation of the Collins asymmetry, discussed in Sec. 2.3.3.1.

The final results for the Sivers asymmetry are shown in Fig. 6.3. For positive hadrons a significant positive asymmetry is present. The result for negative hadrons is small and within statistical errors compatible with zero. So far only statistical errors are shown. In the next sections the systematical error of the results will be investigated. A detailed discussion of the results will be given in Sec. 6.6.

6.4 Monte Carlo Studies

The aim of these studies is to investigate how sensitive the measurements of Collins and Sivers asymmetries are with respect to the used extraction method and to changes of the acceptance of the detector. This is of particular importance for the Sivers asymmetry, since here a deviation of the results between first half and second half of data taking is present, as will be discussed in Sec. 6.5.2.

For the tests the same Monte Carlo sample, which was used in Sec. 5.5 to study systematics of oppositely charged hadron pairs, is used. After applying all cuts the sample contains in total $27.6 \cdot 10^6$ SIDIS events, corresponding to $18.0 \cdot 10^6$ positive and $14.7 \cdot 10^6$ negative hadrons. Hence on average the multiplicity of charged hadrons is 1.18 per event, which perfectly agrees with the multiplicity obtained for real data, given in Sec. 6.2.1.

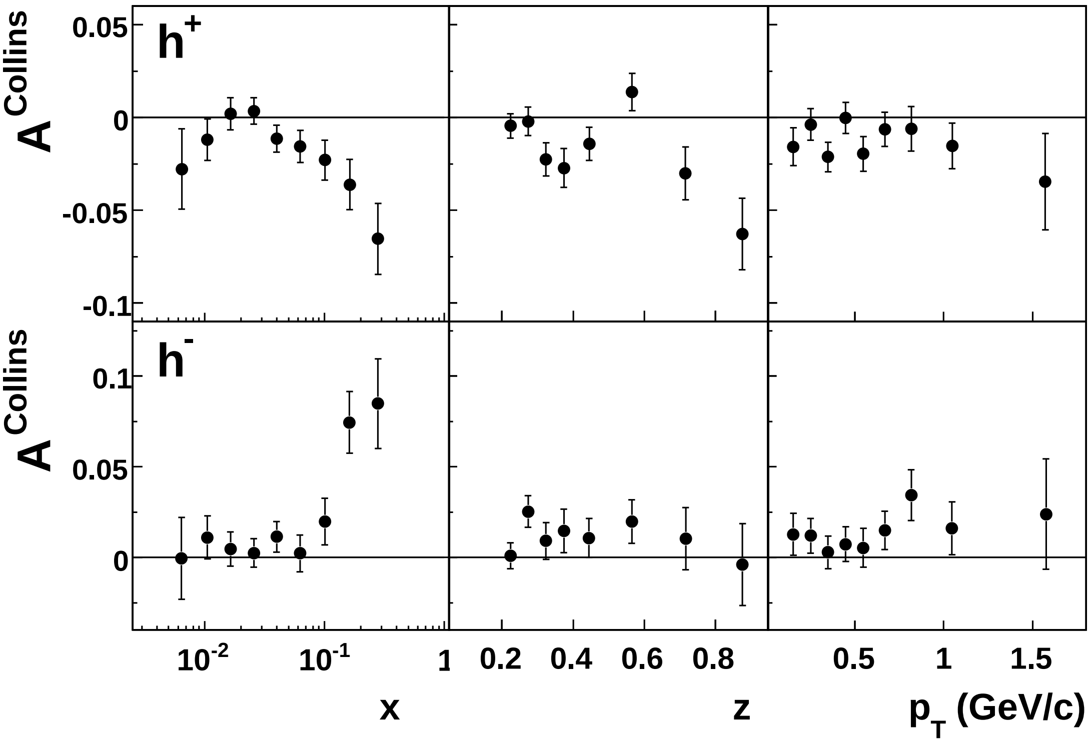

Figure 6.2: Collins asymmetries as a function of x, z and p_T, for positive hadrons (top) and negative hadrons (bottom). Only statistical errors are shown.

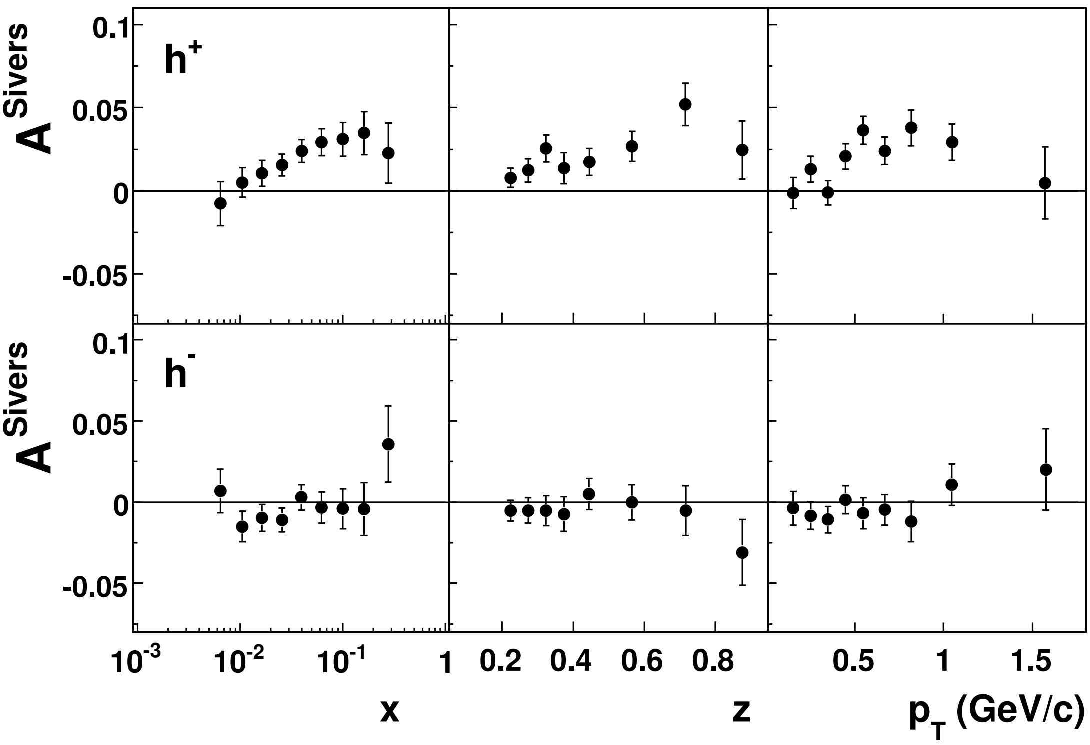

Figure 6.3: Sivers asymmetries as a function of x, z and p_T, for positive hadrons (top) and negative hadrons (bottom). Only statistical errors are shown.

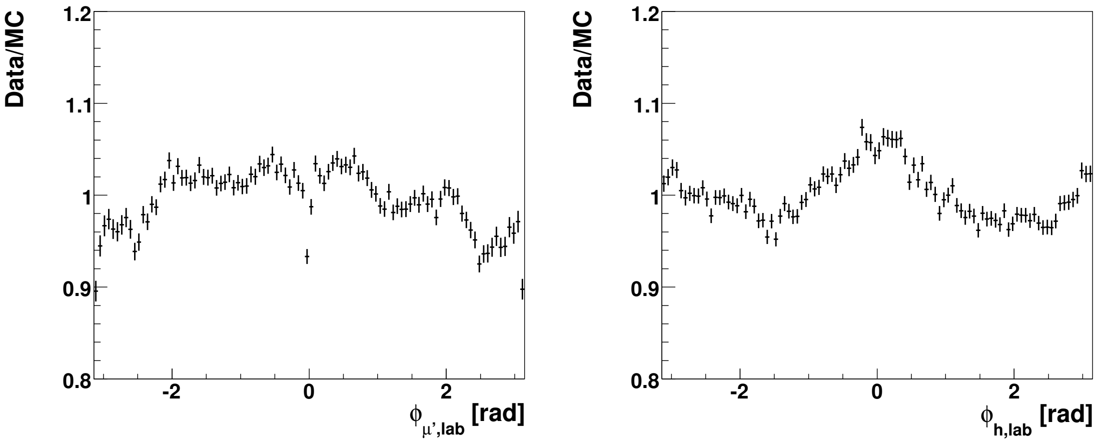

Figure 6.4: Ratio of real data and Monte Carlo data for single hadrons. Left: azimuthal angle of scattered muon. Right: azimuthal angle of hadrons.

In Fig. 6.4 the comparison of real data (week 30) and Monte Carlo data for the azimuthal angle of scattered muon $\phi_{\mu',lab}$ and for charged hadrons $\phi_{h,lab}$ is illustrated. The agreement is better than $\pm 10\,\%$. Hence it is appropriate to use it for acceptance related studies.

The Collins and Sivers asymmetries extracted from the sample without generated asymmetries as a function of x extracted with the unbinned maximum likelihood method are shown in Fig. 6.5 and Fig. 6.6, respectively. Both asymmetries for both charges are compatible with zero.

The extracted results from the data set with generated asymmetries of $A_{MC}^{Collins} = -0.004$ for Collins and $A_{MC}^{Sivers} = 0.006$ for Sivers are shown for all four extraction methods as a function of x, z and p_T in Fig. 6.7 for positive and in Fig. 6.8 for negative hadrons. For Sivers positive and negative hadrons the results are shown in Fig. 6.9 and Fig. 6.10, respectively. The results agree well with the generated ones. However, the results extracted with the one dimensional ratio method (1D DR) for positive hadrons are $2\,\sigma$ away from the generated asymmetries, demonstrating again the limits of this method.

The pulls between one dimensional ratio method and unbinned maximum likelihood are shown in Fig. 6.11, for two dimensional ratio method and unbinned maximum likelihood in Fig. 6.12 and for binned and unbinned maximum likelihood method in Fig. 6.13. The pulls for Sivers of both two dimensional binned methods (2D DR and MF RA) with respect to the unbinned method show mean values compatible with zero, whereas the distributions for Collins are shifted up to 0.4. For the pulls of the one dimensional ratio method with respect to the unbinned method the situation in particular for Sivers is worse. This is again, as already seen for the hadron pairs in Sec. 5.5.1, caused by the convolution of Sivers and Collins asymmetries with the COMPASS acceptance, which cannot be disentangled by the one dimensional ratio method.

For the following tests the results as a function of x, for standard acceptance and generated asymmetries are summarized for Collins in Fig. 6.14 and for Sivers in Fig. 6.15. The four graphs from top to bottom show raw asymmetries, raw Ttest and the false raw asym-

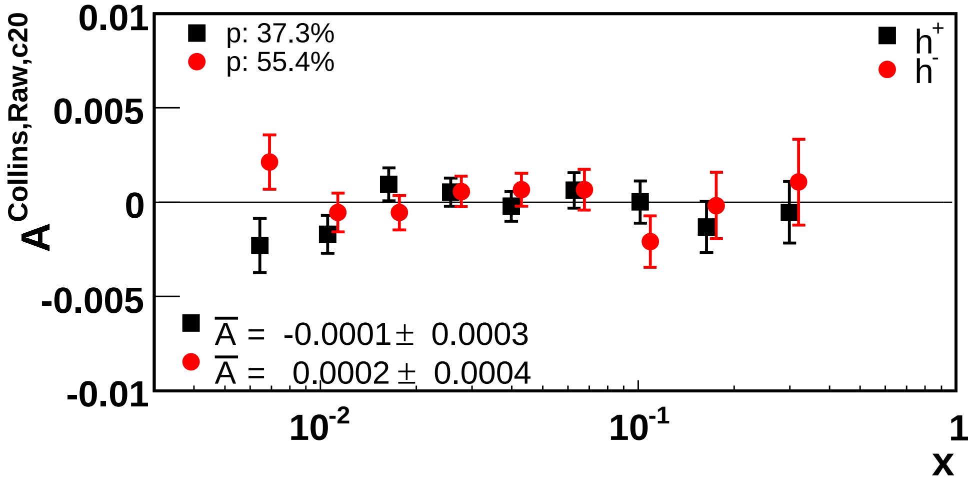

Figure 6.5: Raw Collins asymmetries for positive and negative hadrons for Monte Carlo Data without generated asymmetries extracted with UB SA as a function of x. Mean asymmetries, $\bar{\mathrm{A}}$, and probabilities, p, of χ^2 test with respect to $A_{MC}^{Collins} = 0$ are given.

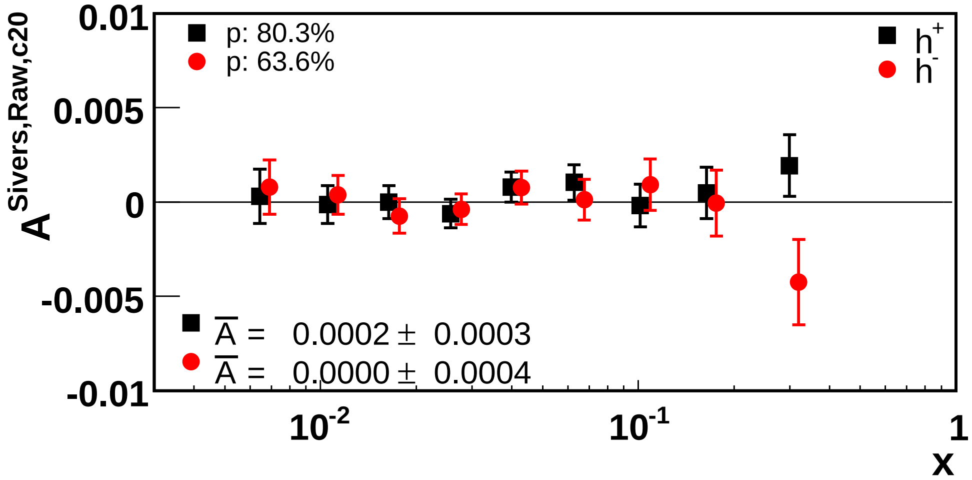

Figure 6.6: Raw Sivers asymmetries for positive and negative hadrons for Monte Carlo Data without generated asymmetries extracted with UB SA as a function of x. Mean asymmetries, $\bar{\mathrm{A}}$, and probabilities, p, of χ^2 test with respect to $A_{MC}^{Sivers} = 0$ are given.

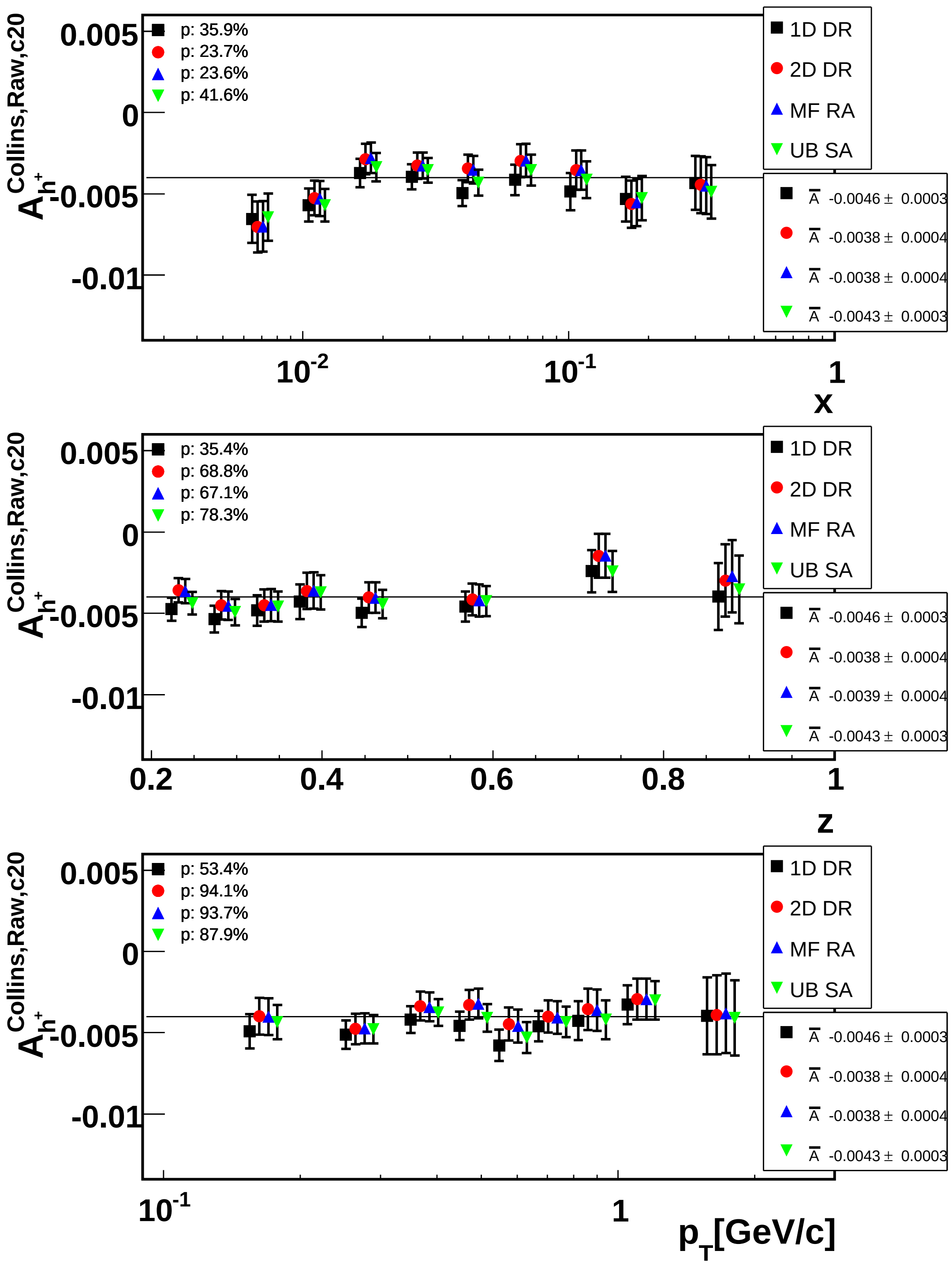

Figure 6.7: Raw Collins asymmetries for positive hadrons for Monte Carlo Data with generated asymmetries as a function of x, z and p_T. Mean asymmetries, $\bar{\text{A}}$, and probabilities, p, of χ^2 test with respect to $A_{MC}^{Collins} = -0.004$ (horizontal lines) are given.

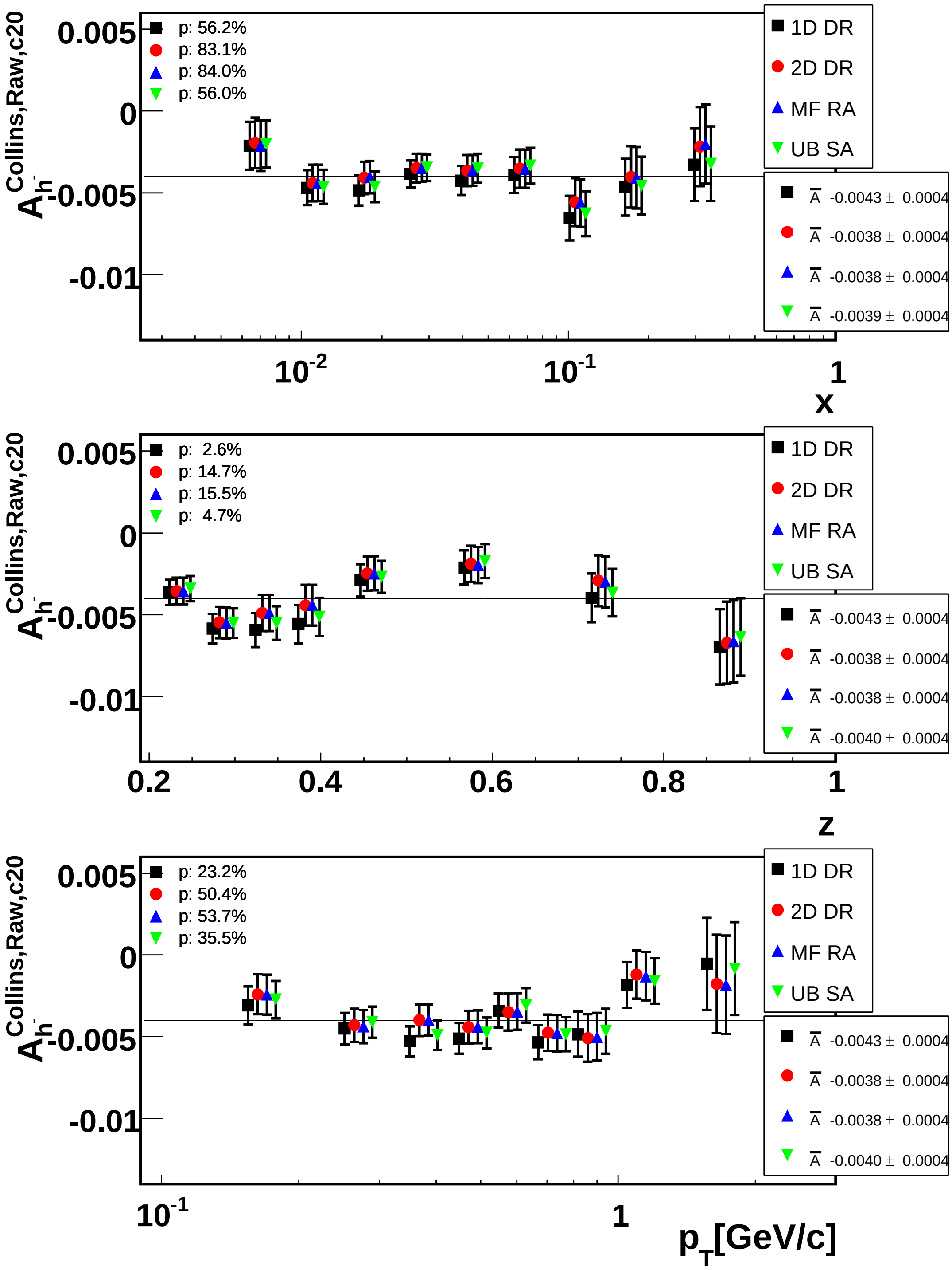

Figure 6.8: Raw Collins asymmetries for negative hadrons for Monte Carlo Data with generated asymmetries as a function of x, z and p_T. Mean asymmetries, Ā, and probabilities, p, of χ^2 test with respect to $A_{MC}^{Collins} = -0.004$ (horizontal lines) are given.

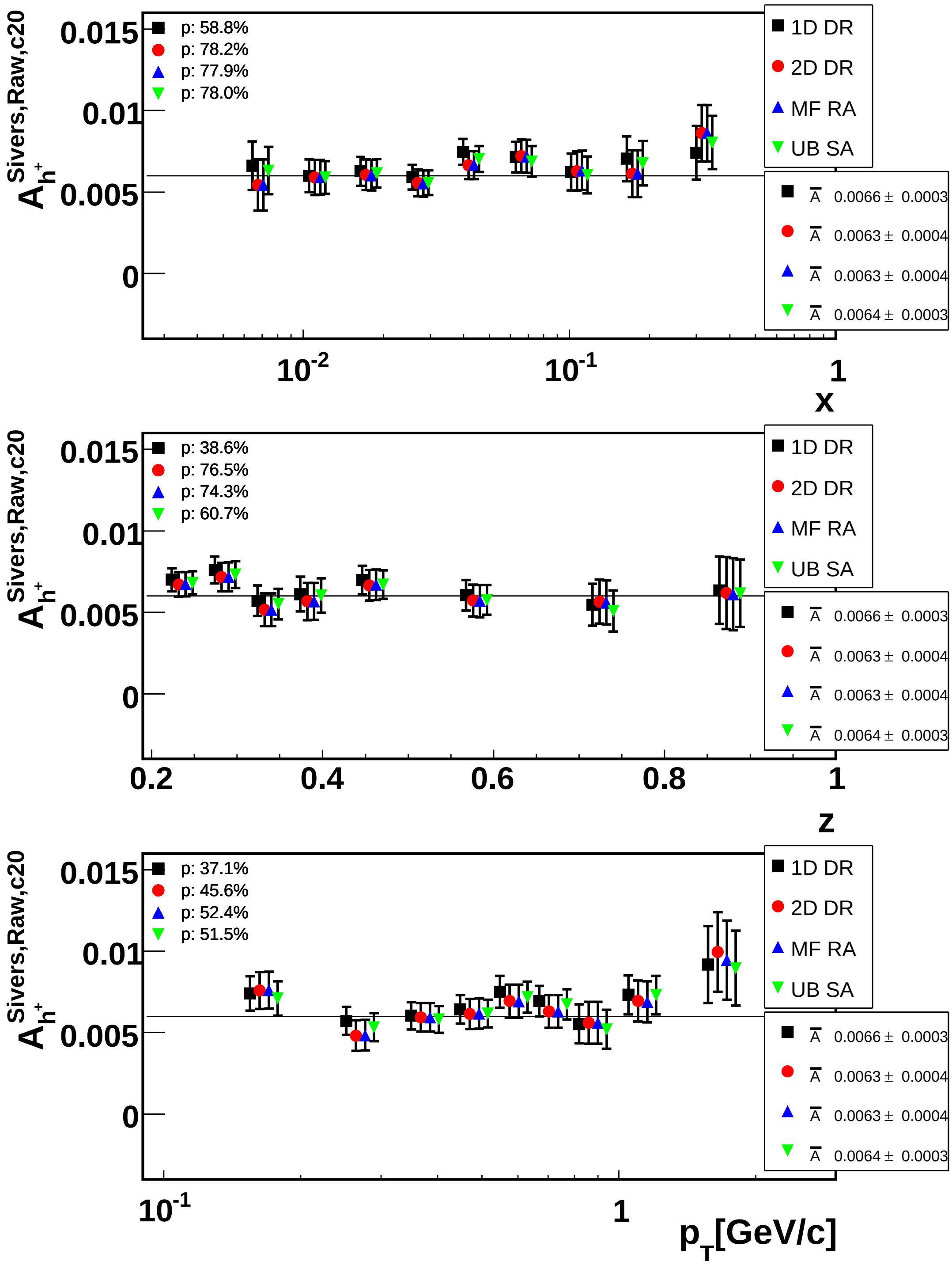

Figure 6.9: Raw Sivers asymmetries for positive hadrons for Monte Carlo Data with generated asymmetries as a function of x, z and p_T. Mean asymmetries, Ā, and probabilities, p, of χ^2 test with respect to $A_{MC}^{Sivers} = 0.006$ (horizontal lines) are given.

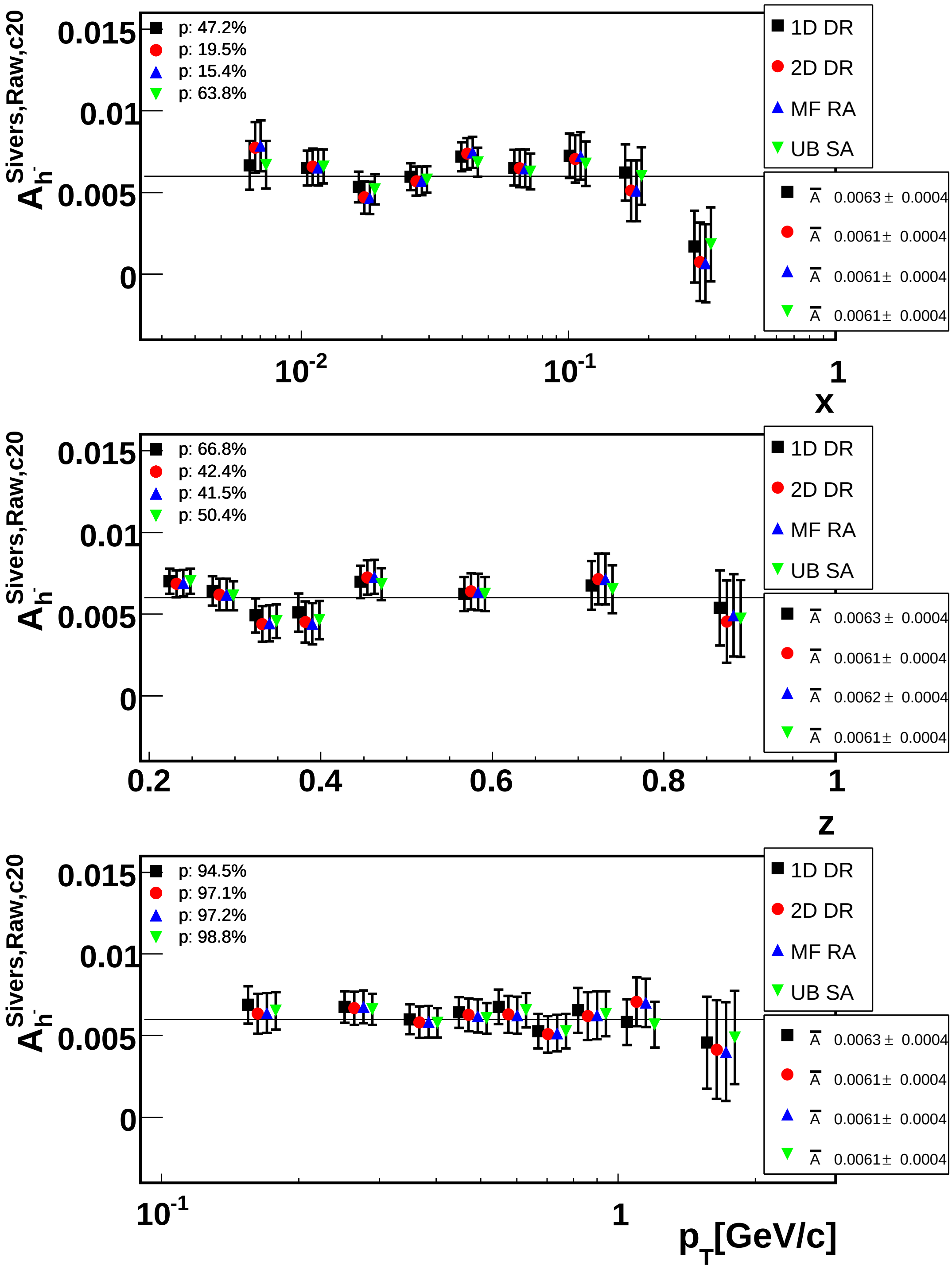

Figure 6.10: Raw Sivers asymmetries for negative hadrons for Monte Carlo Data with generated asymmetries as a function of x, z and p_T. Mean asymmetries, $\bar{\mathrm{A}}$, and probabilities, p, of χ^2 test with respect to $A_{MC}^{Sivers} = 0.006$ (horizontal lines) are given.

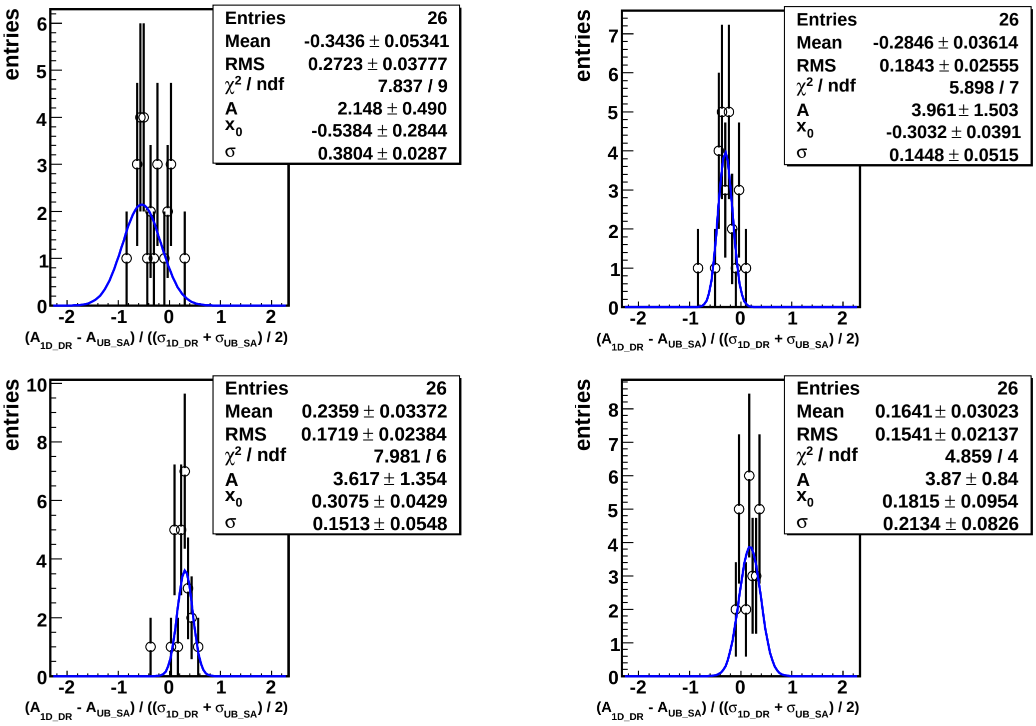

Figure 6.11: Pulls between results of 1D ratio method and unbinned maximum likelihood for Monte Carlo data with generated asymmetries. For Collins on top, for Sivers on bottom. On the left for positive and on the right for negative hadrons.

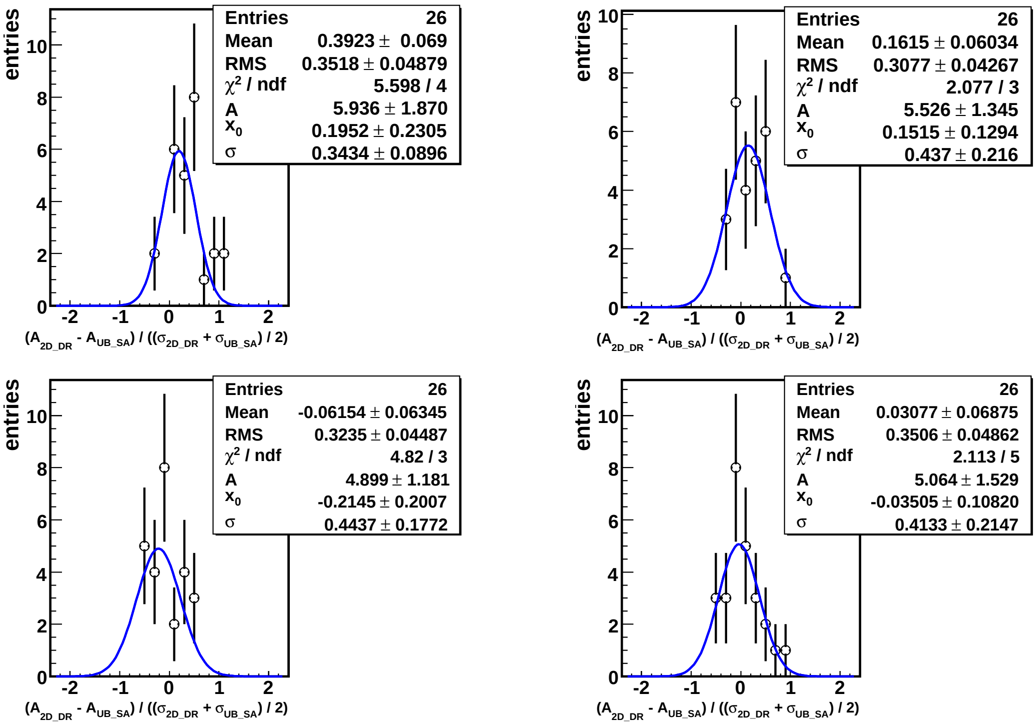

Figure 6.12: Pulls between results of 2D ratio method and unbinned maximum likelihood for Monte Carlo data with generated asymmetries. For Collins on top, for Sivers on bottom. On the left for positive and on the right for negative hadrons.

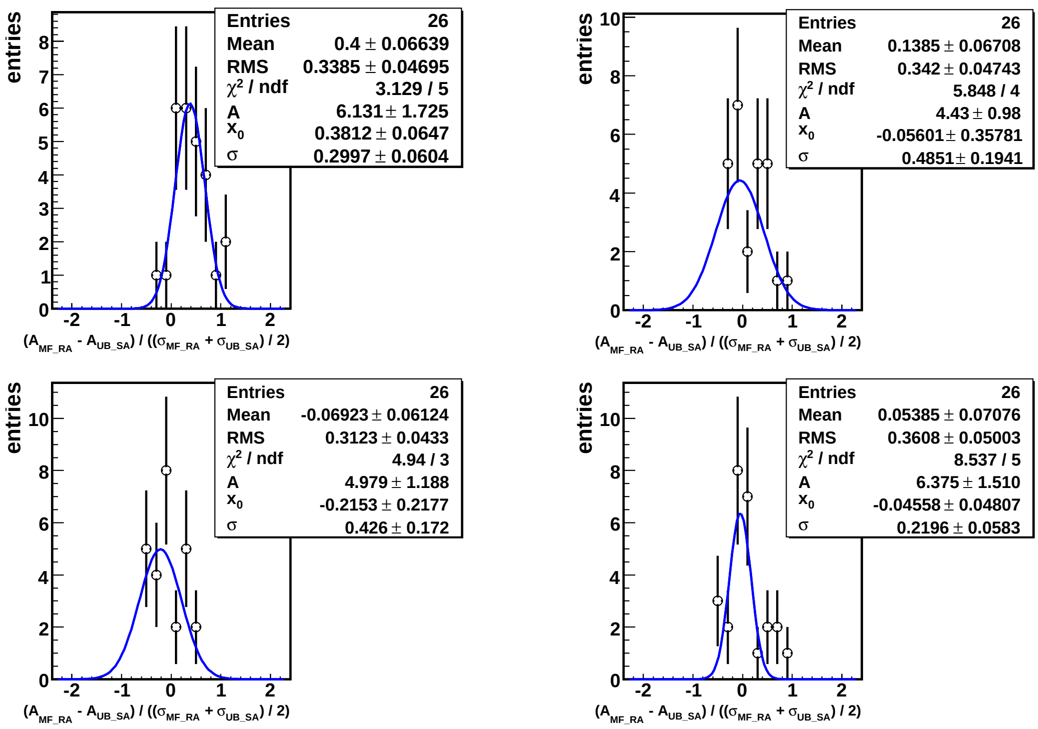

Figure 6.13: Pulls between results of binned and unbinned maximum likelihood for Monte Carlo data with generated asymmetries. For Collins on top, for Sivers on bottom. On the left for positive and on the right for negative hadrons.

metries $A^{(c2-c3)/2}$ and $A^{(c2+c3)/2}$. For both asymmetries Ttest and false asymmetries are compatible with zero. It is noticeable, that the fluctuations of the false asymmetries are uncorrelated to the fluctuations of the real asymmetries. On these results will be referred in Sec. 6.5, when investigating the systematical error of the single hadron results.

6.4.1 Simulation of Changes in Detector Acceptance

As for the hadron pairs (see Sec. 5.5.3) it is studied, if a change in acceptance, between samples with opposite target polarization can cause false asymmetries. Here, this question is even more relevant, since for the Sivers asymmetry of positive hadrons, the results between first half of data taking and second half of data taking differ, as will be discussed in Sec. 6.5.2. The second point is to verify the relevance of the Ttest, again in particular for the Sivers asymmetries, because here huge effects for positive hadrons in the single weeks are present, as will be discussed in Sec. 6.5.4.

For real data the projections on X- and Y-coordinates of the ratio of extrapolated scattered muon tracks to $Z = 600\,\text{cm}$ of the 'total' data set $+--+$ and $-++-$ is shown in Fig. 6.16. On the left weighted with positive hadron and on the right weighted with negative hadron multiplicities, meaning that for each positive/negative hadron the corresponding μ' is considered. In Fig. 6.17 the projection of the ratio of charged hadrons tracks is shown. The distributions for positive and negative hadrons look pretty similar and all deviations are in the order of few percent.

The results obtained for changes only in scattered muon and only in hadron acceptance, as they were performed in Sec. 5.5.3 for the hadron pairs, are omitted, because no systematics could be found. Hence only studies, in which both acceptances have changed will be presented. For the following tests the results for the sample with generated asymmetries of $A_{MC}^{Collins} = -0.004$ and $A_{MC}^{Sivers} = 0.006$ are shown.

Changes in Muon and Hadron Acceptance

The following scenario is simulated

- Scenario 7: 10 % inefficiency in period $+--+$ for scattered muon and hadron tracks with: $20\,\text{cm} < X < 260\,\text{cm}$ and $-240\,\text{cm} < Y < 240\,\text{cm}$.

The results for this scenario are shown in Fig. 6.18. From top to bottom are shown as a function of x for the Collins asymmetry: Raw asymmetries, raw Ttest and the false raw asymmetries $A^{(c2-c3)/2}$ and $A^{(c2+c3)/2}$. The same quantities but for Sivers are shown in Fig. 6.19. Both asymmetries are extracted correctly, however the Ttest shows significant deviations from zero. In particular for Sivers the deviations are huge. Looking at the false asymmetries in the two bottom plots one recognizes for Collins for negative hadrons deviations from zero. These deviations are even more striking for the Sivers false asymmetries. In summary one has to conclude, that for this scenario neither Ttest, nor false asymmetries can be used to correctly estimate the systematical error of the real asymmetries. In particular to incorporate the Ttest results would dramatically overestimate the systematical error.

The same test is repeated but with the additional requirement that the inefficient region in the acceptance is only seen by tracks whose primary vertices are lying in the first target cell, which explicitly breaks the reasonable assumption.

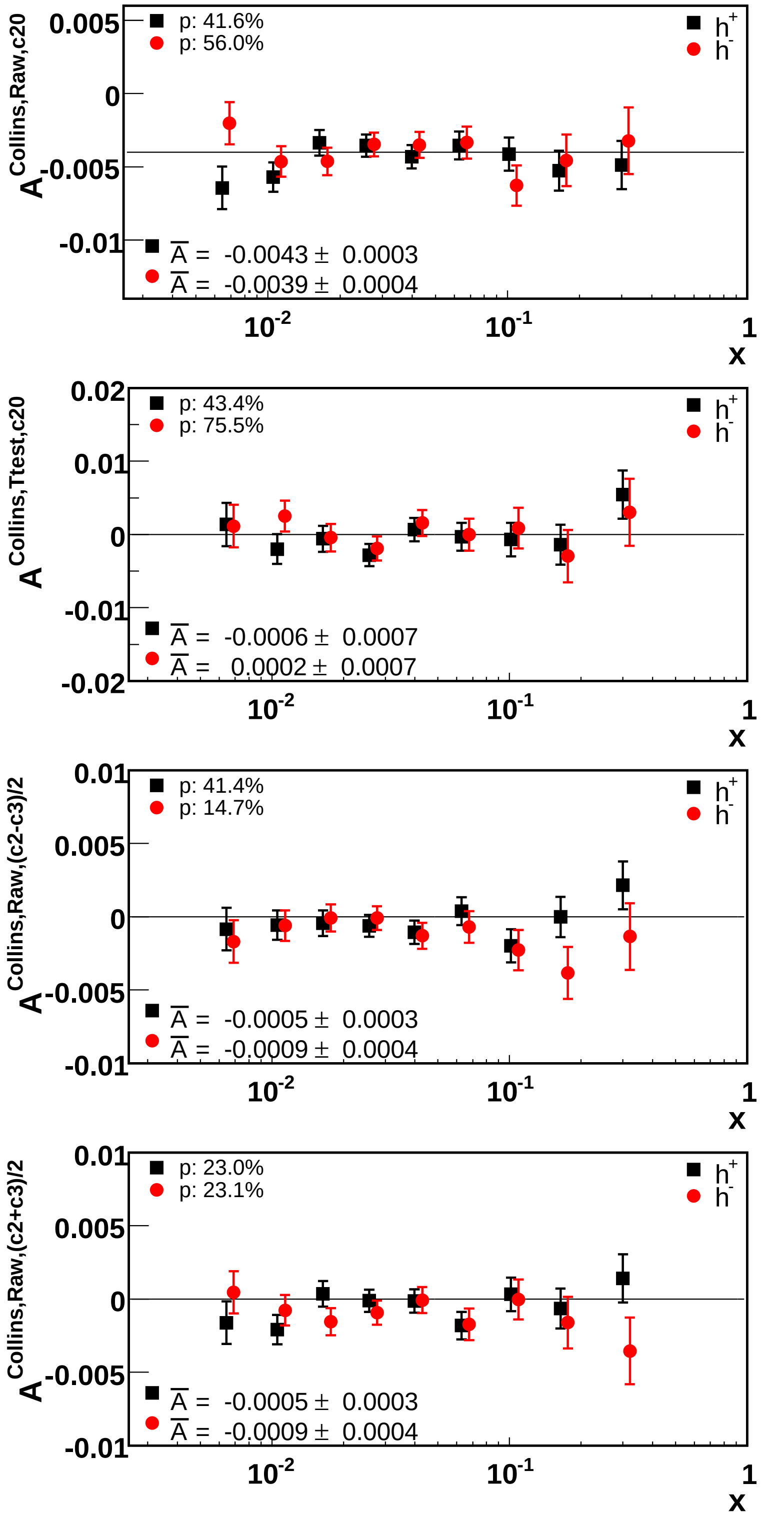

Figure 6.14: Collins results for Monte Carlo data with standard acceptance. From top to bottom: Raw asymmetries, raw Ttest and the false raw asymmetries $A^{(c2-c3)/2}$ and $A^{(c2+c3)/2}$ as a function of x. In the top plot the horizontal line indicates the size of the generated asymmetry.

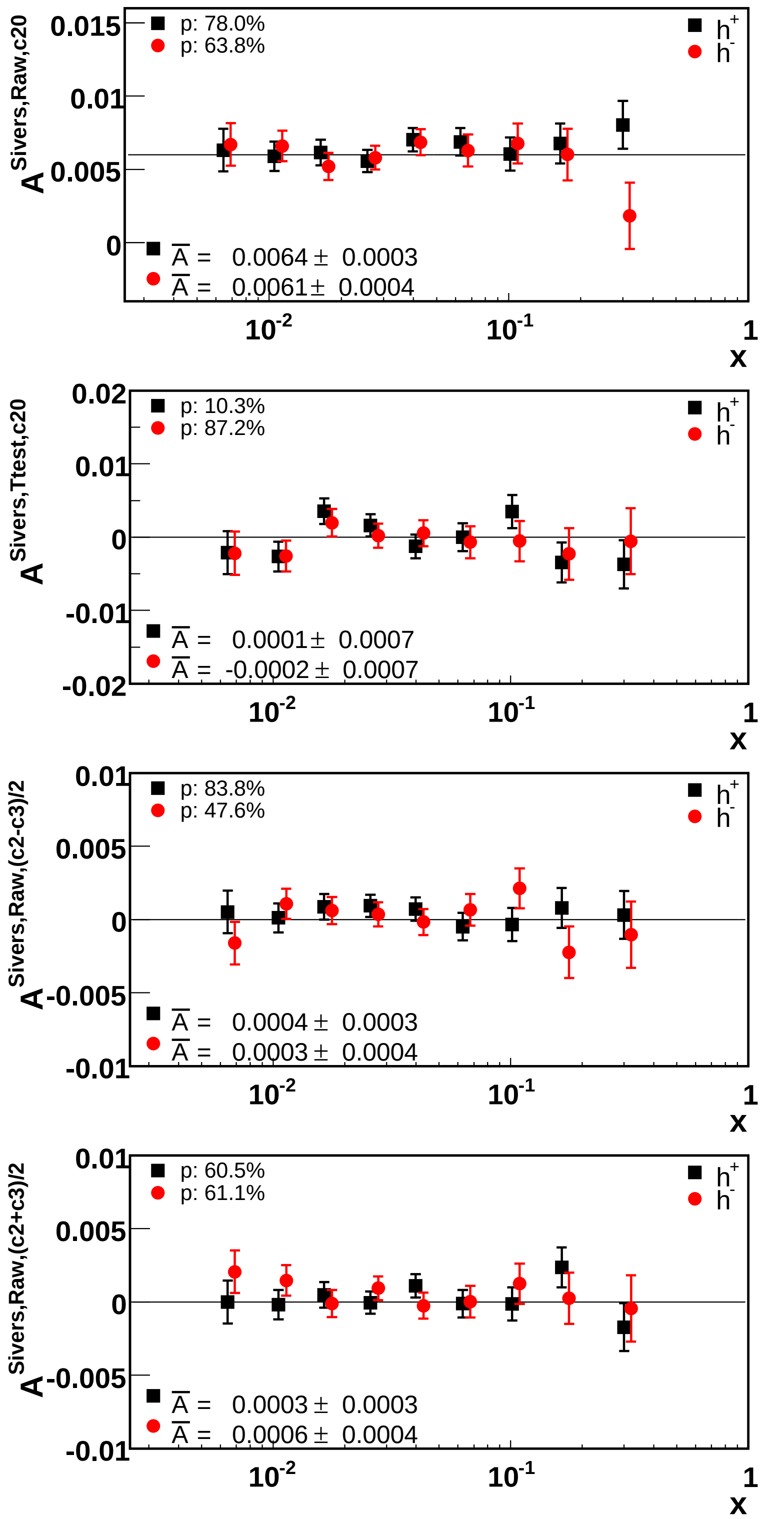

Figure 6.15: Sivers results for Monte Carlo data with standard acceptance. From top to bottom: Raw asymmetries, raw Ttest and the false raw asymmetries $A^{(c2-c3)/2}$ and $A^{(c2+c3)/2}$ as a function of x. In the top plot the horizontal line indicates the size of the generated asymmetry.

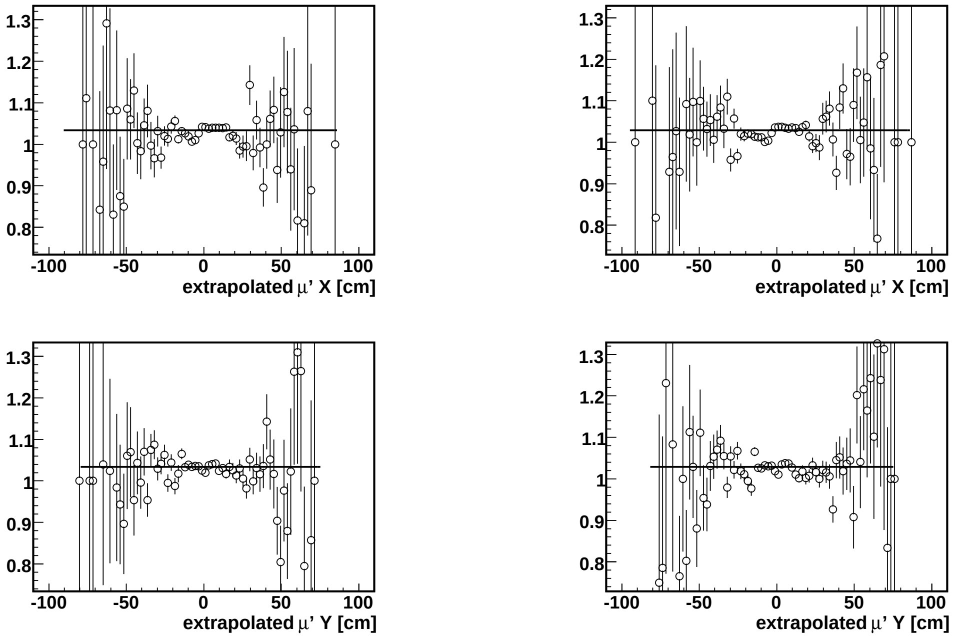

Figure 6.16: Projection on X- and Y-coordinates of ratio of extrapolated μ'-tracks (to $Z = 600\,\text{cm}$) of the 'total' data set $+--+$ and $-++-$ for real data. Left: weighted with positive hadron multiplicity. Right: weighted with negative hadron multiplicity.

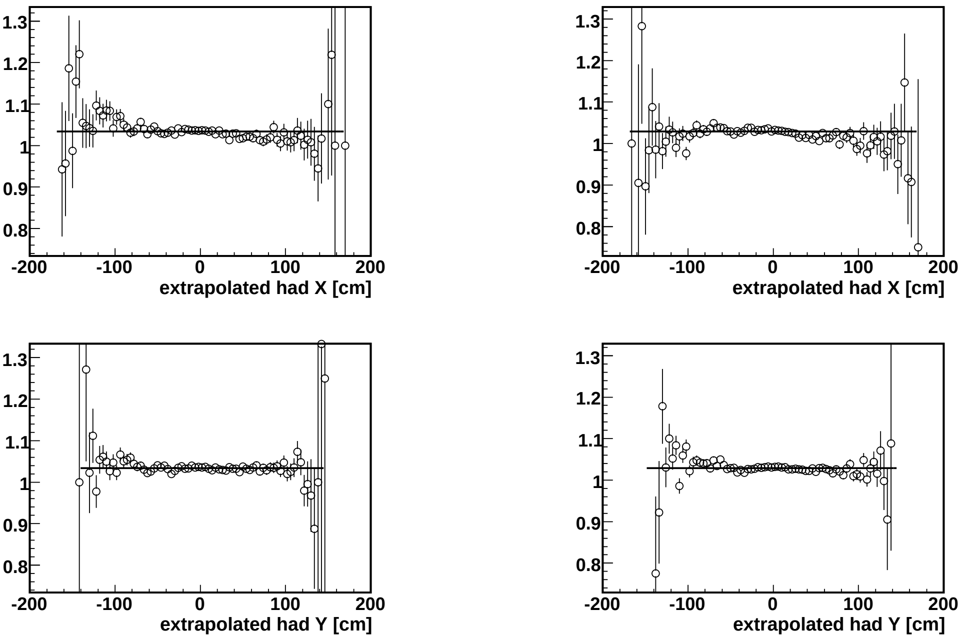

Figure 6.17: Projection on X- and Y-coordinates of ratio of extrapolated hadron tracks (to $Z = 600\,\text{cm}$) of the 'total' data set $+--+$ and $-++-$ for real data. Left: positive hadrons. Right: negative hadrons.

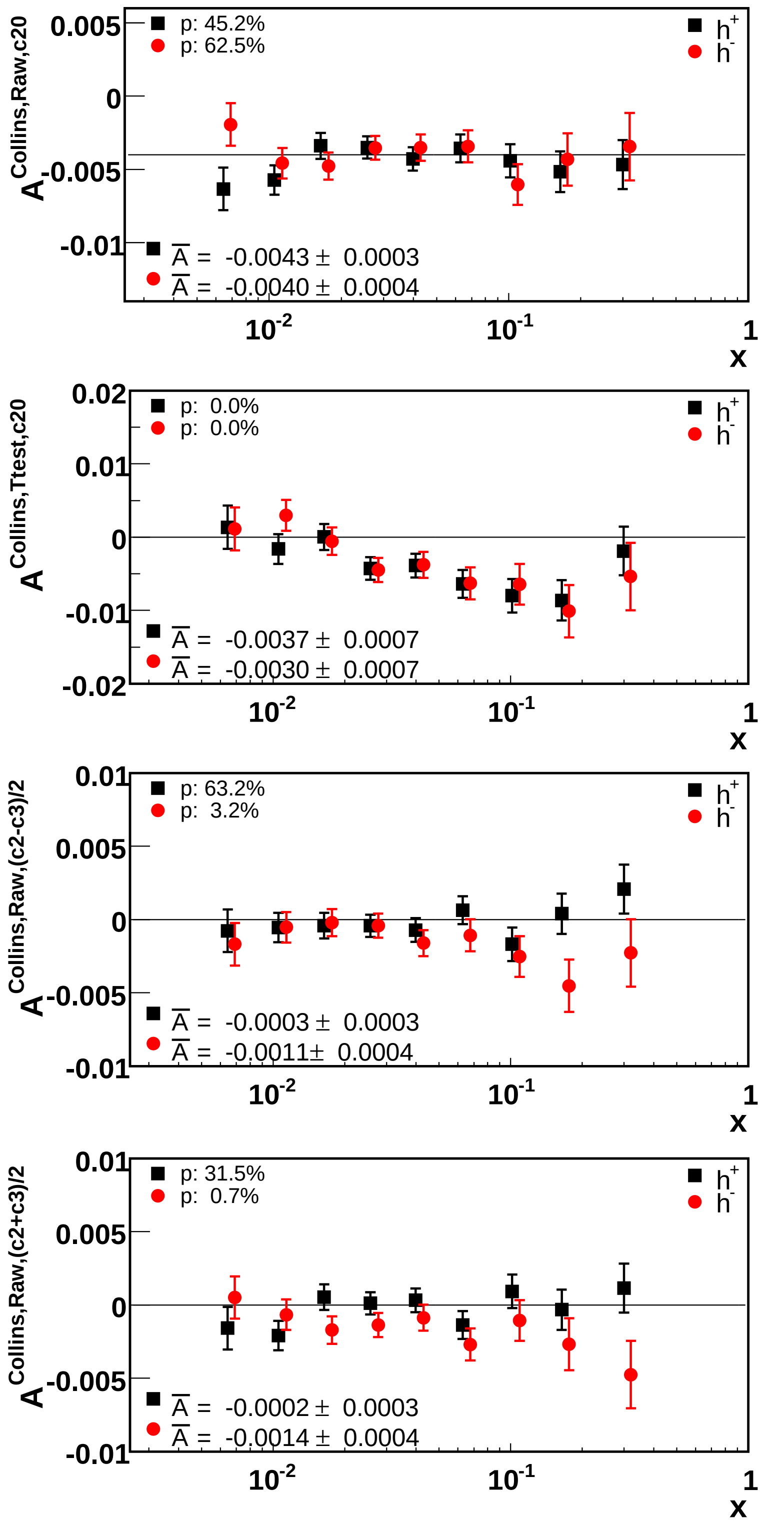

Figure 6.18: Collins results for scenario 7. From top to bottom: Raw asymmetries, raw Ttest and the false raw asymmetries $A^{(c2-c3)/2}$ and $A^{(c2+c3)/2}$ as a function of x. In the top plot the horizontal line indicates the size of the generated asymmetry.

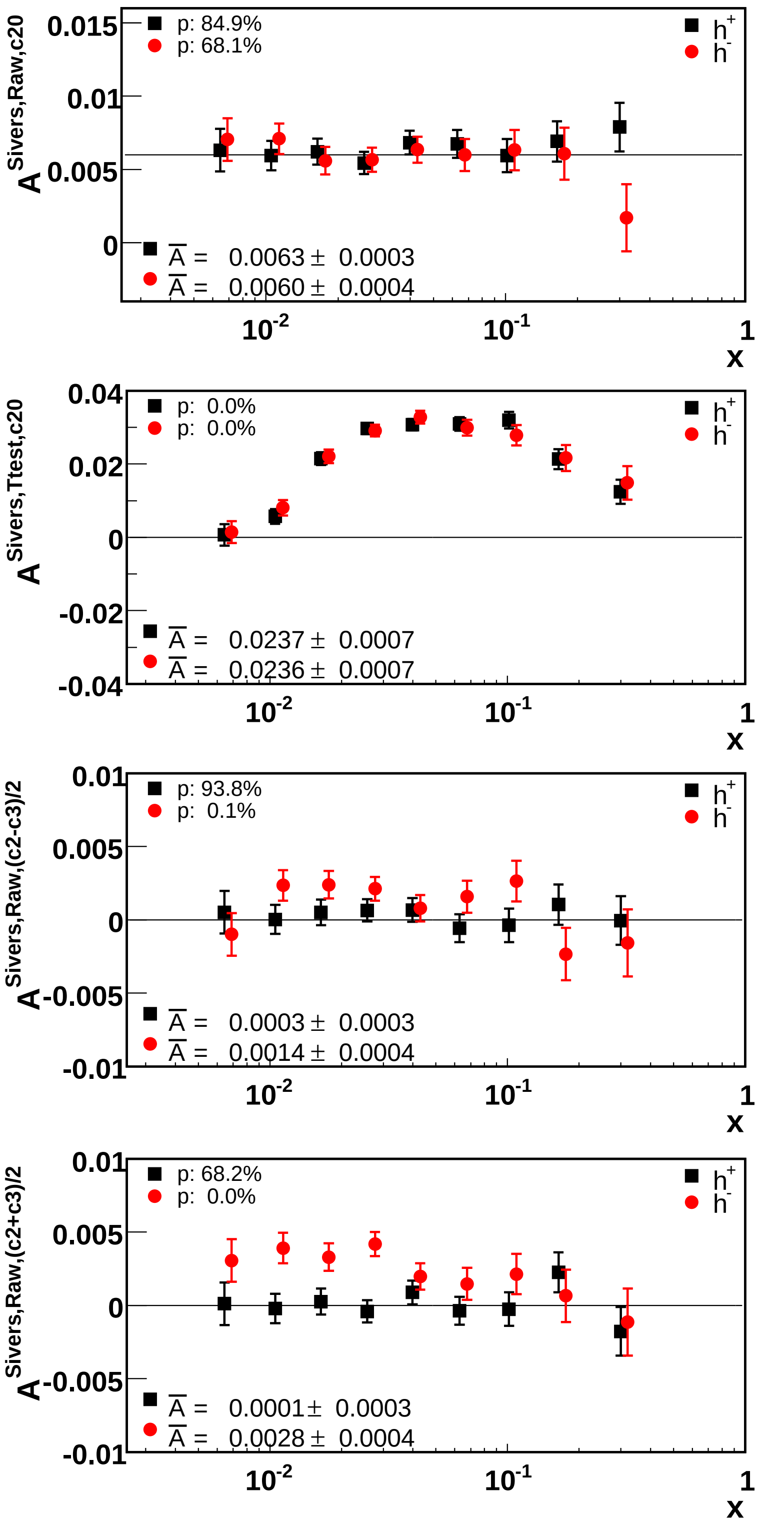

Figure 6.19: Sivers results for scenario 7. From top to bottom: Raw asymmetries, raw Ttest and the false raw asymmetries $A^{(c2-c3)/2}$ and $A^{(c2+c3)/2}$ as a function of x. In the top plot the horizontal line indicates the size of the generated asymmetry.

- Scenario 8: 10 % inefficiency in period $+--+$ for scattered muon and hadron tracks with: 20 cm$< X <$ 260 cm and -240 cm $< Y <$ 240 cm and primary vertex in target cell 1.

The results for Collins are shown in Fig. 6.20. The extracted asymmetries are compatible to the one shown in Fig. 6.14, obtained without change of the acceptance. Indeed the mean asymmetry for negative hadrons differ by one sigma, which holds true for the two false asymmetries, but the result is still compatible with the generated asymmetry of $A_{MC}^{Collins} = -0.004$. The results for Sivers are shown in Fig. 6.21. Here the extracted asymmetry is strongly biased with respect to $A_{MC}^{Sivers} = 0.006$. It is interesting, that now the false asymmetries, shown in the two bottom plots, are correlated to the bias of the real asymmetries.

As a counter check the same inefficiencies as before in scenario 8 are simulated but occurring for the data set with opposite target polarization:

- Scenario 9: 10 % inefficiency in period $-++-$ for scattered muon and hadron tracks with: 20 cm$< X <$ 260 cm and -240 cm $< Y <$ 240 cm and primary vertex in target cell 1.

The results are presented in Fig. 6.22 and 6.23. They are exactly opposite to the results of scenario 8. The Sivers asymmetries are now systematically smaller. But combining the results of scenario 8 and scenario 9 the asymmetries get compatible to the generated ones. In addition Ttest and false asymmetries get compatible with zero, too.

In summary the tests show contrary results. In case of no change in acceptance, the false asymmetries are uncorrelated to the real ones. This holds true, when simulating inefficiencies in the acceptance of one data set. In particular those changes have no impact on the extraction of the asymmetries. However, when one explicitly breaks the reasonable assumption, as done in scenario 8 and 9, the Sivers asymmetry gets significantly biased and the bias gets correlated to the false asymmetries. The combination of the results of scenario 8 and scenario 9 provides unbiased results and the false asymmetries gets compatible with zero. This clearly demonstrates the need of the reasonable assumption and that systematical effects can cancel or at least can get smaller, when combining all the data. This motivates to put the focus of the systematical checks in particular on the 'total' data set, as it was already done before for the analysis of the hadron pairs.

In any case scenario 7 shows, that Ttest cannot be used to judge whether the results are biased or not. More reliable are the false asymmetries. Hence only they will be incorporated in the estimation of the systematical error.

6.5 Systematics of Single Hadron Results

The same checks as for the oppositely charged hadron pairs have been performed to study the systematical error. The definitions of the various tests, which are discussed in the following, are given in the corresponding subsection of the hadron pair section 'Systematic Studies' (Sec. 5.7).

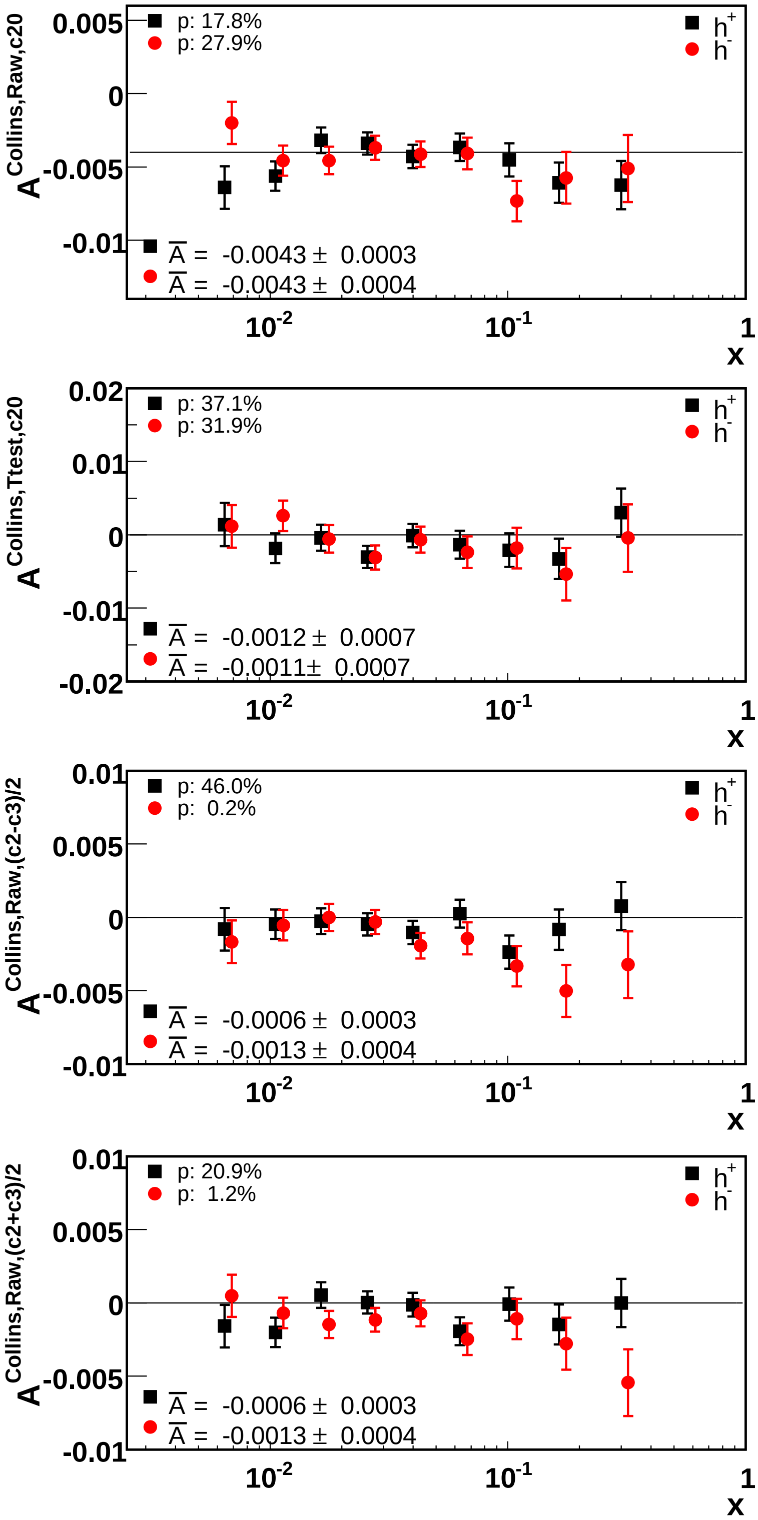

Figure 6.20: Collins results for scenario 8. From top to bottom: Raw asymmetries, raw Ttest and the false raw asymmetries $A^{(c2-c3)/2}$ and $A^{(c2+c3)/2}$ as a function of x. In the top plot the horizontal line indicates the size of the generated asymmetry.

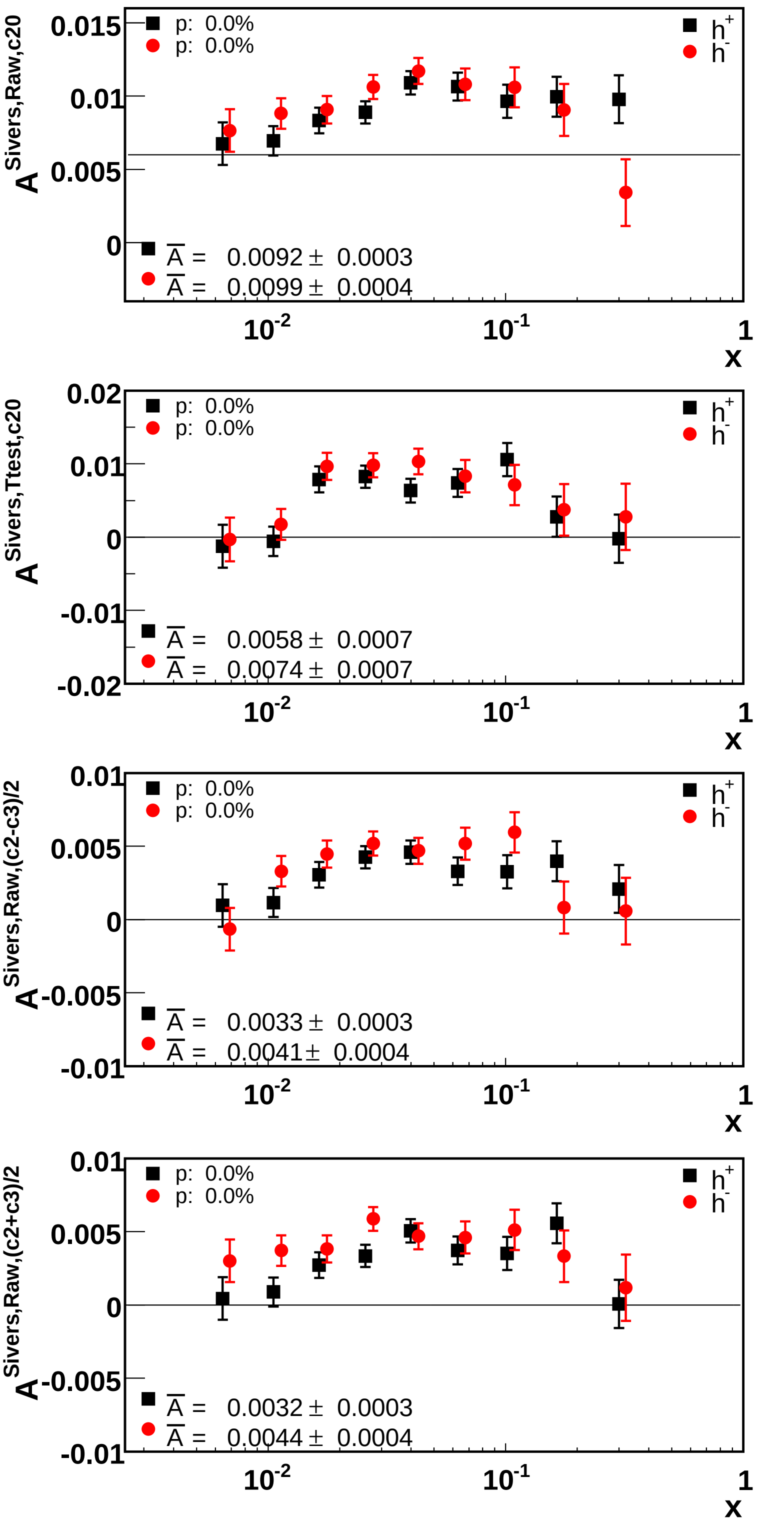

Figure 6.21: Sivers results for scenario 8. From top to bottom: Raw asymmetries, raw Ttest and the false raw asymmetries $A^{(c2-c3)/2}$ and $A^{(c2+c3)/2}$ as a function of x. In the top plot the horizontal line indicates the size of the generated asymmetry.

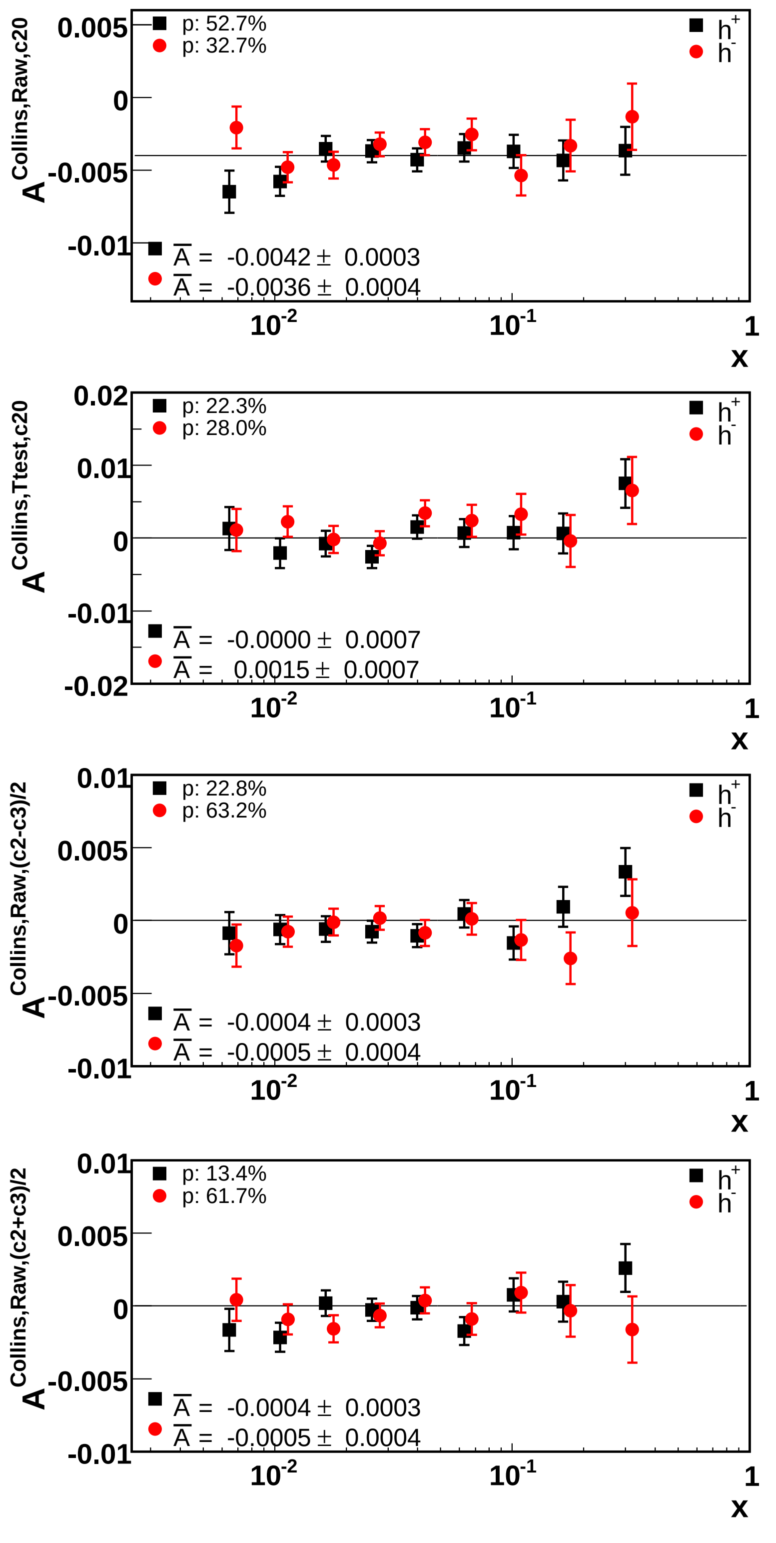

Figure 6.22: Collins results for scenario 9. From top to bottom: Raw asymmetries, raw Ttest and the false raw asymmetries $A^{(c2-c3)/2}$ and $A^{(c2+c3)/2}$ as a function of x. In the top plot the horizontal line indicates the size of the generated asymmetry.

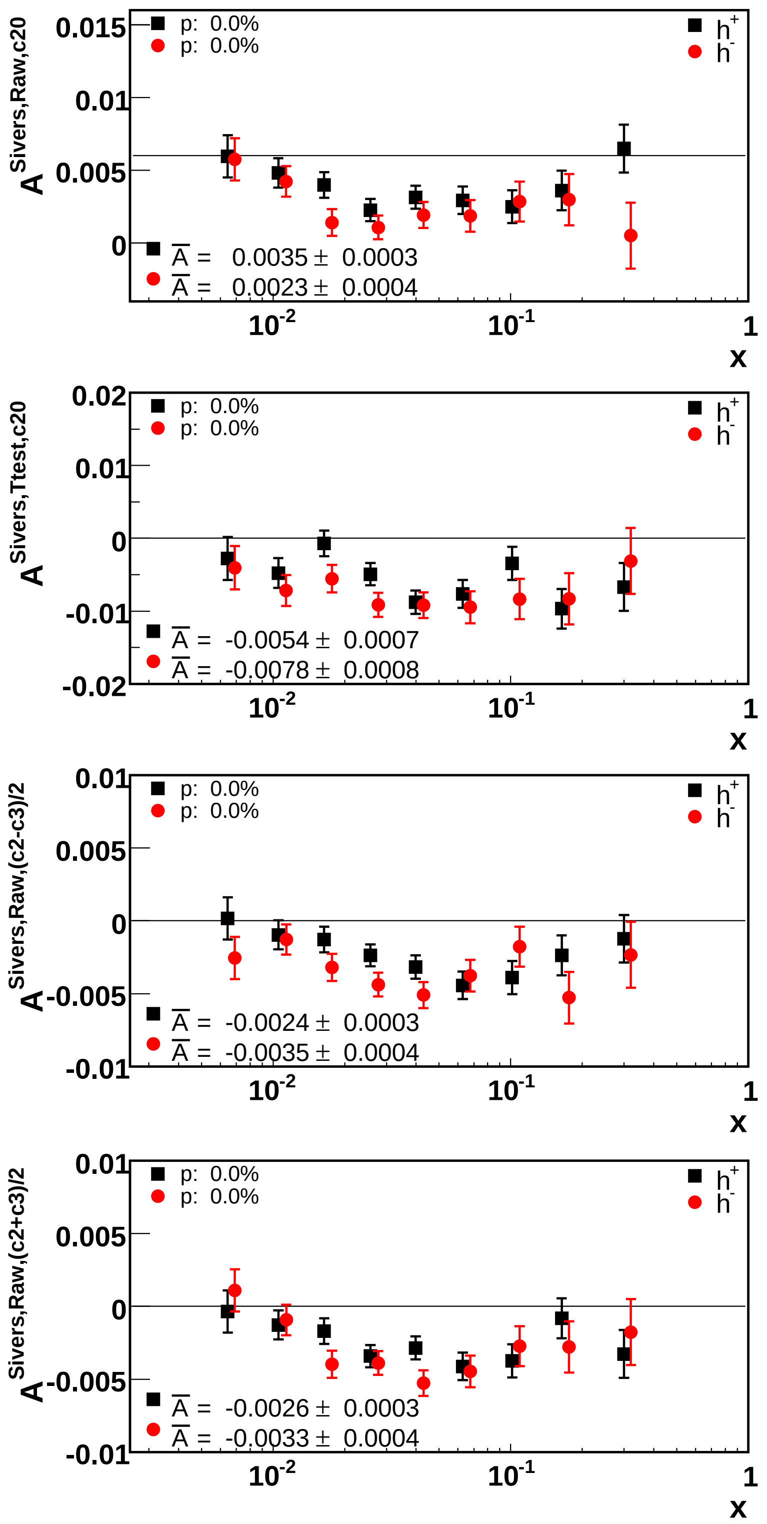

Figure 6.23: Sivers results for scenario 9. From top to bottom: Raw asymmetries, raw Ttest and the false raw asymmetries $A^{(c2-c3)/2}$ and $A^{(c2+c3)/2}$ as a function of x. In the top plot the horizontal line indicates the size of the generated asymmetry.

6.5.1 Compatibility of Estimators

The compatibility of the four extraction methods are checked. The results for Collins and Sivers asymmetries for positive and negative hadrons as a function of x, z and p_T are shown in Fig. C.1 - C.4. The pulls between results obtained with the one dimensional ratio method and the unbinned maximum likelihood are shown in Fig. 6.24. The pulls for negative hadrons for Collins and Sivers asymmetries, have mean values compatible with zero and the width is compatible to the results obtained with Monte Carlo data. This holds true for Sivers for positive hadrons. However, the mean for Collins positive hadrons is shifted and the RMS is larger. The reason of this can be explained by the large Sivers asymmetry present for positive hadrons, whereas for negative hadrons it is compatible with zero. Due to the folding with the COMPASS acceptance this leads, in the case of the one dimensional ratio method, to a bias for the result of Collins for positive hadrons [84]. This effect was confirmed for Monte Carlo data, as discussed in Sec. 5.5.1 for the hadron pairs. Here the difference between the two methods was compatible with zero for the sample without generated asymmetries (Fig. 5.46) and got significantly biased in the presence of non vanishing Collins and Sivers asymmetries (Fig. 5.48).

Fig. 6.25 shows the pulls between the two dimensional ratio method and the unbinned maximum likelihood. The mean and the RMS values for negative hadrons, shown on the right are compatible to the ones shown in Fig. 6.12 obtained with Monte Carlo data. This is also true for Collins for positive hadrons (top left). However, for Sivers, shown on bottom left, the mean of the pull for real data is shifted, whereas for Monte Carlo it is compatible with zero.

In Fig. 6.26 the pulls between binned and unbinned maximum likelihood method are given. Comparing these results with the ones given in Fig. 6.13 for Monte Carlo data, the same observations as before for the two dimensional ratio method and the unbinned maximum likelihood can be made.

In summary: For Monte Carlo data the binned and the unbinned maximum likelihood fits are giving both the correct results within statistical errors. The difference between the two methods, which is present for real data, is taken with half its size into account in the systematical error.

6.5.2 Period Compatibility

The results for the Collins asymmetries for the six double periods as a function of x, z and p_T are shown in Fig. 6.27 for positive hadrons and in Fig. 6.28 for negative hadrons. The corresponding compatibility pulls, derived analogue to Eq. (5.32), are shown in Fig. 6.31 on the left for positive and on the right for negative hadrons. Within the errors both distributions have mean values compatible with zero and sigma values compatible with one, indicating that all six measurements are statistical compatible with each other.

The Sivers asymmetries for the six double periods as a function of x, z and p_T are shown in Fig. 6.29 and Fig. 6.30 for positive and negative hadrons, respectively. For positive hadrons the results for the first three double periods show a non zero mean asymmetry, whereas for the last three periods it is compatible with zero. For negative hadrons all six measurements are compatible with zero. The corresponding pulls are shown in Fig. 6.32.

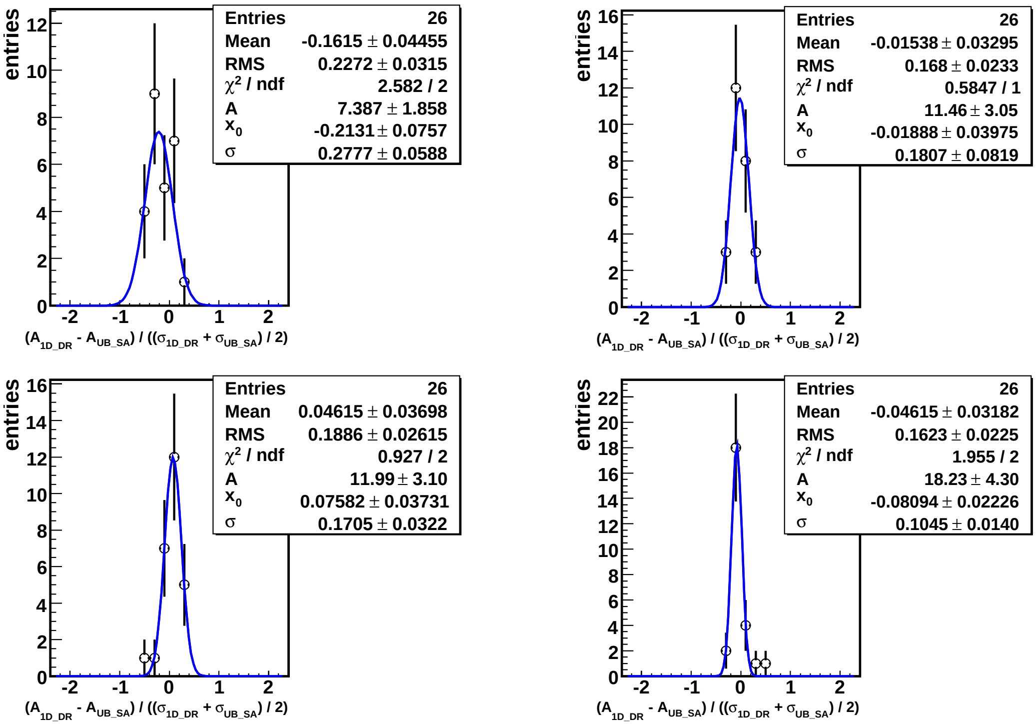

Figure 6.24: Pulls between results of 1D ratio method and unbinned maximum likelihood. For Collins on top and for Sivers on bottom. On the left for positive and on the right for negative hadrons.

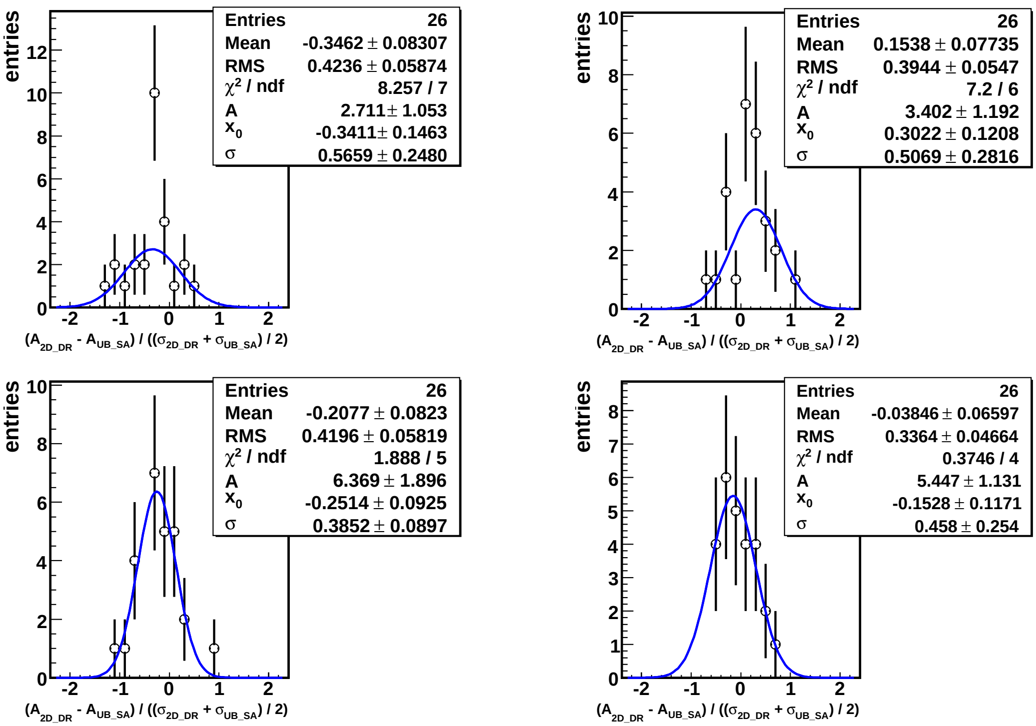

Figure 6.25: Pulls between results of 2D ratio method and unbinned maximum likelihood. For Collins on top and for Sivers on bottom. On the left for positive and on the right for negative hadrons.

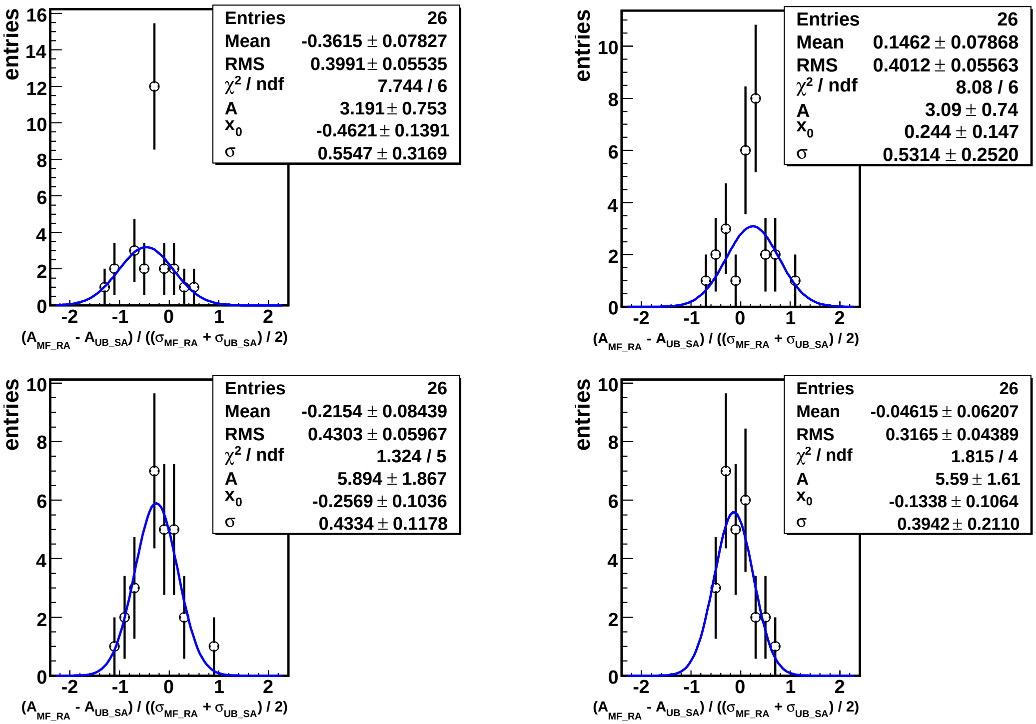

Figure 6.26: Pulls between results of binned and unbinned maximum likelihood. For Collins on top and for Sivers on bottom. On the left for positive and on the right for negative hadrons.

For both charges the mean values are compatible with zero. The sigma values from the fit are within the errors compatible with one. However, the RMS for positive hadrons is 1.18 ± 0.07, thus significantly larger than one, reflecting the already discussed difference between the first and the last three measurements. For negative hadrons the RMS is 1.11 ± 0.06 and also not compatible with one. Compared to the RMS of the pulls for the Collins asymmetries of positive and negative hadrons the measurements of the Sivers asymmetries show a systematically larger spread. This will be taken into account in the systematical error in the following way:

$$\sigma^{sys} \leq \sqrt{\mathrm{RMS}^2 - 1} \cdot \sigma^{stat}. \tag{6.5}$$

Thus for Sivers positive hadrons the systematical error results in 63 % and for negative hadrons in 48 % of the statistical error.

6.5.3 Dtest

As for the hadron pairs in Sec. 5.7.3, the Dtest for the single hadrons is performed accordingly on the (ϕ_h, ϕ_S) grid. The results for the six double periods for positive hadrons are illustrated in Fig. 6.33 and for negative hadrons in Fig. 6.34. The results for negative hadrons are reasonably good (expected is a mean χ^2 of 63, because of 8 x 8 bins in ϕ_h and ϕ_S and one fit parameter). For positive hadrons this holds true except for week 41-42, which shows a significantly biased mean chi square.

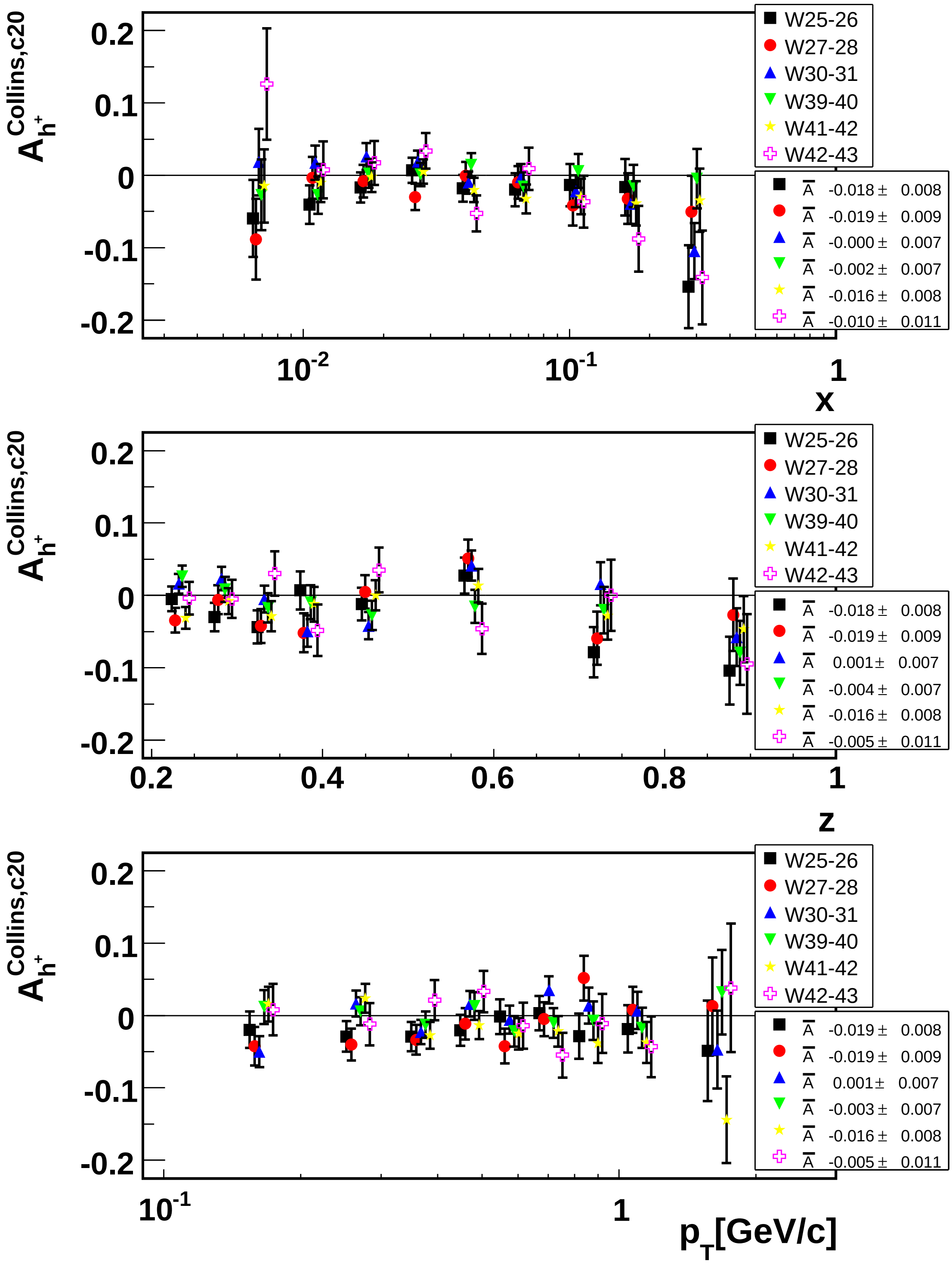

Figure 6.27: Collins asymmetry for positive hadrons for the six double periods as a function of x, z and p_T. Mean asymmetries, $\bar{\mathrm{A}}$, of the six double periods are given.

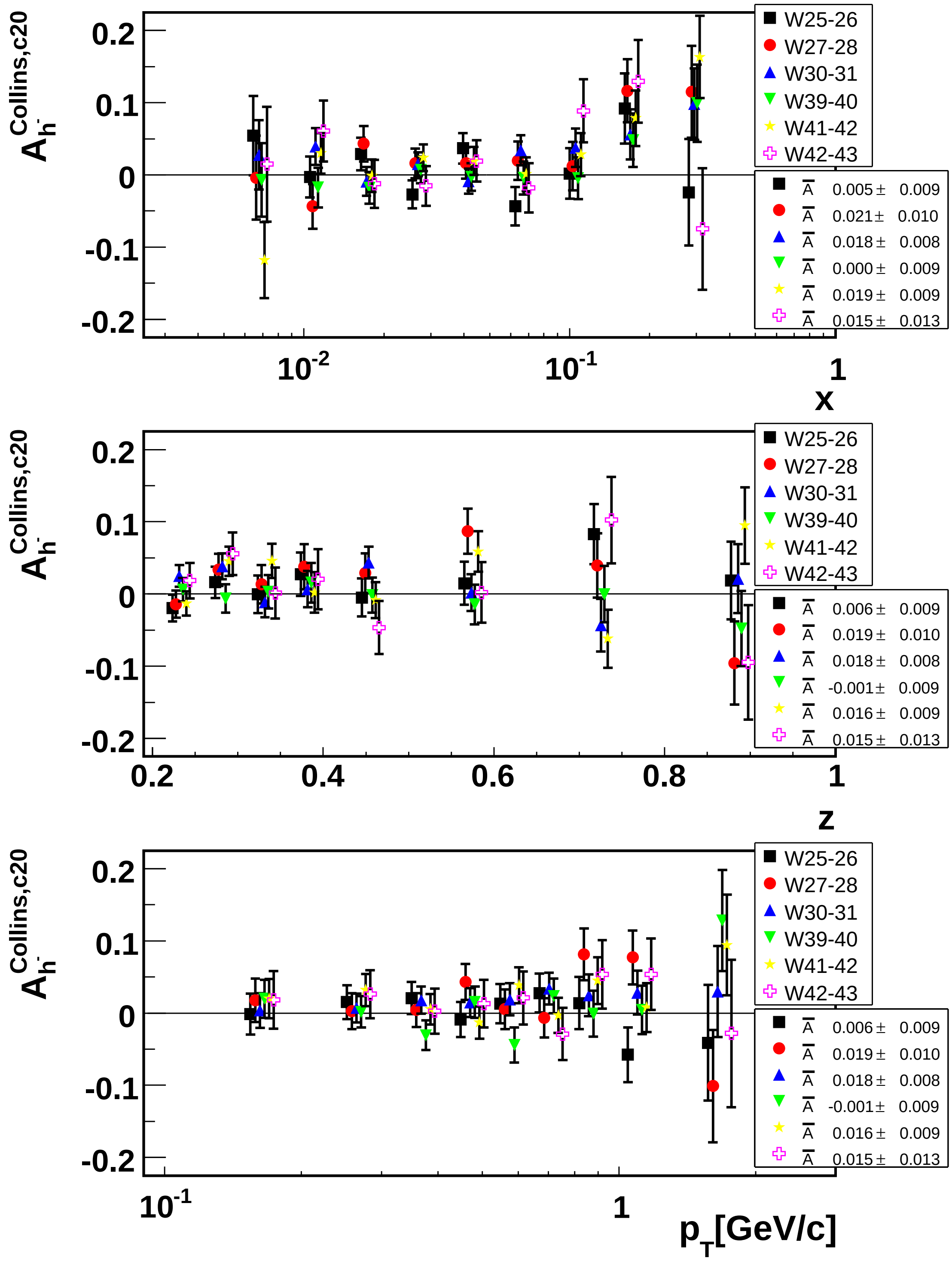

Figure 6.28: Collins asymmetry for negative hadrons for the six double periods as a function of x, z and p_T. Mean asymmetries, $\bar{\mathrm{A}}$, of the six double periods are given.

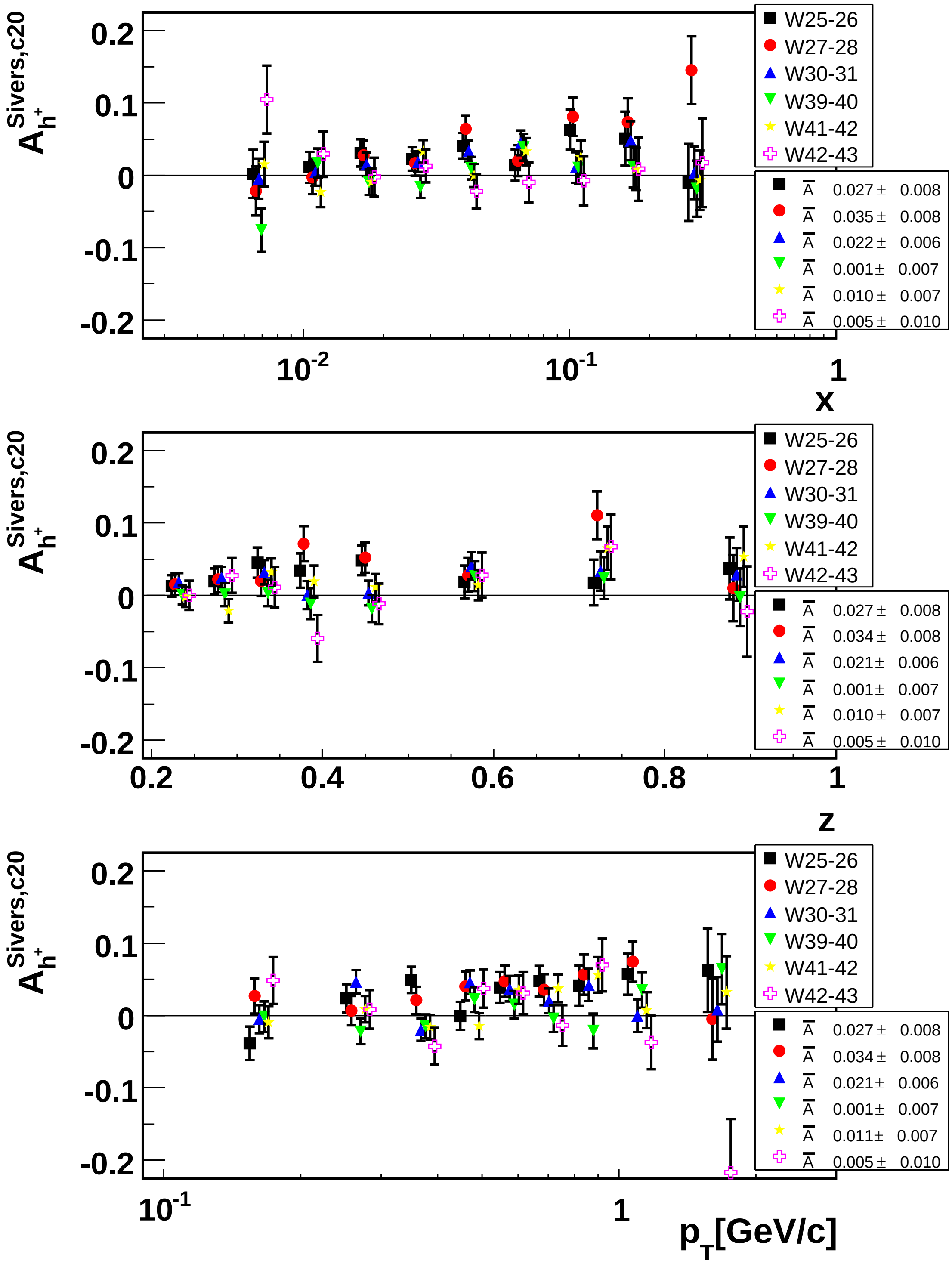

Figure 6.29: Sivers asymmetry for positive hadrons for the six double periods as a function of x, z and p_T. Mean asymmetries, $\bar{\text{A}}$, of the six double periods are given.

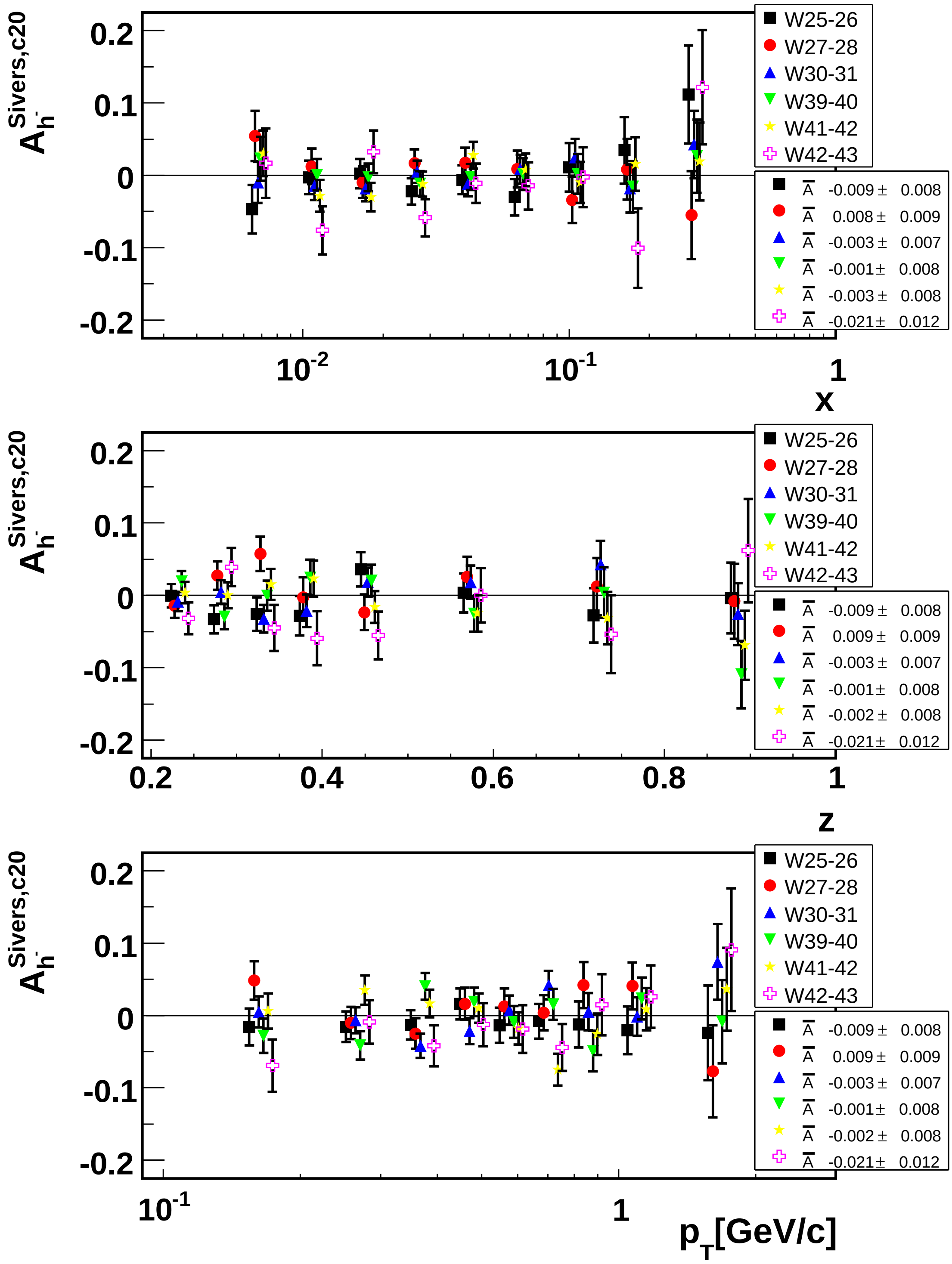

Figure 6.30: Sivers asymmetry for negative hadrons for the six double periods as a function of x, z and p_T. Mean asymmetries, $\bar{\mathrm{A}}$, of the six double periods are given.

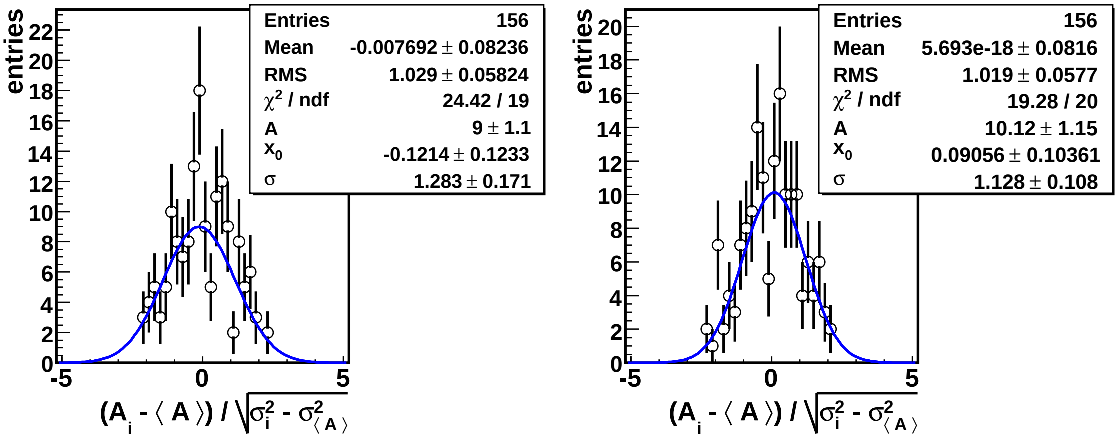

Figure 6.31: Period compatibility pulls of Collins asymmetry for positive (right) and negative (left) hadrons.

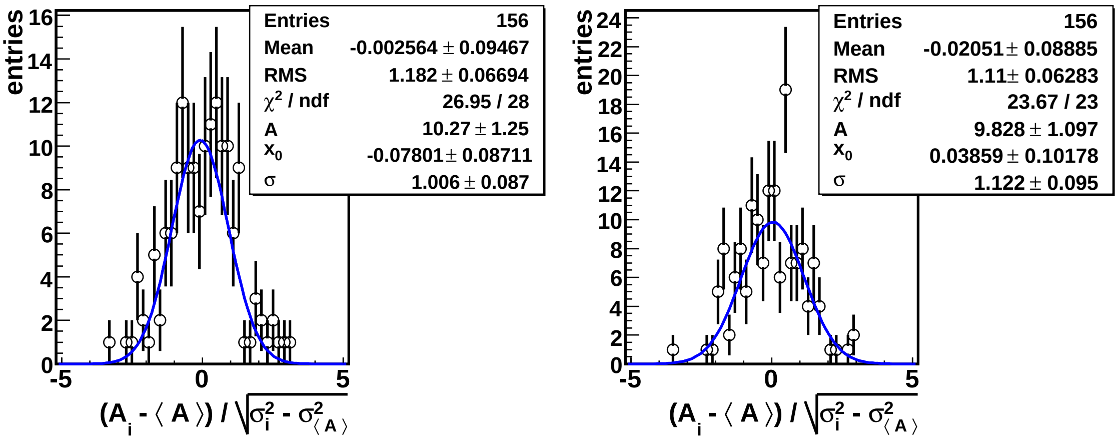

Figure 6.32: Period compatibility pulls of Sivers asymmetry for positive (right) and negative (left) hadrons.

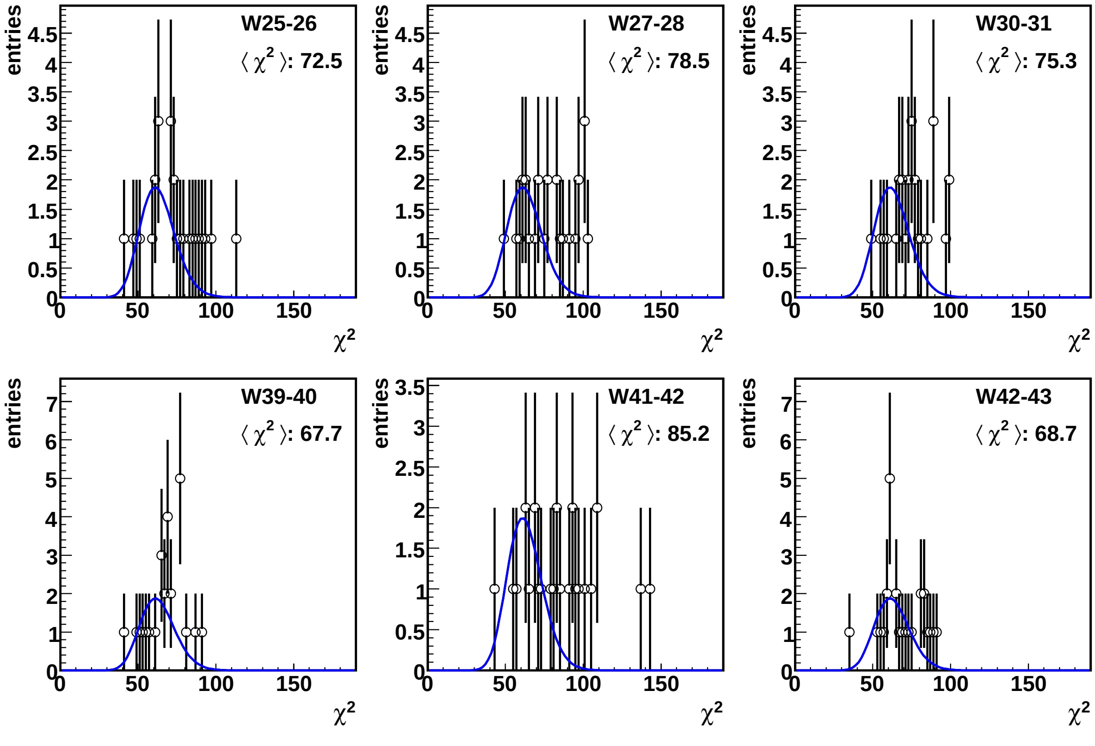

Figure 6.33: χ^2-distribution of Dtest for positive hadrons for the six double periods. The blue line indicates the expected distribution with mean value 63.

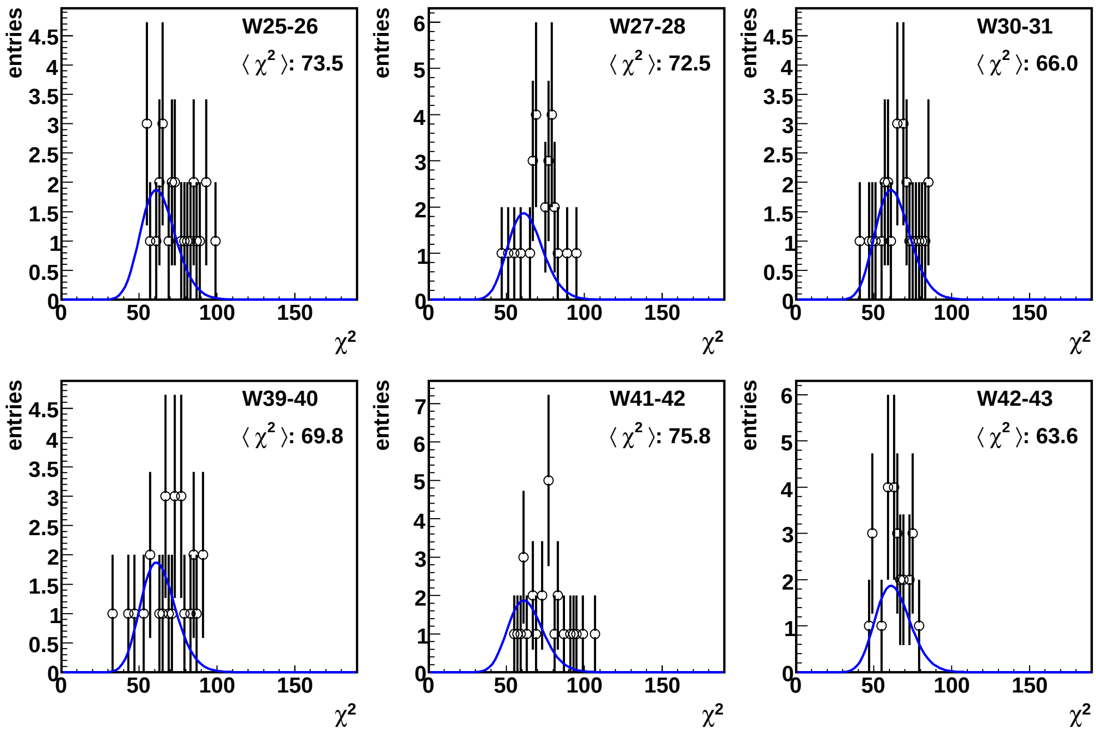

Figure 6.34: χ^2-distribution of Dtest for negative hadrons for the six double periods. The blue line indicates the expected distribution with mean value 63.

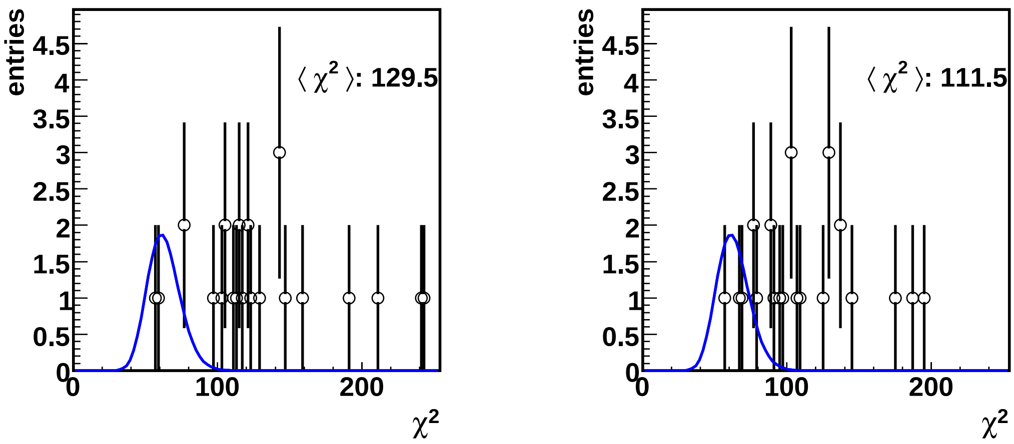

Figure 6.35: χ^2-distribution of Dtest for the 'total' data set. On the left for positive and on the right for negative hadrons. The blue line indicates the expected distribution with mean value 63.

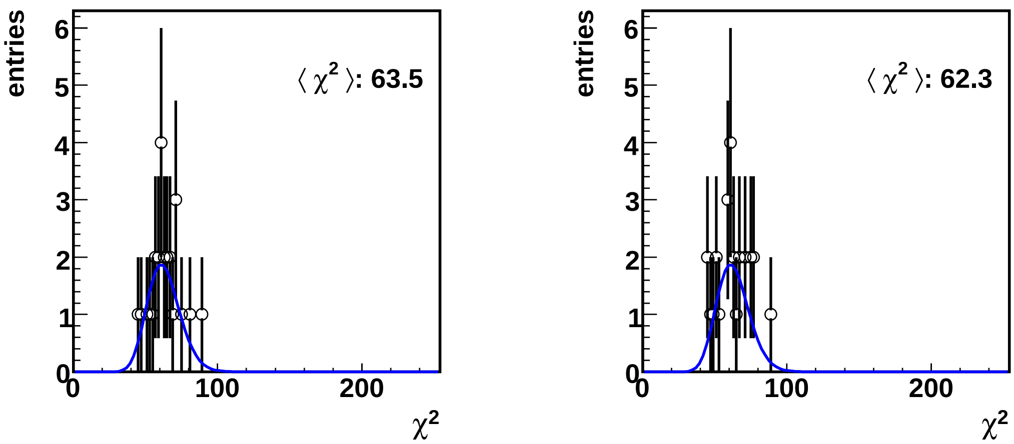

Figure 6.36: χ^2-distribution of Dtest for Monte Carlo data. On the left for positive and on the right for negative hadrons. The blue line indicates the expected distribution with mean value 63.

For the 'total' data set the result is shown in Fig. 6.35. For positive hadrons on the left and for negative hadrons on the right. As one can see both distributions deviate significantly from the theoretically expected trend. The results obtained with Monte Carlo data is shown in Fig. 6.36. Both distributions, for positive and negative hadrons follow the expected behavior and have mean values close to 63. This test clearly signalizes, that the acceptance between the 'total' data sets $+--+$ and $-++-$ has changed. However, the Dtest is no quantitative test, which detects systematical effects which leads to a bias of the Collins and Sivers asymmetries.

6.5.4 Ttest

Analogue to the Ttest for the two hadron pairs, the Ttest for single hadrons is performed (see Sec. 5.7.4). Here 'Collins' and 'Sivers'-like changes in the acceptance are considered, respectively. The Collins results for the six double periods as a function of x are shown in Fig. 6.37. On the top for positive and on the bottom for negative hadrons. For positive hadrons the results for week 39-40 and week 41-42a are not compatible with zero. The probabilities of the χ^2-test are below 0.1 % and the mean values deviate 3.5 σ and 4.0 σ, respectively. For negative hadrons only week 41-42a is not compatible with zero. The result of the Ttest for Collins, performed on the 'total' data set, is illustrated in Fig. 6.38. The result is for both charges not compatible with zero. In particular for positive hadrons the amplitude deviates from zero over almost the whole x-range. As seen in Sec. 5.7.4, the Ttest for hadron pairs is compatible with zero. This implies that the acceptance of hadron pairs in $\sin(\phi_R + \phi_S - \pi)$ is more stable than for single hadrons in $\sin(\phi_h + \phi_S - \pi)$. However, as already discussed this result does not necessarily leads to a bias of the real Collins-asymmetries, as seen in Sec. 6.4.1 with Monte Carlo data for scenario 7, 8 and 9. Hence the false asymmetries, which will be analysed in the following section, have to clarify the systematics of the results.

The Ttest results for Sivers for the six double periods as a function of x are shown in Fig. 6.39. For positive hadrons on the top and for negative hadrons on the bottom. As one can see, only for week 30-31 and week 39-40 the results are compatible with zero. All other weeks show a significant deviation from zero. However, looking at the Ttest of the 'total' data set, shown in Fig. 6.40, one sees that except for the last two points, all values are well compatible with zero. Thus the 'Sivers-like' changes in the acceptance, which are strongly present for the six double periods, cancel when combining all the data. For negative hadrons the results for week 27-18 and week 41-42 strongly deviates from zero and week 30-31 is at the edge of a 3 σ deviation. However, as for positive hadrons, the Ttest result of the 'total' data set is well compatible with zero over almost the whole x-range, leading to the same conclusion as before for the positive hadrons.

Comparing the Ttest results of Sivers for positive hadrons with the real Sivers asymmetries in Fig. 6.31, it is indicated that the asymmetries for periods with positive Ttest, i.e. week 39-40, 41-42a and 42b-43, are compatible with zero. On the other hand the asymmetries for periods with negative Ttest, i.e. week 25-26, 27-28 and 30-31, have a positive asymmetry. However, as already discussed the Ttest of the 'total' data set is well compatible with zero.

6.5.5 False Asymmetries

Analogue to Sec. 5.7.5 Collins and Sivers false asymmetries for positive and negative hadrons are computed, using configuration c2 and c3. The results for $A^{(c2-c3)/2}_{Collins}$ as a function of x for the six double periods for positive and negative hadrons are shown in Fig. 6.41 on top and bottom, respectively. All results are compatible with zero. The results for the 'total' data set are illustrated in Fig. 6.42. For both charges the distributions are well compatible with zero.

For Sivers the results are shown in Fig. 6.43 for the six double periods and in Fig. 6.44 for the 'total' data set. For positive hadrons the mean of week 42b-43 is 3.4 σ off. For negative hadrons week 27-28 and week 41-42a show low probabilities to be compatible with zero. However, for the 'total' data set the results are compatible with zero. Analogue to Eq. (5.43) the deviations from zero are quantified in units of the statistical error (considering all 26 bins in x, z and M_{inv}). They are given in Tab. 6.2 for the six single

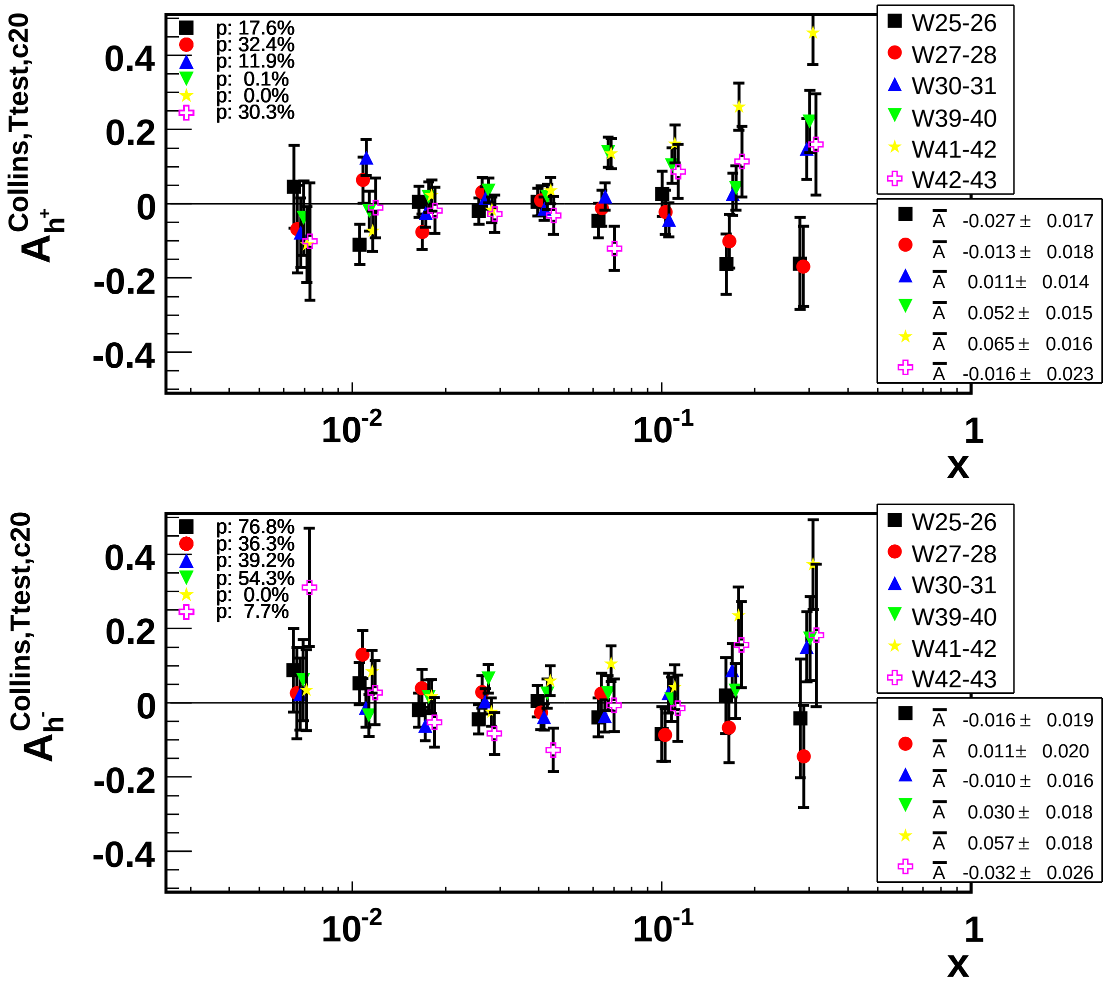

Figure 6.37: Result of Ttest for Collins positive (top) and negative (bottom) hadrons for the six double periods as a function of x. Mean Ttest values, $\bar{\mathrm{A}}$, and probabilities, p, of χ^2 test with respect to zero are given.

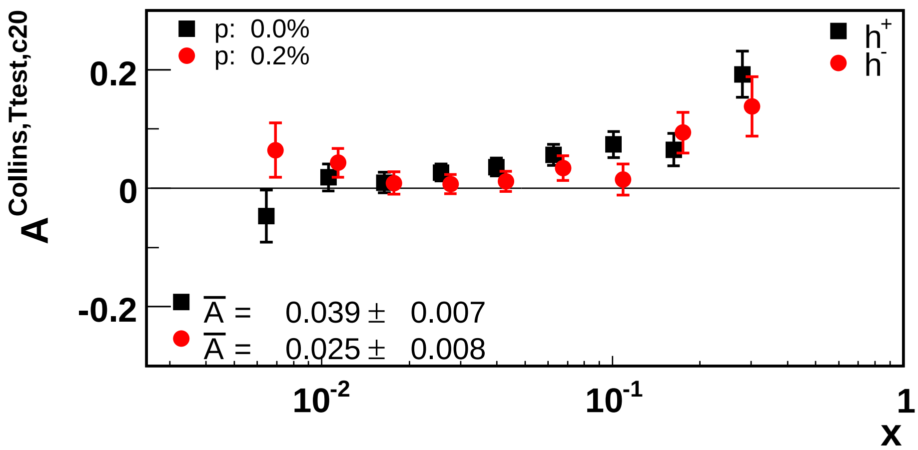

Figure 6.38: Result of Ttest of the 'total' data set for Collins for positive and negative hadrons as a function of x. Mean Ttest values, $\bar{\mathrm{A}}$, and probabilities, p, of χ^2 test with respect to zero are given.

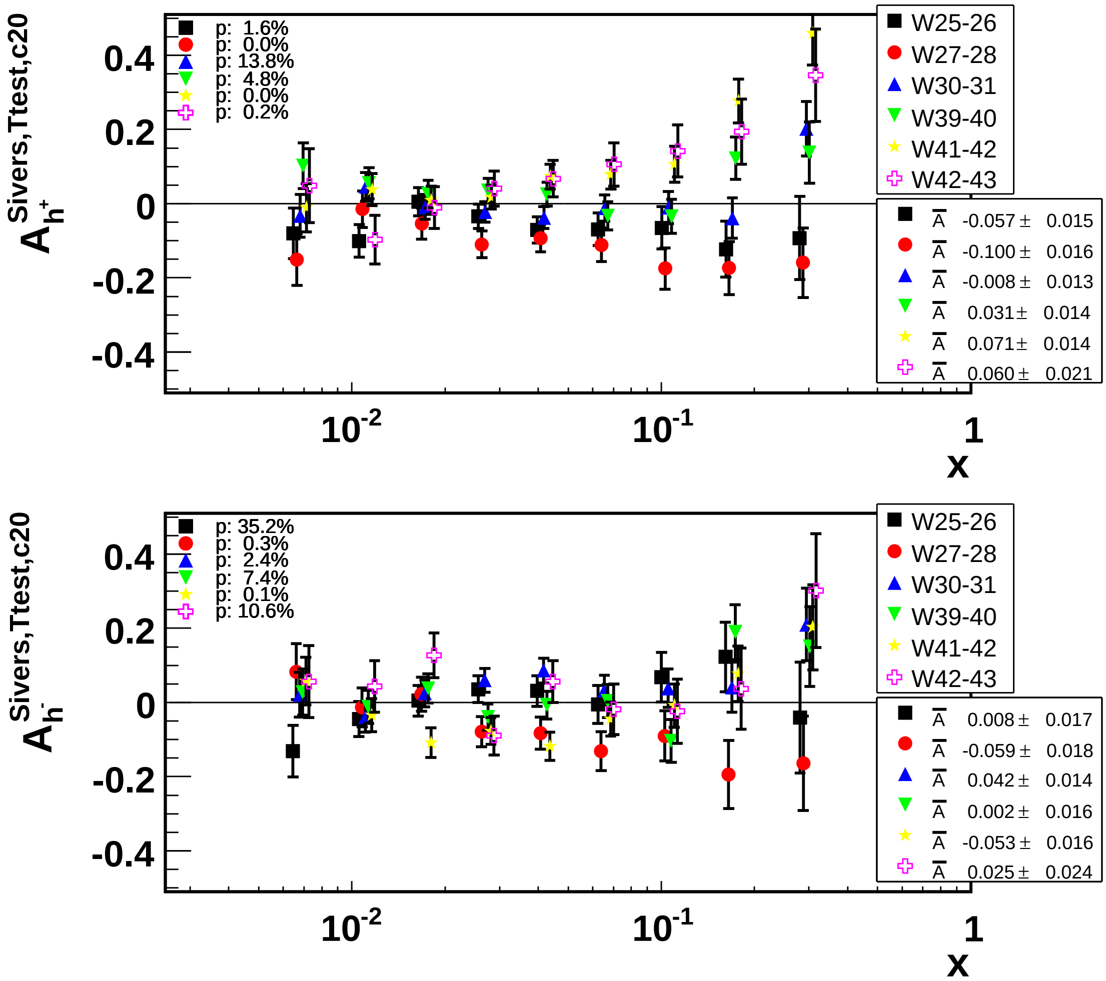

Figure 6.39: Result of Ttest for Sivers positive (top) and negative (bottom) hadrons for the six double periods as a function of x. Mean Ttest values, $\bar{\mathrm{A}}$, and probabilities, p, of χ^2 test with respect to zero are given.

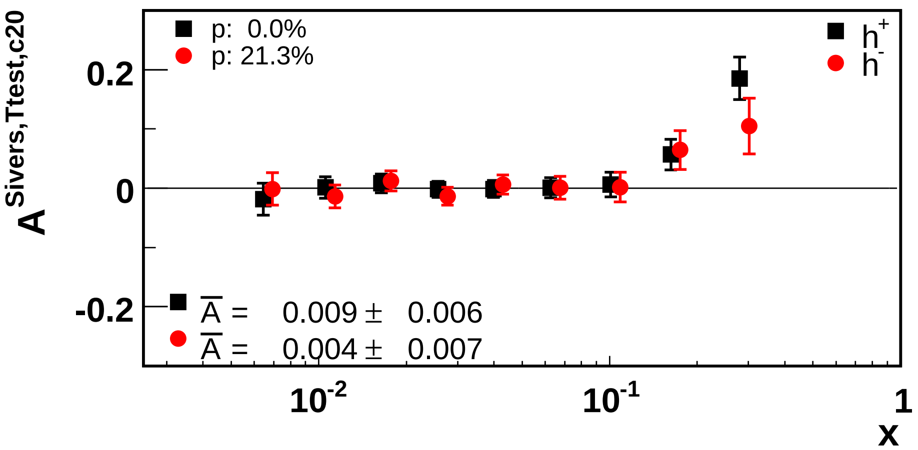

Figure 6.40: Result of Ttest of the 'total' data set for Sivers for positive and negative hadrons as a function of x. Mean Ttest values, $\bar{\mathrm{A}}$, and probabilities, p, of χ^2 test with respect to zero are given.

Table 6.2: $\Delta_{|c2-c3|}/\sigma^{stat}$ for Collins and Sivers for the six double periods, for the 'total' data set and for the Monte Carlo sample.

Week	Collins h^+	Collins h^-	Sivers h^+	Sivers h^-
25-26	0.85	0.69	1.15	0.85
27-28	0.69	0.80	0.60	1.00
30-31	0.77	0.81	1.00	0.75
39-40	0.83	0.81	0.74	0.63
41-42a	0.76	0.84	0.95	1.18
42b-43	0.93	1.04	1.36	0.76
'total' set	0.66	0.86	0.93	0.73
Monte Carlo	0.88	0.93	0.93	0.76

Table 6.3: $\Delta_{|c2+c3|}/\sigma^{stat}$ for Collins and Sivers for the six double periods, for the 'total' data set and for the Monte Carlo sample.

Week	Collins h^+	Collins h^-	Sivers h^+	Sivers h^-
25-26	0.75	1.02	0.80	1.15
27-28	0.74	0.68	0.76	0.96
30-31	0.76	0.80	0.80	0.81
39-40	0.84	0.64	0.90	0.53
41-42a	0.94	0.92	0.85	0.95
42b-43	0.75	0.62	0.85	0.73
'total' set	0.66	0.63	0.89	0.84
Monte Carlo	0.82	0.99	0.58	0.76

periods and for the 'total' data set. The same tests are performed on the Monte Carlo sample. These results are given in the last line of the table. As one can see the values for real data are compatible to those obtained with Monte Carlo data.

For $A_{Collins}^{(c2+c3)/2}$, the weighted mean of the false asymmetries the results for positive and negative hadrons for the six double periods are shown in Fig. 6.45 and for the 'total' data set in Fig. 6.46. Some weeks show a low probability to be compatible with zero. However, the results for the 'total' data set are well compatible with zero. The result, that both false asymmetries $A_{Collins}^{(c2-c3)/2}$ and $A_{Collins}^{(c2+c3)/2}$ are compatible with zero qualifies the non zero Ttest result discussed in the previous section for Collins.

The results for $A_{Sivers}^{(c2+c3)/2}$ are shown in Fig. 6.47 and Fig. 6.48 for positive and negative hadrons, respectively. The results for all weeks and for both charges are statistically compatible with zero. This holds true for the 'total' data set. The deviations in units of the statistical error are given in Tab. 6.3 (considering all 26 bins in x, z and M_{inv}). The comparison of the results for the 'total' data set and the results of the Monte Carlo sample is contradictory. For Collins the results for real data are smaller, whereas for Sivers it is just opposite. The difference for Sivers will be taken into account in the systematical error analogue to Eq. (5.45). For positive hadrons this results in 68 % and for negative hadrons in 36 % of the statistical error.

6.5.6 Left/Right and Top/Bottom Dependence

The results are checked upon their dependence on $\phi_{\mu'}$, the azimuthal angle of the scattered muon in the laboratory frame. Therefore the spectrometer is divided into left and right and into top and bottom. The four parts are defined as follows:

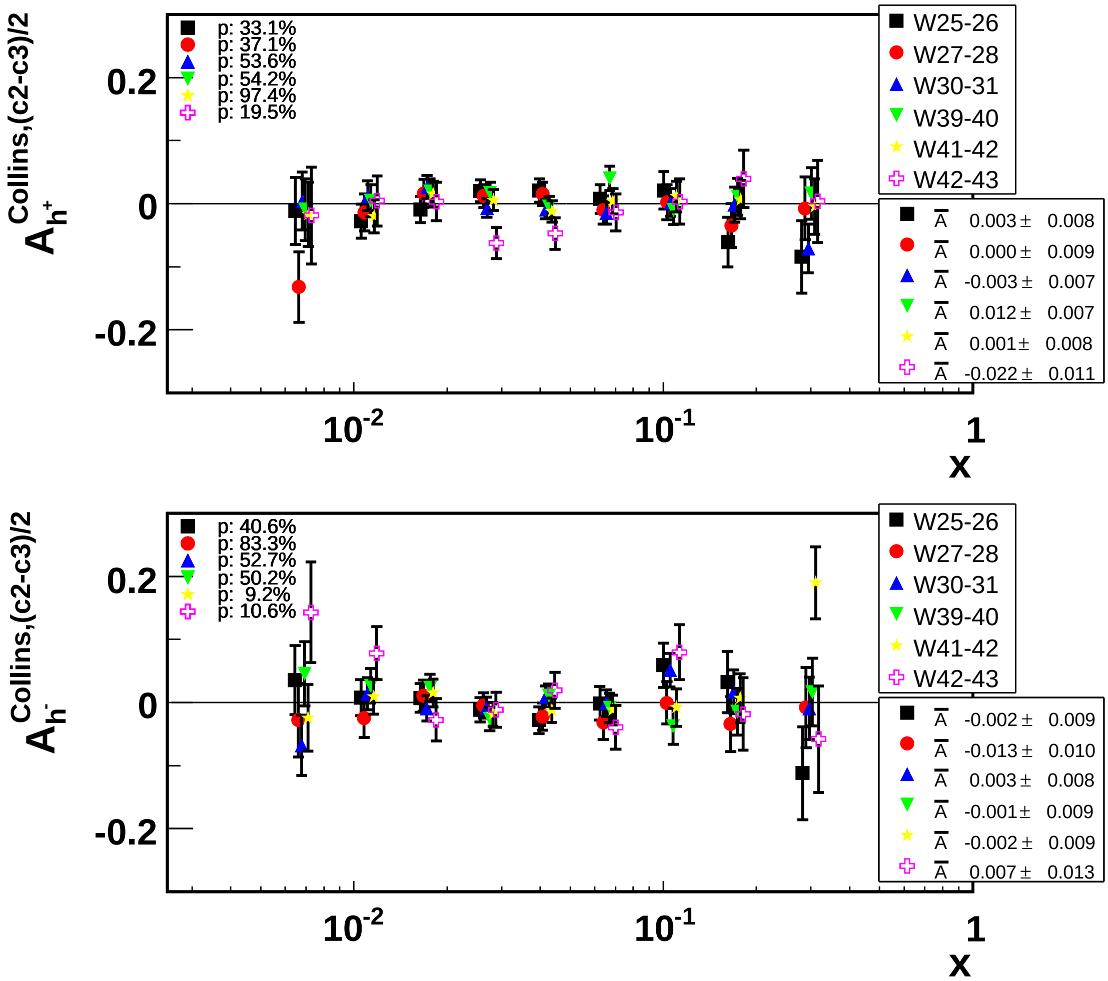

Figure 6.41: Results of $A^{(c2-c3)/2}_{Collins}$ for positive (top) and negative (bottom) hadrons for the six double periods as a function of x. Mean values, $\bar{\mathrm{A}}$, and probabilities, p, of χ^2 test with respect to $A^{(c2-c3)/2}_{Collins} = 0$ are given.

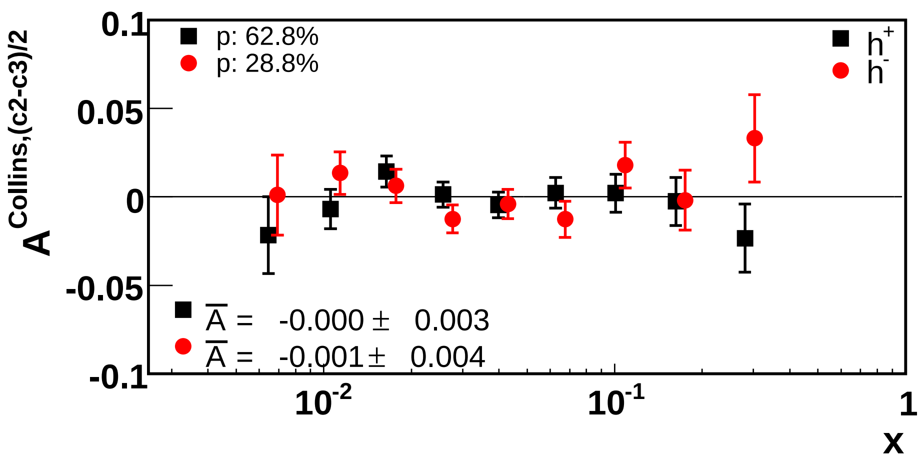

Figure 6.42: Results of $A^{(c2-c3)/2}_{Collins}$ for positive and negative hadrons for the 'total' data set as a function of x. Mean values, $\bar{\mathrm{A}}$, and probabilities, p, of χ^2 test with respect to $A^{(c2-c3)/2}_{Collins} = 0$ are given.

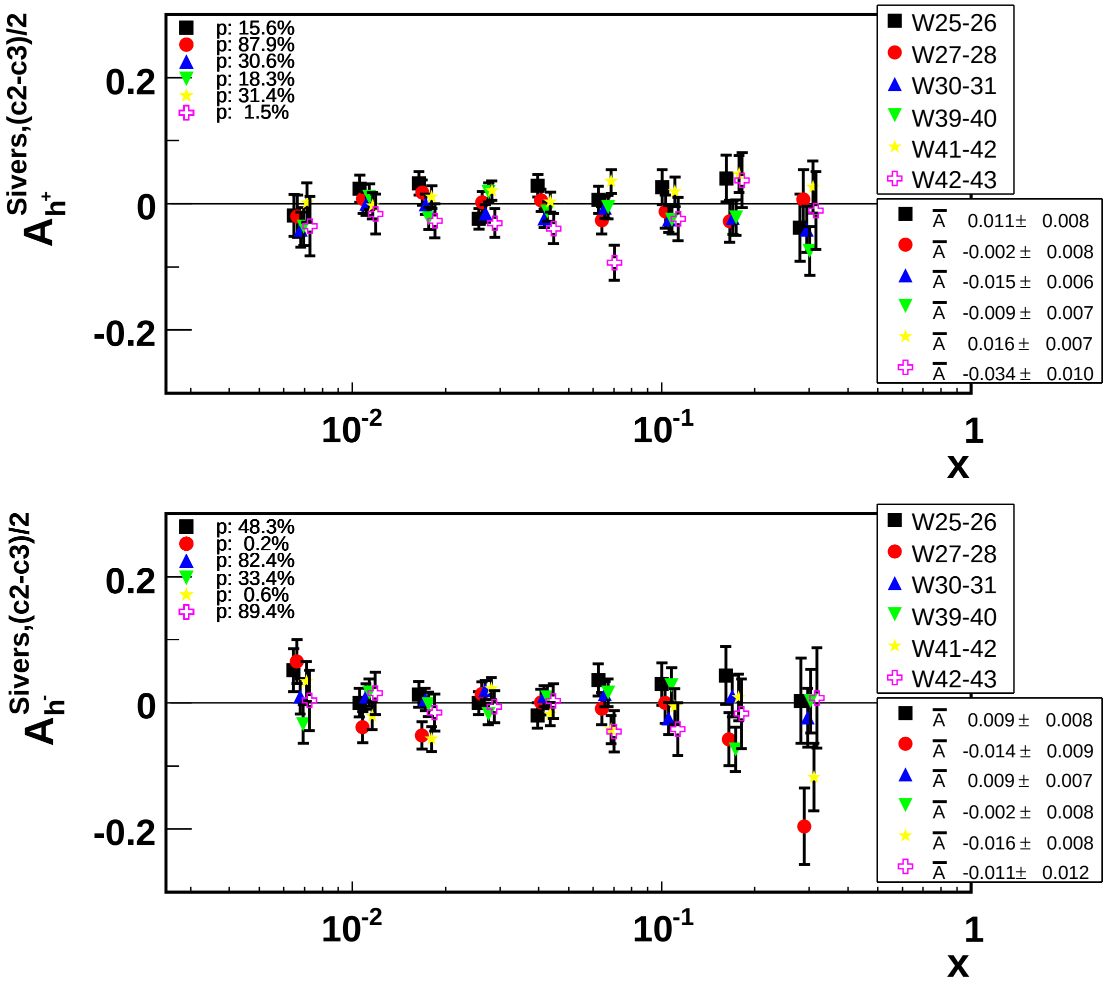

Figure 6.43: Results of $A_{Sivers}^{(c2-c3)/2}$ for positive (top) and negative (bottom) hadrons for the six double periods as a function of x. Mean values, Ā, and probabilities, p, of χ^2 test with respect to $A_{Sivers}^{(c2-c3)/2} = 0$ are given.

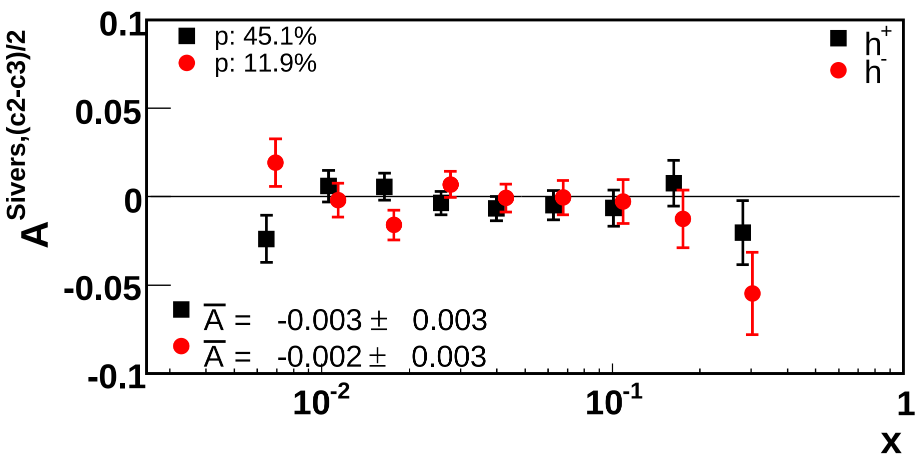

Figure 6.44: Results of $A_{Sivers}^{(c2-c3)/2}$ for positive and negative hadrons for the 'total' data set as a function of x. Mean values, Ā, and probabilities, p, of χ^2 test with respect to $A_{Sivers}^{(c2-c3)/2} = 0$ are given.

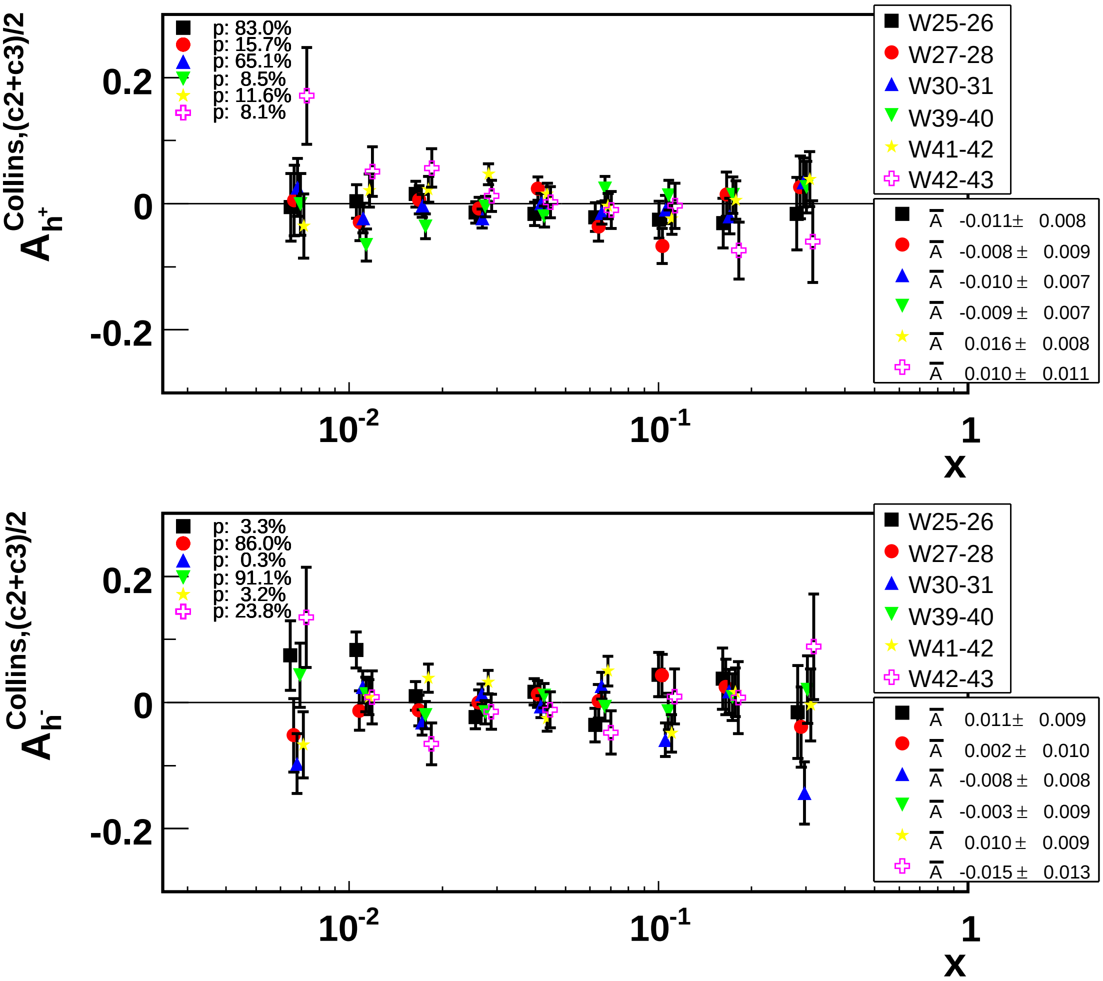

Figure 6.45: Results of $A_{Collins}^{(c2+c3)/2}$ for positive (top) and negative (bottom) hadrons for the six double periods as a function of x. Mean values, $\bar{\mathrm{A}}$, and probabilities, p, of χ^2 test with respect to $A_{Collins}^{(c2+c3)/2} = 0$ are given.

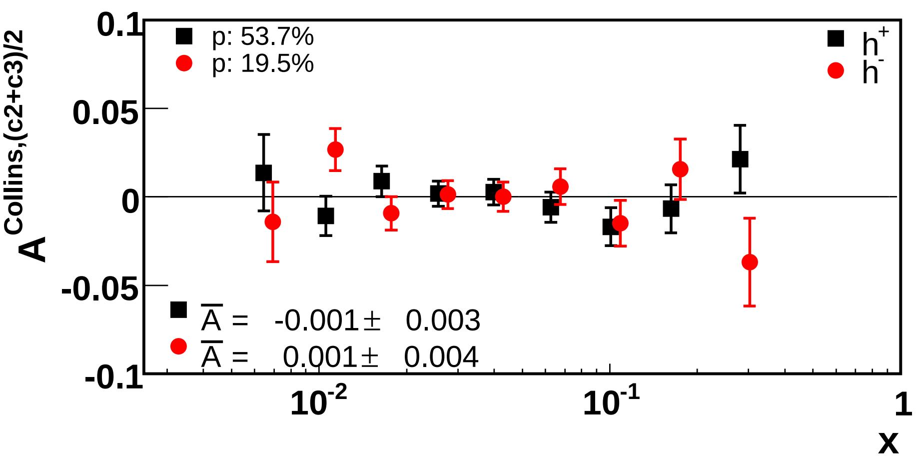

Figure 6.46: Results of $A_{Collins}^{(c2+c3)/2}$ for positive and negative hadrons for the 'total' data set as a function of x. Mean values, $\bar{\mathrm{A}}$, and probabilities, p, of χ^2 test with respect to $A_{Collins}^{(c2+c3)/2} = 0$ are given.

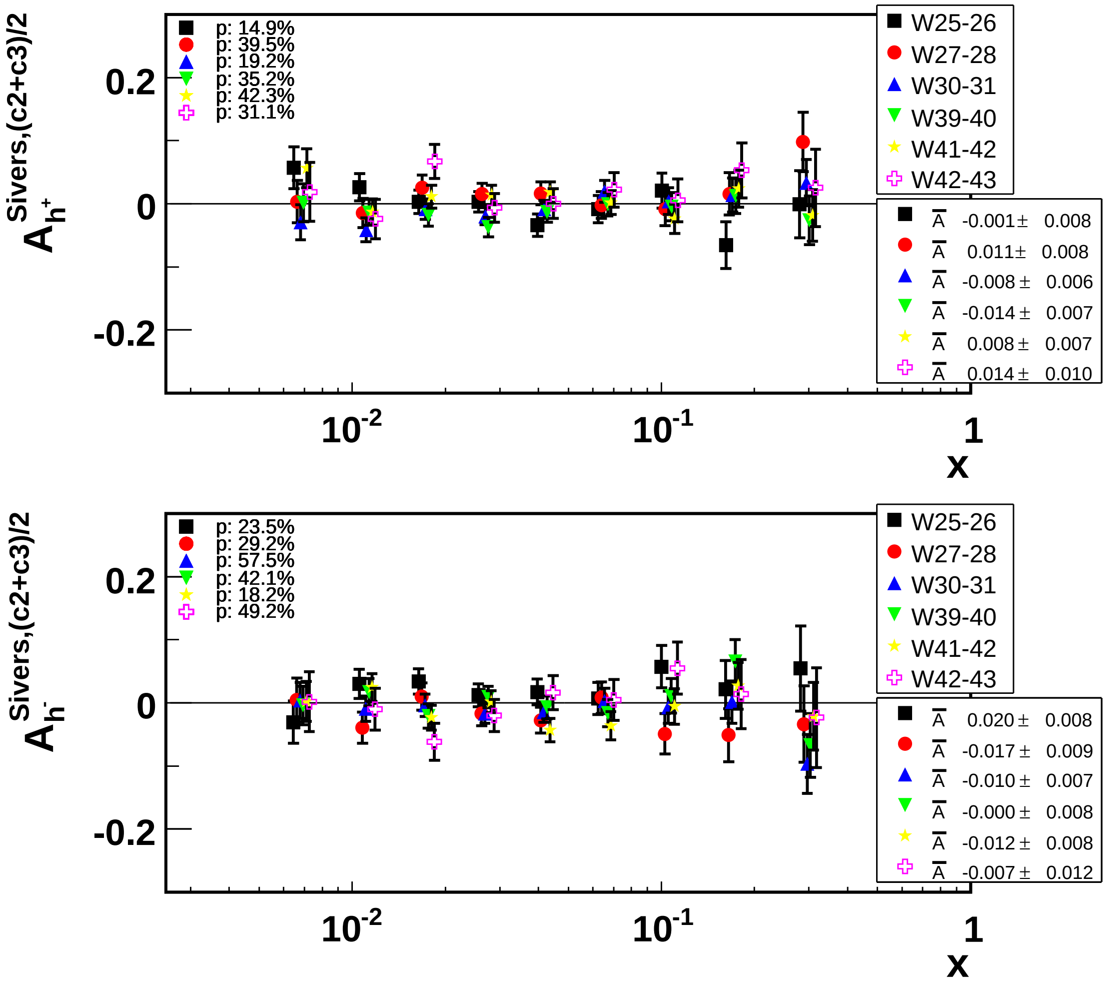

Figure 6.47: Results of $A_{Sivers}^{(c2+c3)/2}$ for positive (top) and negative (bottom) hadrons for the six double periods as a function of x. Mean values, Ā, and probabilities, p, of χ^2 test with respect to $A_{Sivers}^{(c2+c3)/2} = 0$ are given.

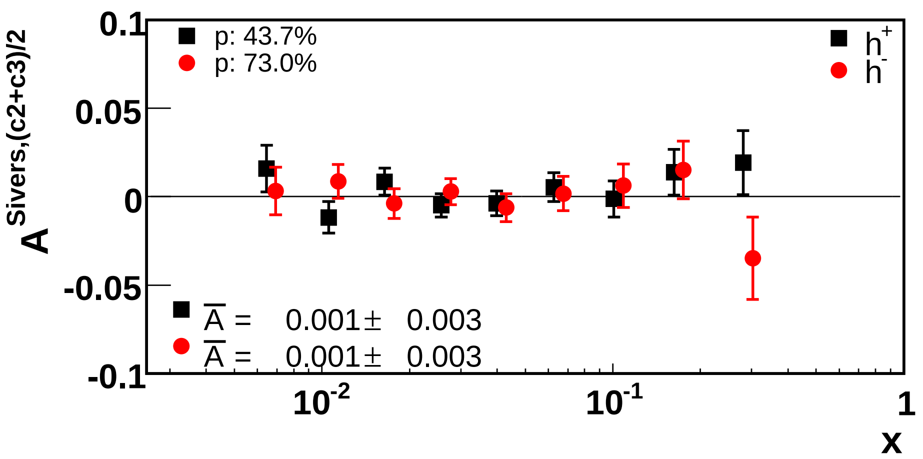

Figure 6.48: Results of $A_{Sivers}^{(c2+c3)/2}$ for positive and negative hadrons for the 'total' data set as a function of x. Mean values, Ā, and probabilities, p, of χ^2 test with respect to $A_{Sivers}^{(c2+c3)/2} = 0$ are given.

- Left (c20s1): $0 \leq \phi_{\mu'} < \pi/2$ and $3/2\pi \leq \phi_{\mu'} < 2\pi$
- Right (c20s2): $\pi/2 \leq \phi_{\mu'} < 3/2\pi$
- Top (c20s3): $0 \leq \phi_{\mu'} < \pi$
- Bottom (c20s4): $\pi \leq \phi_{\mu'} < 2\pi$

The comparison of the four results for Collins positive hadrons is shown in Fig. C.5. The corresponding pulls are shown on the top in Fig. 6.49. On the left for $A^{c20s1}_{Collins}$ and $A^{c20s2}_{Collins}$ (left/right) and on the right for $A^{c20s3}_{Collins}$ and $A^{c20s4}_{Collins}$ (top/bottom). The latter pull shows a shifted mean and an enlarged RMS. Comparison with the results obtained with Monte Carlo Data (Fig. C.9 top) shows, that in both cases the means are shifted. However, the RMS of the pull for top/bottom (top right picture) is smaller than for real data. The results for Collins negative hadrons are shown in Fig. C.6 and the pulls on the bottom in Fig. 6.49. Compared to Monte Carlo results, shown on the bottom in Fig. C.9, the width of the distributions are compatible with each other. But the mean value of the pull for left/right is larger for real data.

The results for Sivers asymmetries for positive hadrons are shown in Fig. C.7 and for negative hadrons in Fig. C.8. The corresponding pulls between left/right and top/bottom results are illustrated in Fig. 6.50. On the top for positive and on the bottom for negative hadrons. The RMS values of all four pulls are compatible with one within the statistical error. The mean values however are not compatible with zero. This is also true for Monte Carlo data (see Fig. C.10), but the deviations from zero of the mean values are smaller.

Even though for Monte Carlo data the pulls are not centered at zero too, the mean values are in general smaller. Therefore the deviations for real data are taken into account in the systematical error. For the evaluation of the systematical error, for each charge and for Collins and Sivers the largest mean value with half its size is taken into account.

6.5.7 Summary of Systematical Error

The summary of the systematical errors for both charges for Collins and Sivers asymmetries is shown in Tab. 6.4. The total systematical error is taken as square root of the squared sum of the single contributions. As in the analysis of the hadron pairs a scale error of 3 % is assigned, taking into account the uncertainties of the target polarization and of the target dilution factor. The systematical errors are finally:

- $\sigma^{sys}_{Collins,h^+} = \sqrt{(0.30 \cdot \sigma^{stat})^2 + \left(0.03 \cdot |A^{Collins,h^+}|\right)^2}$
- $\sigma^{sys}_{Collins,h^-} = \sqrt{(0.20 \cdot \sigma^{stat})^2 + \left(0.03 \cdot |A^{Collins,h^-}|\right)^2}$
- $\sigma^{sys}_{Sivers,h^+} = \sqrt{(1.03 \cdot \sigma^{stat})^2 + \left(0.03 \cdot |A^{Sivers,h^+}|\right)^2}$
- $\sigma^{sys}_{Sivers,h^-} = \sqrt{(0.67 \cdot \sigma^{stat})^2 + \left(0.03 \cdot |A^{Sivers,h^-}|\right)^2}$

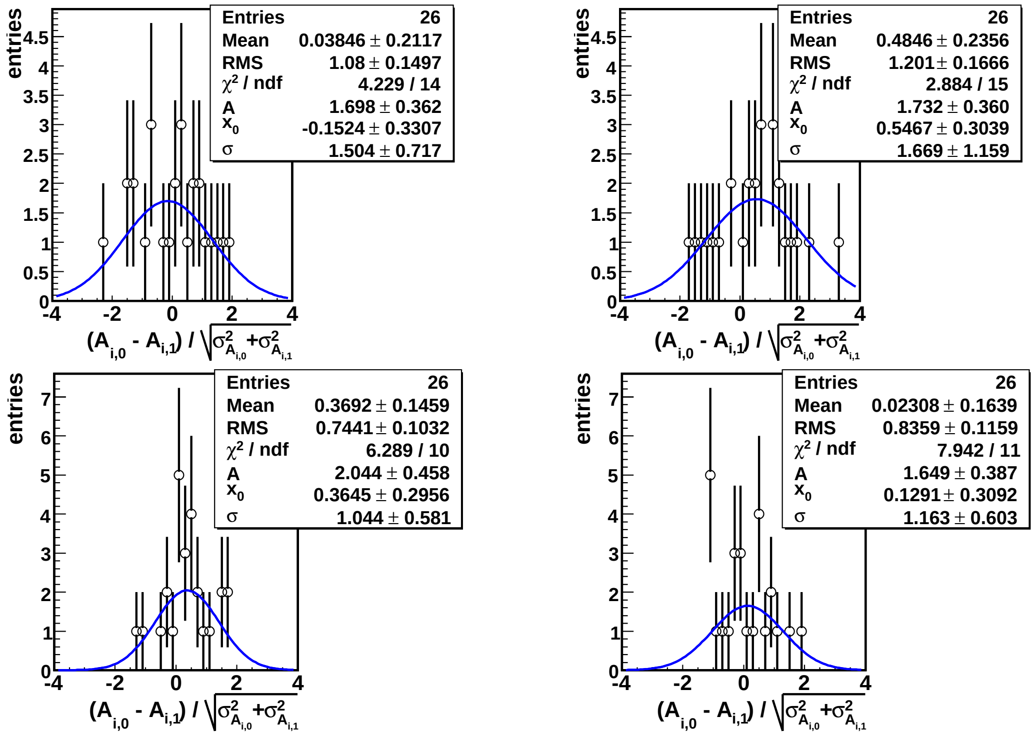

Figure 6.49: Pulls between Collins results for positive (top) and negative (bottom) hadrons. Left: μ' detected in left or right half. Right: μ' detected in top or bottom half.

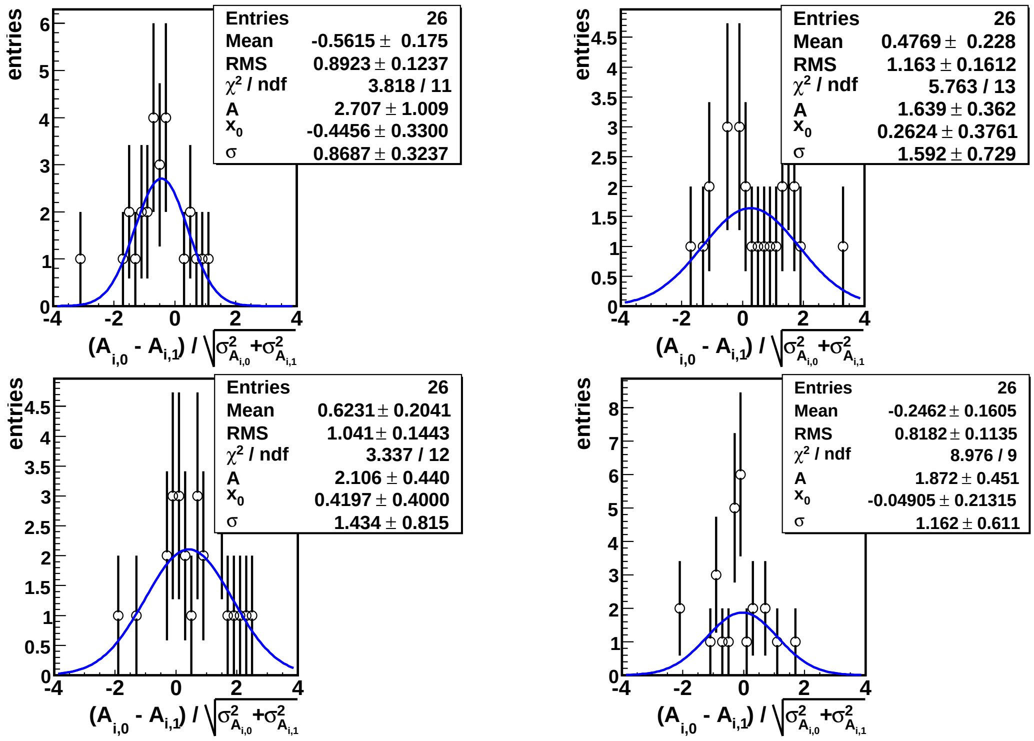

Figure 6.50: Pulls between Sivers results for positive (top) and negative (bottom) hadrons. Left: μ' detected in left or right half. Right: μ' detected in top or bottom half.

Table 6.4: Summary of systematical error for Collins and Sivers asymmetries for positive and negative hadrons. The total error is obtained as square root of the quadratic sum.

Type	$\sigma^{sys}/\sigma^{stat}$			
	Collins h^+	Collins h^-	Sivers h^+	Sivers h^-
estimators	0.18	0.08	0.11	0.03
period compatibility	0	0	0.63	0.48
False asymmetries	0	0	0.68	0.36
Detector segments	0.25	0.18	0.28	0.30
Total	0.30	0.20	1.03	0.67

Very striking is the difference in the size of the systematical errors for Collins and Sivers asymmetries. In addition the systematical errors for positive hadrons is larger than the ones for negative hadrons.

6.6 Final Results

The final results, including the systematical error for the Collins asymmetry as a function of x, z and p_T are presented in Fig. 6.51. For Sivers the results are shown in Fig. 6.52. The mean Collins asymmetries for positive and negative hadrons are:

- $A_{h^+}^{Collins} = -0.011 \pm 0.003_{stat} \pm 0.001_{sys}$
- $A_{h^-}^{Collins} = +0.012 \pm 0.004_{stat} \pm 0.001_{sys}$

The mean Sivers asymmetries for positive and negative hadrons are:

- $A_{h^+}^{Sivers} = +0.018 \pm 0.003_{stat} \pm 0.003_{sys}$
- $A_{h^-}^{Sivers} = -0.005 \pm 0.003_{stat} \pm 0.002_{sys}$

6.6.1 Comparison With Other Experiments and Predictions

In Fig. 6.53 the Collins asymmetries of this thesis for unidentified charged hadrons are compared to the Collins results for identified charged pions of the HERMES group [106]. The HERMES values are scaled with $-1/D_{nn}$. The minus sign takes into account the different definitions of $\Phi_{Collins}$ and the transverse spin transfer coefficient D_{nn} takes care of the different y-domains of the two experiments. For HERMES the D_{nn} values for each bin are approximated with the corresponding mean values of y taken from [107]. Looking at the asymmetries as a function of x one sees that COMPASS provides for the first time results to much smaller values of x. However, the statistical precision of the COMPASS results in the large x-region is worse compared to HERMES. This is due to the small fraction of polarizable protons (target dilution), which directly scales the errors. For the comparison in z and p_T a cut on $x > 0.032$ is applied to adjust the x-range of both experiments. Due to low statistics the last two bins in p_T are combined. The two measurements agree pretty well with each other. This result is not obvious, because HERMES and COMPASS cover quite different domains in Q^2, with $\langle Q^2 \rangle \approx 2.4\,(\mathrm{GeV}/c)^2$ for HERMES and $\langle Q^2 \rangle \approx 5\,(\mathrm{GeV}/c)^2$ for COMPASS, when applying the cut $x > 0.032$.

In Fig. 6.54 the Collins results are compared to recent predictions of Anselmino et al. [108]. The predictions are based on a combined fit of Collins asymmetries for identified charged pions from COMPASS (deuteron) and HERMES (proton) and of the Collins FF measured by Belle [83, 106, 42]. As one can see the data is pretty well described by this prediction. In Fig. 6.55 a recent extraction of the transversity distribution for up and down quarks as a function of x and k_T is shown [108]. It is positive for up quarks and negative for down quarks. Compared to the helicity distribution, which is also shown as dashed line, it is smaller for both quark flavors. This is important since in a non relativistic theory both distributions should be equal, because they can be transformed into each other by a rotation. In the same analysis the favored and the disfavored Collins fragmentation functions have been extracted, too. The results are shown in Fig. 6.56, where the Collins fragmentation function is denoted with $\Delta^N D$. As a result of the large negative Collins asymmetries for negative hadrons the disfavored fragmentation function is negative and approximately three times larger in amplitude than the favored one. It should be kept in mind that some assumptions were needed to obtain the results, namely a Gaussian k_T and p_T dependence of the distribution functions and the fragmentation functions, respectively, to factorize the convolutions in Eq. (6.2). Another assumption is made about the evolution of the Collins FF $\Delta_T^0 D_q^h$ measured by Belle at $Q^2 = 110\,\mathrm{GeV}^2/c^2$ to the much smaller energies of HERMES and COMPASS of about $Q^2 \simeq 2.5\,\mathrm{GeV}^2/c^2$. This Q^2 evolution is not known and it is assumed that it is the same as for the unpolarized FF D_q^h. All these assumptions are not needed, when extracting transversity from the data of two hadron pairs, since the distribution functions and the two hadron fragmentation functions appear already factorized as products in Eq. (5.2) and the Q^2 evolution of the two hadron fragmentation functions, measured by Belle, to COMPASS and HERMES energies is known [49].

The comparison of the Sivers asymmetries of this thesis for unidentified charged hadrons with the published results of HERMES for identified charged pions [110] is shown in Fig. 6.57 as a function of x, z and p_T. For the comparison in z and p_T a cut on $x > 0.032$ is applied to account for the different x-ranges. Again, due to low statistics the last two bins in p_T are combined. The agreement of the two measurements is rather good, whereas the results of this thesis seem to be systematically smaller than the HERMES values. However, keeping in mind the systematical uncertainty, both results are compatible with each other. For negative hadrons both results are compatible with zero.

In Fig. 6.58 recent predictions from Anselmino et al. [111] and Arnold et al [112], are shown, which both are based on a combined fit of HERMES proton [106] and COMPASS deuteron [83] results. The prediction of Arnold et al. seems to describe the results for negative hadrons better than the prediction of Anselmino et al. However, for positive hadrons it seems to be opposite. Especially in the low x-region the data is described better by the prediction of Anselmino et al.

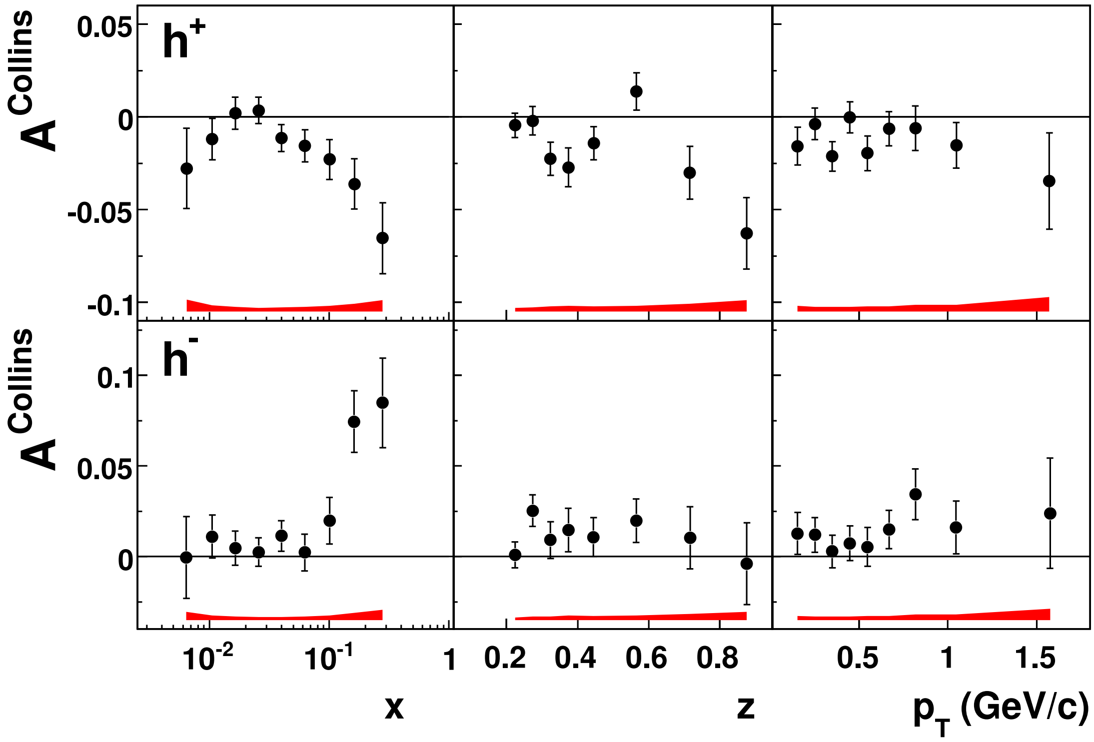

Figure 6.51: Collins asymmetries as a function of x, z and p_T including systematical errors, for positive hadrons (top) and negative hadrons (bottom).

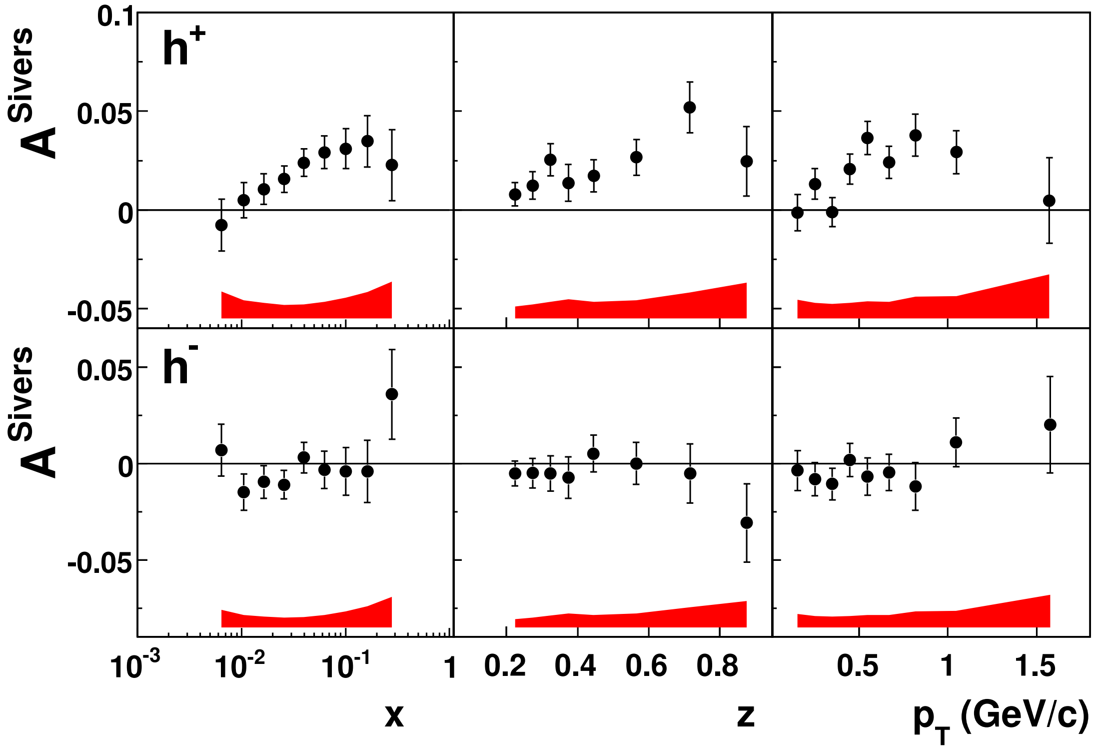

Figure 6.52: Sivers asymmetries as a function of x, z and p_T including systematical errors, for positive hadrons (top) and negative hadrons (bottom).

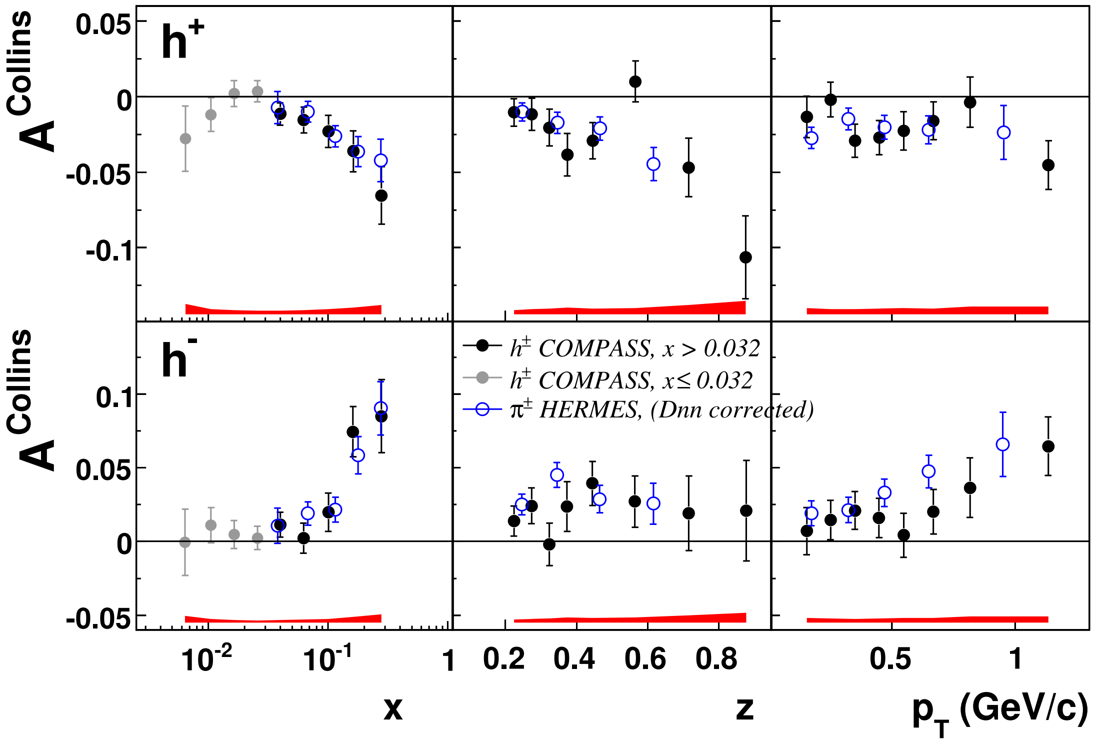

Figure 6.53: Collins asymmetries as a function of x, z and p_T, for positive hadrons (top) and negative hadrons (bottom) compared to HERMES results [106], scaled with $-1/D_{nn}$, as described in the text.

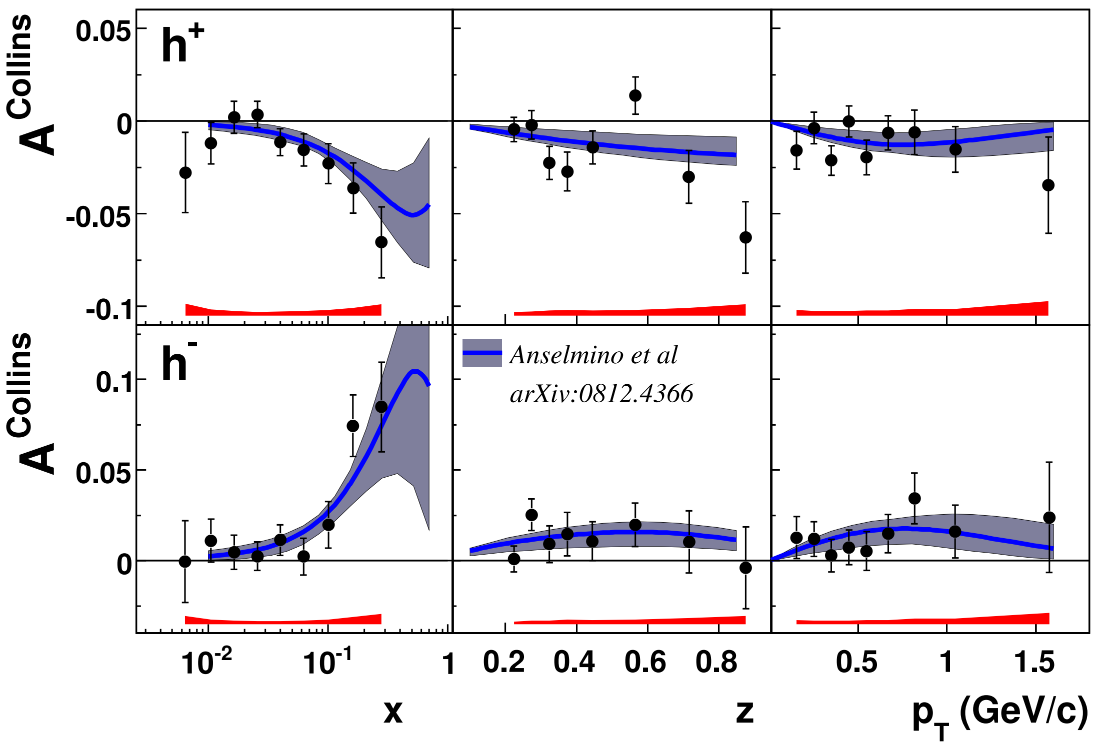

Figure 6.54: Collins asymmetries as a function of x, z and p_T, for positive hadrons (top) and negative hadrons (bottom) compared to predictions [108].

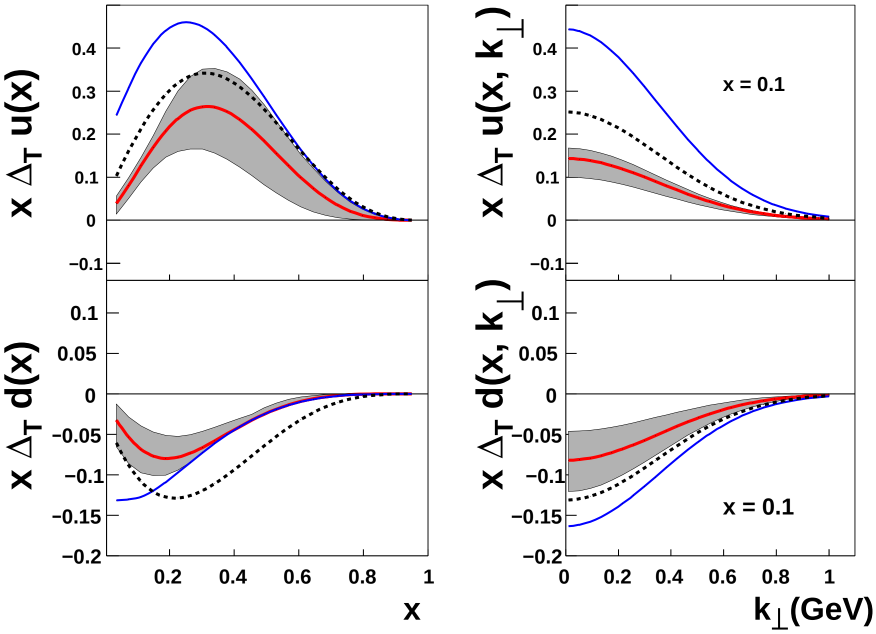

Figure 6.55: Recent extraction of the transversity distribution (red solid line) for up and down quarks at $Q^2 = 2.4\,\mathrm{GeV}^2/c^2$. On the left as a function of x and on the right as a function of $k_\perp$ for $x = 0.1$. The Soffer bound (blue solid line) and the helicity distribution (dashed line) are shown, too [108].

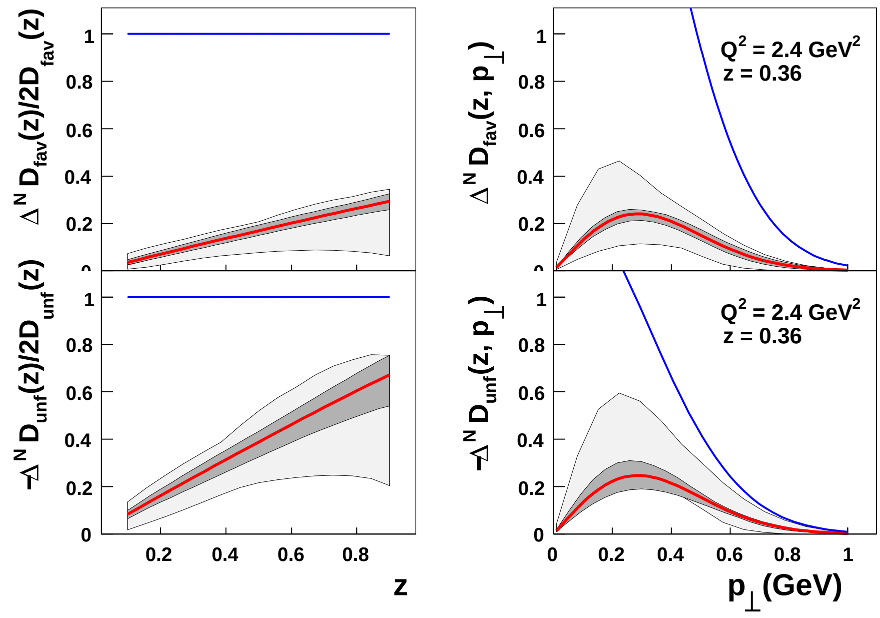

Figure 6.56: Recent extraction of the Collins fragmentation function (red solid line) for favored (top) and unfavored (bottom) fragmentation at $Q^2 = 2.4\,\mathrm{GeV}^2/c^2$. Notice the negative sign of the disfavored fragmentation function. On the right as a function of p_T for $z = 0.36$ and on the left the z dependence of the p_T integrated function. The blue solid line indicates the positivity bound $\Delta^N D \leq 2D_1$. The dark grey shaded area is the uncertainty of this extraction [108] and the light grey shaded area of the previous one [109].

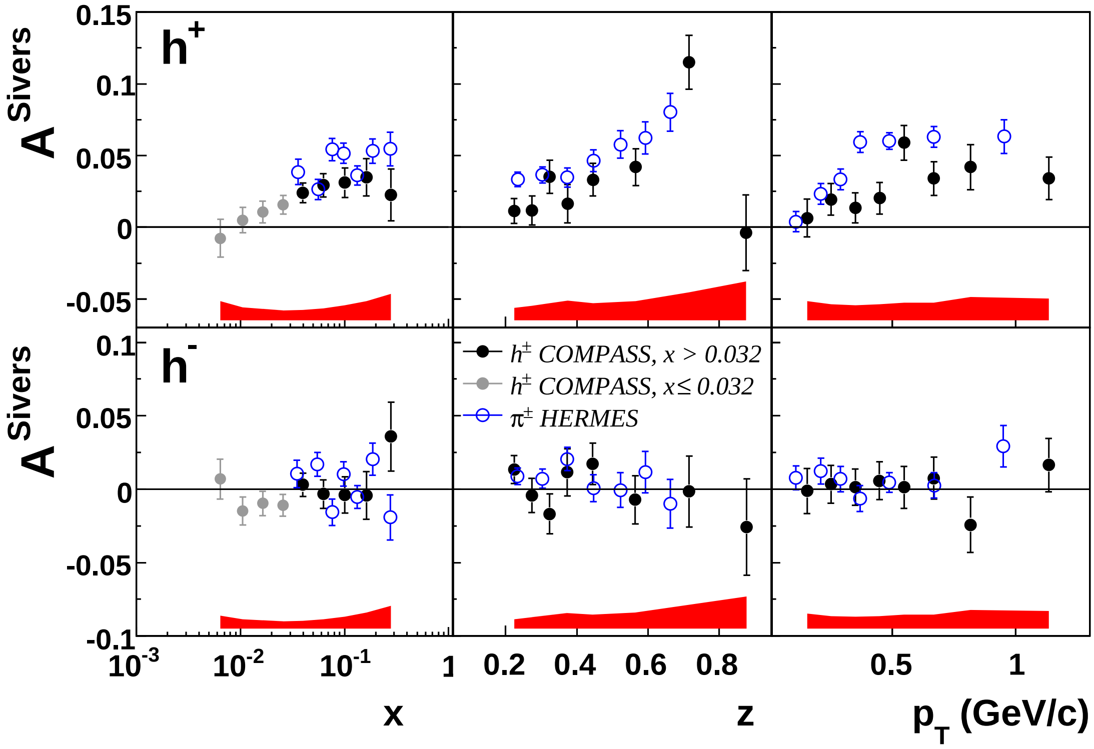

Figure 6.57: Sivers asymmetries as a function of x, z and p_T, for positive hadrons (top) and negative hadrons (bottom) compared to HERMES results [110].

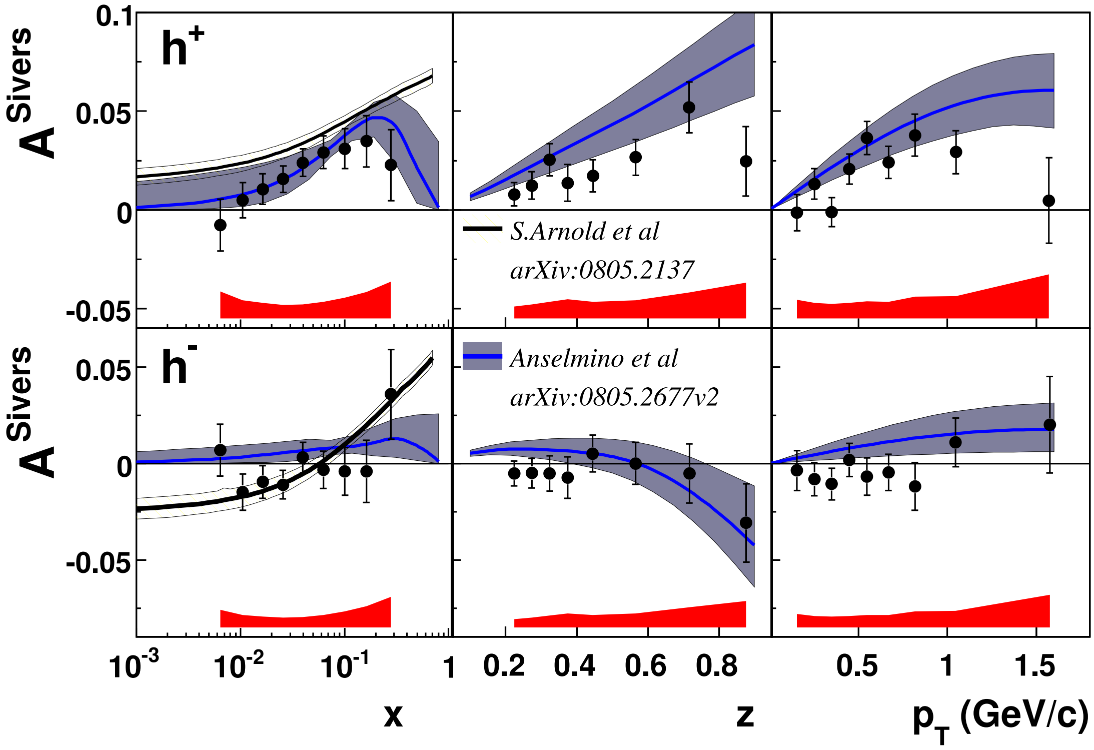

Figure 6.58: Sivers asymmetries as a function of x, z and p_T, for positive hadrons (top) and negative hadrons (bottom) compared to predictions from [111] and [112].

A recent extraction of the Sivers distribution functions at the scale $Q^2 = 2.4\,(\mathrm{GeV}/c)^2$ for u-, d- and s-quarks and as well for the antiquarks $\bar{u}$, $\bar{d}$ and $\bar{s}$ is shown in Fig. 6.59 [111]. The extraction is based on HERMES $\pi^{\pm}$-, π^0- and $K^{\pm}$-Sivers asymmetries for proton target [106] and COMPASS $\pi^{\pm}$- and $K^{\pm}$-Sivers asymmetries for deuteron target [83]. For solving the convolutions in Eq. (6.4), the k_T and p_T dependence of the distribution functions and the fragmentation functions, respectively, was assumed to be Gaussian. On the left the x dependence of the first moment of the k_T integrated Sivers function is shown:

$$\Delta_0^T f^{(1)}(x) = \int \mathrm{d}^2 \boldsymbol{k}_T \frac{\boldsymbol{k}_T}{4M} \Delta_0^T f(x, \boldsymbol{k}_T^2), \tag{6.6}$$

and on the right the k_T dependence of $\Delta_0^T f(x, \boldsymbol{k}_T^2)$. The Sivers function for u-quarks is positive and for d-quarks negative. Remarkable is the size of the Sivers function for $\bar{s}$-quarks, which for $x > 0.1$ and $\boldsymbol{k}_T > 0.3$, respectively, saturates the positivity bound defined in Eq. (2.29). The results for $\bar{u}$-, $\bar{d}$- and s-quarks are less constrained by the available data. The discussion about the result for $\bar{s}$-quarks will be revisited in Sec. 6.6.2, when discussing the K^+-Sivers asymmetries of this thesis and the new HERMES results, which have been published very recently [110].

6.6.2 Results of Identified Pions and Kaons

As for the hadron pairs the RICH detector is used to identify pions and kaons. The same cuts, as described in Sec. 5.3.8, are applied for the identification. Since these cuts are preliminary no systematical uncertainties have been evaluated. For the asymmetries only statistical errors are shown. In Fig. 6.60 and Fig. 6.61 the Collins asymmetries for pions and kaons, compared to the HERMES results [106], are shown. As for unidentified hadrons a cut $x > 0.032$ is applied for the evaluation of the asymmetries in z and p_T. The agreement for pions between COMPASS and HERMES results is good. For positive kaons the agreement is also reasonably good. For negative kaons it is more difficult, because of the large error bars. For COMPASS the results are compatible with zero. For HERMES they are small too but with the tendency to be negative.

The Sivers asymmetries for identified pions and kaons, compared to the HERMES results [110], are shown in Fig. 6.62 and 6.63, respectively. Of course, since 80 % of the particles in COMPASS are pions, the asymmetries are quite similar to the unidentified ones. The measured asymmetry for positive kaons is slightly larger than for positive pions. Compared to the HERMES results they are quite compatible. The results for negative kaons are for both measurements compatible with zero.

Interesting will be the interpretation of the new K^+ Sivers results by theorists, because problems to describe the previous HERMES results, which showed a huge asymmetry at $x \simeq 0.1$ [106] have been reported [111]. This spoiled the consistent description of pion and kaon data, because it could not be described with fragmentation functions used up to that time [113]. However, the use of a more recent set of fragmentation functions [114], which include that $D_{\bar{s}}^{K+} \gg D_{\bar{u}}^{K+}$, and a large Sivers function for $\bar{s}$ quarks makes it possible to describe these large K^+ asymmetries. It will be exiting to see which effect the new, smaller K^+ asymmetries, have on the strange quark Sivers function.

Incorporating these results for identified charged pions and kaons of the Collins and the Sivers asymmetries in the global analyses, will certainly reduce the uncertainties of the

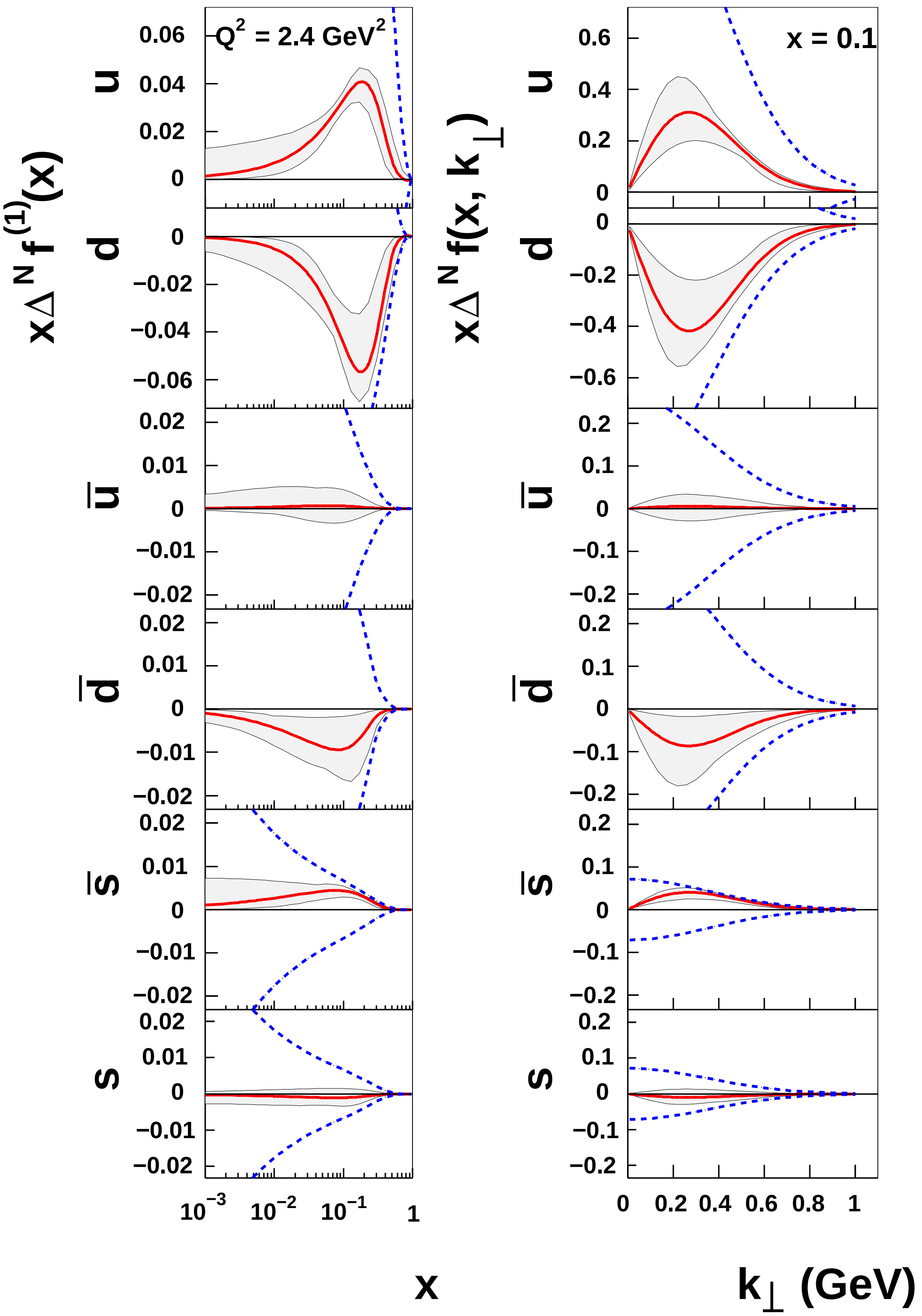

Figure 6.59: Recent extraction of the Sivers distribution functions as a function of x and k_T for the three light quark and antiquark flavors [111]. Here the Sivers function is denoted with $\Delta^N f$. The dashed lines show the positivity limits $|\Delta^N f| = 2f$ defined in Eq. (2.29)), where f is the momentum distribution. See text for further details.

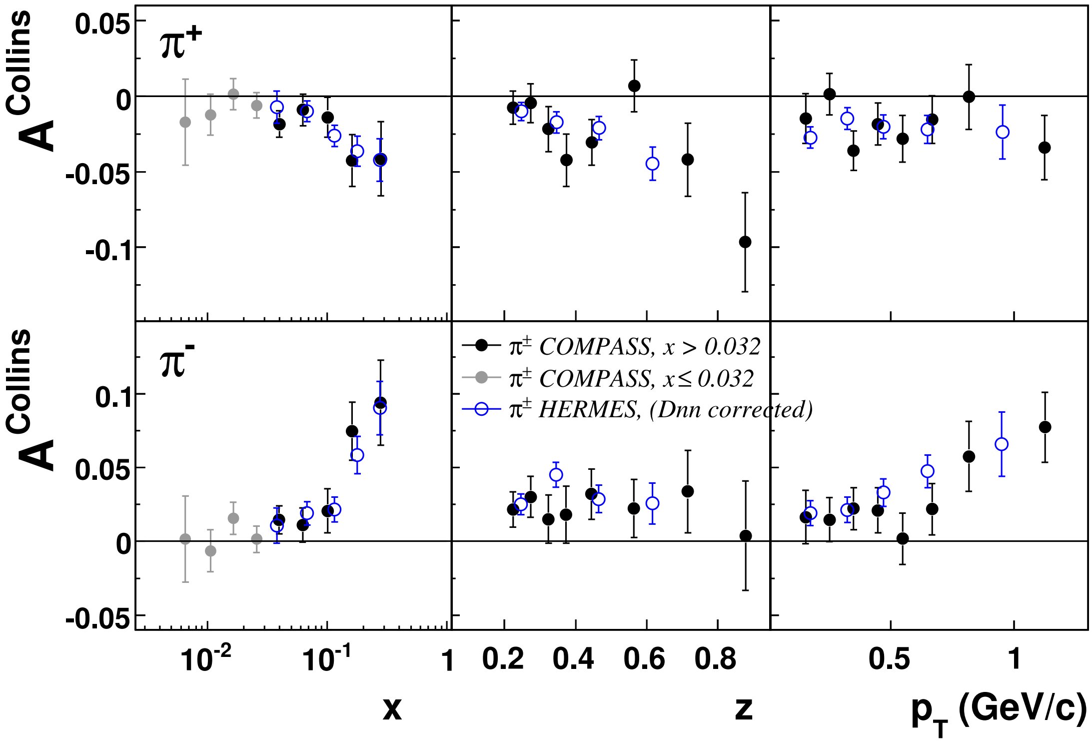

Figure 6.60: Collins asymmetries as a function of x, z and p_T, for positive pions (top) and negative pions (bottom) compared to HERMES results [106], scaled with $-1/D_{nn}$.

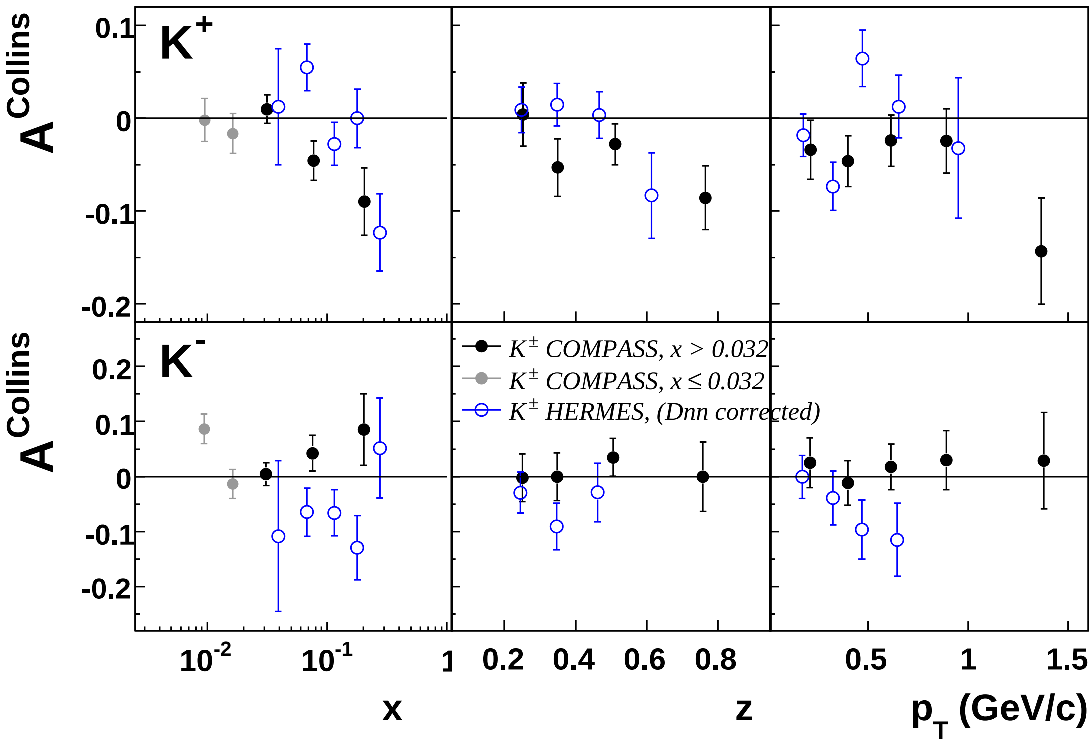

Figure 6.61: Collins asymmetries as a function of x, z and p_T, for positive kaons (top) and negative kaons (bottom) compared to HERMES results [106], scaled with $-1/D_{nn}$.

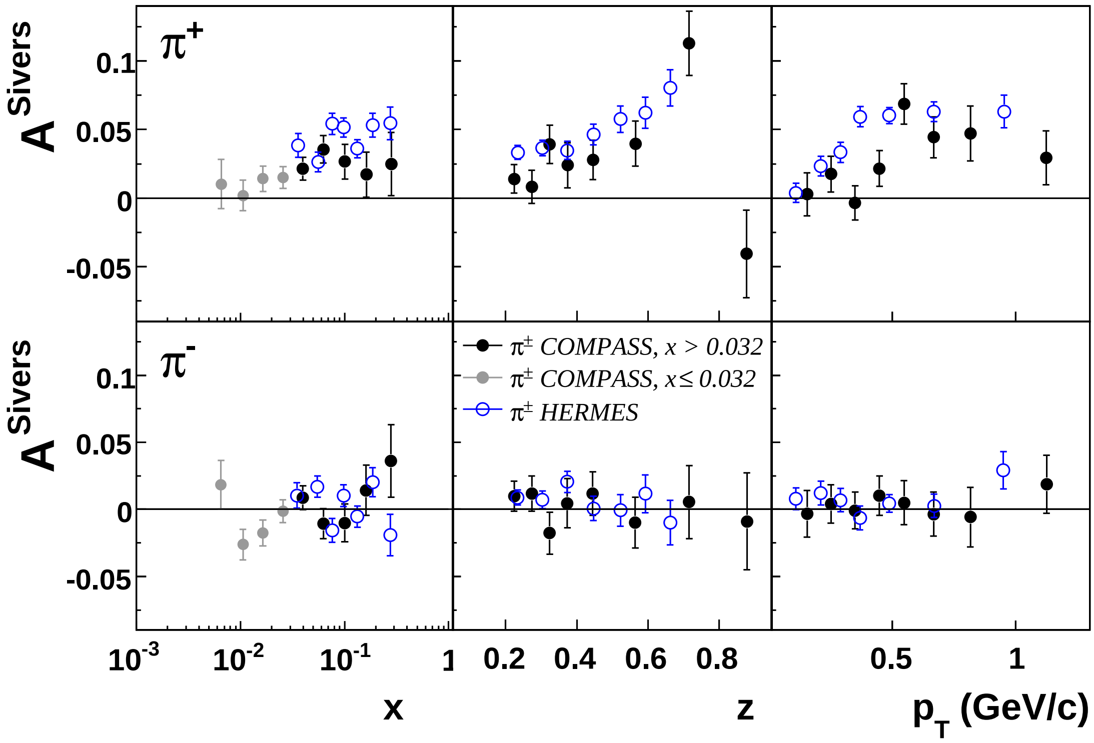

Figure 6.62: Sivers asymmetries as a function of x, z and p_T, for positive pions (top) and negative pions (bottom) compared to HERMES results [110].

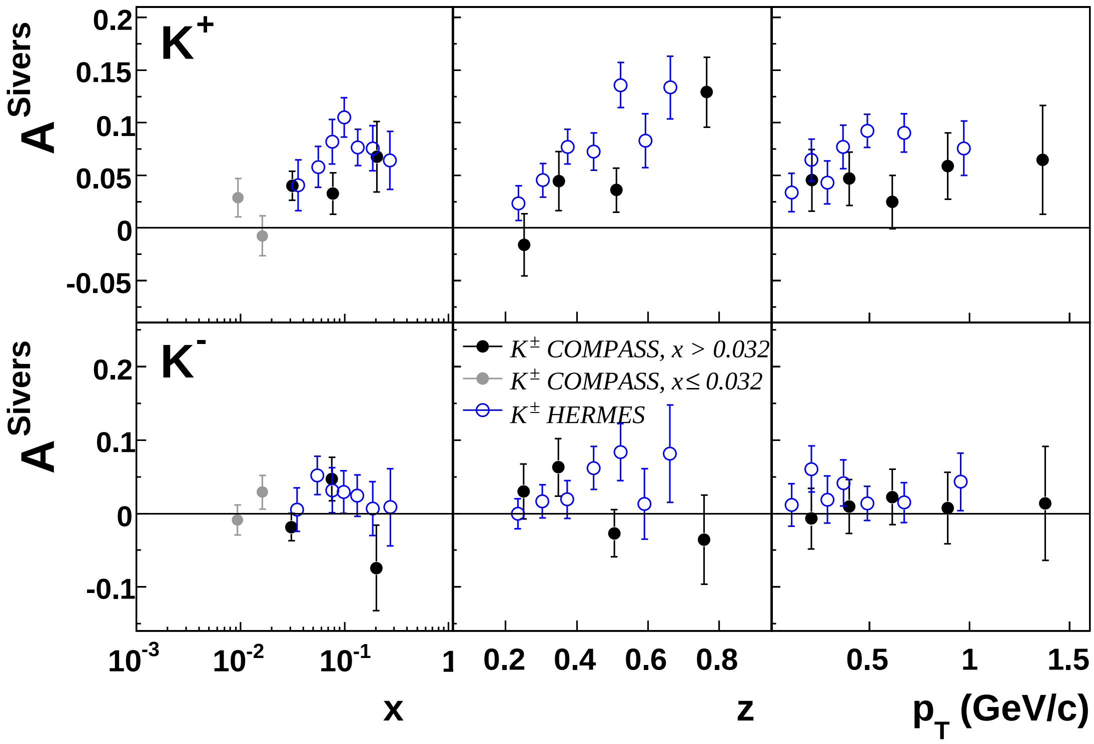

Figure 6.63: Sivers asymmetries as a function of x, z and p_T, for positive kaons (top) and negative kaons (bottom) compared to HERMES results [110].

extractions of the transversity and the Sivers function, respectively. In particular for low x values ($0.003 < x < 0.032$), since at present COMPASS is the only experiment, which covers this region.

7. Summary

In 2007 the COMPASS experiment at CERN has recorded 440 TB of data, scattering a high energy muon beam off transversely polarized protons. In this thesis this data has been analysed for azimuthal single spin asymmetries in the single hadron and the two hadron semi-inclusive deep-inelastic scattering cross-section.

For the extraction of these asymmetries the stability of the detector is essential to minimize systematical uncertainties. In fact, tests with Monte Carlo data showed, that changes in the acceptance of the detector, which do not depend on the Z-position of the primary vertices, i.e. affects the whole target equally, have only a small impact on the extracted asymmetries and are negligible at the present statistical precision. However, introducing a dependence along the target for the change of the acceptance the extracted asymmetries become strongly biased. For monitoring the stability and filtering out deviations, several methods have been developed and applied. In total, about 34 % of the events have been rejected in the analysis.

Several methods have been implemented to extract the asymmetries. In particular a binned maximum likelihood method, using Poisson statistics and an extended unbinned maximum likelihood fit. They have been extensively tested on Monte Carlo data and it could be verified, that they allow for a bias free extraction of the asymmetries. Finally the extended unbinned likelihood method was used for the extraction.

As a main goal the single spin asymmetry A^{RS} present in the semi-inclusive deep-inelastic cross-section of two hadron production has been analysed. This asymmetry is proportional to the product of the transversity distribution and the dihadron interference fragmentation function. The transversity distribution is a leading twist parton distribution function, which is poorly known. It describes the probability to find transversely polarized quarks inside a transversely polarized nucleon.

In this thesis this asymmetry has been extracted for the first time at high Q^2 and for values of Bjorken x in the range of 0.003 - 0.7:

- $A^{RS} = -0.025 \pm 0.004_{stat} \pm 0.003_{sys}$

As a consequence of this measurement it can be concluded that the transversity distribution and the dihadron interference fragmentation function are both sizable. Ultimately, this result can be used in a global fit to determine the transversity distribution function.

As a second goal of this thesis the Collins and the Sivers single spin asymmetries present in the semi-inclusive deep-inelastic cross-section of single hadron production have been analysed. Here the Collins asymmetry $A^{Collins}$ is proportional to a convolution of the transversity distribution and the Collins fragmentation function and the Sivers asymmetry A^{Sivers} is proportional to a convolution of the Sivers distribution and the unpolarized fragmentation function. Both distribution functions appear at leading twist in the cross-section. The Sivers parton distribution function is related to the quark angular orbital momentum inside a transversely polarized nucleon and is therefore of special interest since this could be the crucial piece to solve the nucleon spin puzzle.

The measured Collins asymmetries are sizable in the region $x > 0.05$ for both positive and negative hadrons. They are approximately equal in strength, but opposite in sign. The mean Collins asymmetries for positive and negative hadrons are:

- $A^{Collins}_{h^+} = -0.011 \pm 0.003_{stat} \pm 0.001_{sys}$
- $A^{Collins}_{h^-} = +0.012 \pm 0.004_{stat} \pm 0.001_{sys}$

The size of the Collins asymmetries are approximately only half the size of A^{RS}, emphasizing the good analyzing power of the dihadron interference fragmentation function to measure transversity.

The Sivers asymmetry for positive hadrons is positive over almost the complete x-range. The asymmetry for negative hadrons is small and compatible with zero within the statistical errors. The mean Sivers asymmetries for positive and negative hadrons are:

- $A^{Sivers}_{h^+} = +0.018 \pm 0.003_{stat} \pm 0.003_{sys}$
- $A^{Sivers}_{h^-} = -0.005 \pm 0.003_{stat} \pm 0.002_{sys}$

The Collins and Sivers results of this thesis, extracted for the first time at high Q^2 and for values of Bjorken x in the range of 0.003 - 0.7, can be used in a global analysis. These results will significantly contribute to constraint the transversity and the Sivers functions especially for low Bjorken x.

In the year 2010 the COMPASS experiment will continue to take data with transversely polarized protons. A full year of data taking is foreseen and it is expected that the statistical errors will be improved by a factor of three.

A. Hadron Pairs: Material of Monte Carlo Studies

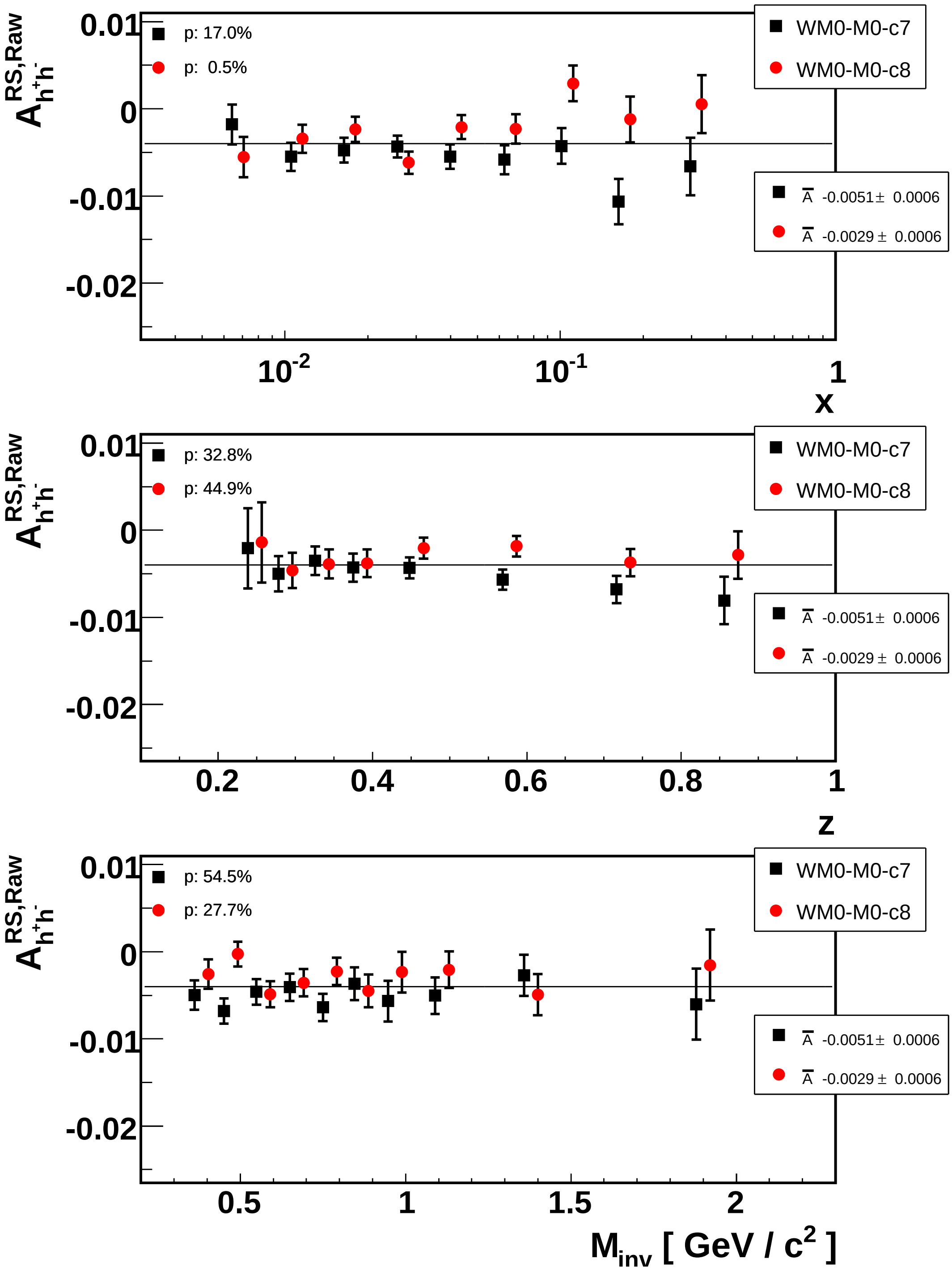

Figure A.1: Raw RS asymmetries for $+--+$ (A^{c7}) and $-++-$ (A^{c8}) Monte Carlo samples with generated asymmetries extracted with UB SA as a function of x, z and M_{inv}. Mean asymmetries, $\bar{\mathrm{A}}$, and probabilities, p, of χ^2 test with respect to $A^{RS}_{MC} = -0.004$ (horizontal lines) are given.

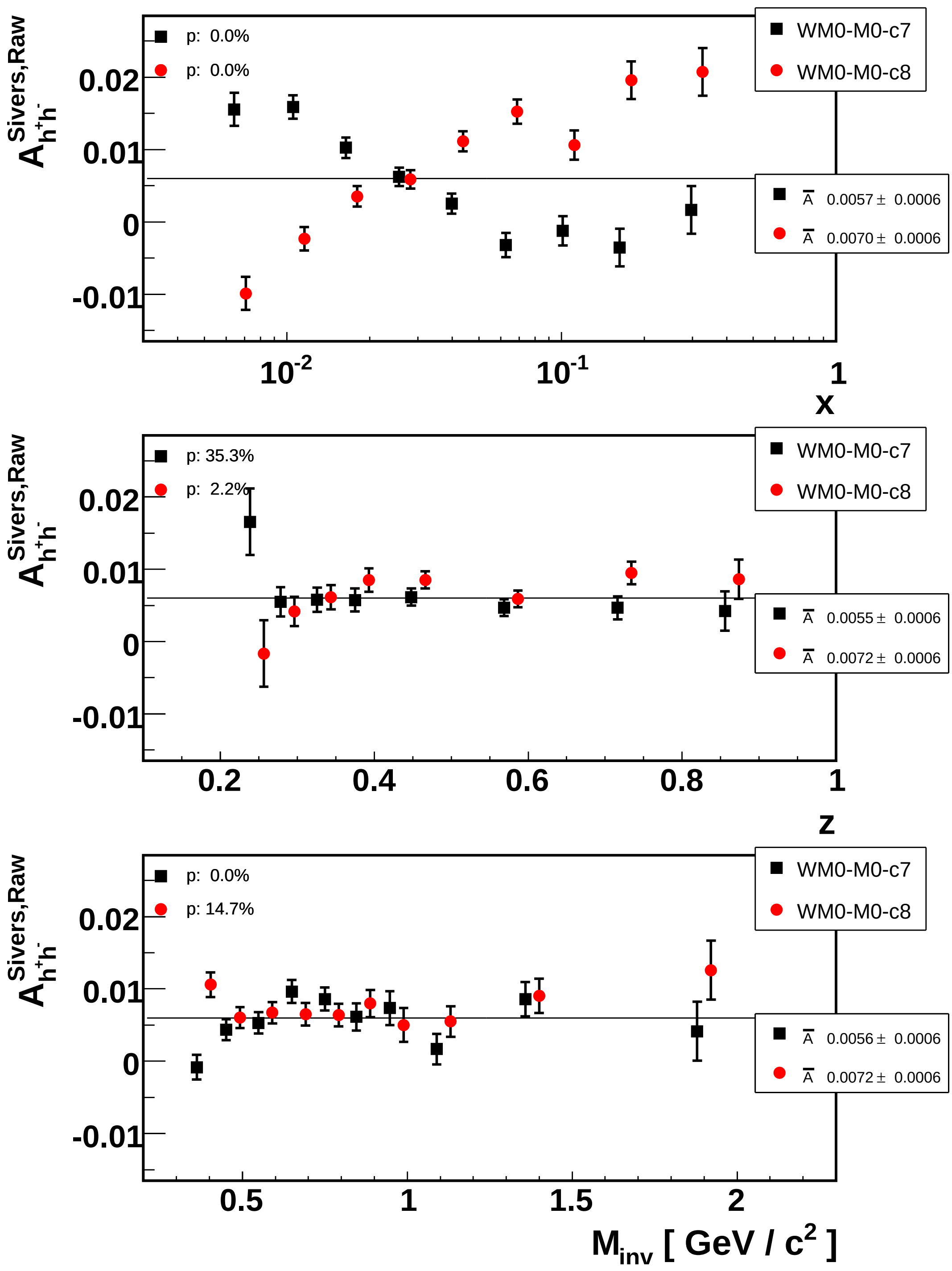

Figure A.2: Raw 'Sivers-like' asymmetries for $+--+$ (A^{c7}) and $-++-$ (A^{c8}) Monte Carlo samples with generated asymmetries extracted with UB SA as a function of x, z and M_{inv}. Mean asymmetries, Ā, and probabilities, p, of χ^2 test with respect to $A^{Sivers}_{MC} = 0.006$ (horizontal lines) are given.

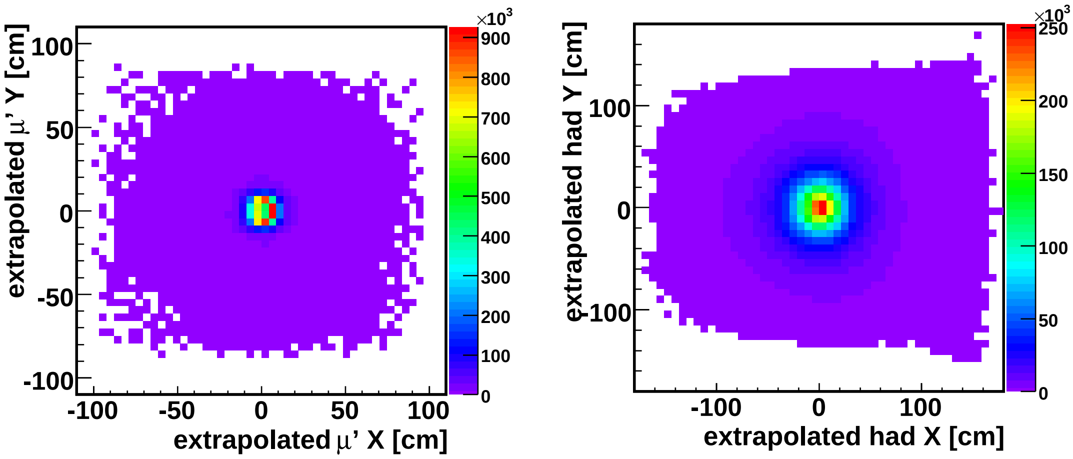

Figure A.3: XY-distribution of extrapolated scattered muon tracks (left) and hadron tracks (right) at $Z = 600\,\mathrm{cm}$ for Monte Carlo data.

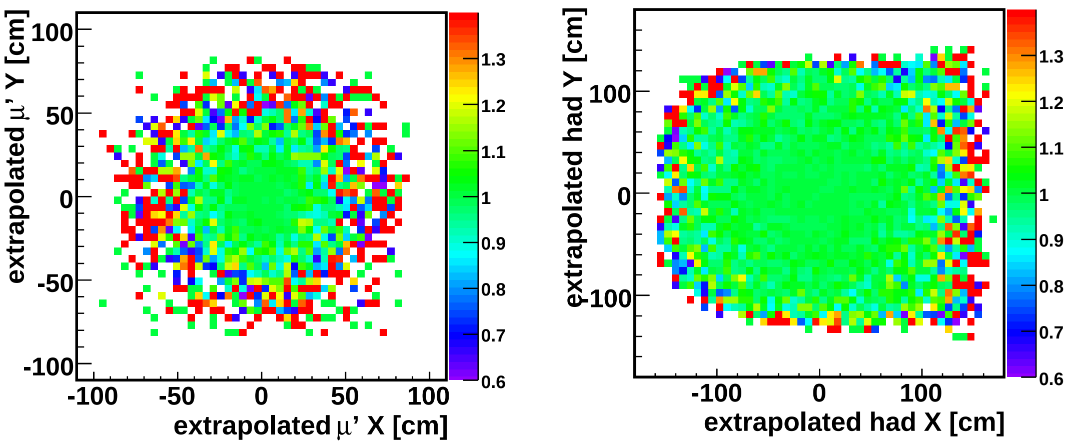

Figure A.4: Ratios of XY-distribution of $+--+$ and $-++-$ samples for extrapolated scattered muon tracks (left) and hadron tracks (right) at $Z = 600\,\mathrm{cm}$ for Monte Carlo data.

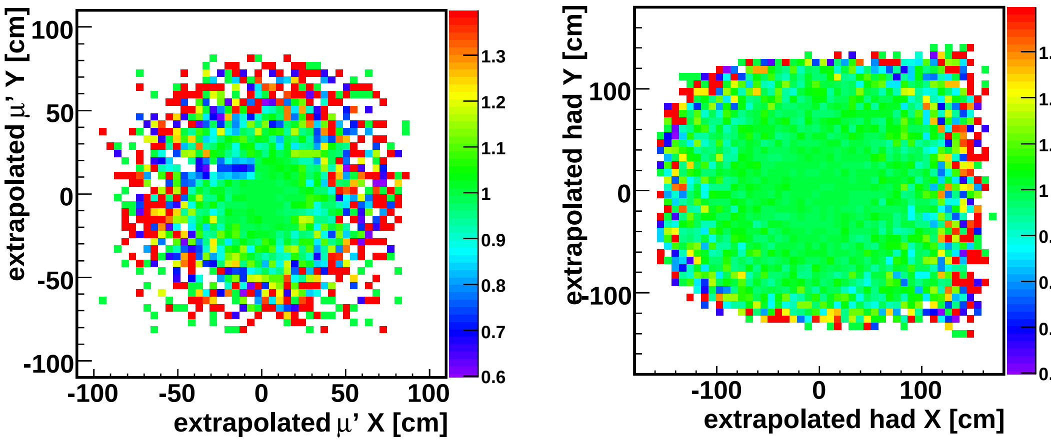

Figure A.5: Ratios of XY-distribution of $+--+$ and $-++-$ samples for extrapolated scattered muon tracks (left) and hadron tracks (right) at $Z = 600\,\mathrm{cm}$ for scenario 1.

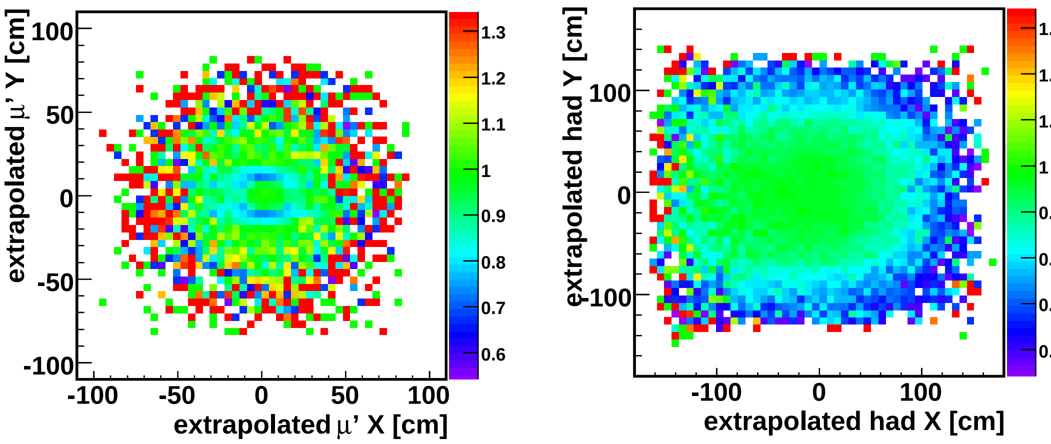

Figure A.6: Ratios of XY-distribution of $+--+$ and $-++-$ samples for extrapolated scattered muon tracks (left) and hadron tracks (right) at $Z = 600\,\mathrm{cm}$ for scenario 2.

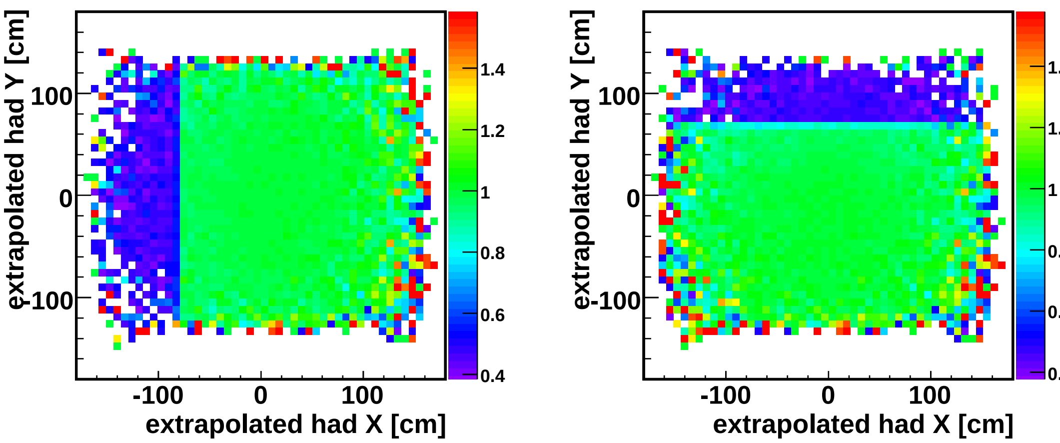

Figure A.7: Ratios of XY-distribution of $+--+$ and $-++-$ samples for extrapolated hadron tracks at $Z = 600\,\mathrm{cm}$. Left: scenario 3. Right: scenario 4.

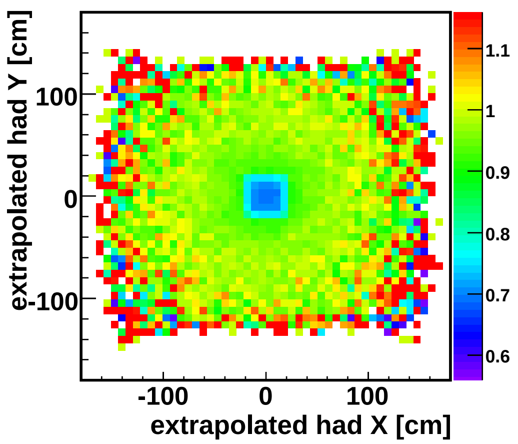

Figure A.8: Ratios of XY-distribution of $+--+$ and $-++-$ samples for extrapolated hadron tracks at $Z = 600\,\text{cm}$ for scenario 5.

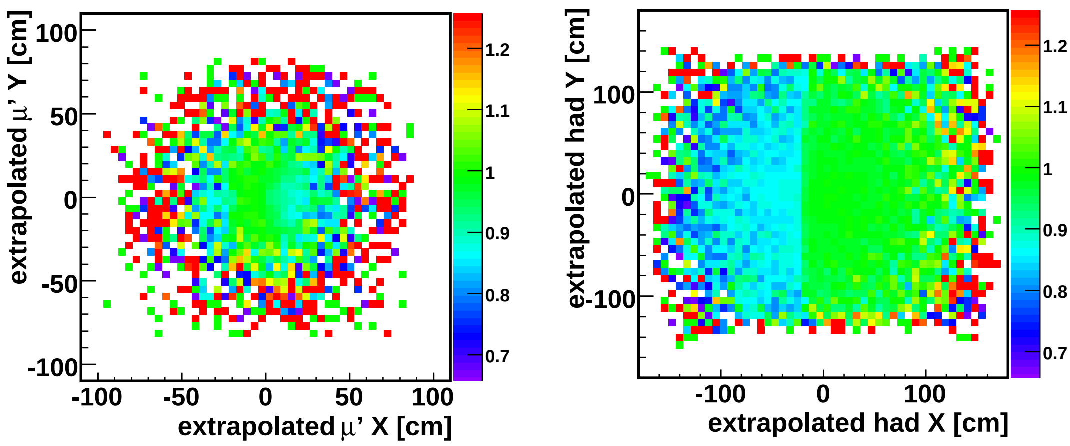

Figure A.9: Ratios of XY-distribution of $+--+$ and $-++-$ samples for extrapolated scattered muon (left) and hadron (right) tracks at $Z = 600\,\text{cm}$ for scenario 6.

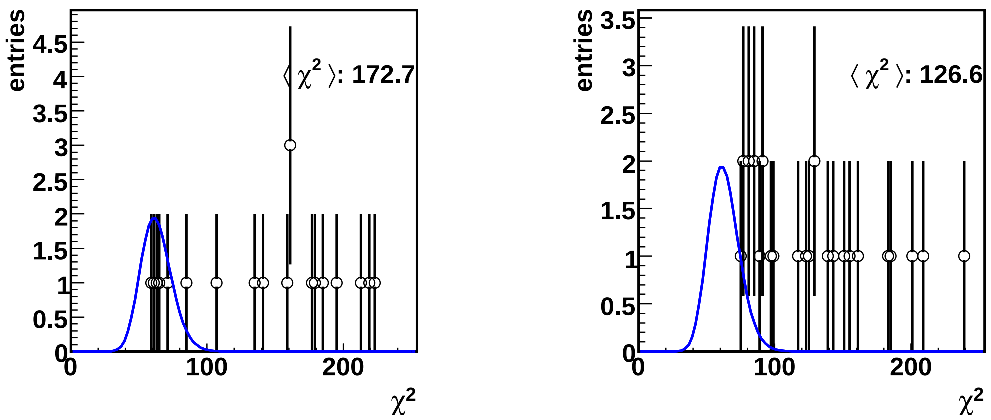

Figure A.10: χ^2-distribution of Dtest for Monte Carlo data. On the left for scenario 3 and on the right for scenario 5. The blue line indicates the theoretical expected distribution with mean value 63.

B. Hadron Pair Asymmetries

B.1 Binning

The following bins in x, z and M_{inv} are used for h^+h^--pairs:

x	z	$M_{inv}[\text{GeV}/c^2]$
$01: 0.003 < x \leq 0.008$	$01: 0.20 < z \leq 0.25$	$01: 0.00 < M_{inv} \leq 0.40$
$02: 0.008 < x \leq 0.013$	$02: 0.25 < z \leq 0.30$	$02: 0.40 < M_{inv} \leq 0.50$
$03: 0.013 < x \leq 0.020$	$03: 0.30 < z \leq 0.35$	$03: 0.50 < M_{inv} \leq 0.60$
$04: 0.020 < x \leq 0.032$	$04: 0.35 < z \leq 0.40$	$04: 0.60 < M_{inv} \leq 0.70$
$05: 0.032 < x \leq 0.050$	$05: 0.40 < z \leq 0.50$	$05: 0.70 < M_{inv} \leq 0.80$
$06: 0.050 < x \leq 0.080$	$06: 0.50 < z \leq 0.65$	$06: 0.80 < M_{inv} \leq 0.90$
$07: 0.080 < x \leq 0.130$	$07: 0.65 < z \leq 0.80$	$07: 0.90 < M_{inv} \leq 1.00$
$08: 0.130 < x \leq 0.210$	$08: 0.80 < z \leq 1.00$	$08: 1.00 < M_{inv} \leq 1.20$
$09: 0.210 < x \leq 1.000$		$09: 1.20 < M_{inv} \leq 1.60$
		$10: 1.60 < M_{inv} \leq 100$

B.2 Comparison of the Two Approaches to Built Final Asymmetries

In Fig. B.1 the final results as a function of x, z and M_{inv} for the two approaches are shown. The result 'W25-43' is obtained in fitting the 'total' data set and the result 'weighted mean' is obtained by building the weighted mean of the results of the six double periods. Both results are well compatible with each other. The pulls between the two results are shown in Fig. B.2. The mean is compatible with zero and the largest deviation is smaller than 40 % of the statistical error.

B.3 Numerical Values

B.4 Kinematical Correlation Plots

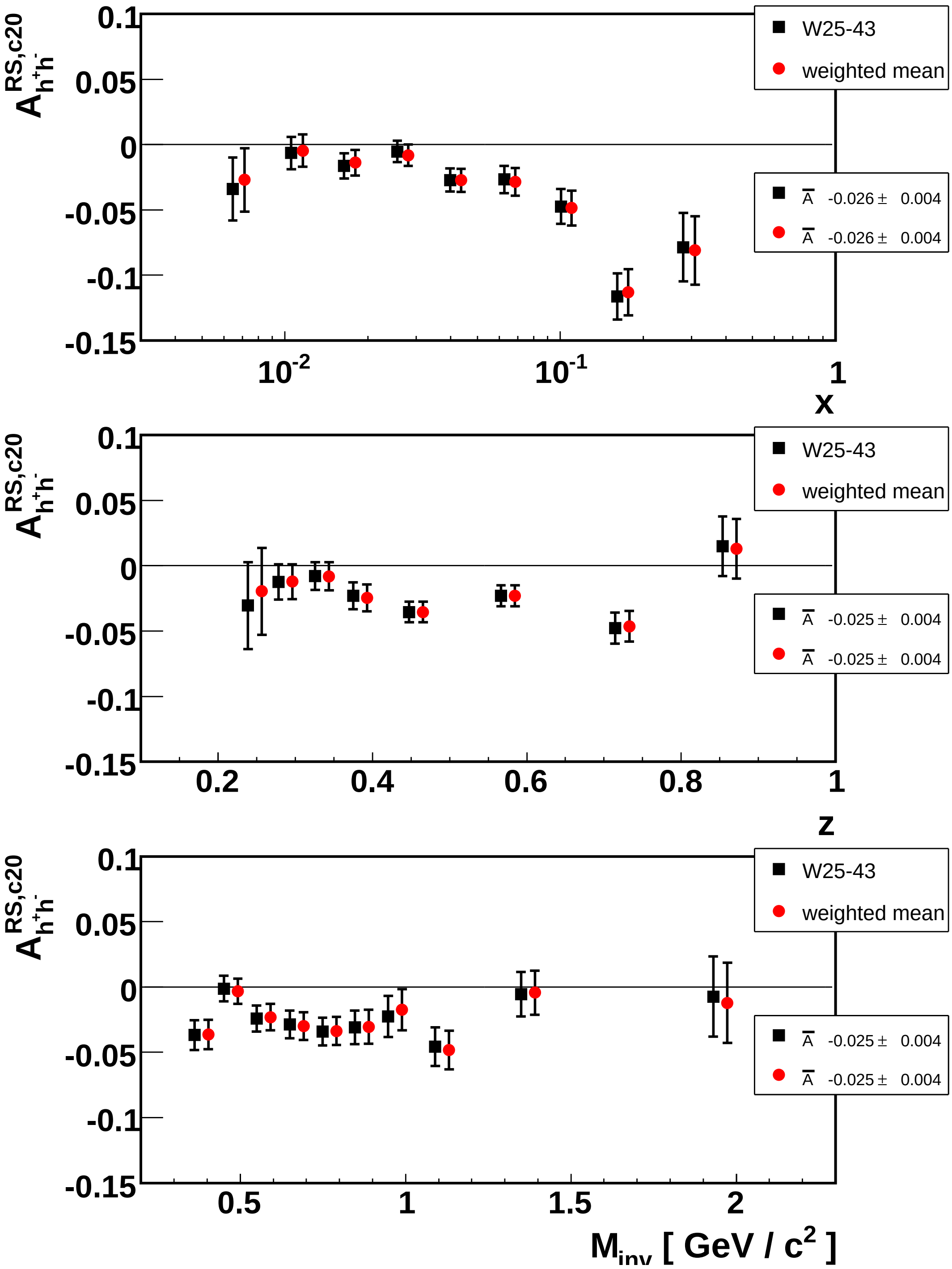

Figure B.1: Comparison of results extracted with UB SA obtained by fitting the 'total' data set (W25-43) and obtained as weighted mean of the results of the six double periods. Mean asymmetries, Ā, are given.

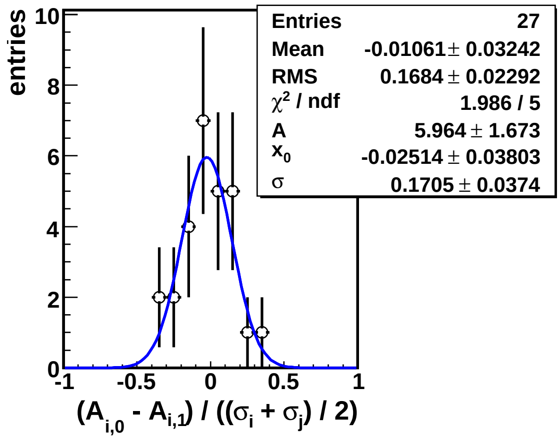

Figure B.2: Pulls between results extracted with UB SA obtained by fitting the 'total' data set and obtained as weighted mean of the results of the six double periods.

Table B.1: Numerical values for RS asymmetry binned in x. The systematical error is $\sigma_i^{sys} = \sqrt{(0.71 \cdot \sigma_i^{stat})^2 + (0.03 \cdot |A_i|)^2}$. Q^2 is given in $(\mathrm{GeV}/c^2)^2$ and M_{inv} is given in GeV/c^2. The mean target polarization P is 83 %. In Fig. B.3 $\langle Q^2 \rangle$, $\langle y \rangle$, $\langle z \rangle$ and $\langle M_{inv} \rangle$ are shown in bins of x.

bin range	$A^{RS} \pm \sigma_{stat}$	$\langle Q^2 \rangle$	$\langle y \rangle$	$\langle x \rangle$	$\langle z \rangle$	$\langle M_{inv} \rangle$	$\langle D_{nn} \rangle$	$\langle f \rangle$	$\langle D_{nn} f P \rangle$
(0.003:0.008]	-0.034 ± 0.024	1.23	0.65	0.006	0.44	0.744	0.61	0.14	0.072
(0.008:0.013]	-0.006 ± 0.012	1.48	0.47	0.011	0.45	0.699	0.80	0.14	0.095
(0.013:0.020]	-0.016 ± 0.010	1.75	0.36	0.016	0.46	0.656	0.88	0.14	0.106
(0.020 0.032]	-0.005 ± 0.008	2.10	0.28	0.026	0.47	0.610	0.93	0.14	0.111
(0.032:0.050]	-0.027 ± 0.009	2.82	0.24	0.040	0.48	0.576	0.94	0.14	0.113
(0.050:0.080]	-0.027 ± 0.011	4.37	0.23	0.063	0.48	0.565	0.95	0.15	0.114
(0.080:0.130]	-0.047 ± 0.013	6.90	0.23	0.101	0.48	0.552	0.95	0.15	0.117
(0.130:0.210]	-0.116 ± 0.018	10.79	0.22	0.161	0.48	0.533	0.95	0.16	0.123
(0.210:1.000]	-0.079 ± 0.026	22.13	0.26	0.280	0.48	0.526	0.93	0.17	0.134

Table B.2: Numerical values for RS asymmetry binned in z. The systematical error is $\sigma_i^{sys} = \sqrt{(0.71 \cdot \sigma_i^{stat})^2 + (0.03 \cdot |A_i|)^2}$. Q^2 is given in $(\mathrm{GeV}/c^2)^2$ and M_{inv} is given in GeV/c^2. The mean target polarization P is 83 %. In Fig. B.4 $\langle Q^2\rangle$, $\langle y\rangle$, $\langle x\rangle$ and $\langle z\rangle$ are shown in bins of x.

bin range	$A^{RS} \pm \sigma_{stat}$	$\langle Q^2\rangle$	$\langle y\rangle$	$\langle x\rangle$	$\langle z\rangle$	$\langle M_{inv}\rangle$	$\langle D_{nn}\rangle$	$\langle f\rangle$	$\langle D_{nn} f P\rangle$
(0.20:0.25]	-0.030 ± 0.033	3.44	0.45	0.03	0.24	0.506	0.80	0.14	0.096
(0.25:0.30]	-0.012 ± 0.013	3.36	0.38	0.04	0.28	0.576	0.86	0.14	0.103
(0.30:0.35]	-0.008 ± 0.011	3.32	0.34	0.04	0.33	0.630	0.88	0.14	0.106
(0.35:0.40]	-0.023 ± 0.010	3.31	0.32	0.04	0.37	0.671	0.89	0.15	0.108
(0.40:0.50]	-0.035 ± 0.008	3.30	0.31	0.04	0.45	0.719	0.90	0.15	0.109
(0.50:0.65]	-0.023 ± 0.008	3.28	0.30	0.05	0.57	0.783	0.91	0.15	0.110
(0.65:0.80]	-0.048 ± 0.012	3.19	0.29	0.05	0.71	0.856	0.91	0.15	0.111
(0.80:1.00]	0.015 ± 0.023	2.97	0.34	0.03	0.85	0.918	0.88	0.14	0.106

Table B.3: Numerical values for RS asymmetry binned in M_{inv}. The systematical error is $\sigma_i^{sys} = \sqrt{(0.71 \cdot \sigma_i^{stat})^2 + (0.03 \cdot |A_i|)^2}$ is given in $(\mathrm{GeV}/c^2)^2$ and M_{inv} is given in GeV/c^2. The mean target polarization P is 83 %. In Fig. B.5 $\langle Q^2\rangle$, $\langle y\rangle$, $\langle z\rangle$ and $\langle M_{inv}\rangle$ are shown in bins of x.

bin range	$A^{RS} \pm \sigma_{stat}$	$\langle Q^2\rangle$	$\langle y\rangle$	$\langle x\rangle$	$\langle z\rangle$	$\langle M_{inv}\rangle$	$\langle D_{nn}\rangle$	$\langle f\rangle$	$\langle D_{nn} f P\rangle$
(0.0:0.4]	-0.037 ± 0.011	3.32	0.30	0.05	0.41	0.361	0.90	0.15	0.110
(0.4:0.5]	-0.001 ± 0.010	3.29	0.30	0.05	0.43	0.451	0.90	0.15	0.110
(0.5:0.6]	-0.024 ± 0.010	3.30	0.31	0.04	0.44	0.549	0.90	0.15	0.109
(0.6:0.7]	-0.029 ± 0.011	3.29	0.32	0.04	0.46	0.650	0.90	0.15	0.108
(0.7:0.8]	-0.034 ± 0.011	3.24	0.32	0.04	0.48	0.749	0.89	0.15	0.108
(0.8:0.9]	-0.031 ± 0.013	3.27	0.33	0.04	0.49	0.846	0.89	0.15	0.107
(0.9:1.0]	-0.022 ± 0.016	3.31	0.33	0.04	0.50	0.947	0.88	0.15	0.107
(1.0:1.2]	-0.046 ± 0.015	3.28	0.34	0.04	0.52	1.090	0.88	0.14	0.106
(1.2:1.6]	-0.005 ± 0.017	3.28	0.36	0.04	0.55	1.349	0.86	0.14	0.104
(1.6:8.0]	-0.007 ± 0.031	3.37	0.41	0.03	0.60	1.930	0.83	0.14	0.099

Table B.4: Numerical values for integrated RS asymmetry. Q^2 is given in $(\mathrm{GeV}/c^2)^2$ and M_{inv} is given in GeV/c^2.

$A^{RS} \pm \sigma_{stat} \pm \sigma_{sys}$	$\langle Q^2\rangle$	$\langle y\rangle$	$\langle x\rangle$	$\langle z\rangle$	$\langle M_{inv}\rangle$	$\langle D_{nn}\rangle$	$\langle f\rangle$	$\langle P\rangle$	$\langle D_{nn} f P\rangle$
-0.025 ± 0.004 ± 0.003	3.29	0.32	0.04	0.47	0.718	0.89	0.15	0.83	0.108

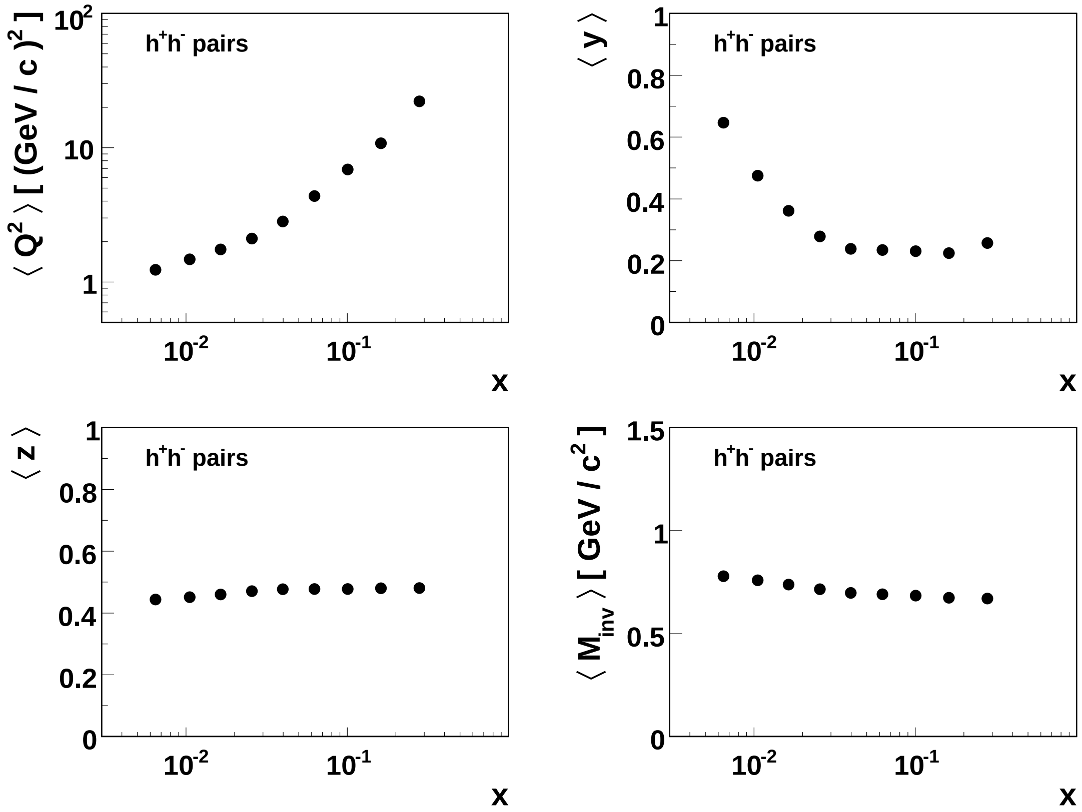

Figure B.3: Kinematical correlation plots versus bins in x of h^+h^--pair sample.

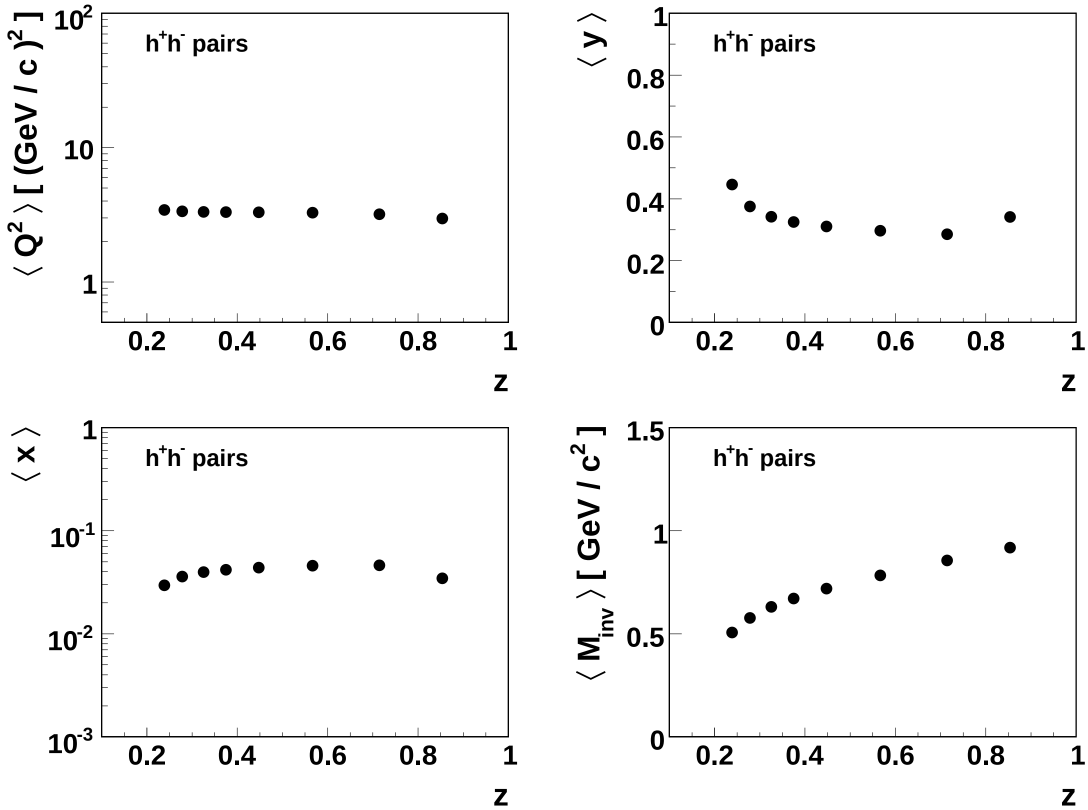

Figure B.4: Kinematical correlation plots versus bins in z of h^+h^--pair sample.

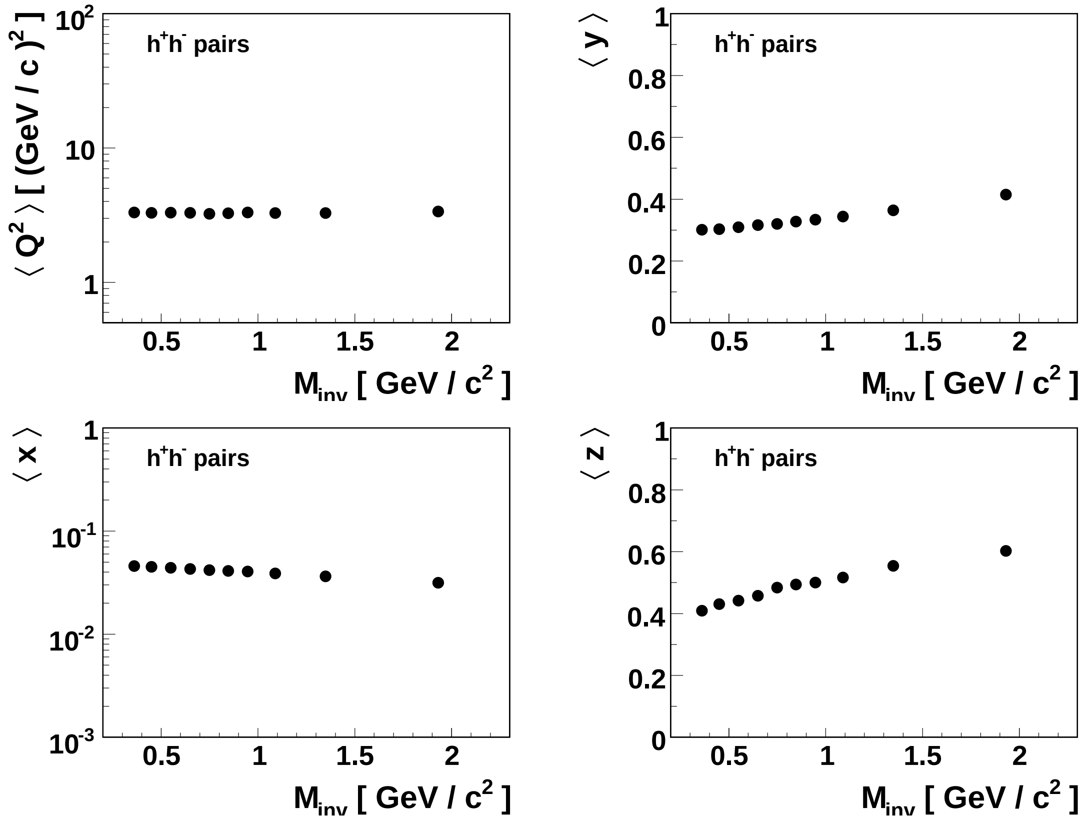

Figure B.5: Kinematical correlation plots versus bins in M_{inv} of h^+h^--pair sample.

C. Single Hadron Asymmetries

C.1 Binning

The following bins in x, z and p_T has are used for the analysis of single hadrons :

x	z	p_T[GeV/c]
$01 : 0.003 < x \leq 0.008$	$01 : 0.20 < z \leq 0.25$	$01 : 0.10 < M_{inv} \leq 0.20$
$02 : 0.008 < x \leq 0.013$	$02 : 0.25 < z \leq 0.30$	$02 : 0.20 < M_{inv} \leq 0.30$
$03 : 0.013 < x \leq 0.020$	$03 : 0.30 < z \leq 0.35$	$03 : 0.30 < M_{inv} \leq 0.40$
$04 : 0.020 < x \leq 0.032$	$04 : 0.35 < z \leq 0.40$	$04 : 0.40 < M_{inv} \leq 0.50$
$05 : 0.032 < x \leq 0.050$	$05 : 0.40 < z \leq 0.50$	$05 : 0.50 < M_{inv} \leq 0.60$
$06 : 0.050 < x \leq 0.080$	$06 : 0.50 < z \leq 0.65$	$06 : 0.60 < M_{inv} \leq 0.75$
$07 : 0.080 < x \leq 0.130$	$07 : 0.65 < z \leq 0.80$	$07 : 0.75 < M_{inv} \leq 0.90$
$08 : 0.130 < x \leq 0.210$	$08 : 0.80 < z \leq 1.00$	$08 : 0.90 < M_{inv} \leq 1.30$
$09 : 0.210 < x \leq 1.000$		$09 : 1.30 < M_{inv} \leq 25.0$

C.2 Systematic Studies: Additional Material

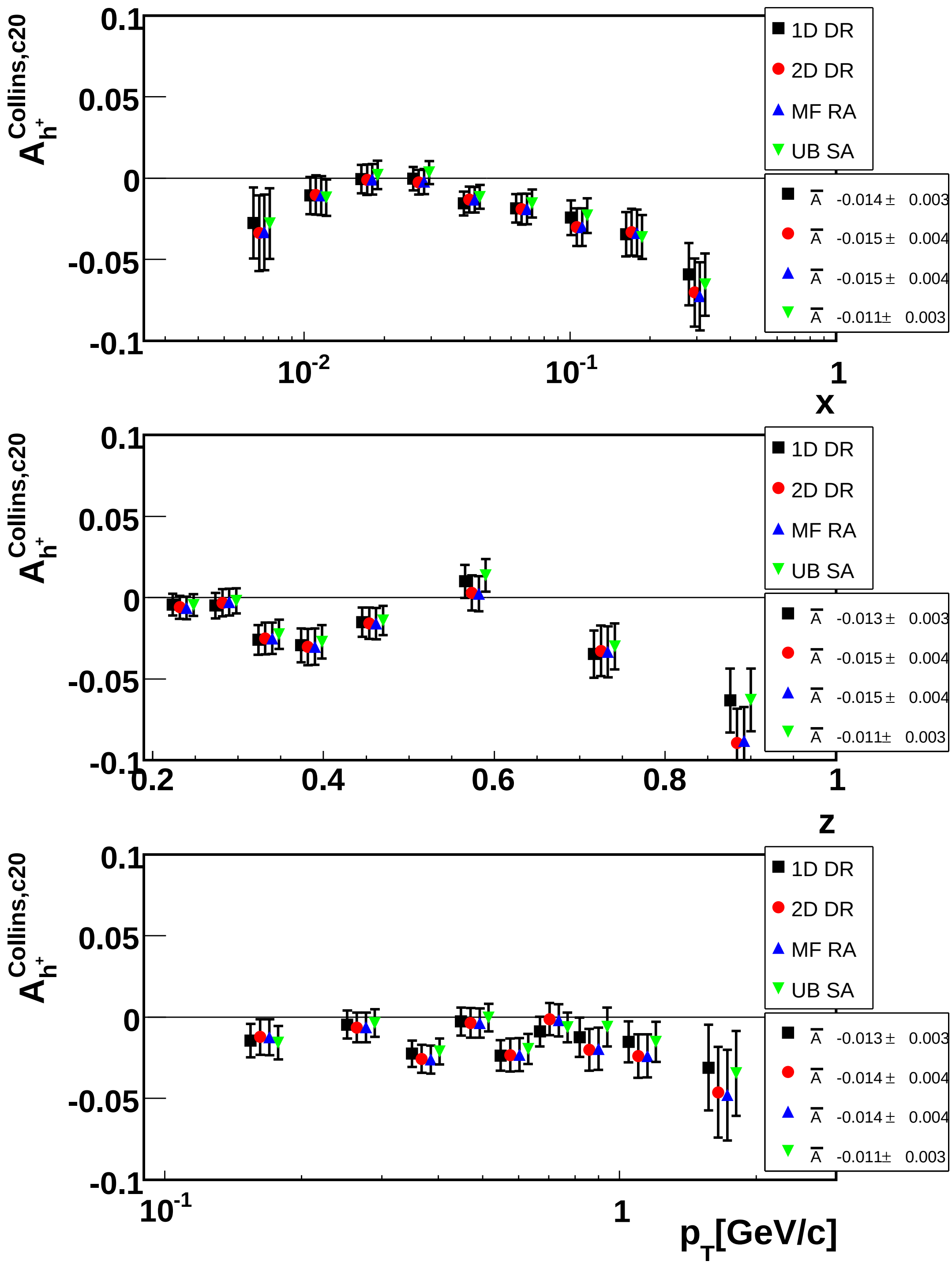

Figure C.1: Collins asymmetries for positive hadrons extracted with the four different methods as a function of x, z and p_T. Mean asymmetries, Ā, are given.

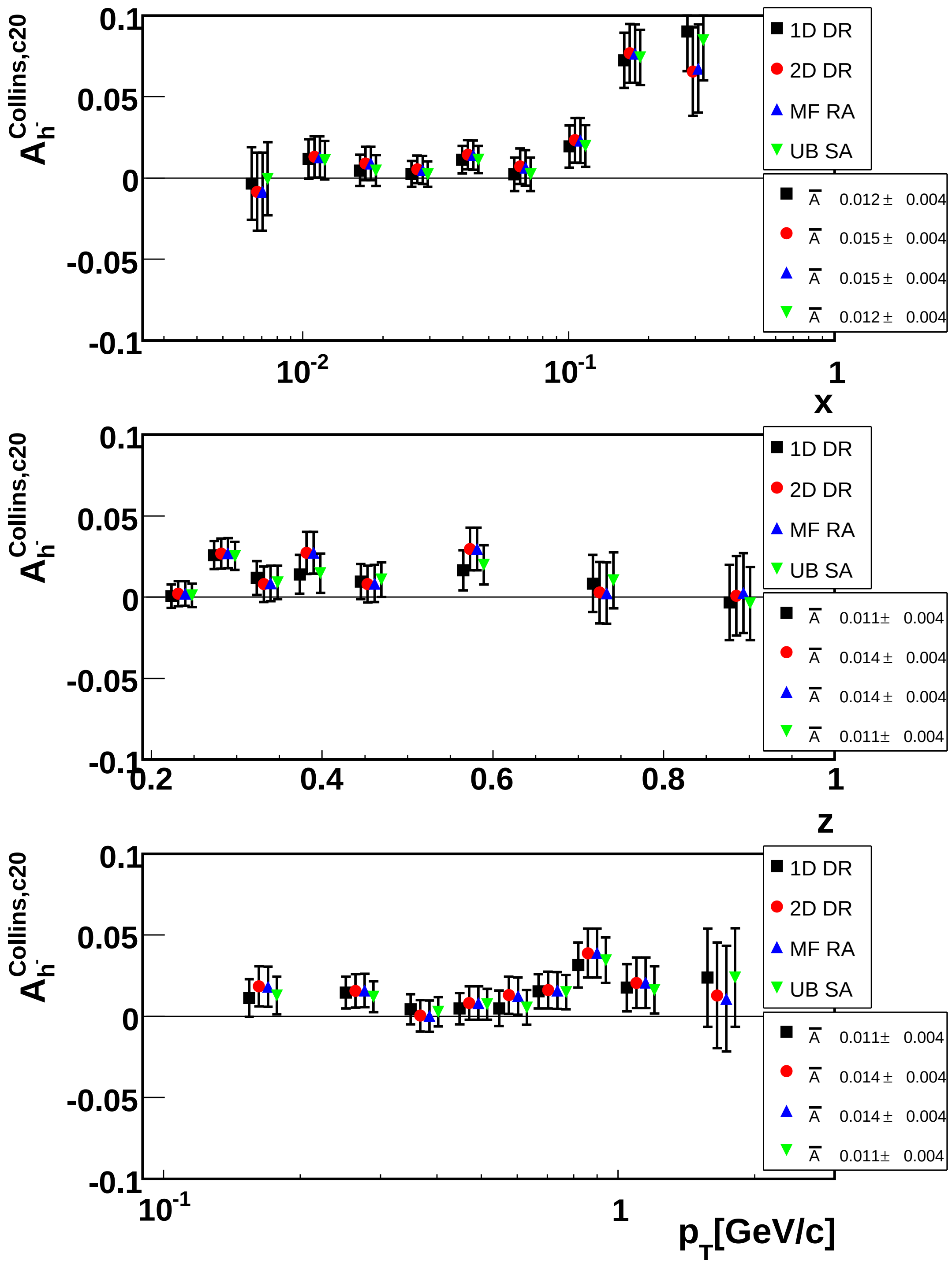

Figure C.2: Collins asymmetries for negative hadrons extracted with the four different methods as a function of x, z and p_T. Mean asymmetries, $\bar{\mathrm{A}}$, are given.

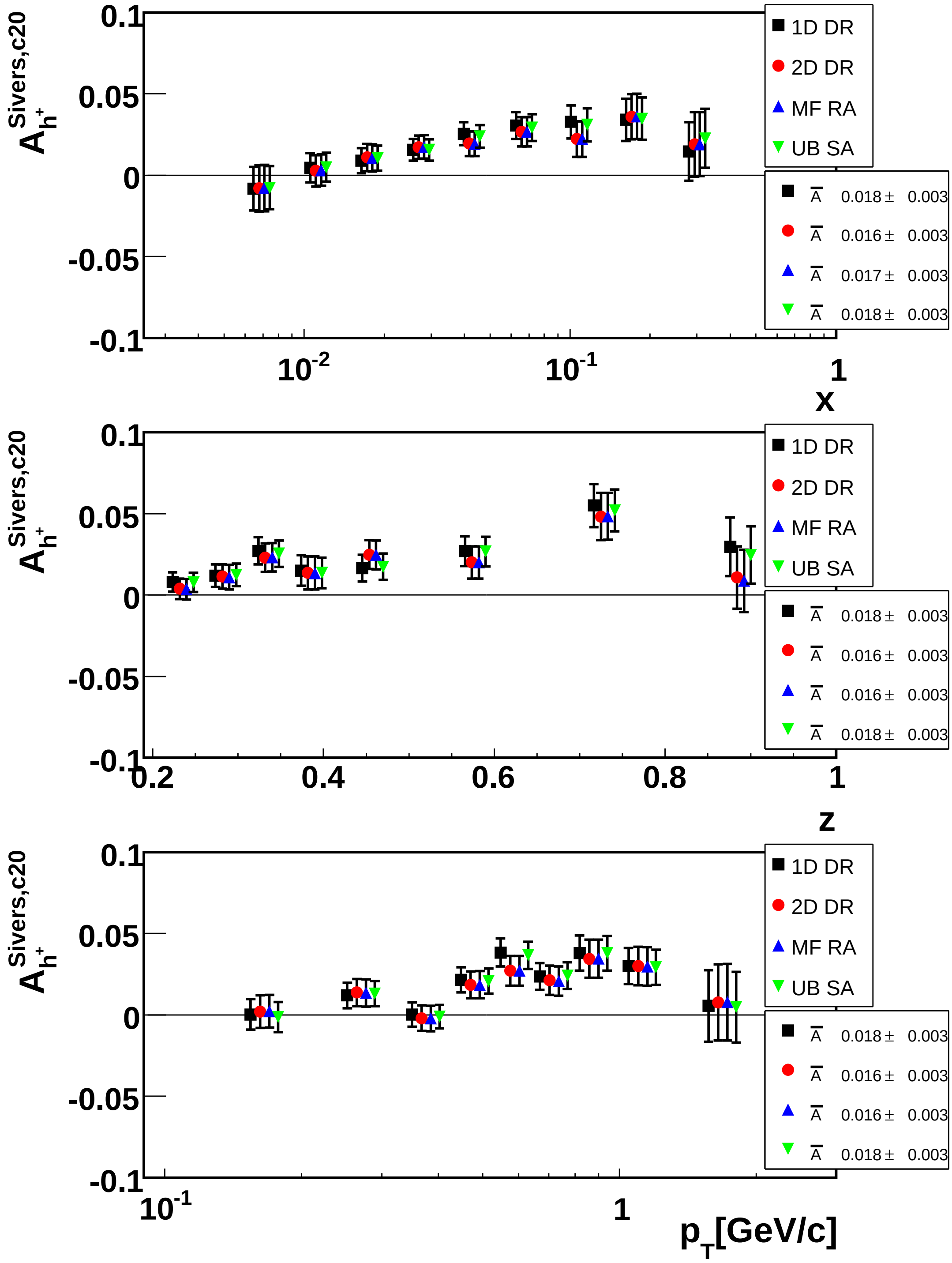

Figure C.3: Sivers asymmetries for positive hadrons extracted with the four different methods as a function of x, z and p_T. Mean asymmetries, $\bar{\mathrm{A}}$, are given.

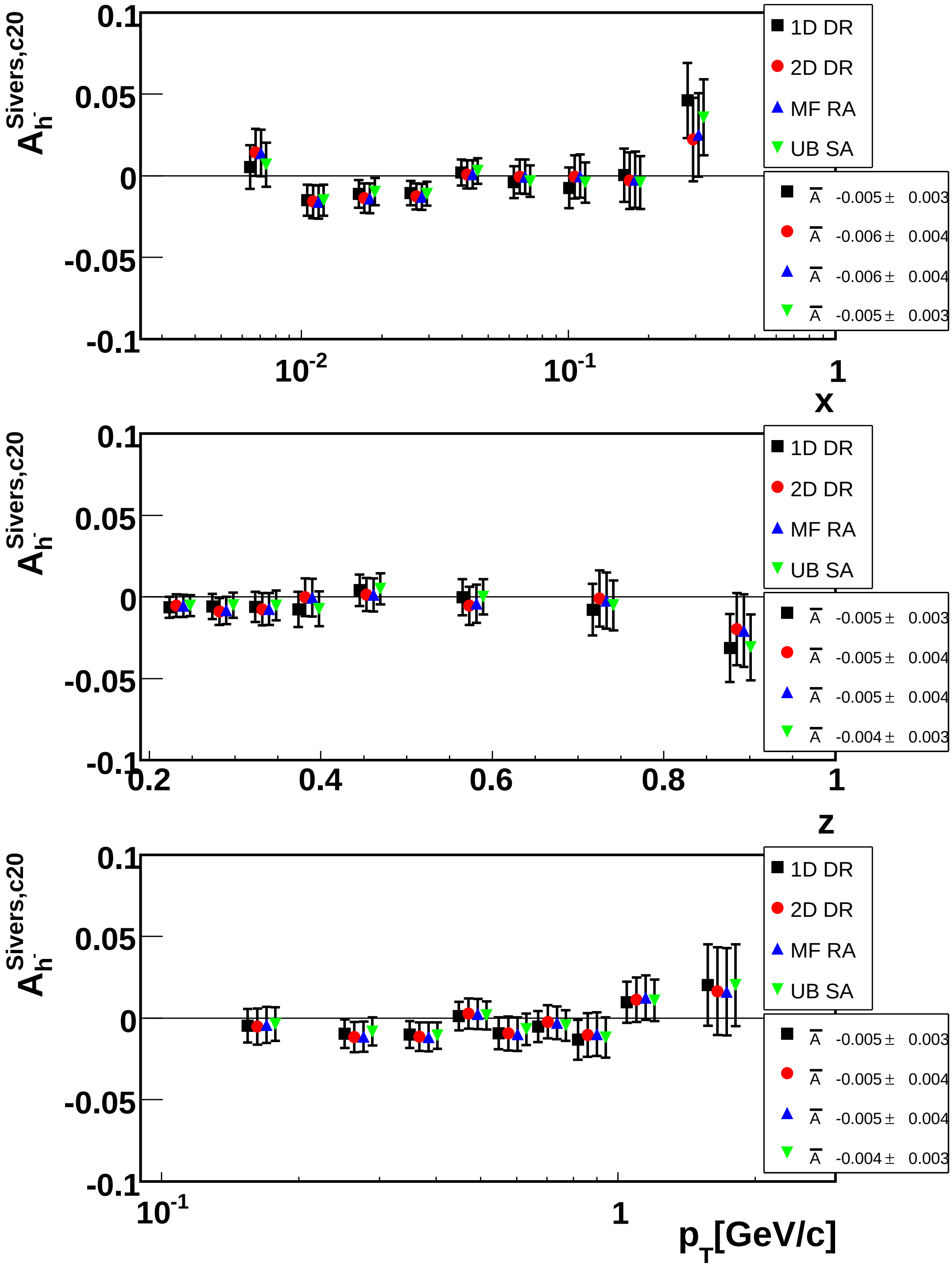

Figure C.4: Sivers asymmetries for negative hadrons extracted with the four different methods as a function of x, z and p_T. Mean asymmetries, $\bar{A}$, are given.

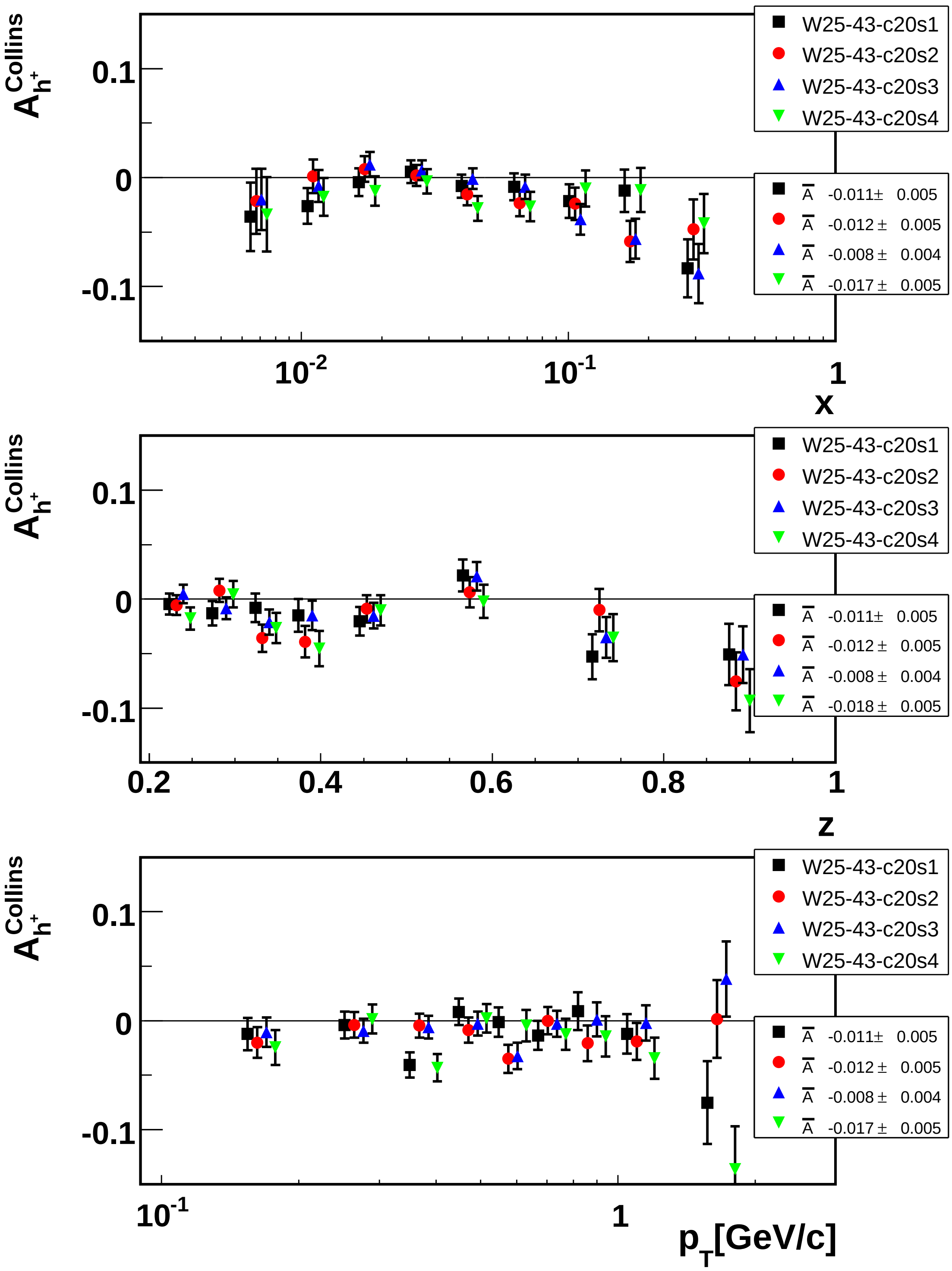

Figure C.5: Collins asymmetries for positive hadrons for segmenting the detector in left (c20s1), right (c20s2), top (c20s3) and bottom (c20s4). Mean asymmetries, $\bar{\mathrm{A}}$, are given.

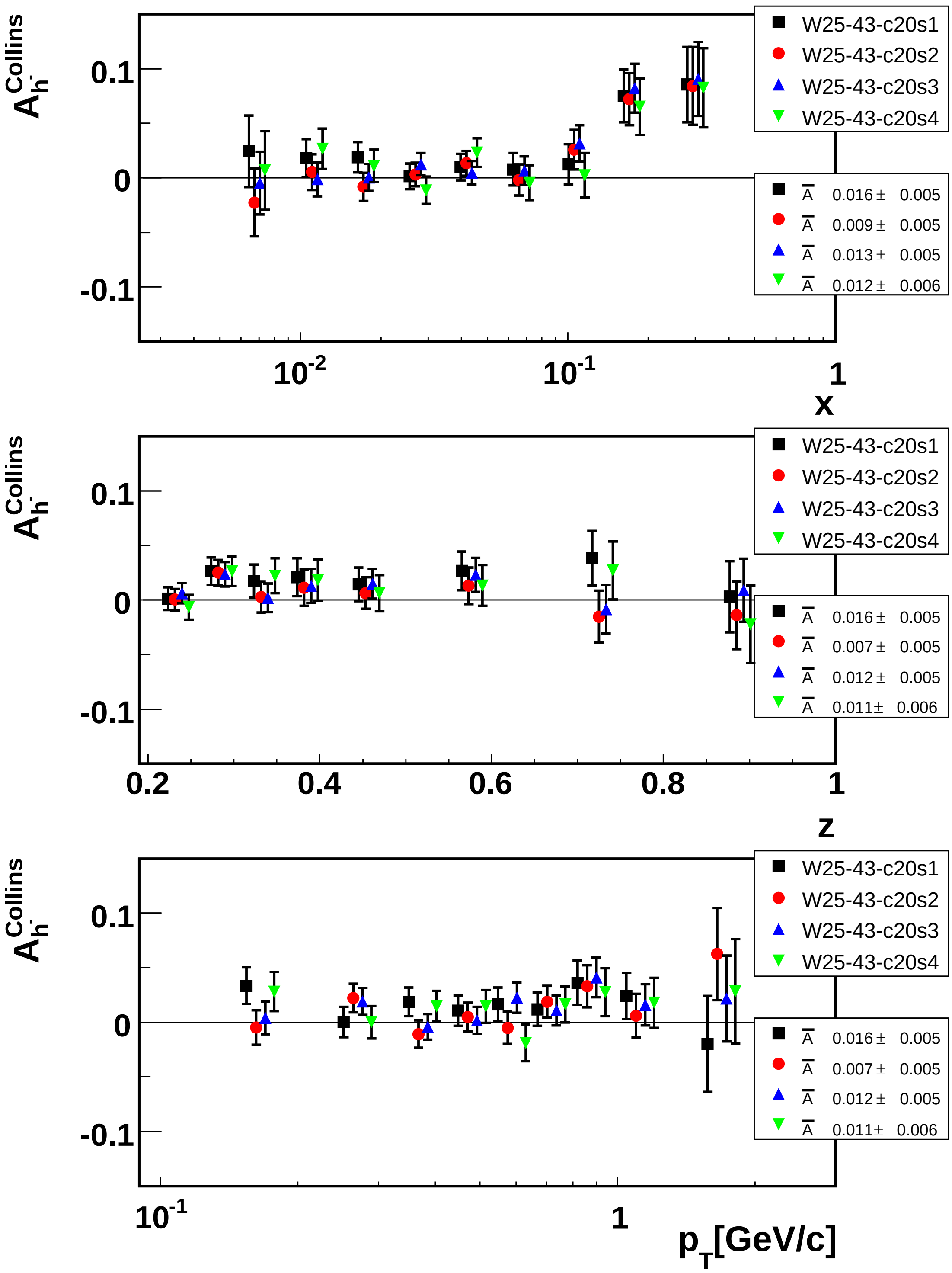

Figure C.6: Collins asymmetries for negative hadrons for segmenting the detector in left (c20s1), right (c20s2), top (c20s3) and bottom (c20s4). Mean asymmetries, Ā, are given.

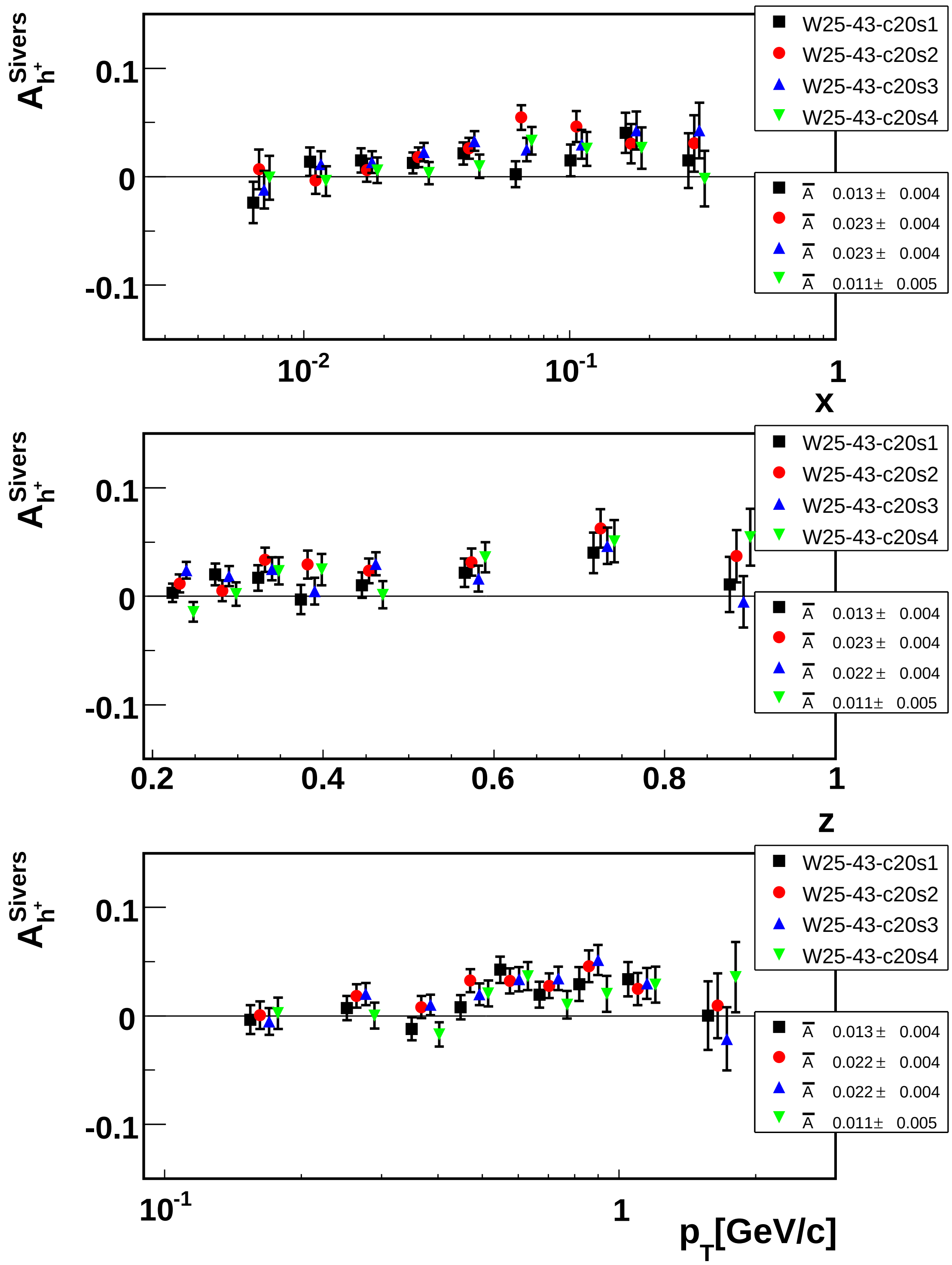

Figure C.7: Sivers asymmetries for positive hadrons for segmenting the detector in left (c20s1), right (c20s2), top (c20s3) and bottom (c20s4). Mean asymmetries, Ā, are given.

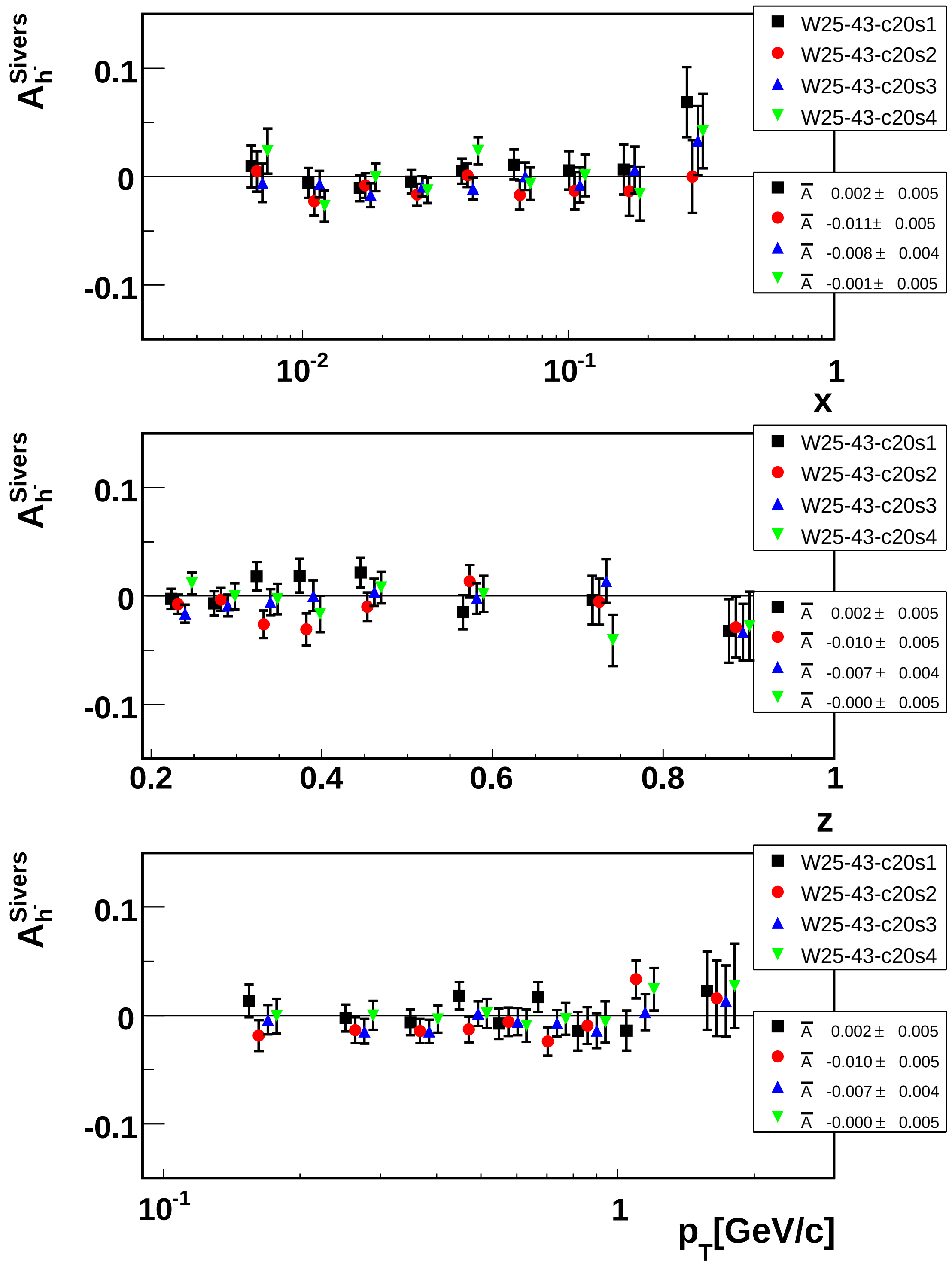

Figure C.8: Sivers asymmetries for negative (bottom) hadrons for segmenting the detector in left (c20s1), right (c20s2), top (c20s3) and bottom (c20s4). Mean asymmetries, Ā, are given.

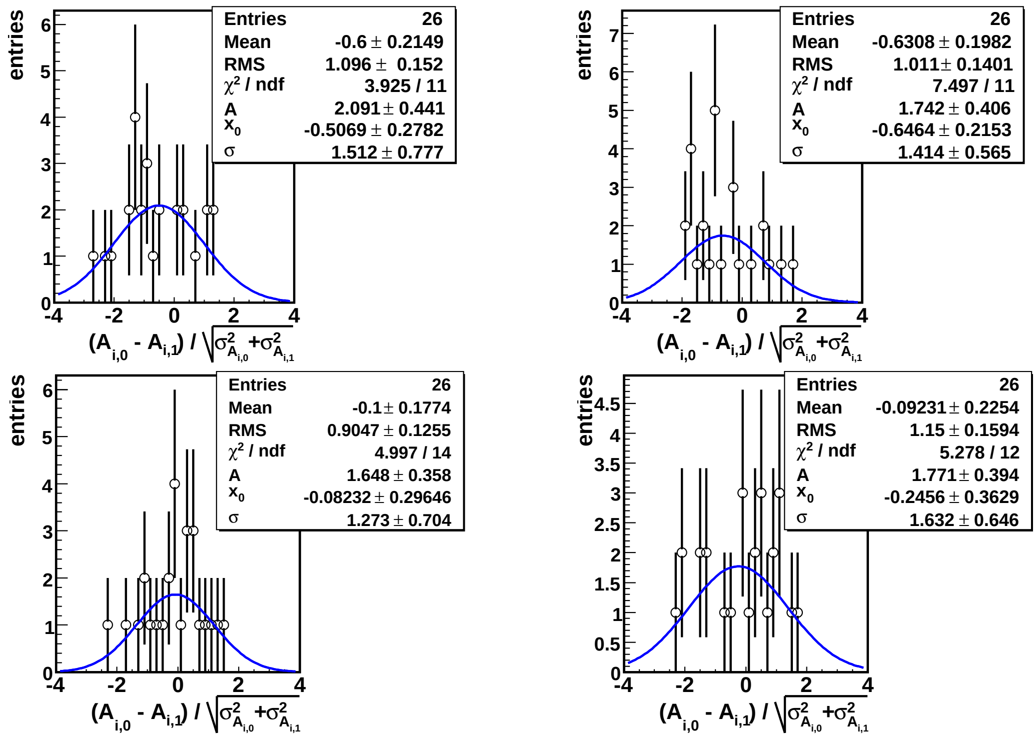

Figure C.9: Pulls between Collins results for positive (top) and negative (bottom) hadrons for Monte Carlo. Left: μ' detected in left or right half. Right: μ' detected in top or bottom half.

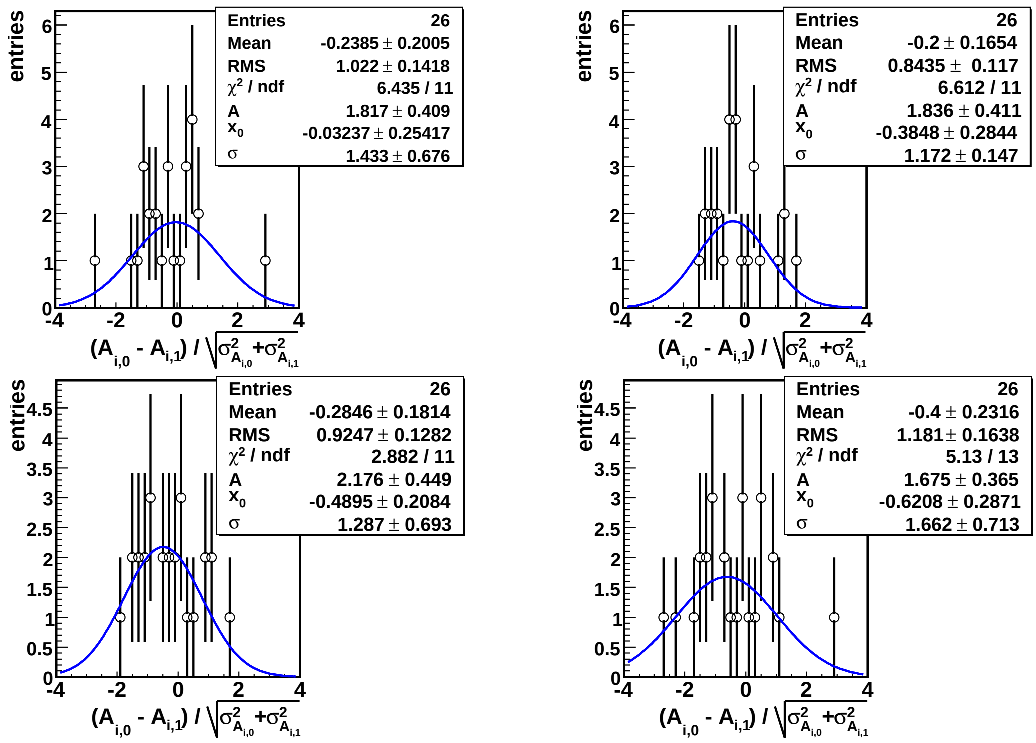

Figure C.10: Pulls between Sivers results for positive (top) and negative (bottom) hadrons for Monte Carlo. Left: μ' detected in left or right half. Right: μ' detected in top or bottom half.

References

[1] M. Gell-Mann, "A Schematic Model of Baryons and Mesons", *Phys. Lett.* **8** (1964) 214–215.

[2] G. Zweig, "An SU_3 model for strong interaction symmetry and its breaking", *CERN preprints* **TH-401, TH-412** (1964) .

[3] R. P. Feynman, "Very high-energy collisions of hadrons", *Phys. Rev. Lett.* **23** (1969) 1415–1417.

[4] D. J. Gross and F. Wilczek, "ULTRAVIOLET BEHAVIOR OF NON-ABELIAN GAUGE THEORIES", *Phys. Rev. Lett.* **30** (1973) 1343–1346.

[5] H. D. Politzer, "RELIABLE PERTURBATIVE RESULTS FOR STRONG INTERACTIONS?", *Phys. Rev. Lett.* **30** (1973) 1346–1349.

[6] **PLUTO** Collaboration, C. Berger *et al.*, "Evidence for Gluon Bremsstrahlung in e+ e- Annihilations at High-Energies", *Phys. Lett.* **B86** (1979) 418.

[7] **European Muon** Collaboration, J. Ashman *et al.*, "A measurement of the spin asymmetry and determination of the structure function g(1) in deep inelastic muon proton scattering", *Phys. Lett.* **B206** (1988) 364.

[8] J. P. Ralston and D. E. Soper, "Production of Dimuons from High-Energy Polarized Proton Proton Collisions", *Nucl. Phys.* **B152** (1979) 109.

[9] **FNAL-E704** Collaboration, D. L. Adams *et al.*, "Analyzing power in inclusive pi+ and pi- production at high x(F) with a 200-GeV polarized proton beam", *Phys. Lett.* **B264** (1991) 462–466.

[10] M. Burkardt, A. Miller, and W. D. Nowak, "Spin-polarized high-energy scattering of charged leptons on nucleons", *Rept. Prog. Phys.* **73** (2010) 016201, `arXiv:0812.2208 [hep-ph]`.

[11] V. Barone and G. P. Ratcliffe, "Transverse Spin Physics", World Scientific, 2002.

[12] V. Barone, A. Drago, and P. G. Ratcliffe, "Transverse polarisation of quarks in hadrons", *Phys. Rept.* **359** (2002) 1–168, `arXiv:hep-ph/0104283`.

[13] R. L. Jaffe, "Spin, twist and hadron structure in deep inelastic processes", `arXiv:hep-ph/9602236`.

[14] A. V. Manohar, "An introduction to spin dependent deep inelastic scattering", arXiv:hep-ph/9204208.

[15] **Particle Data Group** Collaboration, C. Amsler *et al. Phys. Lett.* **B667** (2008) 194–201. and 2009 partial update for the 2010 edidion, http://pdg.lbl.gov.

[16] J. D. Bjorken, "Asymptotic Sum Rules at Infinite Momentum", *Phys. Rev.* **D179** (1969) 1547–1553.

[17] C. G. Callan and J. D. Gross, "The asymptotic behavior of electroproduction cross sections is shown to contain information about the constitution of the electric current.", *Phys. Rev. Lett.* **22** (1968) 156–159.

[18] M. Anselmino, A. Efremov, and E. Leader, "The theory and phenomenology of polarized deep inelastic scattering", *Phys. Rept.* **261** (1995) 1–124, arXiv:hep-ph/9501369.

[19] A. Bacchetta, "Probing the transverse spin of quarks in deep inelastic scattering", arXiv:hep-ph/0212025.

[20] P. J. Mulders and J. Rodrigues, "Transverse momentum dependence in gluon distribution and fragmentation functions", *Phys. Rev.* **D63** (2001) 094021, arXiv:hep-ph/0009343.

[21] R. L. Jaffe and X.-D. Ji, "Chiral odd parton distributions and polarized Drell-Yan", *Phys. Rev. Lett.* **67** (1991) 552–555.

[22] **QCDSF** Collaboration, M. Gockeler *et al.*, "Quark helicity flip generalized parton distributions from two-flavor lattice QCD", *Phys. Lett.* **B627** (2005) 113–123, arXiv:hep-lat/0507001.

[23] M. Wakamatsu, "Comparative analysis of the transversities and the longitudinally polarized distribution functions of the nucleon", *Phys. Lett.* **B653** (2007) 398–403, arXiv:0705.2917 [hep-ph].

[24] I. C. Cloet, W. Bentz, and A. W. Thomas, "Transversity quark distributions in a covariant quark- diquark model", *Phys. Lett.* **B659** (2008) 214–220, arXiv:0708.3246 [hep-ph].

[25] P. J. Mulders and R. D. Tangerman, "The complete tree-level result up to order 1/Q for polarized deep-inelastic leptoproduction", *Nucl. Phys.* **B461** (1996) 197–237, arXiv:hep-ph/9510301.

[26] K. Goeke, A. Metz, and M. Schlegel, "Parameterization of the quark-quark correlator of a spin- 1/2 hadron", *Phys. Lett.* **B618** (2005) 90–96, arXiv:hep-ph/0504130.

[27] A. Bacchetta and G. Schnell, "Summary talk of EINN'09 workshop on TMDs", 8th European Research Conference on "Electromagnetic Interactions with Nucleons and Nuclei" (EINN 2009), Milos Island, September, 2009.

[28] D. W. Sivers, "Single Spin Production Asymmetries from the Hard Scattering of Point-Like Constituents", *Phys. Rev.* **D41** (1990) 83.

[29] A. Bacchetta, M. Boglione, A. Henneman, and P. J. Mulders, "Bounds on transverse momentum dependent distribution and fragmentation functions", *Phys. Rev. Lett.* **85** (2000) 712–715, `arXiv:hep-ph/9912490`.

[30] J. Soffer, "Positivity constraints for spin dependent parton distributions", *Phys. Rev. Lett.* **74** (1995) 1292–1294, `arXiv:hep-ph/9409254`.

[31] **Fermilab E704** Collaboration, A. Bravar *et al.*, "Single-spin asymmetries in inclusive charged pion production by transversely polarized antiprotons", *Phys. Rev. Lett.* **77** (1996) 2626–2629.

[32] J. C. Collins, "Fragmentation of transversely polarized quarks probed in transverse momentum distributions", *Nucl. Phys.* **B396** (1993) 161–182, `arXiv:hep-ph/9208213`.

[33] S. J. Brodsky, D. S. Hwang, and I. Schmidt, "Final-state interactions and single-spin asymmetries in semi-inclusive deep inelastic scattering", *Phys. Lett.* **B530** (2002) 99–107, `arXiv:hep-ph/0201296`.

[34] J. C. Collins, "Leading-twist Single-transverse-spin asymmetries: Drell- Yan and Deep-Inelastic Scattering", *Phys. Lett.* **B536** (2002) 43–48, `arXiv:hep-ph/0204004`.

[35] A. V. Belitsky, X. Ji, and F. Yuan, "Final state interactions and gauge invariant parton distributions", *Nucl. Phys.* **B656** (2003) 165–198, `arXiv:hep-ph/0208038`.

[36] M. Burkardt and D. S. Hwang, "Sivers asymmetry and generalized parton distributions in impact parameter space", *Phys. Rev.* **D69** (2004) 074032, `arXiv:hep-ph/0309072`.

[37] M. Burkardt, "Spin-Orbit Correlations and Single-Spin Asymmetries", `arXiv:0709.2966 [hep-ph]`.

[38] M. Boglione and P. J. Mulders, "Time-reversal odd fragmentation and distribution functions in p p and e p single spin asymmetries", *Phys. Rev.* **D60** (1999) 054007, `arXiv:hep-ph/9903354`.

[39] D. Boer and P. J. Mulders, "Time-reversal odd distribution functions in leptoproduction", *Phys. Rev.* **D57** (1998) 5780–5786, `arXiv:hep-ph/9711485`.

[40] A. Bacchetta *et al.*, "Semi-inclusive deep inelastic scattering at small transverse momentum", *JHEP* **02** (2007) 093, `arXiv:hep-ph/0611265`.

[41] A. Bacchetta, M. Radici, F. Conti, and M. Guagnelli, "Weighted azimuthal asymmetries in a diquark spectator model", `arXiv:1003.1328 [hep-ph]`.

[42] **Belle** Collaboration, R. Seidl *et al.*, "Measurement of Azimuthal Asymmetries in Inclusive Production of Hadron Pairs in e+e- Annihilation at $\sqrt{s} = 10.58$ GeV", *Phys. Rev.* **D78** (2008) 032011, `arXiv:0805.2975 [hep-ex]`.

[43] M. Burkardt, "Impact parameter dependent parton distributions and transverse single spin asymmetries", *Phys. Rev.* **D66** (2002) 114005, arXiv:hep-ph/0209179.

[44] M. Burkardt, "Chromodynamic lensing and transverse single spin asymmetries", *Nucl. Phys.* **A735** (2004) 185–199, arXiv:hep-ph/0302144.

[45] A. V. Efremov, L. Mankiewicz, and N. A. Tornqvist, "Jet handedness as a measure of quark and gluon polarization", *Phys. Lett.* **B284** (1992) 394–400.

[46] X. Artru and J. C. Collins, "Measuring transverse spin correlations by 4 particle correlations in e+ e- $\rightarrow$ 2 jets", *Z. Phys.* **C69** (1996) 277–286, arXiv:hep-ph/9504220.

[47] A. Bacchetta and M. Radici, "Two-hadron semi-inclusive production including subleading twist", *Phys. Rev.* **D69** (2004) 074026, arXiv:hep-ph/0311173.

[48] A. Bianconi, S. Boffi, R. Jakob, and M. Radici, "Two-hadron interference fragmentation functions. I: General framework", *Phys. Rev.* **D62** (2000) 034008, arXiv:hep-ph/9907475.

[49] F. A. Ceccopieri, M. Radici, and A. Bacchetta, "Evolution equations for extended dihadron fragmentation functions", *Phys. Lett.* **B650** (2007) 81–89, arXiv:hep-ph/0703265.

[50] A. Bacchetta and M. Radici, "Partial-wave analysis of two-hadron fragmentation functions", *Phys. Rev.* **D67** (2003) 094002, arXiv:hep-ph/0212300.

[51] X. Artru, "The transverse spin", arXiv:hep-ph/0207309.

[52] F. Massmann, " Messung transversaler Spineffekte mittels zwei Hadronen Korrelation am COMPASS-Experiment", Phd thesis, University of Bonn, June, 2008.

[53] G. Bunce, N. Saito, J. Soffer, and W. Vogelsang, "Prospects for spin physics at RHIC", *Ann. Rev. Nucl. Part. Sci.* **50** (2000) 525–575, arXiv:hep-ph/0007218.

[54] **COMPASS** Collaboration, "COMPASS Medium and Long Term Plans", Letter of Intend, CERN-SPSC-2009-003, January, 2009.

[55] **COMPASS** Collaboration, "COMPASS-II Proposal", in preparation for submission to CERN SPSC, May, 2010.

[56] **PAX** Collaboration, V. Barone *et al.*, "Antiproton proton scattering experiments with polarization", arXiv:hep-ex/0505054.

[57] **COMPASS** Collaboration, A. Ferrero, "Measurement of transverse Lambda and Antilambda polarization at COMPASS", *AIP Conf. Proc.* **915** (2007) 436–440.

[58] **COMPASS** Collaboration, T. Negrini, "Lambda polarization with a transversely polarized proton target at the COMPASS experiment", *AIP Conf. Proc.* **1149** (2009) 656–659.

[59] **COMPASS** Collaboration, P. Abbon *et al.*, "The COMPASS Experiment at CERN", *Nucl. Instrum. Meth.* **A577** (2007) 455–518, `arXiv:hep-ex/0703049`.

[60] P. Jasinski, "Private communications", (2010) .

[61] M. Hodenberg, "First Measurement of the Gluon Polarisation in the Nucleon using D Mesons at COMPASS", Phd thesis, University of Freiburg, November, 2005.

[62] A. Abragam, "The principles of nuclear magnetism", Clarendon Press, 1961. International series of monographs on physics.

[63] COMPASS Polarized Target Group, "Technical drawing of 40 mm NH3 target 2007", (2007) . `http://wwwcompass.cern.ch/compass/detector/target/Drawings/NH3target07v01bw.pdf`.

[64] C. Bernet *et al.*, "The COMPASS trigger system for muon scattering", *Nucl. Instrum. Meth.* **A550** (2005) 217–240.

[65] J. Barth, R. Pankin, and J. Pretz, "Study of large Q^2 trigger", COMPASS note 2008-7, September, 2008.

[66] R. K. Bock, H. Grote, D. Notz, M. Regler, and M. Regler, (ed.), "Data analysis techniques for high-energy physics experiments", *Camb. Monogr. Part. Phys. Nucl. Phys. Cosmol.* **11** (2000) 1–434.

[67] R. Brun *et al.*, "Root Users Guide 5.22", `http://root.cern.ch/`.

[68] M. Stolarski, "Update on status of 2007 data", COMPASS Analysis Meeting, August, 2007.

[69] H. Wollny, "Update on data quality 2007", COMPASS Analysis Meeting, August, 2008.

[70] H. Wollny, "Status of 2007 data quality", COMPASS Analysis Meeting, November, 2008.

[71] H. Wollny, "Data quality of new production and $\pm$ hadron pairs", COMPASS Transversity Meeting, January, 2009.

[72] H. Wollny, "Data quality of new production and 2h analysis", COMPASS Transversity Meeting, February, 2009.

[73] C. Schill, "Check of Pseudo-Efficiencies for all Detector Planes in 2007; Transversity Data -> Suggestions for Data Reproduction", COMPASS Transversity Meeting, November, 2008.

[74] S. Koblitz, "Determination of the Gluon Polarisation from Open Charm Production at COMPASS", Phd thesis, University of Mainz, October, 2008.

[75] A. Richter, "2007 Data Quality Checks: K^0-Tests ", COMPASS Transversity Meeting, March, 2008.

[76] A. Richter, "Quality Checks - Transverse 2007 Data K^0 test - new production", COMPASS Transversity Meeting, February, 2009.

[77] H. Wollny, "Stability of reconstruction quantities", COMPASS Analysis Meeting, September, 2007.

[78] J. Barwind, "Azimuthal Asymmetries in polarized Vector-Meson Production at the COMPASS Experiment", Diploma thesis, University of Freiburg, October, 2008.

[79] F. Heinsius, "Definitions of beam track, scattered muon and vertex", CORAL FAQ, May, 2006.

[80] G. Pesaro, "RICH fine tuning", COMPASS Analysis Meeting, January, 2009.

[81] **COMPASS** Collaboration, V. Y. Alexakhin *et al.*, "First measurement of the transverse spin asymmetries of the deuteron in semi-inclusive deep inelastic scattering", *Phys. Rev. Lett.* **94** (2005) 202002, `arXiv:hep-ex/0503002`.

[82] **COMPASS** Collaboration, E. S. Ageev *et al.*, "A new measurement of the Collins and Sivers asymmetries on a transversely polarised deuteron target", *Nucl. Phys.* **B765** (2007) 31–70, `arXiv:hep-ex/0610068`.

[83] **COMPASS** Collaboration, M. Alekseev *et al.*, "Collins and Sivers asymmetries for pions and kaons in muon-deuteron DIS", *Phys. Lett.* **B673** (2009) 127–135, `arXiv:0802.2160 [hep-ex]`.

[84] A. Kotzinian, "Remarks on acceptance effects in asymmetry extraction", COMPASS note 2007-2, Februar, 2007.

[85] A. Vossen, "Transverse Spin Asymmetries at the COMPASS Experiment", Phd thesis, University of Freiburg, April, 2008.

[86] G. Mallot, "Principle of a bias-free "2D" transverse asymmetry fit", COMPASS Analysis Meeting, September, 2007.

[87] D. Levenberg, "A Method for the Solution of Certain Problems in Least Squares", Quart. Appl. Math. 2, pages 164-168, 1944.

[88] D. Marquardt, "An Algorithm for Least-Squares Estimation of Nonlinar Parameters", SIAM J. Appl. Math., 11:431-441, 1963.4.

[89] B. Gough, "GNU Scientific Library Reference Manual", 2nd Edition. Network Theory Ltd., 2006. ISBN 0954161734., 1963.4.

[90] A. Kotzinian, "Some studies on azimuthal asymmetry extraction", COMPASS Analysis Meeting, May, 2007.

[91] A. Martin *et al.*, "On the role of the acceptance in the Unbinned Maximum Likelihood Method", COMPASS note 2009-13, November, 2009.

[92] T. Sjostrand, L. Lonnblad, and S. Mrenna, "PYTHIA 6.2: Physics and manual", `arXiv:hep-ph/0108264`.

[93] A. D. Martin, R. G. Roberts, W. J. Stirling, and R. S. Thorne, "Parton distributions incorporating QED contributions", *Eur. Phys. J.* **C39** (2005) 155–161, `arXiv:hep-ph/0411040`.

[94] R. L. Jaffe, X.-m. Jin, and J. Tang, "Interference Fragmentation Functions and the Nucleon's Transversity", *Phys. Rev. Lett.* **80** (1998) 1166–1169, `arXiv:hep-ph/9709322`.

[95] **HERMES** Collaboration, A. Airapetian *et al.*, "Evidence for a Transverse Single-Spin Asymmetry in Leptoproduction of pi+pi- Pairs", *JHEP* **06** (2008) 017, `arXiv:0803.2367 [hep-ex]`.

[96] X.-R. Lu, "Single-spin asymmetry in electro-production of pi+ pi- pairs from a transversely polarized proton target at the HERMES experiment",. DESY-THESIS-2008-034.

[97] A. Bacchetta, "Private communications", (2009) .

[98] M. Anselmino *et al.*, "Transversity and Collins Fragmentation Functions: Towards a New Global Analysis", `arXiv:0807.0173 [hep-ph]`.

[99] A. Bacchetta, F. A. Ceccopieri, A. Mukherjee, and M. Radici, "Asymmetries involving dihadron fragmentation functions: from DIS to e+e- annihilation", *Phys. Rev.* **D79** (2009) 034029, `arXiv:0812.0611 [hep-ph]`.

[100] J. She, Y. Huang, V. Barone, and B.-Q. Ma, "Transversity from two pion interference fragmentation", *Phys. Rev.* **D77** (2008) 014035, `arXiv:0711.0817 [hep-ph]`.

[101] A. Bacchetta and M. Radici, "Modeling dihadron fragmentation functions", *Phys. Rev.* **D74** (2006) 114007, `arXiv:hep-ph/0608037`.

[102] A. Vossen *et al.*, "First Measurement of the Interference Fragmentation Function in e^+e^- at Belle", `arXiv:0912.0353 [hep-ex]`.

[103] **COMPASS** Collaboration, R. Joosten, "Transversity signals in two hadron correlation at COMPASS", *AIP Conf. Proc.* **792** (2005) 957–960.

[104] **COMPASS** Collaboration, R. Joosten, "Transversity signals in two hadron correlation at COMPASS", *AIP Conf. Proc.* **915** (2007) 646–649.

[105] **COMPASS** Collaboration, A. Vossen, "Measurement of Transverse Spin Effects at COMPASS", `arXiv:0705.2865 [hep-ex]`.

[106] **HERMES** Collaboration, M. Diefenthaler, "HERMES measurements of Collins and Sivers asymmetries from a transversely polarised hydrogen target", `arXiv:0706.2242 [hep-ex]`.

[107] U. Elschenbroich, "Transverse spin structure of the proton studied in semi-inclusive DIS", *Eur. Phys. J.* **C50** (2007) 125–250.

[108] M. Anselmino *et al.*, "Update on transversity and Collins functions from SIDIS and e+ e- data", *Nucl. Phys. Proc. Suppl.* **191** (2009) 98–107, `arXiv:0812.4366 [hep-ph]`.

[109] M. Anselmino *et al.*, "Transversity and Collins functions from SIDIS and e+ e- data", *Phys. Rev.* **D75** (2007) 054032, `arXiv:hep-ph/0701006`.

[110] **HERMES** Collaboration, A. Airapetian *et al.*, "Observation of the Naive-T-odd Sivers Effect in Deep- Inelastic Scattering", *Phys. Rev. Lett.* **103** (2009) 152002, `arXiv:0906.3918 [hep-ex]`.

[111] M. Anselmino *et al.*, "Sivers Effect for Pion and Kaon Production in Semi-Inclusive Deep Inelastic Scattering", *Eur. Phys. J.* **A39** (2009) 89–100, `arXiv:0805.2677 [hep-ph]`.

[112] S. Arnold, A. V. Efremov, K. Goeke, M. Schlegel, and P. Schweitzer, "Sivers effect at Hermes, Compass and Clas12", `arXiv:0805.2137 [hep-ph]`.

[113] S. Kretzer, "Fragmentation functions from flavour-inclusive and flavour-tagged e+ e- annihilations", *Phys. Rev.* **D62** (2000) 054001, `arXiv:hep-ph/0003177`.

[114] D. de Florian, R. Sassot, and M. Stratmann, "Global analysis of fragmentation functions for pions and kaons and their uncertainties", *Phys. Rev.* **D75** (2007) 114010, `arXiv:hep-ph/0703242`.

Acknowledgments

This work would not have been possible without the people supporting me. Therefore I would like to thank:

- Prof. Dr. Horst Fischer for his excellent supervision in all the stages of my work.
- Prof. Dr. Kay Königsmann, for giving me the opportunity to write my thesis in his department as part of the COMPASS collaboration.
- Tillmann Guthörl, Katharina Schmidt, Rainer Joosten and Christian Schill for their careful proofreading and their constructive suggestions.
- Anselm Vossen and Wolfgang Käfer for introducing me to the world of COMPASS data analysis.
- The COMPASS collaboration, for the communicative atmosphere and the valuable input I got.
- My colleagues who shared the office with me. The former members of the group, Roland Hagemann, Donghee Kang and Jochen Barwind and my current colleagues Katharina Schmidt and Johannes ter Wolbeek for the good and relaxed atmosphere.
- Andreas Mutter for keeping the LINUX cluster running.
- Rainer Fastner for ensuring my daily caffeine intake.
- The whole working group for good company and help in all aspects of the working day: Andreas Mutter, Christian Schill, Christiane Imlintz, Elisabeth Gruber, Elisabeth Wursthorn, Florian Herrmann, Frank Nerling, Johannes ter Wolbeek, Julia Vogel, Katharina Schmidt, Khalil Rehmani, Louis Lauser, Rainer Fastner, Sebastian Schopferer, Susanne Rombach-Mikl and Tillmann Guthörl